Is trivalent manganese a ubiquitous part of the total dissolved manganese in soil solutions?

Doctoral thesis

for

the award of the doctoral degree

of the Faculty of Mathematics and Natural Sciences

of the University of Cologne

submitted by

Constantin Lux

accepted in the year 2026

„Die Wissenschaft sorgt dafür, dass Menschen Wahrheit
und Objektivität erreichen; sie lehrt die Menschen,
die Realität mit Staunen und Bewunderung zu akzeptieren,
ganz zu schweigen von der tiefen Ehrfurcht und Freude
vor der natürlichen Ordnung der Dinge.“

– Lise Meitner

Abstract

Dissolved trivalent manganese (Mn^{3+}) plays a critical role in natural environments by influencing key biogeochemical processes, including soil organic matter decomposition and carbon storage, organic pollutant degradation, and (trace) element cycling. Analytical advances in marine chemistry have demonstrated that natural organic ligands (NOLs) can complex and stabilize Mn^{3+}. A spectrophotometric approach combined with kinetic modeling, referred to as the porphyrin method, allows discrimination between dissolved divalent Mn (Mn^{2+}) and Mn^{3+}–NOL complexes.

In soils, however, Mn^{3+} has long been considered thermodynamically unstable and assumed to rapidly disproportionate into dissolved Mn^{2+} and solid Mn^{IV}. Due to the absence of reliable analytical methods, the $Mn^{2+}\leftrightarrow Mn^{IV}$ paradigm prevailed for decades, and dissolved Mn^{3+} was neglected, representing a critical knowledge gap in soil biogeochemistry. This thesis addresses this gap through three interrelated studies designed to overcome methodological limitations, elucidate mechanisms of Mn^{3+}–NOL complex formation, and demonstrate their persistence across broad pH and redox conditions. The overarching objective was to determine whether Mn^{3+} represents a ubiquitous part of total dissolved Mn (Mn_T) in soil solutions.

The porphyrin method was applied to forest floor solutions and soil solutions from an acidic forest site. Confronted with novel challenges in this analytical “black box”, the method was adapted to account for sample acidity and coloration, thereby improving its precision. As a result, Mn^{3+}–NOL complexes were reliably distinguished from Mn^{2+}, constituting up to 87% of dissolved Mn_T. The results provided the first evidence that Mn^{3+} is considerably more stable in soils than had previously been assumed. To explore principal mechanisms of Mn^{3+}–NOL complex formation, the pH-dependent and time-dependent dissolution of synthetic Mn oxides (birnessite and manganite) in the presence of forest floor-derived NOLs was investigated using batch experiments. Dissolved Mn_T speciation revealed that both oxidative and reductive abiotic reaction pathways promoted Mn^{3+}–NOL complex formation. The complexes were particularly stable under circumneutral pH conditions but exhibited metastability under strongly acidic conditions. To assess their relevance under typical environmental conditions, the formation and stability of Mn^{3+}–NOL complexes were investigated in redoximorphic soils. Microcosm experiments conducted

under defined redox conditions, complemented by *in situ* field investigations, provided laboratory- and field-based evidence of Mn^{3+}–NOL complexes. Both biotic and abiotic oxidative and reductive processes contributed to their formation across broad redox regimes, with proportions up to 90% relative to dissolved Mn_T. The findings indicate that waterlogging–aeration cycles promote transient Mn^{3+}–NOL complex formation.

In summary, this dissertation demonstrates that Mn^{3+}–NOL complexes are a substantial component of dissolved Mn_T in soils. By addressing the critical knowledge gap, this work provides mechanistic insight into Mn^{3+} formation pathways, necessitates a revision of the classical $Mn^{2+} \leftrightarrow Mn^{IV}$ paradigm, and opens new avenues for investigating the biogeochemical implications of Mn^{3+} in terrestrial ecosystems.

Zusammenfassung

Gelöstes dreiwertiges Mangan (Mn^{3+}) spielt in natürlichen Umgebungen eine entscheidende Rolle, indem es wichtige biogeochemische Prozesse beeinflusst, darunter die Zersetzung organischer Stoffe im Boden und die Kohlenstoffspeicherung, den Abbau organischer Schadstoffe und den Kreislauf von (Spuren-)Elementen. Analytische Fortschritte in der marinen Chemie haben gezeigt, dass natürliche organische Liganden (NOLs) Mn^{3+} komplexieren und stabilisieren können. Ein spektrophotometrischer Ansatz in Kombination mit kinetischer Modellierung, bezeichnet als Porphyrin-Methode, ermöglicht die Unterscheidung zwischen gelöstem zweiwertigem Mn (Mn^{2+}) und Mn^{3+}–NOL Komplexen.

In Böden galt Mn^{3+} jedoch lange Zeit als thermodynamisch instabil und es wurde angenommen, dass es rasch in gelöstes Mn^{2+} und fest gebundenes Mn^{IV} disproportioniert. Aufgrund des Fehlens zuverlässiger Analysemethoden setzte sich das Mn^{2+}↔Mn^{IV}-Paradigma jahrzehntelang durch und gelöstes Mn^{3+} wurde vernachlässigt, gleichbedeutend mit einer kritischen Wissenslücke in der Bodenbiogeochemie. Diese Arbeit befasst sich mit diesem Forschungsdefizit durch drei aufeinander aufbauende Studien, die darauf abzielen methodische Herausforderungen zu überwinden, die Mechanismen der Entstehung von Mn^{3+}–NOL Komplexen aufzuklären und ihre Persistenz über einen breiten pH- und Redoxbereich hinweg nachzuweisen. Das übergeordnete Ziel war es zu bestimmen, ob Mn^{3+} ein ubiquitärer Bestandteil des gelösten Mn_T in Bodenlösungen ist.

Die Porphyrin-Methode wurde an Auflagelösungen und Bodenlösungen eines sauren Waldstandortes angewendet. Angesichts neuer Herausforderungen in dieser analytischen „Black Box” wurde die Methode angepasst, um die Azidität und Färbung der Proben zu berücksichtigen und so die Präzision der Methode zu verbessern. Dadurch konnten Mn^{3+}–NOL Komplexe zuverlässig von Mn^{2+} unterschieden werden, die bis zu 87 % des gelösten Mn_T ausmachten. Die Ergebnisse lieferten den ersten Beweis dafür, dass Mn^{3+} in Böden wesentlich stabiler ist als bisher angenommen. Um die Hauptmechanismen der Mn^{3+}–NOL Komplexbildung zu untersuchen, wurde die pH-abhängige und zeitabhängige Auflösung von synthetischen Mn-Oxiden (Birnessit und Manganit) in Gegenwart von aus Waldböden stammenden NOLs in Batch-Experimenten untersucht. Die Speziierung von gelöstem Mn_T zeigte, dass sowohl oxidative als auch reduktive abiotische Reaktionswege

die Bildung von Mn^{3+}–NOL Komplexen begünstigten. Die Komplexe waren unter nahezu neutralen pH-Bedingungen besonders stabil, zeigten jedoch unter stark sauren Bedingungen Metastabilität. Um ihre Relevanz unter typischen Umweltbedingungen zu bewerten, wurden die Bildung und Stabilität von Mn^{3+}–NOL Komplexen in redoximorphen Böden untersucht. Mikrokosmos-Experimente unter definierten Redoxbedingungen, ergänzt durch *in situ*-Felduntersuchungen, lieferten labor- und feldbasierte Nachweise für Mn^{3+}–NOL Komplexe. Sowohl biotische als auch abiotische oxidative und reduktive Prozesse trugen über ein breites Spektrum von Redoxbereichen hinweg zu ihrer Bildung bei, dabei erreichten sie einen Anteil von bis zu 90% am gelöstem Mn_T. Die Ergebnisse deuten darauf hin, dass Zyklen von Vernässung und Belüftung die vorübergehende Bildung von Mn^{3+}–NOL Komplexen fördern.

Zusammenfassend zeigt diese Dissertation, dass Mn^{3+}–NOL Komplexe ein wesentlicher Bestandteil des gelösten Mn_T in Böden sind. Durch die Schließung dieser kritischen Wissenslücke liefert diese Arbeit mechanistische Einblicke in die Bildungswege von Mn^{3+}, fordert eine Überarbeitung des klassischen $Mn^{2+} \leftrightarrow Mn^{IV}$-Paradigmas und eröffnet neue Wege für die Untersuchung der biogeochemischen Auswirkungen von Mn^{3+} in terrestrischen Ökosystemen.

Acknowledgements

First of all, I am deeply grateful to my supervisor, Prof. Dr. Tim Mansfeldt, for his continuous support, constructive discussions, thoughtful guidance, and the many opportunities he has provided, which have been essential for completing this thesis and for my development as a researcher.

Furthermore, I would like to express my sincere gratitude to:

- Prof. Dr. Thilo Rennert for reviewing this thesis, and Prof. Dr. Patrick Grunert for chairing the examination committee;
- the German Research Foundation (DFG) for financial support under the contract number Ma 2143/17-1, which made this research possible;
- Dr. Kristof Dorau and Dr. Stephan Opitz for their valuable assistance, constructive discussions, and reliable collaboration;
- Karin Greef for her consistent support and encouragement, which were always greatly appreciated;
- Dr. Martin Greve from the Research Institute for Forest Ecology and Forestry (FAWF) of the State of Rhineland-Palatinate, Trippstadt, Germany, for assistance in supplying the samples;
- Dr. Rainer Dohrmann and Dr. Kristian Ufer from the Federal Institute for Geosciences and Natural Resources (BGR), Hannover, Germany, as well as Prof. Dr. Sanjay Mathur and Prof. Dr. Matthias Wickleder from the Department of Chemistry, University of Cologne, Germany, for providing support with essential laboratory analyses;
- Nicole Mantke, whose technical expertise and dedicated assistance were invaluable;
- my (former) colleagues at AG Mansfeldt (Dr. Kristof Dorau, Jana Glombitza, Karin Greef, Katharina Huesmann, Esther Krist and Stefanie Staß) for their constructive feedback and the motivating, productive working atmosphere.

I would like to thank my family for their steadfast confidence and encouragement, which have always been a vital source of motivation for me. Finally, I would like to express my deepest gratitude to Jana Glombitza. Her encouragement, patience, and unwavering support have been invaluable throughout this journey, providing me with the strength to persevere.

Adenau, February 2026 Constantin Lux

Table of contents

List of figures

List of tables

Abbreviations

A	absorption ratio
AAS	atomic absorption spectrometry
AOS	average oxidation state
ATR FT-IR	attenuated total reflection Fourier-transform infrared spectroscopy
BET	Brunauer–Emmett–Teller method
BIX	biological index
DIC	dissolved inorganic carbon
DOC	dissolved organic carbon
DOC_{loss}	loss in dissolved organic carbon
DOM	dissolved organic matter
EC	electrical conductivity
EEM	excitation-emission matrix
E_H	redox potential
Em	emission
Ex	excitation
FDOM	fluorescent dissolved organic matter
Fe_d	dithionite-extractable iron
Fe_o	oxalate-extractable iron
Fe_T	total dissolved iron
FI	fluorescence index
HIX	humification index
HMW	high-molecular-weight
IC	inorganic carbon
ICP OES	inductively coupled plasma optical emission spectrometry
IR	inorganic reductant
LBB	leucoberbelin blue
LMW	low-molecular-weight
LMWOA	low-molecular-weight organic acid
MA	molar absorption

MnP	manganese peroxidase
Mn_T	total dissolved manganese
$Mn_{T(NOL)}$	(total dissolved Mn by) NOL-induced dissolution
MW	molecular weight
MR	moderately reducing conditions
NOL	natural organic ligand
OC	organic carbon
OM	organic matter
OX	(re)oxidizing conditions
PA	polyamide
POM	particulate organic matter
PP	polypropylene
PZC	point of zero charge
redox	reduction-oxidation
RMSE	root mean square error
S	spectral slope
SEM	scanning electron microscopy
SOM	soil organic matter
S_R	spectral slope ratio
SR	strongly reducing conditions
SSA	specific surface area
T(4-CP)P	α,β,γ,δ-tetrakis(4-carboxyphenyl)porphine
TC	total carbon
TN	total nitrogen
WR	weakly reducing conditions
XRD	X-ray powder diffraction
XRF	X-ray fluorescence spectroscopy

List of chemical elements, compounds and minerals

C	carbon
Ca^{2+}	dissolved divalent calcium
$CaCl_2$	calcium chloride
$Ca^{II}CO_3$	calcium carbonate
Cd^{2+}	dissolved divalent cadmium
$CdCl_2$	cadmium chloride
Cl^-	chloride ion
CO_2	carbon dioxide
CO_3^{2-}	carbonate
Fe	iron
Fe^{2+}	dissolved ferrous iron
Fe^{3+}	dissolved ferric iron
Fe^{II}	solid divalent iron
Fe^{III}	solid trivalent iron
$FeCO_3$	siderite
FeS	mackinawite
FeS_2	pyrite
H^+	hydrogen ion, proton
H_2S	hydrogen sulfide
HNO_3	nitric acid
HS^-	hydrosulfide
$KMnO_4$	potassium permanganate
Mn	manganese
Mn^{2+}	dissolved divalent manganese
Mn^{2+}–NOL	natural organic ligand-bound divalent manganese
Mn^{3+}	dissolved trivalent manganese
Mn^{3+}–NOL_{strong}	strongly bound dissolved trivalent manganese
Mn^{3+}–NOL_{weak}	weakly bound dissolved trivalent manganese
Mn^{II}	solid divalent manganese
$Mn^{II}Mn^{III}{}_2O_4$	hausmannite

Mn^{III}	solid trivalent manganese
Mn^{IV}	solid tetravalent manganese
$MnCl_2 \cdot 4H_2O$	manganese chloride tetrahydrate
$MnCO_3$	rhodochrosite
MnO_2	manganese dioxide
MnS	manganese sulfide
Na	sodium
NaN_3	sodium azide
$NaNO_3$	sodium nitrate
NaOH	sodium hydroxide
NH_4OH	ammonium hydroxide
NO_2^-	nitrite
NO_3^-	nitrate
O_2	molecular oxygen
$O_2^{\bullet-}$	superoxide (radical)
PO_4^{3-}	phosphate
S^{2-}	sulfide
SO_4^{2-}	sulfate
β–$Mn^{III}OOH$	feitknechtite
γ–$Mn^{III}O(OH)$	manganite
δ–$Mn^{III/IV}O_2$	birnessite

Chapter 1: Introduction

Manganese (Mn) is a widely distributed, redox-active micronutrient found in soils, sediments, surface waters and groundwater systems, and the atmosphere (Li et al., 2021). In aqueous environments, Mn predominantly occurs in the +2, +3, +4, and +6 oxidation states (Hem, 1963), enabling participation in diverse redox and enzymatic reactions (e.g., Hofrichter, 2002; Stumm and Morgan, 1996).

In soils, Mn speciation is primarily controlled by redox potential (E_H) and pH (Greathouse et al., 2014). Thermodynamically, dissolved divalent Mn (Mn^{2+}) is predicted to dominate under low-oxygen and increasingly acidic conditions, while solid $Mn^{III/IV}$ (hydr)oxides are favored in the presence of oxygen and at neutral to alkaline conditions (Hem, 1963). Dissolved Mn^{2+} occurs as a free cation, as a minor mineral constituent, or as insoluble phosphates and carbonates (Tebo et al., 2004). Traditionally, Mn^{2+} has been considered the dominant dissolved form contributing to total dissolved Mn (Mn_T), an assumption that has been challenged in marine geochemical systems throughout the last two decades. In particular, recent studies indicate that dissolved trivalent Mn (Mn^{3+}), stabilized by natural organic ligands (NOLs), may represent a substantial and previously overlooked fraction of Mn_T (Madison et al., 2011, 2013; Oldham et al., 2015). These Mn^{3+}–NOL complexes have since been increasingly recognized across soils, sediments, and marine environments, and are thought to play key roles in biogeochemical processes such as soil organic matter (SOM) decomposition, carbon (C) storage, and transformation of organic pollutants (Keiluweit et al., 2015; Oldham et al., 2015, 2017a–c, 2019; Stendahl et al., 2017; Wang et al., 2018; Zhang et al., 2023). Yet substantial uncertainties remain regarding their formation and stability under natural soil conditions. Understanding Mn_T speciation, with particular emphasis on Mn^{3+}–NOL complex formation and stability, is therefore essential for interpreting Mn mobility, reactivity, and its broader role in soil elemental cycling.

This chapter situates Mn^{3+} as an emerging and potentially relevant component of dissolved Mn_T in soil solutions. It provides an overview of the dissolved Mn_T species, Mn oxides, and SOM-derived NOLs as critical components in biotic and abiotic pathways of Mn^{3+}–NOL complex formation. In addition, analytical approaches for Mn_T determination and speciation are critically reviewed, highlighting recent methodological advances that

have enabled the qualitative and quantitative detection of Mn^{3+}–NOL complexes in natural soil solutions (Madison et al., 2011; Oldham et al., 2015). The final section outlines the scientific motivation and the preliminary research hypotheses addressed in three complementary studies designed to answer the overarching research question: "*Is trivalent manganese a ubiquitous part of the total dissolved manganese in soil solutions?*"

1.1 Manganese in the environment

Manganese is one of the most abundant trace metals in the Earth's crust (~790 mg kg^{-1}), ranking ninth overall and third among transition metals (Rudnick and Gao, 2014; Wiberg et al., 2017). In soils, Mn primarily originates from the weathering of Mn-bearing bedrock minerals and is commonly associated with ferromagnesian silicates as well as Fe-containing non-silicate minerals from the spinel (e.g., magnetite) and rutile (e.g., ilmenite) groups (Gilkes and McKenzie, 1988). Surface soil Mn mass fractions vary widely, ranging from <7–9,000 mg kg^{-1} globally, with typical mean values between 270 and 530 mg kg^{-1} (He et al., 2010). Soils developed from mafic (basic) volcanic rocks, such as Fe- and Mg-rich basalt or gabbro, or from Fe- and Mg-rich shales, contain high Mn mass fractions (>1,000 and 600 mg kg^{-1}, respectively). In contrast, soils derived from granite or sandstone exhibit lower Mn mass fractions (400 and 170 mg kg^{-1}, respectively) (Gilkes and McKenzie, 1988). Soluble Mn in soil solutions ranges from 20–30,000 µg L^{-1} in acidic forest soils and <1–3,000 µg L^{-1} in temperate arable soils (Amelung et al., 2018). Near the Earth's surface, Mn^{2+} is readily oxidized to solid Mn^{III} and Mn^{IV}, forming insoluble $Mn^{III/IV}$ (hydr)oxide minerals (hereafter "Mn oxides"), which play central roles in soil redox dynamics, cation exchange reactions and trace element cycling (Gilkes and McKenzie, 1988; Post, 1999).

Beyond its natural occurrence, Mn is widely used in industry, including batteries, catalysts, electrode materials, metal alloys, steel production, and medical imaging (Cloyd et al., 2018; Lee et al., 2025; Lv et al., 2021; Matsanga et al., 2025). Electrolytic Mn residues from industrial processes may infiltrate soils via leachates, representing a significant anthropogenic source of contamination (Wu et al., 2022).

Biologically, Mn is an essential micronutrient for microorganisms, plants, animals, and humans. It participates in photosynthesis, litter decomposition, pollutant degradation,

scavenging of reactive oxygen species, amino acid and chlorophyll synthesis, pathogen defense, hormone signaling, and formation of secondary metabolites such as lignin and flavonoids (e.g., Berg et al., 2007; Millaleo et al., 2010; Obeng et al., 2024; Wu et al., 2022; Zhang et al., 2023). Overexposure disrupts physiological homeostasis and can cause metabolic impairments and neurological disorders, including Parkinson's disease (Crossgrove and Zheng, 2004).

In plants, Mn deficiency or excess impair growth, causing interveinal chlorosis, leaf crinkling, and dark inclusions (Fernando and Lynch, 2015). Manganese bioavailability is influenced by soil pH, E_H, and temperature, while environmental stressors such as drought or acid rain can further exacerbate Mn overaccumulation (Fernando and Lynch, 2015; Sparrow and Uren, 2014).

In soils, Mn^{3+} acts as a key mediator in biogeochemical processes, including the decomposition of SOM, influencing terrestrial C balance (e.g., Berg et al., 2007; Keiluweit et al., 2015; Stendahl et al., 2017). During litter decomposition, Mn^{2+} released from senesced leaves is oxidized to reactive Mn^{3+} and subsequently to insoluble $Mn^{III/IV}$ oxides (Herndon et al., 2014; Keiluweit et al., 2015). Manganese peroxidase (MnP), a lignin-modifying enzyme, catalyzes the oxidation of Mn^{2+} to Mn^{3+}, which is stabilized by organic chelators. These Mn^{3+}–NOL complexes act as diffusible oxidants, initiating radical-mediated depolymerization and transforming lignocellulosic compounds (Hofrichter, 2002).

Beyond natural organic matter (OM) turnover, soluble Mn^{3+}–NOL complexes react more rapidly with organic pollutants than solid Mn oxides, accessing microsites unavailable to MnO_2 and facilitating their degradation (Sun et al., 2021; Wang et al., 2018; Zhang et al., 2023). Dissolved Mn^{3+} rapidly oxidizes Fe^{2+}, further illustrating its high reactivity (Kostka et al., 1995). These processes emphasize the environmental significance of Mn^{3+}–NOL complexes and the necessity for accurate quantification to elucidate their formation, stability, and persistence in soils.

1.2 Dissolved manganese – rise of dissolved trivalent manganese

In aqueous solution, Mn^{2+} is generally considered the dominant soluble Mn species due to its symmetrical half-filled d^5 (t_{2g}^3 e_g^2) electron configuration (Rudolph and Irmer, 2013) (Figure 1.1). Dissolved Mn^{2+} primarily forms octahedral complexes with aqua (H_2O),

hydroxide (OH^-), or oxido (O^{2-}) ligands (Gilkes and McKenzie, 1988; Luther, 2005). The $Mn(H_2O)_6^{2+}$ cation acts as a labile Lewis acid and readily undergoes ligand exchange. This lability facilitates inner-sphere complexation and one- or two-electron transfer reactions at Mn^{III} and Mn^{IV} oxide surfaces (Luther, 2005). Solid Mn^{IV} favors strong interactions with π-donor ligands due to unoccupied eg* orbitals (Luther, 2005) (Figure 1.1). Accordingly, Mn^{2+} and Mn^{IV} were long considered the dominant Mn forms in natural waters (Leeper, 1947; Wang et al., 2024).

Dissolved Mn^{3+} was historically underestimated because its d^4 (t_{2g}^3 e_g^1) configuration induces a Jahn–Teller-distorted octahedral geometry, promoting rapid disproportionation to Mn^{2+} and Mn^{IV} oxides in the absence of stabilizing NOLs [Eq. 1] (Biedermann and Palombari, 1978; Davies, 1969; Gilkes and McKenzie, 1988; Jahn and Teller, 1937).

$$2Mn^{3+}\,(aq) + 2H_2O \rightarrow MnO_2\,(s) + Mn^{2+}\,(aq) + 4H^+ \qquad \log_{10} K \approx 7\text{–}9 \qquad \text{[Eq. 1]}$$

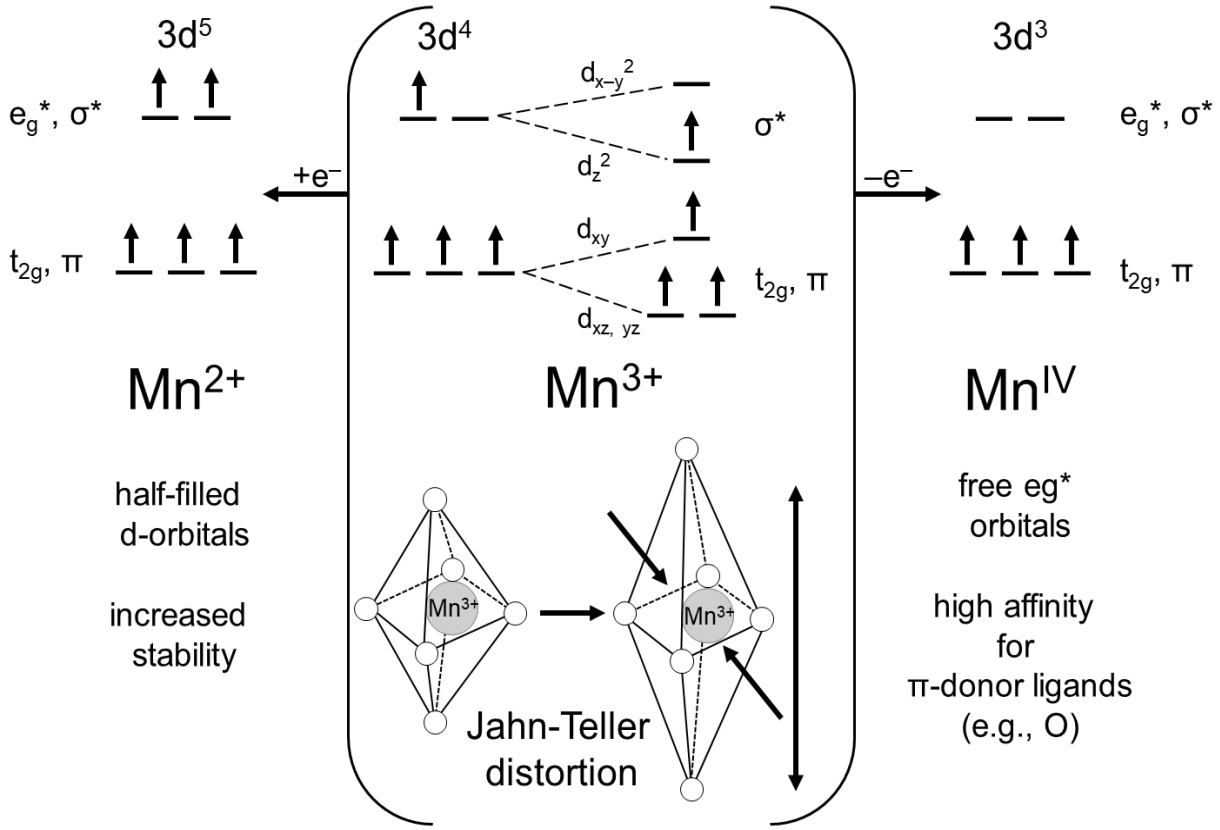

Figure 1.1 Electron configuration for Mn^{2+}, Mn^{3+} and Mn^{IV} ions and the ligand-field splitting for Mn^{3+} including the octahedral Jahn–Teller distortion (own illustration).

Davies (1969) proposed that Mn^{3+} could be stabilized by decreased pH, increased Mn^{2+} concentration, or complexation with OM. Earlier work assumed the presence of Mn^{3+} in aqueous solutions. Dion and Mann (1946) recovered Mn^{3+} from soils using phosphate/pyrophosphate extractions, identifying hydrated oxides ($Mn_2O_3 \cdot xH_2O$) or hydroxides ($Mn(OH)_3$), providing indirect evidence. Systematic indications of Mn^{3+} in soils were later reported by Heintze and Mann (1949) and Gottfreund et al. (1983), who proposed ligand-stabilized Mn^{3+} in soil extracts and the vadose-to-saturated transition zone. However, these observations were limited to laboratory systems or to operationally defined extractions, i.e., methods that may not reflect in situ Mn speciation, and were excluded from conceptual models of natural soils and aquatic environments. Consequently, Mn^{3+} was effectively considered negligible for decades.

Over the past decade, advances in analytical methods have shown that Mn^{3+} can persist in aqueous solutions when stabilized by NOLs across diverse ecosystems, including marine and estuarine waters and water treatment systems (Johnson et al., 2018; Luther, 2015; Madison et al., 2011, 2013; Oldham et al., 2015, 2017a–c; Thibault de Chanvalon and Luther, 2019). Mn^{3+}–NOL complexes typically occur in the low nanomolar to low micromolar range, demonstrating that they can constitute a quantitatively relevant fraction of dissolved Mn_T (Madison et al., 2011; Thibault de Chanvalon and Luther, 2019).

In aquatic environments, the thermodynamic instability of Mn^{3+} requires stabilization by NOLs, including low-molecular-weight organic acids (LMWOAs) (e.g., oxalate, citrate) and humic substances. These ligands strongly influence Mn^{3+}–NOL complex formation, stability, and reactivity in natural systems (Oldham et al., 2017a; Xi et al., 2025). The kinetics of Mn^{3+}–NOL complex formation range from seconds to days, depending on environmental conditions such as E_H, pH, NOL availability, soil mineralogy, ionic strength, and temperature (Li et al., 2021; Madison et al., 2011; Oldham et al., 2015; Wang et al., 2024). These complexes act as key intermediates in Mn^{2+} oxidation and Mn^{IV} reduction, linking abiotic and biotic pathways and challenging the classical $Mn^{2+} \leftrightarrow Mn^{IV}$ paradigm (Li et al., 2021; Wang et al., 2024). Accordingly, quantitative data on Mn^{3+} are essential for improving predictive biogeochemical models and for accurately representing Mn redox dynamics in soils.

1.3 Manganese oxides in soils

Manganese oxides are ubiquitous in soils, sediments, and most geological systems, where they participate in various chemical reactions that influence groundwater and bulk soil composition (Post, 1999). More than 30 Mn oxide minerals have been identified, including over 15 Mn oxide phases abundant in soils (Feng et al., 2007; Post, 1999), which govern precipitation–dissolution dynamics and Mn bioavailability (Martin, 2005; Tebo et al., 2004). Manganese oxides are typically poorly crystalline, brown-black minerals of largely biogenic origin and occur as fine-grained aggregates, concretions, or coatings on other minerals (Post, 1999; Tebo et al., 2004). They are the most important Mn-bearing minerals in soils and are among the most reactive natural oxidizing agents on Earth (Greathouse et al., 2014; Post, 1999; Remucal and Ginder-Vogel, 2014).

Solid Mn occurs in several oxidation states (+2, +3, +4) within both monovalent and mixed-valent Mn oxides, including MnO (manganosite), Mn_2O_3 (bixbyite), Mn_3O_4 (hausmannite), and various MnO_2 polymorphs (e.g., α-hollandite, β-pyrolusite/feitknechtite, γ-nsutite/ramsdellite/manganite, ρ-birnessite, and δ-birnessite) (Fischel et al., 2024). In Mn oxides, each Mn atom is coordinated by six oxygen atoms, forming an MnO_6 octahedron, representing the fundamental structural unit. Phyllomanganates (layered Mn oxides, e.g., birnessite) consist of stacked sheets of edge-sharing MnO_6 octahedra, whereas tectomanganates (tunnel Mn oxides, e.g., cryptomelane and pyrolusite) comprise edge- and corner-sharing MnO_6 octahedra forming rigid three-dimensional networks (Post, 1999). Both structural types commonly host cations (Na^+, K^+, Ca^{2+}) or water molecules in their interlayers or tunnels (Remucal and Ginder-Vogel, 2014).

Although less abundant than Fe- and Al-(hydr)oxides, Mn oxides critically regulate the mobility and transformation of nutrients and contaminants in soils (Borch et al., 2010). Manganese oxides oxidize diverse organic and inorganic compounds (Li et al., 2021). These oxides contribute to soil health by acting as scavengers and oxidants of highly mobile organic contaminants, including phenolic compounds, antibiotics, dyes, and pesticides (Altzitser et al., 2025; Li et al., 2022; Li et al., 2024) as well as inorganic pollutants such as arsenic, cadmium, chromium, lead, and selenium (Li et al., 2015; Oscarson et al., 1981; Scott and Morgan, 1996; Stepniewska et al., 2004; Villalobos et al., 2005). Minerals

like birnessite, manganite, and hausmannite are redox-active sorbents and surface catalysts in soils (Borch et al., 2010; Li et al., 2021). Despite typically lower adsorptive capacities, Mn oxides are stronger oxidants than Fe oxides, largely due to higher E_H values (Kleber et al., 2021). Their high reactivity arises from properties such as large and highly variable specific surface areas (Borch et al., 2010), high oxidation potentials (Li et al., 2021), widely varying points of zero charge (e.g., Ramstedt et al., 2004; Tan et al., 2008), structural vacancies (Li et al., 2021; Post, 1999), and the Mn oxidation state, which determines their E_H and reactivity. Notably, Mn^{III} oxides exhibit higher E_H values (1.51 V) than Mn^{IV} oxides (1.23 V) (Greathouse et al., 2014), enabling more efficient oxidation of organic and inorganic compounds. In addition, Mn oxides serve as electron acceptors for Mn-reducing bacteria in anaerobic respiration processes (Ehrlich, 1987; Myers and Nealson, 1988a) and chemically oxidize Fe^{2+} (Myers and Nealson, 1988b), thereby influencing Mn cycling and bioavailability in soils.

Given their structural diversity, high redox reactivity, and sensitivity to environmental conditions, Mn oxides actively influence Mn cycling at the mineral–water interface. Monovalent or mixed-valent Mn oxides enable the investigation of abiotic and biotic precipitation–dissolution pathways, particularly in the presence of NOLs. Chapter 1.5 therefore synthesizes current knowledge on key reaction pathways that may promote the formation of Mn^{3+}–NOL complexes during NOL–Mn oxide interactions.

1.4 Soil organic matter – a source of natural organic ligands

Soil organic matter constitutes a heterogeneous pool of organic compounds derived predominantly from plant, microbial, and faunal inputs, including litter, root exudates and detritus, and mycorrhizal hyphae (Kögel-Knabner, 2002; Paul, 2016; Schmidt et al., 2011). This pool includes a broad spectrum of molecules, such as aromatic compounds, lignin monomers, carbohydrates, lipids, polysaccharides, and phenolic structures (Schmidt et al., 2011). Although SOM typically accounts for only 1–5% of the soil mass, it plays a pivotal role in shaping soil properties, functions, and overall soil health (Hatten and Liles, 2019). Based on specific gravity and size, SOM is commonly classified into dissolved organic matter (DOM), particulate organic matter (POM), and mineral-associated organic matter (Cotrufo and Lavallee, 2022; Lavallee et al., 2020).

Dissolved organic matter is a complex pool of soluble organic compounds (Herbert and Bertsch, 1995). Operationally, DOM is defined as the fraction passing through a 0.45 µm (occasionally 0.20 µm) filter and remains in solution, thereby distinguishing it from POM (Thurman, 1985; Zsolnay, 2003). This definition provides a framework for investigating DOM-mediated metal complexation and speciation, which influence metal solubility, transport, and toxicity (Aiken et al., 2011; Nebbioso and Piccolo, 2013). Dissolved organic matter typically constitutes only a minor fraction (0.04–0.2%) of total SOM (Zsolnay, 1996), yet it represents the most mobile, biogeochemically reactive, and dynamically cycling SOM fraction (Bolan et al., 2011; Gmach et al., 2020). Reported DOM concentrations range from 5–500 mg C L^{-1} in forest soils and from 5–500 mg C L−1 in arable soils (Amelung et al., 2018).

The majority of DOM originates from photosynthetically fixed C. Primary sources include plant-derived inputs, such as leaf litter, throughfall and stemflow, root exudates, and decaying fine roots, as well as decomposition products, metabolic by-products, and leachates derived from older, microbially processed SOM (Bolan et al., 2011). Among these sources, leaching from plant litter and humus is generally regarded as a major contributor to DOM fluxes in many soil systems (Kaiser and Kalbitz, 2012). Consequently, the chemical signature of DOM reflects a continuum from relatively fresh plant-derived compounds to progressively oxidized, microbially transformed OM (Kaiser and Kalbitz, 2012), resulting in a wide diversity of functional groups capable of metal complexation.

Dissolved organic matter facilitates the transport of metals, nutrients, and organic contaminants within the soil profile, contributes to C replenishment at depth, and serves as a substrate for microbial activity (Chantigny et al., 2007). The molecular composition of DOM ranges from high-molecular-weight (HMW) to low-molecular-weight (LMW) compounds (Herbert and Bertsch, 1995; Nebbioso and Piccolo, 2013), many of which possess functional groups capable of coordinating metal ions. Given this functional heterogeneity, DOM reactivity towards metals is better described by ligand functionality than by bulk molecular composition.

Accordingly, within this study, metal-reactive DOM constituents are collectively referred to as NOLs, representing a functional rather than a strictly compositional classification. These ligands consist predominantly of C, with substantial contributions from oxygen, hydrogen, nitrogen, phosphorus, and sulfur (Bolan et al., 2011). They comprise LMWOAs

(e.g., oxalate, citrate, malate), phenols, amino acids, humic and fulvic substances, and siderophore-like chelators (Aiken et al., 2011).

Natural organic ligands influence metal speciation, modify surface charges of particles, alter sorption behavior towards mineral surfaces, bias mineral dissolution and precipitation, and affect redox and photochemical reactions. Coordination of metal cations occurs via functional groups such as carboxylates, phenols, amines, and thiols, whose binding affinities, complex stabilities, and ligand densities span several orders of magnitude (Aiken et al., 2011).

By forming stable inner-sphere chelate complexes (conceptually represented in Eq. 2), NOLs can stabilize metals in solution and, in some cases, kinetically inhibit redox reactions, thereby preserving metastable oxidation states under environmentally relevant conditions (Aiken et al., 2011).

$$M^{n+}\,(aq) + nNOL\,(aq) \rightarrow M\text{–}(NOL)_n\,(aq) \qquad \text{[Eq. 2]}$$

While complexation of divalent (e.g., Cd^{2+}, Cu^{2+}, Fe^{2+}) and trivalent metals (e.g., Al^{3+}, Cr^{3+}, Fe^{3+}) is well documented (e.g., Daugherty et al., 2017; Liu et al., 2021; Weng et al., 2002), the complexation and stabilization of Mn^{3+} in the presence of NOLs in soil solutions remains poorly understood. Dissolved Mn^{3+} is highly redox-active, short-lived, and analytically challenging to quantify, and its interactions with NOLs have not been systematically investigated under soil-relevant conditions. This knowledge gap limits the prediction of Mn speciation and redox cycling in soils, motivating the focus of this thesis.

1.5 Aquatic geochemistry of manganese – dissolved trivalent manganese

Recent reviews have emphasized the environmental significance of Mn^{3+} and highlighted its increasing importance in the Mn geochemical cycle (Li et al., 2021; Wang et al., 2024; Xi et al., 2025). Mechanistically, dissolved Mn^{3+} serves as a key intermediate during the stepwise one-electron oxidation of dissolved Mn^{2+} to high-valent solid Mn^{IV}, and during the reverse reductive processes (Luther, 2005).

In freshwater and marine systems, Mn^{2+} is typically oxidized by O_2 to form poorly crystalline Mn oxides (Morgan, 2005). Recent studies in marine chemistry revealed pathways for Mn^{3+}–NOL complex formation under oxic, suboxic, and anoxic conditions

(Madison et al., 2013; Oldham et al., 2017a–c). Both oxidative and reductive pathways, whether abiotic or biotic, contribute to Mn^{3+}–NOL complex formation in solution or the mineral–water interface. The reaction equations presented here are conceptual rather than stoichiometrically balanced.

Biotic Mn^{2+} oxidation typically dominates over abiotic oxidation in natural systems and proceeds via two sequential one-electron transfers, forming Mn^{3+}–NOL complex intermediates as the rate-limiting step prior to Mn oxide formation [Eqs. 3 and 4] (Morgan, 2005; Oldham et al., 2017b; Tebo, 1991; Webb et al., 2005).

$$Mn^{2+}\ (aq) + NOL\ (aq) + O_2 + bacteria_{(cat.)} \rightarrow Mn^{3+}\text{–}NOL\ (aq) + O_2^{\bullet -} \quad \text{[Eq. 3]}$$

$$Mn^{3+}\text{–}NOL\ (aq) + O_2 + bacteria_{(cat.)} \rightarrow MnO_2\ (s) + NOL^{-}\ (aq) \quad \text{[Eq. 4]}$$

Abiotic Mn^{2+} oxidation involves Mn^{2+}–NOL complex formation [Eq. 5] and subsequent oxidation by dissolved O_2 to Mn^{3+}–NOL [Eq. 6] (Oldham et al., 2017b). Alternatively, oxidized NOLs may directly oxidize Mn^{2+} [Eq. 7] (Oldham et al., 2017a). Surface-catalyzed Mn^{2+} oxidation proceeds via inner-sphere complexation [Eq. 8], with outer-sphere complexation disfavored due to limited orbital overlap (Luther, 2005; Morgan, 2005).

$$Mn^{2+}\ (aq) + NOL\ (aq) \rightarrow Mn^{2+}\text{–}NOL\ (aq) \quad \text{[Eq. 5]}$$

$$Mn^{2+}\text{–}NOL\ (aq) + O_2 \rightarrow Mn^{3+}\text{–}NOL\ (aq) + O_2^{\bullet -} \quad \text{[Eq. 6]}$$

$$Mn^{2+}\ (aq) + NOL_{ox}\ (aq) \rightarrow Mn^{3+}\text{–}NOL_{red}\ (aq) \quad \text{[Eq. 7]}$$

$$Mn^{2+}\ (aq) + NOL\ (aq) + mineral\ surface_{(cat.)}\ (s) \rightarrow Mn^{3+}\text{–}NOL\ (aq) + e^{-} \quad \text{[Eq. 8]}$$

Dissolution of Mn oxides may proceed via (i) dissimilatory reduction mediated by anaerobic bacteria (e.g., *Shewanella* sp. and *Geobacter* sp.) [Eq. 9], (ii) ligand-promoted dissolution via reductive [Eq. 10] or non-reductive [Eq. 11] pathways, and (iii) proton (H^+)-promoted dissolution [Eq. 12], including potential transient formation of Mn^{3+}–NOL complexes (Li et al., 2021; Oldham et al., 2017a–c; Wang et al., 2024; Xi et al., 2025).

$$Mn^{IV}\ (s) + NOL\ (aq) + e^{-} + bacteria_{(cat.)} \rightarrow Mn^{3+}\text{–}NOL_{ox}\ (aq) \quad \text{[Eq. 9]}$$

$$Mn^{IV}\ (s) + NOL\ (aq) + e^{-} \rightarrow Mn^{3+}\text{–}NOL\ (aq) \quad \text{[Eq. 10]}$$

$$Mn^{III}\ (s) + NOL\ (aq) \rightarrow Mn^{3+}\text{–}NOL\ (aq) \quad \text{[Eq. 11]}$$

$Mn^{IV}O_2$ (s) + $4H^+$ + $2e^-$ → Mn^{2+} (aq) + $2H_2O$ [Eq. 12]

Finally, Mn^{3+}–NOL formation and degradation are closely coupled to other elemental cycles. In particular, MnO_2 may be reduced by inorganic reductants (IRs) such as Fe^{2+} [Eq. 13], while Mn^{3+}–NOL complexes are possibly susceptible to reductive degradation by strong IRs such as Fe^{2+} and H_2S [Eq. 14] (Oldham et al., 2017b).

$Mn^{IV}O_2$ (s) + IR (aq) + NOL (aq) → Mn^{3+}–NOL (aq) + IR^+ (aq) [Eq. 13]

Mn^{3+}–NOL (aq) + IR (aq) → Mn^{2+} (aq) + NOL (aq) + IR^+ (aq) [Eq. 14]

In soils, Mn distribution is governed by coupled processes including reduction–oxidation, precipitation–dissolution, adsorption–desorption, and complexation (Li et al., 2021). These processes are controlled by redox conditions, pH, ambient temperature, microbial activity, and SOM content and composition, often comprising terrestrial humic substances (Adriano, 2001; Oldham et al., 2017a–c; Sparrow and Uren, 2014). Following Reddy et al. (2023), soil redox conditions can be classified by the preferential electron acceptor: oxidizing (> +300 mV, O_2 reduction); weakly reducing (+100 to +300 mV, $Mn^{III/IV}$ and nitrate (NO_3^-) reduction); moderately reducing (+100 to –100 mV, Fe^{III} reduction); and strongly reducing (< –100 mV, sulfate (SO_4^{2-}) and carbon dioxide (CO_2) reduction). In general, Mn solubility increases under reducing (E_H < +300 mV) and acidic (pH < 5.5) soil conditions, due to the reductive dissolution of $Mn^{III/IV}$ oxides to soluble Mn^{2+}. In contrast, $Mn^{III/IV}$ oxides precipitate under aerobic conditions at pH > 5.5 (Amelung et al., 2018; Patrick and Turner, 1968; Reddy et al., 2023).

The formation of Mn^{3+}–NOL complexes in soils requires the presence of NOLs as well as supporting biotic and abiotic pathways. While these pathways are well documented in marine systems, they are equally relevant in terrestrial environments. Therefore, three linked hypotheses are tested: (i) NOLs originating from SOM drive Mn^{3+}–NOL complex formation, (ii) both biotic and abiotic processes govern their formation, and (iii) Mn^{3+}–NOL complexes can form under varying redox and pH conditions typical of soils. By viewing soils as a comparable yet complex analogue to marine systems, this work highlights the importance of quantitatively assessing Mn^{3+} to improve our comprehension of environmental Mn redox chemistry.

1.6 Determination and speciation of dissolved manganese – a method review

The historical underrepresentation of reported dissolved Mn^{3+} in soil and sediment studies primarily reflects analytical limitations rather than its actual absence. Conventional spectrometric methods such as inductively coupled plasma mass spectrometry, inductively coupled plasma optical emission spectrometry (ICP OES), and flame atomic absorption spectrometry provide precise Mn_T quantification but cannot discriminate Mn^{2+} from Mn^{3+} (Madison et al., 2011). Early spectrophotometric and extraction-based approaches, including the formaldoxime method (Brewer and Spencer, 1971), the 1-(2-pyridylazo)-2-naphthol method (Chin et al., 1992), and the superior porphyrin method (Ishii et al., 1982; Chiswell and O'Halloran, 1991), also quantified only Mn_T. This methodological blind spot likely led to systematic misinterpretations of Mn redox dynamics in soils for decades.

To overcome these limitations, major methodological advances arose in marine geochemistry, where Mn^{3+} was increasingly recognized as a significant redox species. These include electrochemical techniques, leucoberbelin blue (LBB) assays, improved spectrophotometric protocols, and subtraction-based approaches (Dellwig et al., 2012; Faulkner et al., 1994; Jones et al., 2019; Madison et al., 2011; Oldham et al., 2015; Schnetger and Dellwig, 2012; Trouwborst et al., 2006; Yakushev et al., 2009).

A major breakthrough was the revised porphyrin method, originally developed by Ishii et al. (1982), introduced by Madison et al. (2011) and modified by Oldham et al. (2015), which enables Mn_T speciation at an environmentally relevant micromolar range (0.05–10 µM). Applied to marine systems, the method revealed that Mn^{3+} can constitute up to 100% of Mn_T, challenging the assumption that Mn^{3+} is inherently short-lived in natural environments (Madison et al., 2011, 2013; Oldham et al., 2015, 2017b). These findings established Mn^{3+} as a stable and environmentally significant redox species with implications for (trace) metal cycling, OM transformation, and sediment diagenesis. Recent colorimetric chemosensors for Mn^{3+} detection (Lee et al., 2015) are limited to pH 7–11 and are therefore of limited applicability in soils.

While the porphyrin method has been extensively applied in marine systems, its systematic use in soil solutions remains largely unexplored. Applying Mn speciation

methods to soil solutions remains challenging due to chemical complexity. This thesis therefore extends Mn_T speciation into a domain where its role has been largely neglected.

1.7 Mn speciation – the porphyrin method

Dissolved Mn_T speciation was determined using the advanced spectrophotometric porphyrin method of Madison et al. (2011) and Oldham et al. (2015), originally introduced by Ishii et al. (1982). In this method, α,β,γ,δ-tetrakis(4-carboxyphenyl)porphine (T(4-CP)P) (Figure 1.2) was employed to determine Mn_T speciation, including Mn^{2+}, Mn^{3+}–NOL_{weak} complexes and Mn^{3+}–NOL_{strong} complexes based on a kinetic rate modeling approach (Madison et al., 2011). Porphyrin complexes provide high analytical selectivity and sensitivity due to metal coordination at the tetradentate N_4 binding site of the macrocycle (Biesaga et al., 2000). Operationally, dissolved Mn_T is defined as the fraction passing a 0.2 µm filter (Madison et al., 2011).

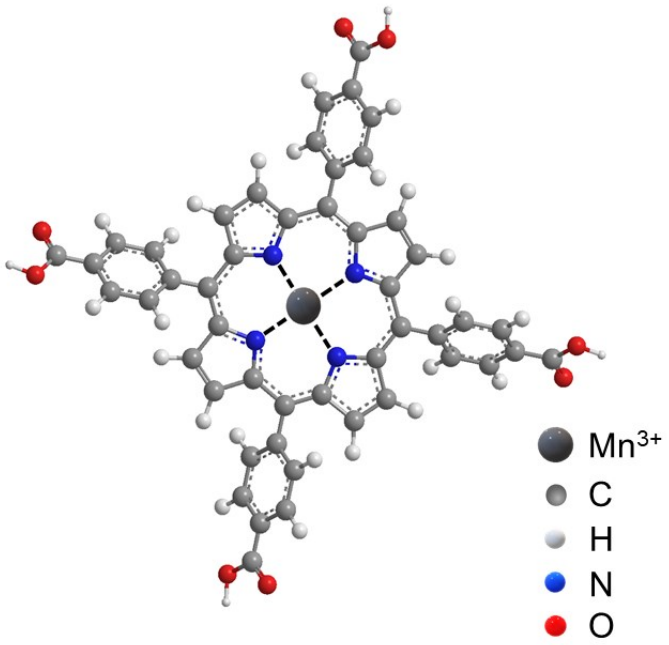

Figure 1.2 Three-dimensional visualization of the Mn^{3+}–T(4-CP)P complex (own illustration).

Measurements were performed by UV/Vis spectroscopy following Madison et al. (2011) and Oldham et al. (2015). The absorption coefficient (ε = 95,340 M^{-1} cm^{-1}) was determined using manganese(II) chloride tetrahydrate ($MnCl_2 \cdot 4H_2O$) standards (0.1–10 µM) (Madison et al., 2011). Sample volumes were adjusted to ensure Mn_T

concentrations remained within the analytical detection range. Absorbance was recorded for up to 15 minutes or until a stable plateau indicated completion of the porphyrin substitution reaction.

Figure 1.3 shows the schematic experimental procedure of the conducted Mn_T speciation analysis. From each environmental sample, two aliquots were analyzed. Aliquot A (non-reduced sample) was measured in triplicate to quantify Mn^{2+} and Mn^{3+}–NOL_{weak} complexes. Aliquot B (reduced sample) was treated with a strong reducing agent (e.g., hydroxylamine hydrochloride) to convert all Mn species to Mn^{2+}, enabling quantification of Mn^{3+}–NOL_{strong} complexes in triplicate. Together, these measurements provide comprehensive Mn_T speciation.

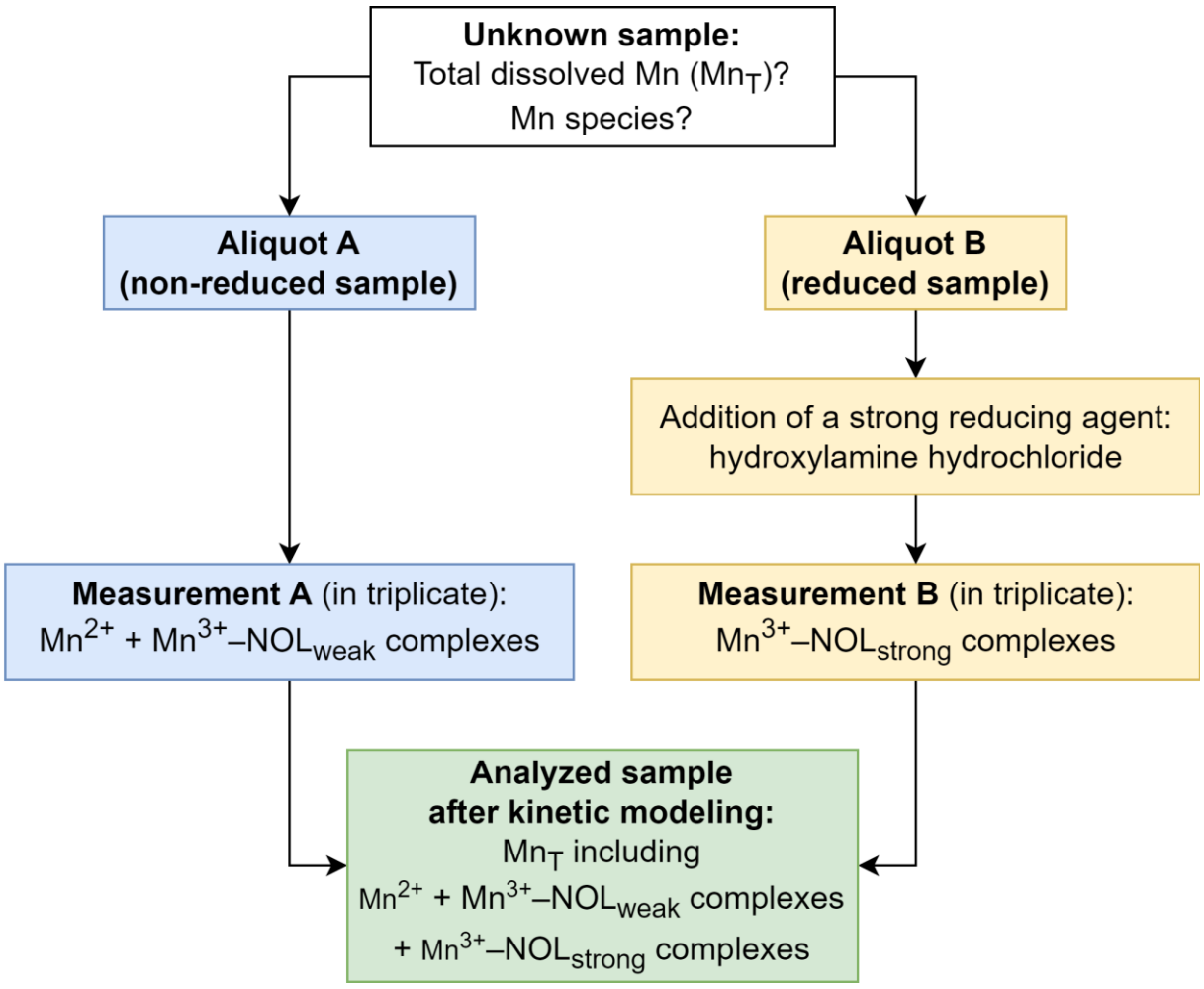

Figure 1.3 Experimental procedure of the porphyrin method for the speciation of Mn_T, including Mn^{2+}, Mn^{3+}–NOL_{weak} complexes, and Mn^{3+}–NOL_{strong} complexes (own illustration).

The method relies on time-resolved metal substitution reactions with T(4-CP)P. Dissolved Mn^{2+} and Mn^{3+} species form complexes that can be spectrophotometrically detected at the Soret band (468 nm) (Madison et al., 2011; Oldham et al., 2015). The relevant reactions are summarized in Eqs. 15a,b and 16. In the first reaction, Cd^{2+}, complexed as Cd^{2+}–T(4-CP)P, is displaced by Mn^{2+}, forming Mn^{2+}–T(4-CP)P [Eq. 15a], which is subsequently oxidized to Mn^{3+} by dissolved O_2 [Eq. 15b]. This oxidation step is assumed rate-determining and defines the rate constant k_1. In the second reaction, Mn^{3+} is directly complexed by T(4-CP)P. While this complexation step occurs via ligand exchange, it is slower than that of Mn^{2+} because the reaction kinetics, quantified by rate constant k_2, depend on the binding strengths of the original Mn^{3+}–NOL_{weak} complex [Eq. 16]. However, if Mn^{3+} is complexed by NOLs that act as strong chelating agents and cannot be outcompeted by T(4-CP)P, the reaction does not proceed. In such cases, the addition of a strong reducing agent (e.g., hydroxylamine hydrochloride) is required to reduce Mn^{3+} to Mn^{2+} (Oldham et al., 2015), to re-enable the substitution reaction [Eq. 15a].

$$Mn^{2+} + Cd^{2+}\text{–T(4-CP)P} \rightarrow Cd^{2+} + Mn^{2+}\text{–T(4-CP)P} \qquad \text{[Eq. 15a]}$$

$$Mn^{2+}\text{–T(4-CP)P} + O_2 \xrightarrow{\text{fast, } k_1} Mn^{3+}\text{–T(4-CP)P} \qquad \text{[Eq. 15b]}$$

$$Mn^{3+} + Cd^{2+}\text{–T(4-CP)P} \xrightarrow{k_2} Cd^{2+} + Mn^{3+}\text{–T(4-CP)P} \qquad \text{[Eq. 16]}$$

Depending on the Mn species present in an environmental sample, distinct operationally-defined reaction kinetics are observed:

(i) Samples containing only Mn^{2+} (non-reduced sample) show a monotonic increase toward an asymptotic plateau (Figure 1.4), corresponding to the conversion of Mn^{2+} to Mn^{3+}–T(4-CP)P, which can be adequately described by a two-parameter first-order kinetic model [Eq. 17].

$$y = a \cdot (1 - e^{-k_1 \cdot t}) \qquad \text{[Eq. 17]}$$

with a = Mn^{2+} concentration (µmol L^{-1}); k_1 = Mn^{2+} rate constant (s^{-1}); t = reaction time (s).

(ii) In the presence of Mn^{3+}–NOL_{weak} complexes (non-reduced sample), the kinetic curve is flattened as a result of the overlap of rapid Mn^{2+} complexation described in Eq. 17 and the kinetically delayed ligand exchange of Mn^{3+} released from Mn^{3+}–NOL_{weak} complexes

(Figure 1.4). This behavior in a non-reduced sample is described by a four-parameter kinetic expression [Eq. 18]:

$$y = a \cdot (1 - e^{-k_1 \cdot t}) + b \cdot (1 - e^{-k_2 \cdot t}) \quad \text{[Eq. 18]}$$

with a = Mn^{2+} concentration (µmol L^{-1}); b = Mn^{3+} concentration (µmol L^{-1}); k_1 = Mn^{2+} rate constant (s^{-1}); k_2 = Mn^{3+} rate constant (s^{-1}); t = reaction time (s).

(iii) Samples containing Mn^{3+}–NOL_{strong} complexes ($Mn_{T(hydroxylamine)}$) also exhibit a kinetic behavior that can be described by Eq. 17 following the addition of the strong reducing agent hydroxylamine in excess (Figure 1.4). The reduction of strongly bound Mn^{3+} to Mn^{2+} liberates Mn^{2+} from kinetically inert complexes, resulting in an increased asymptotic maximum of the kinetic curve.

Operationally, the concentration of Mn^{3+}–NOL_{strong} complexes is calculated as the difference between the Mn_T concentrations of the reduced and the non-reduced sample [Eq. 19]. This calculation assumes quantitative reduction of Mn^{3+} to Mn^{2+} under conditions of excess reductant (Oldham et al., 2015).

$$Mn^{3+}\text{–}NOL_{strong}\ \text{complexes} = Mn_{T(hydroxylamine)} - (Mn^{2+} + Mn^{3+}\text{–}NOL_{weak}\ \text{complexes}) \quad \text{[Eq. 19]}$$

Finally, samples containing all Mn species require a combined interpretation of Eqs. 17 and 18, reflecting the contributions of Mn^{2+}, Mn^{3+}–NOL_{weak} complexes, and Mn^{3+}–NOL_{strong} complexes.

Kinetic modeling was performed using custom R scripts developed in RStudio (version 1.4.1106) with R (version 4.0.5). Nonlinear least-squares fitting was carried out using the *nlmrt* package (version 2016.3.2) (Nash, 2016; R Core Team, 2021). The custom R scripts for the modeling process of the three-parameter and five-parameter equations are provided in the Appendix (A–1 and A–2).

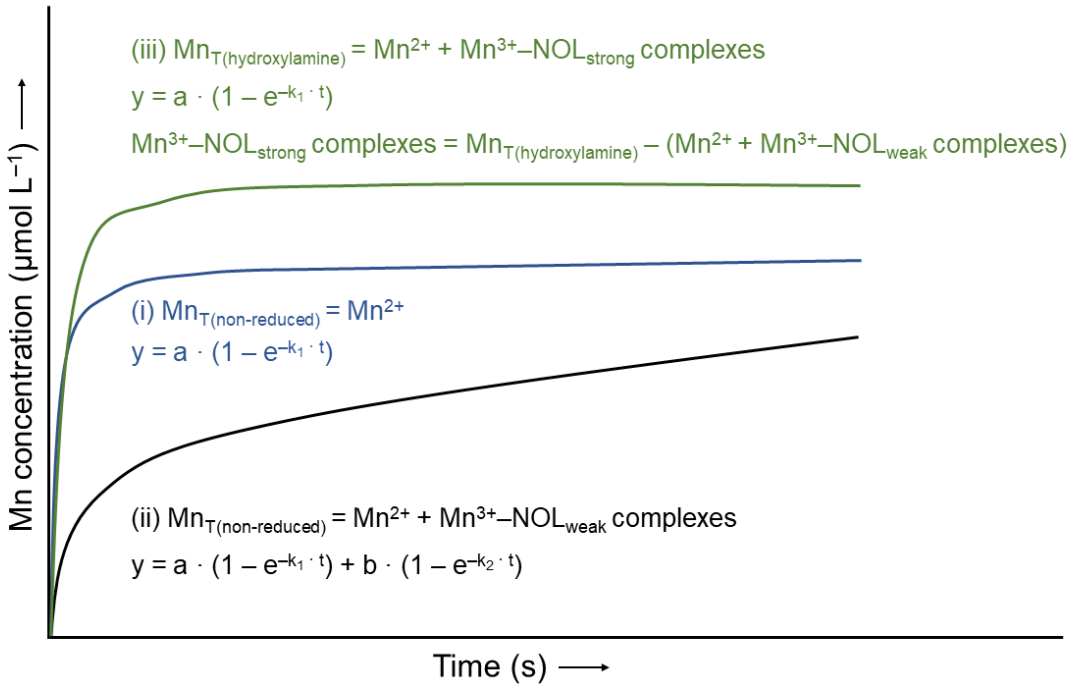

Figure 1.4 Schematic illustration of the curve shapes showing the reaction kinetics over time as observed by time-resolved UV/Vis scan corresponding to the three kinetic scenarios (i–iii) (own illustration).

1.8 Study sites

Three study sites were selected to investigate Mn speciation in soil solutions, providing a multi-environment framework to assess the potential formation of Mn^{3+}–NOL complexes under contrasting soil conditions.

The first study site (49°44′33.38″ N, 7°11′47.61″ E, 600 m a.s.l.) is located near Idar-Oberstein, Rhineland-Palatinate, Germany. It is part of the permanent environmental monitoring station #101, managed by the federal state authority Research Institute for Forest Ecology and Forestry (FAWF), of the state of Rhineland-Palatinate, in Trippstadt. The predominant soil type at this location is a Dystric Cambisol (IUSS Working Group WRB, 2022) with mor humus covered by spruce (*Picea abies* (L.) H. Karst.) (FAWF, 2016). Pre-installed suction cups and lysimeters allow *in situ* sampling of forest floor solutions and soil solutions, enabling Mn speciation under natural conditions. This setting is particularly relevant given the proposed role of Mn^{3+}–NOL complexes in SOM decomposition and C cycling in forest ecosystems (Hofrichter, 2002; Keiluweit et al., 2015; Stendahl et al., 2017).

The second site (54°8′1″ N, 8°58′28″ E; 0.5 m a.s.l.) is located in the Polder Speicherkoog, Schleswig-Holstein, Northern Germany. Groundwater fluctuations strongly influence this site, which is situated in a non-cultivated field within an agrarian landscape, with vegetation dominated by willow bushes (*Salix spp.*), elder bushes (*Sambucus nigra*), and fireweed (*Epilobium angustifolium*). The soil, a Calcaric Gleysol (IUSS Working Group WRB, 2022), developed from Holocene calcareous marine sediments (Hoffmann, 1991). Seasonally fluctuating redox conditions, ranging from oxidizing to strongly reducing conditions (Dorau and Mansfeldt, 2016; Mansfeldt, 2003, 2004), provide an ideal setting to study Mn speciation under variable redox regimes. Previous studies at this site assumed dissolved Mn_T to consist exclusively of Mn^{2+} due to analytical limitations (Mansfeldt, 2003, 2004), highlighting the need for a reassessment of the site-specific Mn_T composition.

A complementary small-scale field study was conducted at a third site (54°7′3″ N, 8°56′7″ E; 0 m a.s.l.) in a tidally influenced area within the Wadden Sea (UNESCO World Heritage Site, Meldorf Bight), approximately 3 km west of the Speicherkoog site and ~30 m from the shoreline. The soil is classified as a Salic Tidalic Fluvisol (IUSS Working Group WRB, 2022), providing an opportunity to investigate Mn speciation across the marine–terrestrial interface and bridging the gap between terrestrial soils and marine environments.

Collectively, these three sites offer complementary environmental settings to explore the formation of Mn^{3+}–NOL complexes under varying soil conditions**.** Key physicochemical properties, including pH, E_H, water saturation, trace metal content, and NOL composition, serve as contextual factors that may critically influence Mn speciation.

1.9 Research motivation

Current conceptual models of the Mn cycle do not consider Mn^{3+} a stable or ubiquitous component of dissolved Mn_T in soils, representing a critical knowledge gap. Although the “redox wheel” describing Mn cycling between dissolved Mn^{2+} and solid Mn^{IV} has been extensively studied with respect to key parameters such as E_H, pH, and temperature (Gotoh and Patrick, 1972; Patrick and Turner, 1968; Schwab and Lindsay, 1983; Sparrow and Uren, 2014), reliable methods to quantify dissolved Mn^{3+} under environmentally relevant soil conditions are still lacking. As a result, Mn^{3+} has been largely overlooked in soil

studies, despite evidence for its role in trace metal cycling, SOM transformation, and other biogeochemical processes (e.g., Keiluweit et al., 2015; Oldham et al., 2017b,c). Understanding Mn^{3+} dynamics is directly relevant to C cycling and has implications for broader ecosystem functioning. Robust Mn speciation is therefore essential to elucidate the role of Mn^{3+} and revise the $Mn^{2+}\leftrightarrow Mn^{IV}$ paradigm (Figure 1.5).

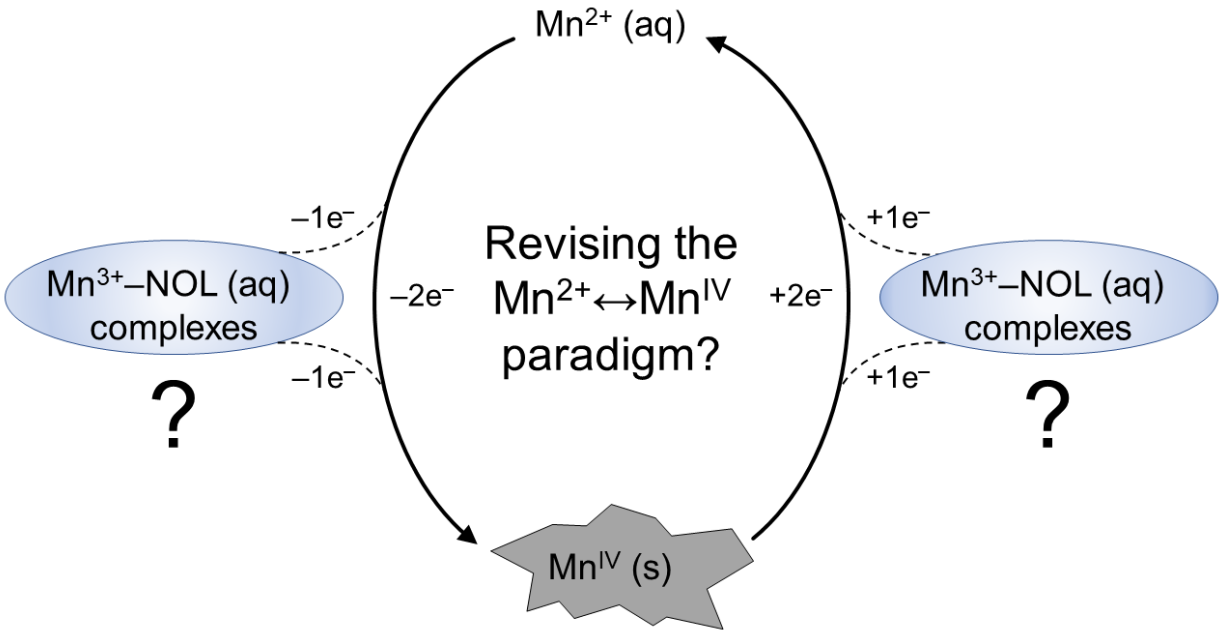

Figure 1.5 Schematic representation of the manganese (Mn) redox cycle suggesting a possible revision of the classical $Mn^{2+}\leftrightarrow Mn^{IV}$ paradigm based on emerging evidence for Mn^{3+}–NOL complexes. NOL = natural organic ligand (own illustration).

Aims and research hypothesis

The principal methodological aim of this thesis is to adapt, apply, and further modify the porphyrin method to enable reliable qualitative and quantitative speciation of Mn_T, including Mn^{2+}, Mn^{3+}–NOL_{weak} complexes and Mn^{3+}–NOL_{strong} complexes in soil solutions. Building on this aim, the overarching research question is addressed: "*Is trivalent manganese a ubiquitous part of the total dissolved manganese in soil solutions?*".

Based on this question, the following preliminary research hypotheses are formulated:

I. The porphyrin method can be adapted to soil solutions in order to speciate dissolved Mn_T.
II. Terrestrial SOM-derived NOLs stabilize dissolved Mn^{3+}.
III. Abiotic and biotic redox pathways contribute to Mn^{3+}–NOL complex formation.

IV. Mn^{3+}–NOL complexes are part of dissolved Mn_T under varying redox and pH conditions.

V. Dissolved Mn^{3+}, in the form of Mn^{3+}–NOL complexes, is a ubiquitous part of dissolved Mn_T in soil solutions.

The dissertation comprises three successive studies that demonstrate emerging evidence of Mn^{3+}–NOL complexes under environmentally relevant soil conditions.

Study I (Chapter 2) provides experimental evidence that Mn^{3+}–NOL complexes are a substantial component of dissolved Mn_T in acidic forest soils. Analyses of *in situ* forest floor solutions and soil solutions using the porphyrin method combined with kinetic modeling, revealed substantial proportions of Mn^{3+}–NOL complexes. These complexes accounted for 10–87% of dissolved Mn_T in forest floor solutions and 0.5–74% in soil solutions. The findings challenge the conventional view that Mn^{2+} dominates in forest floor solutions and soil solutions, suggesting that Mn^{3+}–NOL complexes play an important role in redox processes, trace-metal behavior, and overall Mn cycling in acidic forest soils.

Study II (Chapter 3) demonstrates that Mn^{3+}–NOL complexes can constitute a substantial but previously underestimated fraction of dissolved Mn_T in terrestrial environments. In batch experiments, forest floor-derived NOL extracts were reacted with synthetic manganese oxides (birnessite and manganite) as a function of time (1–168 h, 7 steps) and pH (3–7, 5 steps). Spectrophotometric speciation combined with kinetic modeling revealed that Mn^{3+}–NOL complexes accounted for up to 87 ± 18% of dissolved Mn_T for birnessite, and up to 69 ± 14% for manganite, depending on pH and reaction time. The formation and stability of these complexes were strongly pH-dependent, with lower stability under strongly acidic conditions, but substantial persistence under circumneutral to mildly acidic pH conditions. Proposed abiotic mechanisms for Mn^{3+}–NOL complex formation under oxidizing conditions include ligand-promoted non-reductive dissolution, ligand-promoted reductive dissolution, H^+-promoted dissolution, and ligand exchange. The study establishes Mn^{3+}–NOL complexes as a non-negligible component in forest floor solutions formed during NOL–Mn oxide interactions.

Study III (Chapter 4) provides an initial insight into redox-dependent Mn_T speciation in redoximorphic soils. Microcosm experiments with incubated Calcaric Gleysol material subjected to defined redox cycles revealed that Mn^{3+}–NOL complexes form under both

oxidizing and reducing conditions, with proportions up to 36.4 ± 29.8%, depending on soil horizon and redox regime. Field measurements confirmed the presence of Mn^{3+}–NOL complexes in the Calcaric Gleysol (≤52.5 ± 2.7%) and the Salic Tidalic Fluvisol (≤90.0 ± 0.9%). Although Mn^{2+} dominates under most redox conditions, Mn^{3+}–NOL complexes are redox-active and persistent. The study highlights that site-specific properties, such as E_H, pH, and NOL composition, control the formation, stabilization, and degradation of Mn^{3+}–NOL complexes, emphasizing the need to include them in geochemical models for accurate predictions of soil Mn dynamics.

Chapter 5 provides a comprehensive discussion of the key findings, draws overarching conclusions, critically reflects on the employed porphyrin method, and presents recommendations for future research directions.

Chapter 2: Evidence of trivalent manganese in acidic forest soils

Journal of Plant Nutrition and Soil Science (JPNSS) (2023) 186: 321–329

Author: Constantin Lux[1] (CL)

Co-author: Tim Mansfeldt[1] (TM)

Formatting and orthography are adapted to the dissertation style.

This publication aimed to adapt the porphyrin method as a key analytical approach for the speciation of dissolved Mn_T in soil solutions, enabling differentiation between dissolved Mn^{2+} and Mn^{3+} in different soil environments. Potential analytical challenges were identified and addressed. Application, testing, and validation were performed through targeted investigations of *in situ* acidic forest floor solutions and soil solutions. This work provides the methodological foundation for all subsequent studies on Mn^{3+}–NOL complexes in the dissertation.

Author contributions are presented by category, including conceptualization and methodology, fundamental methodological advances, sample acquisition, sample preparation, formal analysis, software and data curation, investigation, visualization, writing – original draft, writing – review and editing, validation, supervision, project administration and funding acquisition. Within each category, authors are listed in order of their initials to indicate their respective contributions.

Conceptualization and methodology: CL and TM; fundamental methodological advances: CL; sample acquisition: CL; sample preparation: CL; formal analysis: CL; software and data curation: CL; investigation: CL; visualization: CL; writing – original draft: CL and TM; writing – review and editing: CL and TM; validation: TM; supervision: TM; project administration: TM; funding acquisition: TM.

The manuscript was submitted to the “Journal of Plant Nutrition and Soil Science (JPNSS)” and published on 18 March 2023. DOI: 10.1002/jpln.202200271

[1] Institute of Geography, Faculty of Mathematics and Natural Sciences, Department of Geosciences, University of Cologne, Albertus-Magnus-Platz, D-50923 Cologne, Germany.

Abstract

Background: Evidence of trivalent manganese (Mn^{3+}) in the aqueous phase of soils is unknown so far although this strong oxidant has large environmental implications.

Aims: We aimed to modify a spectrophotometric protocol (porphyrin method) and to discriminate between Mn^{2+} and Mn^{3+} in the aqueous phase of forest soils based on kinetic modeling.

Methods: We investigated manganese speciation in 12 forest floor solutions and 41 soil solutions from an acidic forest site by adjusting pH and correcting for absorbance.

Results: The solutions showed broad ranges in pH (3.4−6.3), dissolved organic carbon (DOC, 1.78−77.1 mg C L^{-1}), and total Mn (Mn_T, 23.9−908 µg L^{-1}). For acidic solutions, a pH-buffer was added to increase the pH of the solutions to 7.5−8.0, and background absorption was corrected for colored solutions, that is, solutions high in DOC. This was done to accelerate the reaction kinetics and avoid overestimation of Mn_T concentrations. After the pH and color adjustments, the comparison of Mn_T concentrations between the porphyrin method and optical emission spectrometry showed good agreement. Trivalent Mn, which is stabilized by organic ligands, constitutes significant proportions in both forest floor solutions (10−87%) and soil solutions (0.5−74%).

Conclusions: The dissolved Mn^{3+} is present in acidic forest soils. Thus, we revise the paradigm that this species is not stable and encourage to apply the revised method to other soils.

Keywords: dissolved organic carbon, forest floor solution, organic ligand, pH, soil solution, UV/vis-absorption

2.1 Introduction

Understanding the environmental behavior of the trace metal manganese is difficult because of its number of possible valence states. It was assumed that natural waters are dominated by the divalent form (Mn^{2+}) and its related aqueous inorganic and organic species, whereas the trivalent (Mn^{3+}) and tetravalent (Mn^{4+}) forms occur exclusively as colloids. The presence of Mn^{3+} in aqueous phases has been ignored for its thermodynamic instability owing to its tetragonally distorted electron configuration (Jahn−Teller distortion). Hence, it spontaneously and rapidly disproportionates to Mn^{2+} and Mn^{4+} (Equation 1) (Biedermann & Palombari, 1978; Davies, 1969). Further, Mn^{4+} hydrolyzes and precipitates into an oxide (Equation 1):

$$2Mn^{3+}_{(aq)} + 2H_2O \rightarrow Mn^{+IV}O_{2(s)} + Mn^{2+}_{(aq)} + 4H^+ \qquad \log_{10} K \approx 7-9. \qquad (1)$$

In addition to its thermodynamic instability, the occurrence of Mn^{3+} in natural waters was not reported because of the absence of a direct method for the determination of Mn^{2+} and Mn^{3+}. Madison et al. (2011) modified a spectrophotometric method to simultaneously determine dissolved Mn^{2+}, Mn^{3+}, and total Mn (Mn_T, sum of Mn^{2+} and Mn^{3+}). This method was based on a kinetically controlled metal substitution reaction and will be hereinafter referred to as the porphyrin method. It has been subsequently shown that Mn^{3+} accounts for a significant proportion of the total soluble Mn pool in anoxic and suboxic marine and estuarine sediment pore waters, stratified sea water bodies, and oxygenated marine waters (Madison et al., 2011, 2013; Oldham et al., 2015, 2019, 2021; Oldham, Jones, et al., 2017; Oldham, Miller, et al., 2017; Oldham, Mucci, et al., 2017; Thibault de Chanvalon & Luther, 2019). In these waters, Mn^{3+} is complexed with organic ligands, thus stabilizing the trivalent species and preventing rapid disproportionation.

Soil pore water represents the aqueous phase in soils and is called soil solution. Water percolating through the organic layer of forest soils is called forest floor solution. The abundance of soluble Mn in the soil solution ranges from 20 to 30,000 µg L^{-1} in acidic forest soils of the temperate zone (Blume et al., 2016).

The behavior of Mn in soils is associated with pH, redox potential, and the soil solid phase composition (e.g., clay minerals and organic matter). Mobilization of Mn in soils, for example, under reducing conditions, has been studied both in the laboratory (Gotoh & Patrick, 1972; Patrick & Henderson, 1981; Patrick & Jugsujinda, 1992) and in the field

(Gao et al., 2002; Hseu et al., 2000; Mansfeldt, 2004). In these studies, dissolved Mn was determined by either atomic absorption spectrometry (AAS) or inductively coupled plasma optical emission spectrometry (ICP OES), thus allowing no Mn speciation. Either the authors did not discuss Mn species or they assumed that dissolved Mn was exclusively in the reduced form (Mn^{2+}) (Mansfeldt, 2004; Patrick & Jugsujinda, 1992). Textbooks also consider Mn^{2+} as the principal dissolved Mn species, particularly under reducing and acidic soil conditions (e.g., Essington, 2015; Sposito, 2016). Considering the recent advances in Mn speciation in marine and estuarine environments, analysis of dissolved Mn species in soils is imperative. In earlier publications, the occurrence of Mn^{3+} in soil extracts and in the vadose to saturated transition zone has been postulated (Dion & Mann, 1946; Gottfreund & Schweisfurth, 1983). However, quantification of Mn^{3+} in soil solutions has not been performed yet. Knowledge of Mn^{3+} is not only of fundamental scientific interest but also of environmental significance because this strong oxidant is attributed to, among others, its critical involvement in the breakdown of soil organic matter (Berg et al., 2007; Hofrichter, 2002; Jones et al., 2020; Keiluweit et al., 2015), oxidation of particulate organic carbon to the greenhouse gas carbon dioxide (Jones et al., 2018), and degradation of organic contaminants (Hu et al., 2017).

This study includes two objectives. First, to adapt the porphyrin method to the matrix of the aqueous phase of forest soils to eliminate or minimize interferences. The potential interferences identified in the samples are extremely low pH and intense colors induced by dissolved organic matter (DOM). Second, application of the modified method to forest floor solutions and soil solutions to gain insights into the distribution of dissolved Mn species in acidic forest soils. To address these objectives, we analyzed 12 forest floor solutions and 41 soil solutions from an environmental monitoring station in Germany. We used the adapted porphyrin method to determine dissolved Mn_T and discriminate between Mn^{2+} and Mn^{3+}.

2.2 Material and Methods

2.2.1 Study site

Sampling was conducted at the permanent environmental monitoring station #101 at Idar-Oberstein (49°44′33.38″ N, 7°11′47.61″ E), Rhineland-Palatinate, Germany. This site

is managed by the federal state authority Research Institute for Forest Ecology and Forestry of the state of Rhineland-Palatinate in Trippstadt. The site consists of Dystric Cambisol (IUSS Working Group WRB, 2015) and mor humus, which is covered by spruce (*Picea abies* (L.) H. Karst.) (FAWF, 2016).

2.2.2 Sampling

A total of 53 samples were collected in the study. Forest floor solutions (L and O horizons) were collected in amber glass flasks via pre-installed free-drainage lysimeters without root exclusion made of synthetic material and covered by a mesh. Soil solutions were obtained via pre-installed ceramic suctions cups (P80, Oikos, Göttingen, Germany) at the depths of 30 (Bv horizon) and 80 cm (Cv horizon). All solutions were stored in polyethylene flasks in a cool and dark place. Forest floor solutions and soil solutions were sampled from both limed and non-limed areas. Samples from lysimeters and suction cups were collected individually in contrast to the federal analyses protocol; thus, no composite samples were made. In the laboratory, the samples were filtered through 0.2-µm filters (cellulose acetate, Sartorius, Göttingen) using acid cleaned filtration units (polycarbonate, Sartorius, Göttingen) and stored in amber glass flasks at 4 °C to reduce changes in sample composition (GAFA, 2022). For each sample, an aliquot of 10 mL was mixed with 10 µL of concentrated nitric acid (suprapur®, 65%) for a subsequent ICP OES analysis.

2.2.3 Experimental analysis

General analyses

The pH of forest floor solution and soil solution was measured potentiometrically using a glass electrode (SenTIX 81; WTW, Weilheim, Germany). Electric conductivity (EC) was determined using a conductivity electrode (SevenEasy; Mettler Toledo, Gießen, Germany). Trace metals were analyzed by ICP OES (Spectro Green Line Series, Kleve, Germany) using Merck IV standard solution (Merck Chemicals, Darmstadt, Germany). Total dissolved organic C (DOC) was subjected to high-temperature catalytic oxidation to CO_2 at 850 °C and subsequently quantified by a nondispersive infrared analyzer (Dimatoc 2000; Dimatec, Essen, Germany). Dissolved inorganic C was measured with the same apparatus by quantifying the CO_2 generated following the addition of hydrochloric acid

(10%) and was subtracted from total dissolved C. Sample injection volume was 100 µL. All samples were measured in triplicate.

The molar absorptivity of DOM was determined using an ultraviolet/visible spectrophotometer (LAMBDA™ 25; Perkin Elmer, Rodgau, Germany) at 254 nm. A 1.0 cm pathlength quartz cuvette was used to perform the scan, and all samples were measured against ultrapure water in duplicate at room temperature (Weishaar et al., 2003).

Manganese speciation

Mn species were spectrophotometrically determined based on kinetic modeling at Soret band 468 nm using α,β,γ,δ-tetrakis(4-carboxyphenyl)porphine (T(4-CP)P) according to the initial protocol by Madison et al. (2011). A kinetically controlled metal substitution reaction promoted by oxygen takes place wherein a pre-inserted divalent cadmium ion (Cd^{2+}) in the porphyrin ring is replaced by Mn^{2+}, while Mn^{3+} replaces the Cd^{2+} center without oxygen promotion. The different binding affinities of Mn^{2+} and Mn^{3+} lead to discriminable reaction rates described by kinetic modeling of a pseudo-first order reaction (Madison et al., 2011; Luther et al., 2015; Oldham et al., 2015). All chemicals used were of analytical grade, and solutions were prepared with ultrapure water (18.2 MΩ). Absorbance was measured using a spectrophotometer (LAMBDA™ 25) and a glass cuvette with 1.0 cm pathlength and 3 mL volume. The absorption coefficient (ε = 95,340 M^{-1} cm^{-1}) was determined using manganese(II) chloride tetrahydrate ($MnCl_2 \cdot 4H_2O$) standards (0.1−10 µM), and was similar to that of Madison et al. (2011), that is, ε = 95,400 M^{-1} cm^{-1}. Standards and samples were measured against a reagent blank at room temperature in triplicate. The samples were diluted in the cuvette depending on their Mn concentration to achieve a total Mn concentration in the range of 0.1−10 µM. Absorbance was monitored for 15 min at 5 s intervals to obtain consistent kinetic results. From the kinetics, we determined the concentrations of (1) Mn_T, (2) Mn^{2+} including free Mn^{2+} and Mn^{2+} complexed with both inorganic and organic ligands, and (3) Mn^{3+} associated with organic ligands that formed relatively weak complexes (Mn^{3+}_{weak}). To evaluate the possible presence of strongly bound Mn (Mn^{3+}_{strong}), the strong reducing agent hydroxylamine was added in excess (>50 times) to a subsample depending on the expected Mn_T concentration following the methods of Oldham et al. (2015). The difference between the reduced ($Mn_{T(hydroxylamine)}$)

and non-reduced sample (Mn^{2+} + Mn^{3+}_{weak}) represents the concentration of Mn^{3+}_{strong} as follows:

$$Mn^{3+}_{strong} = Mn_{T(hydroxylamine)} - (Mn^{2+} + Mn^{3+}_{weak}). \quad (2)$$

The limit of detection of Mn_T was at 18.7 µg L^{-1} and determined by absorbance of blank adding three times its standard deviation. To test the accuracy of total Mn concentrations, the spectrophotometric measurements were compared with those of ICP OES analysis.

pH adjustment

Because of the acidic pH of the samples (3.4−6.3), an additional pH buffer (sodium bicarbonate) was added to adjust the sample pH to the required range of 7.5−8.0 (Charbonnier & Anschutz, 2019). This pH adjustment was useful in preventing the slowing down of the porphyrin reaction. With respect to the matrix of the forest floor solutions and soil solutions, the amount of the buffer (0.25 g L^{-1}) was reduced to a minimum to reduce potential impacts on the reaction kinetics. The buffer volume (1460−2360 µL) was adjusted to the reagents and sample to achieve a total cuvette volume of 3 mL.

Absorbance correction

The forest floor solutions showed significant inherent coloration because of high amounts of DOM. Therefore, a background correction was necessary. The sample quantity equivalent to that used in the porphyrin method was taken in the cuvette and filled up with ultrapure water. All measurements were performed against 3 mL ultrapure water at 468 nm for the same duration as the corresponding speciation measurement. The resulting background absorbance was subtracted from the Mn absorbance measurement as correction.

Kinetic modeling

The kinetic modeling of Mn^{2+}, Mn^{3+}_{weak}, and Mn^{3+}_{strong} species was performed in RStudio 1.4.1106 using R 4.0.5 and the nlmrt package (version 2016.3.2) (Nash, 2016; R Core Team, 2021). Because the start of the reaction did not coincide with the first recorded

measurement point owing to manual operation, an additional parameter (t_0) was implemented in both modeling equations to estimate the starting point of the recorded kinetic data (Equations 3 and 4).

Three-parameter equation:

$$Mn^{2+} \cdot (1 - e^{-k_1 \cdot (t - t_0)}), \quad (3)$$

with Mn^{2+} = Mn^{2+} concentration (µg L^{-1}); k_1 = Mn^{2+} rate constant (s^{-1}); t = reaction time (s); and t_0 = reaction start (s)

Five-parameter equation:

$$Mn^{2+} \cdot (1 - e^{-k_1 \cdot (t - t_0)}) + Mn^{3+} \cdot (1 - e^{-k_2 \cdot (t - t_0)}) \quad (4)$$

with Mn^{2+} = Mn^{2+} concentration (µg L^{-1}); Mn^{3+} = Mn^{3+} concentration (µg L^{-1}); k_1 = Mn^{2+} rate constant (s^{-1}); k_2 = Mn^{3+} rate constant (s^{-1}); t = reaction time (s); and t_0 = reaction start (s)

First, the parameters (Equations 3 and 4) were estimated by the *wrapnls* method that attempts to solve the nonlinear sum of squares problem by using *nlxb* algorithm. In this step, lower and upper limits for the individual parameters (Mn^{2+}, Mn^{3+}, k_1, k_2, t_0) are set manually to define a fixed interval for the estimation procedure. This allows the *nlxb* algorithm to make a more accurate first approximation of the parameters. Second, the nonlinear least squares (*nls*) method based on the stats package (version 3.6.2) was executed for a more precise estimation of the parameters (Nash, 1990; R Core Team, 2020). The goodness of both fits to the data was determined by calculating the root mean square error (RMSE). The implementation of t_0 in both equations was necessary to obtain proper rate constants. Subsequently, the modeled k_1 and k_2 values of the samples were compared with the rate constants of the $MnCl_2 \cdot 4H_2O$ standards. We determined slower reaction rates for the $MnCl_2 \cdot 4H_2O$ standards (reaction ended in approximately 90 s) that were an order of magnitude lower than those reported by Madison et al. (2011). We accounted for this deviation in the modeling of the Mn species.

2.3 Results

Table 2.1 presents the pH and EC of all 53 forest floor solutions and soil solutions sampled from the non-limed and limed study sites. The pH ranged from strong acidic (pH 3.4, non-limed forest floor) to slight acidic (pH 6.3, limed forest floor) conditions. Mean pH increased from 3.5 to 4.2 in the non-limed site reaching the maximum at the 30-cm depth, which remained constant up to 80-cm depth. In the limed site, the pH was 4.3 at all depths. The EC increased with increasing depth and was twice as high as that at the non-limed site, except for the forest floor. At both sites, the mean DOC concentrations peaked in the forest floor with 38.6 and 58.0 mg C L^{-1} and decreased sharply in the mineral horizons to ≈ 4.0 mg C L^{-1}. The molar absorptivity revealed two special features: for the corresponding depths, it was always higher on the limed site and from the 30-cm depths it increased to the 80-cm depths.

Table 2.1 pH, electrical conductivity (EC), dissolved organic carbon (DOC) concentrations, and molar absorptivity at 254 nm of forest floor solutions and soil solutions from non-limed and limed forest sites.

			pH		EC (µS cm^{-1})	
Samples	**n**	**Depth (cm)**	**Range**	**Mean**	**Range**	**Mean**
Forest floor solution (non-limed)	5	+5	3.4–3.5	3.5 ± 0[a]	74–100	85 ± 9
Soil solution (non-limed)	11	30	4.0–4.5	4.2 ± 0.2	23–127	59 ± 26
Soil solution (non-limed)	12	80	3.9–4.3	4.2 ± 0.1	77–142	97 ± 18
Forest floor solution (limed)	7	+5	3.6–6.3	4.3 ± 0.8	33–67	47 ± 10
Soil solution (limed)	6	30	4.0–4.7	4.3 ± 0.3	81–262	59 ± 26
Soil solution (limed)	12	80	4.1–4.5	4.3 ± 0.2	94–368	214 ± 75

[a] Standard error of the mean.

Table 2.1 (continued)

Samples	n	Depth (cm)	DOC (mg L^{-1})		Molar absorptivity at 254 nm (L mol^{-1} cm^{-1})	
			Range	Mean	Range	Mean
Forest floor solution (non-limed)	5	+5	37.2–77.1	58.0 ± 13.4	514–530	528 ± 13
Soil solution (non-limed)	11	30	2.49–13.7	8.00 ± 3.21	195–384	307 ± 55
Soil solution (non-limed)	12	80	1.78–12.0	3.97 ± 2.74	170–1207	378 ± 269
Forest floor solution (limed)	7	+5	26.3–58.0	38.6 ± 13.0	566–666	597 ± 37
Soil solution (limed)	6	30	8.04–28.4	16.7 ± 6.54	334–441	395 ± 38
Soil solution (limed)	12	80	2.08–6.93	3.96 ± 1.42	222–972	479 ± 227

[a] Standard error of the mean.

Figure 2.1A demonstrates the effect of the buffer solution added to acidic forest floor solution from the non-limed study site as the first modification. Initially, the sample had a pH of 3.5 that was significantly lower than the required pH (7.5−8.0) for the kinetic reaction. Further, the substitution reaction showed a slower reaction kinetic, and a fit could not be applied. After adding the buffer solution and bringing the sample pH to the required range, the substitution reaction was significantly accelerated, as represented by proper rate constants (k_1 = 0.0183 s^{-1} and k_2 = 0.0045 s^{-1}).

Figure 2.1B shows the second modification, that is, the subtraction of the background absorption. It is the same sample as in Figure 2.1A. The procedure generated with 84.3 µg L^{-1} lower Mn findings than the uncorrected sample (122 µg L^{-1}). Hence, the colorization of samples can lead to an overestimation of the Mn concentrations. The modeled speciation revealed Mn^{2+} (69.9 µg L^{-1}) as the dominant species, followed by Mn^{3+}_{weak} (14.4 µg L^{-1}). The goodness of fit showed conformity to the data with an RMSE of 0.0009. In summary, the forest floor solutions showed considerably high background absorbances (>0.01 A), whereas the soil solutions in the mineral horizons revealed negligible background absorbance associated with DOM.

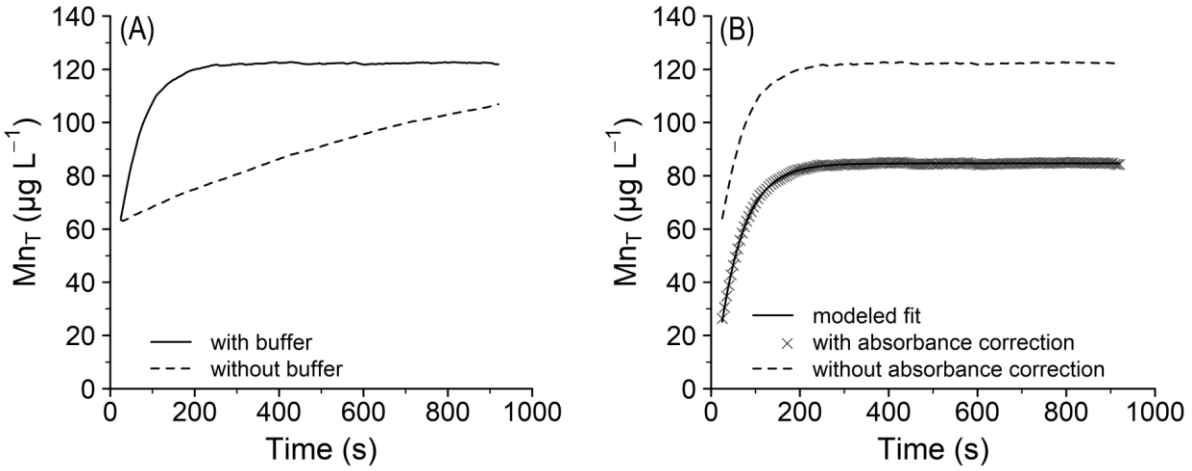

Figure 2.1 (A) Effect of added pH-buffer ($NaHCO_3$) solution to an acidic forest floor solution (pH 3.5) on reaction kinetics and (B) the elimination of the dissolved organic carbon colorization induced background absorption at 468 nm with the visualization of the modeled fit over the corrected data set.

To test the accuracy of the Mn_T concentrations determined by the spectrophotometric method, the forest floor solutions and soil solutions were additionally analyzed by ICP OES. As shown in Figure 2.2, there was a very high agreement between both methods. Overall, the ratio of $Mn_{T\ porphyrin}/Mn_{T\ ICP\ OES}$ ranged from 0.90 to 1.15 with a mean of 1.01 ± 0.06. However, two samples showed significantly lower Mn concentrations for the spectrophotometric method. Notably, the ratio of $Mn_{T\ porphyrin}/Mn_{T\ ICP\ OES}$ in Bv and Cv horizons was 1.00 ± 0.05, while in the forest floor solutions it was higher (1.06 ± 0.07).

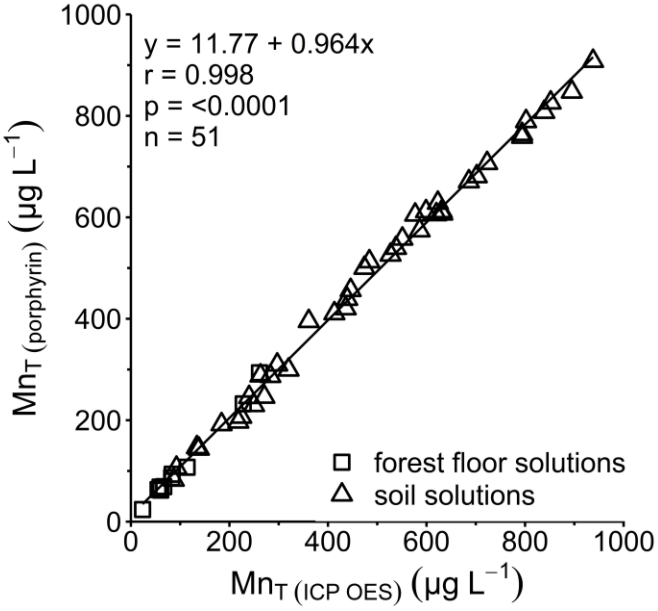

Figure 2.2 Linear regression of porphyrin kinetic modeled total manganese concentrations in forest floor solutions and soil solutions against concentrations determined by inductively coupled plasma optical emission spectrometry (ICP OES).

The modeling algorithms applied to the three- and five-parameter equations allowed not only the determination of dissolved Mn_T but also the speciation of dissolved Mn^{2+}, Mn^{3+}_{weak}, and Mn^{3+}_{strong} (Table 2.2). The total Mn concentrations ranged from 23.9 to 908 µg L^{-1}. At both sites, Mn_T concentrations continuously increased with increasing depth and were of similar range in the soil solutions of similar magnitude. However, in the forest floor solutions, Mn_T concentrations were slightly more than twice as high at the limed site than those at the non-limed site. Considering the species distribution, it was clear that Mn^{2+} was the dominant Mn species (53.1−81.5%) followed by the Mn^{3+}_{weak} species (18.5−46.9%), which was true for both sites and all depths. Mn^{3+}_{strong} occurred only in traces (up to 6.4%) and was exclusively detectable in the 30-cm depth.

Mean rate constants k_1 (0.0488 ± 0.0199 s^{-1}) and k_2 (0.0152 ± 0.0114 s^{-1}) were modeled for 51 samples. The modeled values of k_2 were at least a factor of 3 smaller than k_1, and the modeling of the five-parameter equation revealed an RMSE of less than 0.003 (0.001 ± 0.0007).

Table 2.2 Manganese speciation in forest floor solutions and soil solutions from non-limed and limed forest sites.

			Mn_T		**Mn^{2+}**			
Samples	**n**	**Depth (cm)**	**Range (µg L^{-1})**	**Mean (µg L^{-1})**	**Range (µg L^{-1})**	**Mean (µg L^{-1})**	**Range (%)**	**Mean (%)**
Forest floor solution (non-limed)	5	+5	23.9–96.0	67.6 ± 24.9[a]	14.5–72.7	33.5 ± 21.6	21.2–89.3	53.1 ± 28.2
Soil solution (non-limed)	11	30	82.3–439	278 ± 104	55.5–304	165 ± 66.0	25.4–83.9	61.7 ± 16.5
Soil solution (non-limed)	12	80	395–908	673 ± 145	361–786	519 ± 130	60.8–91.4	77.5 ± 9.61
Forest floor solution (limed)	5	+5	69.1–294	157 ± 89.8	31.3–99.0	57.5 ± 23.3	13.5–90.2	55.1 ± 34.1
Soil solution (limed)	6	30	106–526	261 ± 139	68.0–465	176 ± 135	40.0–88.5	64.0 ± 17.2
Soil solution (limed)	12	80	144–847	590 ± 168	143–621	468 ± 129	55.1–99.4	81.5 ± 14.3

Abbreviation: n.d., not detectable.
[a] Standard error of the mean.

Table 2.2 (continued)

			Mn^{3+}_{weak}			
Samples	**n**	**Depth (cm)**	**Range (µg L^{-1})**	**Mean (µg L^{-1})**	**Range (%)**	**Mean (%)**
Forest floor solution (non-limed)	5	+5	2.56–55.6	34.2 ± 21.7	10.7–78.8	46.9 ± 28.2
Soil solution (non-limed)	11	30	26.3–323	108 ± 83.7	13.9–73.6	36.3 ± 16.7
Soil solution (non-limed)	12	80	33.9–299	154 ± 77.4	4.90–39.2	22.5 ± 9.61
Forest floor solution (limed)	5	+5	10.7–253	99.2 ± 106	9.77–86.5	44.9 ± 34.1
Soil solution (limed)	6	30	24.4–179	78.9 ± 52.4	9.29–57.7	33.1 ± 17.4
Soil solution (limed)	12	80	0.80–316	123 ± 101	0.56–44.9	18.5 ± 14.3

Abbreviation: n.d., not detectable.

[a] Standard error of the mean.

Table 2.2 (continued)

			Mn^{3+}_{strong}			
Samples	**n**	**Depth (cm)**	**Range (µg L^{-1})**	**Mean (µg L^{-1})**	**Range (%)**	**Mean (%)**
Forest floor solution (non-limed)	5	+5	n.d.	n.d.	n.d.	n.d.
Soil solution (non-limed)	11	30	0–10.7	5.68 ± 2.93	0.55–3.65	2.00 ± 0.97
Soil solution (non-limed)	12	80	n.d.	n.d.	n.d.	n.d.
Forest floor solution (limed)	5	+5	n.d.	n.d.	n.d.	n.d.
Soil solution (limed)	6	30	3.32–11.9	6.66 ± 2.86	1.83–6.35	2.90 ± 1.55
Soil solution (limed)	12	80	n.d.	n.d.	n.d.	n.d.

Abbreviation: n.d., not detectable.

[a] Standard error of the mean.

2.4 Discussion

The effect of liming on the Mn cycling in acidic forest soils is not discussed here because it is outside the scope of the study. We selected the site such that the aqueous samples had a varying range of pH and colorization. Thus, we will first address the methodological adaptions and then discuss the results, keeping in mind that dissolved Mn^{3+} data from terrestrial environments are not yet available.

Different reaction kinetics are necessary to differentiate between the two Mn species. As demonstrated by Madison et al. (2011) and Thibault de Chanvalon and Luther (2019), the fastest complexation rate (k_2) of the Mn^{3+} species is nearly one order of magnitude or at least a factor of 3 lower than the Mn^{2+} complexation rate (k_1). However, our results showed slower reaction kinetics for Mn^{2+} and Mn^{3+} but satisfy the condition $k_1 \geq 3k_2$ as reported by Thibault de Chanvalon and Luther (2019). Because the complexation in all samples was not finished in approximately 90 s (e.g., Figure 2.1A), a discrimination between Mn^{2+} and Mn^{3+} was possible in forest floor solutions and soil solutions. More recently, the kinetic evaluation of the porphyrin method has been criticized (Kim et al., 2022). It was stated that the method should be more applicable to single ligand solutions showing the binding affinities of Mn to isolated organic molecules. The complexity of environmental samples, however, complicates this modeling. Characterizing the diversity of potential Mn^{3+}-forming ligands would require a more differentiated mathematical approach to incorporate the rate constants of each ligand. Regarding Mn^{3+} species and complexity of DOM composition in field samples, we opine that this might never be achieved. However, we would like to point out that possible limitations of the kinetic method are a motivation to further develop methodological modifications concerning, for example, chemical pretreatment before analysis.

pH of forest floor solutions and particularly soil solutions from forest sites are often well below the range required for the porphyrin method, that is, below 7.5−8.0; thus, a pH buffer must be added to such samples. Otherwise, the reaction kinetics of the substitution reaction (Cd^{2+} is replaced by either Mn^{2+} or Mn^{3+}) are slowed down because of the high proton concentration (Figure 2.1A). After adding buffer, reaction kinetics showed an accelerated substitution reaction as expressed by improved rate constants. Without the pH correction, the data cannot be fitted. Thus, it is necessary to check and correct the pH

not only in case of soil solutions, but also of aqueous environmental samples where low pH is expected (e.g., mining waters and contaminated ground waters). Charbonnier and Anschutz (2019) determined Mn_T in acidified pore waters and extracts by the porphyrin method after pH correction.

Terrestrial DOC often generates a prominent sample-inherent colorization in the visible wavelength range (Kalbitz et al., 2000), which is also the wavelength at which the method works (468 nm). This contrasts with seawater samples for which the method had originally been adapted (Madison et al., 2011). Our results indicate that background absorbance caused by intensive sample-inherent colorization leads to a continuous overestimation of the Mn concentrations because of excessive absorbance signal at 468 nm in forest floor solutions (Figure 2.1B). By subtracting the background absorbance, a corrected Mn_T concentration can be obtained which coincides with ICP OES data. Because forest floor solutions are always colored, it is necessary to consider the background absorption of these samples. Typically, soil solutions showed much lower DOC concentrations than forest floor solutions and are, therefore, hardly colored to not colored at all (Kalbitz et al., 2000). If soil solutions are colored, however, their background absorption must be considered, which is true for other kind of environmental samples. For example, in a study on water treatment, Mn^{3+} could not be analyzed because of highly colored water samples (Johnson et al., 2018).

During the last decade, Mn^{3+} has been identified in estuarine and marine waters or sediment porewaters both under oxic and anoxic conditions (Madison et al., 2011, 2013; Oldham et al., 2015, 2019, 2021; Oldham, Jones, et al., 2017; Oldham, Miller, et al., 2017; Oldham, Mucci, et al., 2017; Thibault de Chanvalon & Luther, 2019) and in waters from a water treatment study (Johnson et al., 2018). Thus, our study revealed that Mn^{3+} was not only present in all samples but also a major component of the total dissolved Mn pool in a terrestrial environment. Moreover, Mn^{3+} is stabilized by natural organic ligands such as DOC as observed in the present study, which is the largest component of DOM (Table 2.1). Dissolved organic matter is composed of a heterogeneous continuum of complex high- to low-molecular weight organic molecules that are known for their metal binding capacity having substantial effect on metal speciation (Aiken et al., 2011; Tipping, 2002).

After adding a reductant, such as hydroxylamine, to aqueous samples, an increase in dissolved Mn_T has been observed when the Madison et al. (2011) protocol was followed (Oldham et al., 2015; Oldham, Jones, et al., 2017). The authors assumed that the porphyrin ligand could not substitute Mn^{3+}_{strong} complexes. After adding the reductant, the Mn^{3+} in these complexes was rapidly reduced to porphyrin-reactive Mn^{2+}. Hence, when a sample is treated with a reductant and a subsample is not treated, two operationally defined Mn^{3+}-ligand classes, weak and strong, can be detected and quantified. Strongly complexed Mn^{3+} was of minor importance in this study (Table 2.2). Its exclusive occurrence in the 30-cm soil depth cannot be clearly attributed to any reason because of the low concentrations. Slightly higher proportions of Mn^{3+}_{strong} (up to 16%) were reported in marine pore waters in the shores, whereas this species was below the detection limit in the pelagic area (Oldham et al., 2019). This was attributed to a greater proportion of terrestrial ligands occurring at the shore. They assumed that the ligands were more varied and bound Mn more strongly than sedimentary marine ligands. In contrast, the ligands in this study, which were exclusively of terrestrial origin, did not appear to bind Mn^{3+} strongly enough to be substituted by the porphyrin ligand.

The Mn_T concentrations determined using the porphyrin method in the forest floor solutions were slightly higher than those determined by ICP OES. We assume that this discrepancy was caused by the precipitation of organic Mn complexes that were insoluble at pH <2, because the ICP OES samples were acidified for sample preservation. This effect was restricted to the DOC-rich forest floor solutions. In the DOM-poor mineral soil solutions (Bv and Cv horizons), the precipitation appeared to be absent or low and hence was not detected. Porphyrin method has shown higher Mn_T concentrations in marine waters and pore waters in comparison to those of AAS method (Oldham, Jones, et al., 2017; Oldham et al., 2019), which was because of the removal of some humic Mn^{3+} complexes after acidification. Possible loss of Mn after acidification for sample stabilization should be considered when analyzing DOM-rich soil samples.

In forest ecosystems, the litter layer plays a significant role in the redox cycling of Mn. Mn is absorbed by plant roots and present in live foliage in its reduced form (Mn^{2+}); during foliar decomposition along with the enrichment of Mn in the foliar litter, it also occurs as Mn^{3+} after oxidation at microsites of active decay and later as Mn^{III} or Mn^{IV} in Mn oxides (Keiluweit et al., 2015). This underlines the view that the presence of Mn^{3+} in decomposing

litter could be related to fungal activity because some fungi (Basidiomycota) produce the enzyme manganese peroxidase that reacts with hydrogen peroxide to oxidize Mn^{2+} to Mn^{3+}. Further, Mn^{3+} is stabilized by organic ligands. These Mn^{3+} complexes can attack phenolic lignin moieties which are finally converted to CO_2 and DOM with concomitant reduction of Mn^{3+} to Mn^{2+} closing the redox cycle (Hofrichter, 2002; Jones et al., 2018; Perez & Jeffries, 1992). Undoubtedly, this oxidative pathway from Mn^{2+} to Mn^{3+} occurs in the litter layer of our study site which might be reflected in the presence of dissolved Mn^{3+} in forest floor solutions. However, it should be considered that the forest floor solution comprises not only water percolating through the litter layer (L horizon) but also through the O horizon. In this horizon, significant quantity of litter-derived DOM is removed by sorption and mineralization; meanwhile, new DOM is formed by decomposition of humified material (Fröberg et al., 2003, 2007; Müller et al., 2009); a small fraction of litter-derived DOM remains that moves through the soil without retention (Fröberg et al., 2007). Hence, the DOM in forest floor solutions should be regarded as a mixture of leachates from both fresh litter and humified organic matter. During the passage through the mineral soil, DOM-mobilizing (e.g., desorption and microbial production) and DOM-immobilizing (e.g., sorption and consumption) processes take place continuously which alter both the concentration and composition of DOM (Kaiser & Kalbitz, 2012). Generally, DOM concentrations decrease with soil depth as observed in this study (Table 2.1), and the proportions of more recent plant-derived compounds decrease with soil depth, while those of microbial metabolites and aged/microbially processed plant-derived compounds increase. The sole qualitative parameter that we measured was the molar absorptivity of DOM at 254 nm (Table 2.1), which is associated with aromaticity and molecular weight (Rodríguez et al., 2016; Weishaar et al., 2003). We are aware that this parameter is rather non-specific, but forest floor-DOM appeared to be of higher aromaticity and molecular weight than soil solution-DOM. Although the mean percentages of DOM-bound Mn^{3+} decrease with increasing depth, we observed an increase of the mean molar ratio of Mn^{3+}/DOC ($0.4 \cdot 10^{-4}$ in forest floor solution, $3.4 \cdot 10^{-3}$ at 30-cm depth, and $9.1 \cdot 10^{-3}$ at 80-cm depth). This is a possible indication of a higher binding affinity of organic ligands toward Mn^{3+}. Persistent aqueous Mn^{3+} complexes with naturally occurring high-affinity ligands have been reported, such as those with siderophore, pyrophosphate, and citrate (Harrington et al., 2012; Klewicki & Morgan, 1998; Kostka et al., 1995); sometimes, they

have stability constants that are similar to or greater than Fe^{3+} complexes. Apparently, the proportion of functional groups in DOM that have a high affinity for Mn^{3+} increases with increasing depth.

What could be the further fate of the Mn^{3+} complexes? The behavior of Mn^{3+} is strongly linked to DOM as outlined above. Thus, three scenarios regarding the behavior of Mn^{3+} are possible: (1) when the complexes are retained/degraded in the soil, the Mn^{3+} could be liberated and transformed into $Mn^{(III,IV)}$ oxides; (2) when DOM is newly formed in the soil, inherent new organic ligands may dissolve Mn soil constituents, particularly Mn oxides, without (Mn^{III}) and with (Mn^{IV}) reduction; (3) when the complexes are not retained in the soil, they could be leached and exported to groundwaters or surface water bodies (see the concentrations in the 80-cm soil depth, Table 2.2).

2.5 Conclusions

By correcting too low pH and intense colorization of the samples, the porphyrin method can be applied to distinguish Mn^{2+} and Mn^{3+} in the aqueous phase of forest soils. The data suggested that Mn^{3+} is a non-neglectable component of the total dissolved Mn pool in soil. We postulate that Mn^{3+} is ubiquitous in the aqueous phase of soils because the omnipresent DOM can act as a ligand for this species. Further research should address the occurrence of Mn^{3+} in soils under further boundary conditions, particularly pH, redox potential, and quantity and quality of natural DOM.

Acknowledgments

Financial support was given by *Deutsche Forschungsgemeinschaft (DFG) (German Research Foundation)* under the contract number *Ma 2143/17-1* and is gratefully acknowledged. We are thankful to *Dr. Martin Greve*, *Research Institute for Forest Ecology and Forestry of the State of Rhineland-Palatinate, Trippstadt, Germany*, for assistance in supplying the samples.

Open access funding enabled and organized by Projekt DEAL.

DATA AVAILABILITY STATEMENT

The data that support the findings of this study are available from the corresponding author upon reasonable request.

ORCID

Constantin Lux https://orcid.org/0000-0002-0860-8542

Tim Mansfeldt https://orcid.org/0000-0002-7557-6827

References

Aiken G. R., Hsu-Kim H., & Ryan, J. N. (2011). Influence of dissolved organic matter on the environmental fate of metals, nanoparticles, and colloids. *Environmental Science & Technology*, 45, 3196−3201.

Berg, B., Steffen, K. T., & McClaugherty, C. (2007). Litter decomposition rate is dependent on litter Mn concentrations. *Biogeochemistry*, 82, 29−39.

Biedermann, G., & Palombari, R. (1978). On the hydrolysis of the manganese(III) ion. *Acta Chemica Scandinavica*, 32(5), 381−390.

Blume, H.-P., Brümmer, G.W., Fleige, H., Horn, R., Kandeler, E., Kögel-Knabner, I., Kretzschmar, R., Stahr, K., & Wilke, B.-M. (2016). *Scheffer/Schachtschabel–Soil Science*. Springer.

Charbonnier, C., & Anschutz, P. (2019). Spectrophotometric determination of manganese in acidified matrices from (pore)waters and from sequential leaching of sediments. *Talanta*, 195, 778−784.

Davies, G. (1969). Some aspects of the chemistry of manganese(III) in aqueous solution. *Coordination Chemistry Reviews*, 4(2), 199−224.

Dion, H. G., & Mann, P. J. G. (1946). Three-valent manganese in soils. *The Journal of Agricultural Science*, 36(4), 239−245.

Essington, M. E. (2015). *Soil and water chemistry. An integrative approach* (2nd ed.). CRC Press.

FAWF (2016). Forschungsanstalt für Waldökologie und Forstwirtschaft, Rheinland-Pfalz. https://fawf.wald.rlp.de/index.php?id=12306.

Fröberg, M., Berggren, D., Bergkvist, B., Bryant, C., & Knicker, H. (2003). Contributions of Oi, Oe and Oa horizons to dissolved organic matter in forest floor leachates. *Geoderma*, 113(3-4), 311−322.

Fröberg, M., Berggren Kleja, D., & Hagedorn, F. (2007). The contribution of fresh litter to dissolved organic carbon leached from a coniferous forest floor. *European Journal of Soil Science*, 58(1), 108−114.

Gao, S., Tanji, K. K., Scardaci, S. C., & Chow, A. T. (2002). Comparison of redox indicators in a paddy soil during rice-growing season. *Soil Science Society of America Journal*, 66(3), 805−817.

GAFA, Gutachterausschuss Forstliche Analytik (2022). *Handbuch Forstliche Analytik (HFA), 1. - 6. Ergänzung des Gutachterausschuss Forstliche Analytik.* Bundesministerium für Ernährung, Landwirtschaft und Verbraucherschutz (BMELV) & Nordwestdeutsche Forstliche Versuchsanstalt (NW-FVA).

Gotoh, S., & Patrick Jr, W. H. (1972). Transformation of manganese in a waterlogged soil as affected by redox potential and pH. *Soil Science Society of America Journal*, 36(5), 738−742.

Gottfreund, J., & Schweisfurth, R. (1983). Mikrobiologische Oxidation und Reduktion von Manganspecies. *Fresenius' Journal of Analytical Chemistry*, 316(6), 634−638.

Harrington, J. M., Parker, D. L., Bargar, J. R., Jarzecki, A. A., Tebo, B. M., Sposito, G., & Duckworth, O. W. (2012). Structural dependence of Mn complexation by siderophores: Donor group dependence on complex stability and reactivity. *Geochimica et Cosmochimica Acta*, 88, 106−119.

Hofrichter, M. (2002). Review: Lignin conversion by manganese peroxidase (MnP). *Enzyme and Microbial Technology*, 30, 454−466.

Hseu, Z. Y., Chen, Z. S., & Leu, I. Y. (2000). Soil solution composition, water tables, and redox potentials of anthraquic Ultisols in a toposequence. *Soil Science*, 165(11), 869−880.

Hu, E., Zhang, Y., Wu, S., Wu, J., Liang, L., & He, F. (2017). Role of dissolved Mn(III) in transformation of organic contaminants: Non-oxidative versus oxidative mechanisms. *Water Research*, 111, 234−243.

IUSS Working Group WRB (2015). *World Reference Base for Soil Resources 2014, update 2015.* International soil classification system for naming soils and creating legends for soil maps. World Soil Resources Reports No. 106. FAO.

Johnson, K. L., McCann, C. M., Wilkinson, J.-L., Jones, M., Tebo, B. M., West, M., Elgy, C., Clarke, C. E., Gowdy, C., & Hudson-Edwards, K. A. (2018). Dissolved Mn(III) in water treatment works: Prevalence and significance. *Water Research*, 140, 181−190.

Jones, M. E., Nico, P. S., Ying, S., Regier, T., Thieme, J., & Keiluweit, M. (2018). Manganese-driven carbon oxidation at oxic−anoxic interfaces. *Environmental Science & Technology*, 52(21): 12349−12357.

Jones, M. E., LaCroix, R. E., Zeigler, J., Ying, S. C., Nico, P. S., & Keiluweit, M. (2020). Enzymes, manganese, or iron? Drivers of oxidative organic matter decomposition in soils. *Environmental Science & Technology*, 54(21), 14114−14123.

Kaiser, K., & Kalbitz, K. (2012). Cycling downwards − dissolved organic matter in soils. *Soil Biology and Biochemistry*, 52, 29−32.

Kalbitz, K., Solinger, S., Park J. H., Michalzik, B., & Matzner, E. (2000). Controls on the dynamics of dissolved organic matter in soils: A review. *Soil Science*, 165(4), 277−304.

Keiluweit, M., Nico, P., Harmon, M. E., Mao, J., Pett-Ridge, J., & Kleber, M. (2015). Long-term litter decomposition controlled by manganese redox cycling. *Proceedings of the National Acadamy of Sciences*, 112(38), E5253−E5260.

Kim, B., Lingappa, U. F., Magyar, J., Monteverde, D., Valentine, J. S., Cho, J., & Fischer, W. (2022). Challenges of measuring soluble Mn(III) species in natural samples. *Molecules (Basel, Switzerland)*, 27(5), 1661−1671.

Klewicki, J. K., & Morgan, J. J. (1998). Kinetic behavior of Mn(III) complexes of pyrophosphate, EDTA and citrate. *Environmental Science & Technology*, 32(19), 2916−2922.

Kostka, J. E., Luther III, G. W., & Nealson, K. H. (1995). Chemical and biological reduction of Mn(III)-pyrophosphate complexes: Potential importance of dissolved Mn(III) as an environmental oxidant. *Geochimica et Cosmocimica Acta*, 59(5), 885−894.

Luther III, G. W., Madison, A. S., Mucci, A., Sundby, B., & Oldham, V. E. (2015). A kinetic approach to assess the strengths of ligands bound to soluble Mn(III). *Marine Chemistry*, 173, 93−99.

Madison, A. S., Tebo, B. M., & Luther III, G. W. (2011). Simultaneous determination of soluble manganese(III), manganese(II) and total manganese in natural (pore)waters. *Talanta*, 84(2), 374−381.

Madison, A. S., Tebo, B. M., Mucci, A., Sundby, B., & Luther III, G. W. (2013). Abundant porewater Mn(III) is a major component of the sedimentary redox system. *Science*, 341(6148), 875−878.

Mansfeldt, T. (2004). Redox potential of bulk soil and soil solution concentration of nitrate, manganese, iron, and sulfate in two Gleysols. *Journal of Plant Nutrition and Soil Science*, 167(1), 7−16.

Müller, M., Alewell, C., & Hagedorn, F. (2009). Effective retention of litter-derived dissolved organic carbon in organic layers. *Soil Biology and Biochemistry*, 41(6), 1066−1074.

Nash, J. C. (1990). *Compact numerical methods for computers. Linear Algebra and function minimisation* (2nd ed.). Routledge.

Nash, J. C. (2016). nlmrt: Functions for Nonlinear Least Squares Solution. R package version 2016.3.2. https://CRAN.R-project.org/package=nlmrt

Oldham, V. E., Owings, S. M., Jones, M. R., Tebo, B. M., & Luther III, G. W. (2015). Evidence for the presence of strong Mn(III)-binding ligands in the water column of the Chesapeake Bay. *Marine Chemistry*, 171, 58−66.

Oldham, V. E., Jones, M. R., Tebo, B. M., & Luther III, G. W. (2017). Oxidative and reductive processes contributing to manganese cycling at oxic-anoxic interfaces. *Marine Chemistry*, 195, 122−128.

Oldham, V. E., Miller, M. T., Jensen, L. T., & Luther III, G. W. (2017). Revisiting Mn and Fe removal in humic rich estuaries. *Geochimica et Cosmochimica Acta*, 209, 267−283.

Oldham, V. E., Mucci, A., Tebo, B. M., & Luther III, G. W. (2017). Soluble Mn(III)−L complexes are abundant in oxygenated waters and stabilized by humic ligands. *Geochimica et Cosmochimica Acta*, 199, 238−246.

Oldham, V. E., Siebecker, M. G., Jones, M. R., Mucci, A., Tebo, B. M., & Luther III, G. W. (2019). The speciation and mobility of Mn and Fe in estuarine sediments. *Aquatic Geochemistry*, 25, 3−26.

Oldham, V. E., Chmiel, R., Hansel, C. M., DiTullio, G. R., Rao, D., & Saito, M. (2021). Inhibited manganese oxide formation hinders cobalt scavenging in the Ross Sea. *Global Biogeochemical Cycles*, 35(5), e2020GB006706.

Patrick Jr, W. H., & Henderson, R. E. (1981). A method for controlling redox potential in packed soil cores. *Soil Science Society of America Journal*, 45(1), 35−38.

Patrick Jr, W. H., & Jugsujijnda, A. (1992). Sequential reduction and oxidation of inorganic nitrogen, manganese, and iron in flooded soil. *Soil Science Society of America Journal*, 56(4), 1071−1073.

Perez, J., & Jeffries, T. W. (1992). Roles of manganese and organic acid chelators in regulating lignin degradation and biosynthesis of peroxidases by *Phanerochaete chrysosporium*. *Applied and Environmental Microbiology*, 58(8), 2402−2409.

R Core Team (2020). R: A language and environment for statistical computing. R Foundation for Statistical Computing, Vienna, Austria. URL https://www.R-project.org/

R Core Team (2021). R: A language and environment for statistical computing. R Foundation for Statistical Computing, Vienna, Austria. URL https://www.R-project.org/

Rodríguez, F. J., Schlenger, P., & García-Valverde, M. (2016). Monitoring changes in the structure and properties of humic substances following ozonation using UV-Vis, FTIR and ^{1}H NMR techniques. *Science of the Total Environment*, 541, 623−637.

Sposito, G. (2016). *The chemistry of soils* (3rd ed.). Oxford University Press.

Thibault de Chanvalon, A. T., & Luther III, G. W. (2019). Mn speciation at nanomolar concentrations with a porphyrin competitive ligand and UV-vis measurements. *Talanta*, 200, 15−21.

Tipping, E. (2002). *Cation binding by humic substances. Cambridge Environmental Chemistry Series-12.* Cambridge University Press.

Weishaar, J. L., Aiken, G. R., Bergamaschi, B. A., Fram, M. S., Fujii, R., & Mopper, K. (2003). Evaluation of specific ultraviolet absorbance as an indicator of the chemical composition and reactivity of dissolved organic carbon. *Environmental Science & Technology* 37, 4702−4708.

Chapter 3: Dissolved trivalent manganese in forest soils – interaction of natural organic ligands with manganese oxides

Environmental Science: Processes & Impacts (2025) 27: 2875–2893

Author: Constantin Lux[1] (CL)

Co-authors: Kristian Ufer[2] (KU) and Tim Mansfeldt[1] (TM)

Formatting and orthography are adapted to the dissertation style.

Building on the adaptation of the porphyrin method in the first publication, this follow-up study was designed to investigate the reaction pathways leading to the formation of Mn^{3+}–NOL complexes during the dissolution of Mn oxides by NOLs. The results provide mechanistic insights into both oxidative and reductive abiotic pathways, extending the understanding of Mn^{3+}–NOL formation. This study is essential for interpreting the chemical processes underlying Mn^{3+}–NOL formation in soils, a central topic of the dissertation.

Author contributions are presented by category, including conceptualization and methodology, sample acquisition, sample preparation, laboratory analyses, formal analysis, software and data curation, investigation, visualization, writing – original draft, writing – review and editing, validation, supervision, project administration and funding acquisition. Within each category, authors are listed in order of their initials to indicate their respective contributions.

Conceptualization and methodology: CL and TM; sample acquisition: CL and TM; sample preparation: CL; laboratory analyses: CL and KU; formal analysis: CL; software and data curation: CL; investigation: CL; visualization: CL; writing – original draft: CL; writing – review and editing: CL, KU and TM; validation: TM; supervision: TM; project administration: TM; funding acquisition: TM.

The manuscript was submitted to “Environmental Science: Processes & Impacts” and published on 22 August 2025. DOI: 10.1039/D5EM00388A

[1] Institute of Geography, Faculty of Mathematics and Natural Sciences, Department of Geosciences, University of Cologne, Albertus-Magnus-Platz, D-50923 Cologne, Germany.

[2] Federal Institute for Geosciences and Natural Resources, Stilleweg 2, D-30655 Hannover, Germany

Graphical abstract

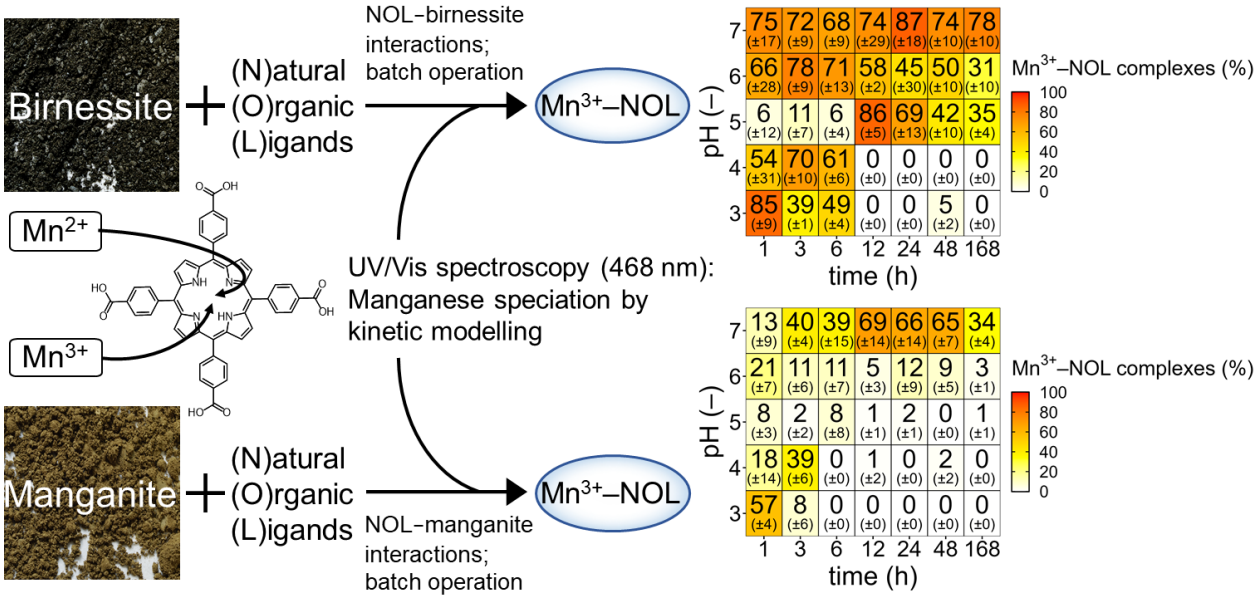

Environmental significance

Dissolved trivalent manganese (Mn^{3+}) participates in geochemical processes, such as the decomposition of organic compounds, and thus affects carbon storage. In soils, however, this species has been neglected. It is, therefore, a valuable subject to study both quantitatively and qualitatively, in order to draw conclusions about its formation and stabilization. We investigated the influence of soil-derived natural organic ligands (NOLs) on the pH- and time-dependent dissolution of two synthetic Mn oxides. Subsequently, the speciation of the resulting total dissolved Mn pool was performed based on kinetic modeling. Our results demonstrate that terrestrial NOLs complex and stabilize Mn^{3+} as Mn^{3+}–NOL complexes. We propose that Mn^{3+}–NOL complexes are a non-negligible compound in soils, and that this species should be considered in biogeochemical modeling.

Abstract

The presence of dissolved trivalent manganese (Mn^{3+}) in soils has been neglected largely due to its rapid disproportionation. However, natural organic ligands (NOLs) complex and stabilize Mn^{3+} by the formation of stable Mn^{3+}–NOL complexes. Our objectives were (i) to investigate the influence of NOLs on the dissolution of synthetic Mn oxides, (ii) to perform the speciation analysis of the resulting dissolved total Mn (Mn_T) pool, and (iii) to elucidate the principles governing abiotic formation of Mn^{3+}–NOL complexes. NOLs were obtained by extraction (0.001 M $CaCl_2$, 24 h) from a terrestrial forest floor Oe horizon (moder-like raw humus). In batch operations, NOLs reacted with either birnessite (containing Mn^{IV} and minor Mn^{III}) or manganite (containing solely Mn^{III}). The interaction between NOLs and Mn (hydr)oxides was investigated as a function of time (1–168 h, 7 steps), and pH (3–7, 5 steps). Mn speciation analysis was performed using a spectrophotometric protocol based on kinetic modeling. Results show that the dissolution of the Mn oxides increased with decreasing pH and increasing time. Mean proportions of Mn^{3+}–NOL complexes relative to the Mn_T pool ranged from 0 to 87 ± 18% (birnessite), and from 0 to 69 ± 14% (manganite). A pH-dependent formation of Mn^{3+}–NOL complexes was observed, highlighting pH as the critical parameter. Complex stability decreased with decreasing pH, while an influence of time was only assumed for strongly acidic conditions. Overall, Mn^{3+}–NOL complexes appeared to be metastable at pH 3–5 (birnessite) and below pH 7 (manganite). In addition, the formation of Mn^{3+}–NOL complexes was influenced by the individual properties of the Mn oxides as they were differing in their average oxidation state, point of zero charge, specific surface area and morphology and structure. These properties influence the formation mechanisms of Mn^{3+}–NOL complexes and, consequently, the Mn speciation. For example, they affect NOL adsorption rates and capacities, as well as the transformation and degradation of NOLs. We suggest (i) ligand-promoted non-reductive dissolution, (ii) ligand-promoted reductive dissolution, (iii) H^+-promoted dissolution, and (iv) ligand exchange as the four possible abiotic dissolution mechanisms for Mn release and Mn^{3+}–NOL complex formation. Following dissolution, either Mn^{3+}–NOL complexes were released, or released Mn^{2+} and Mn^{3+} may be complexed by additional NOLs with and without oxidation. We demonstrate that Mn^{3+}–NOL complexes are

important, previously underestimated, constituents of the Mn_T pool in forest floor solutions and propose that they are a non-negligible component in terrestrial environments.

Keywords: Mn speciation, birnessite, manganite, dissolved organic matter, forest floor extract

3.1 Introduction

Manganese (Mn) is a versatile and ubiquitous element. As a product of weathering, Mn accumulates in global surface soils at concentrations ranging from <7 to 9,000 mg kg^{-1} with mean values between 270 and 530 mg kg^{-1}.[1] Its oxidation states range from –3 to +7.[2] In soils, the oxidation states +2, +3 and +4 dominate.[3]

Dissolved divalent Mn (Mn^{2+}) has been assumed to be predominant in aquatic environments, while dissolved trivalent Mn (Mn^{3+}) was considered unstable due to its rapid disproportionation.[4,5] However, various studies have shown that natural organic ligands (NOLs) complex and stabilize Mn^{3+} in marine and estuarine environments, water treatment works, and acidic forest floor solutions as well as soil solutions.[6–14] Analyses of the binding strengths between Mn^{3+} and organic model ligands allow further discrimination between weakly (Mn^{3+}–NOL_{weak}) and strongly bound Mn^{3+} (Mn^{3+}–NOL_{strong}) complexes.[10] Despite the evidence presented so far for its occurrence and dynamics, the formation, persistence, and reactivity of Mn^{3+}–NOL complexes in soils remain largely unexplored. The geochemical behavior of Mn is highly dependent on parameters such as pH and redox potential (E_H),[15] as well as the variability of soil composition, *e.g.*, with respect to Mn oxides.[3]

More than 15 known Mn (oxyhydr)oxide minerals exist,[16,17] and they are widespread in soils. The $Mn^{III/IV}$ (oxyhydr)oxides play the largest role in terms of precipitation/dissolution processes, and Mn bioavailability.[18,19] Birnessite (δ–$Mn^{III/IV}O_2$) is a mixed-valence $Mn^{III/IV}$ oxide classified as a phyllomanganate.[20] It is one of the most abundant Mn oxides in the clay-size fraction (<2 µm) of soils.[21] Due to its high oxidation potential, birnessite oxidizes a wide range of natural organic and inorganic compounds.[22]
Manganite (γ–$Mn^{III}O(OH)$) is the most abundant and stable natural polymorph of Mn oxy(hydroxide) (MnO(OH)) minerals.[17] We selected these two Mn oxides because of their ubiquity in natural environments and their varying physico-chemical properties. These properties include the average oxidation state (AOS), the point of zero charge (PZC), the specific surface area (SSA), and the E_H, as well as the minerals' morphology and structure.

Dissolved organic matter (DOM) is a complex pool of NOLs with various functional groups, *e.g.*, carboxyl (R–COOH) and phenolic (R–OH) groups, and metal-binding

affinities.[23] Low molecular weight organic acids (*e.g.*, citric, oxalic or acetic acid) have carboxyl groups that bind Mn^{3+}.[24–27] Phenolic compounds, such as catechol or 2,3-dihydroxybenzoic acid, are known to form Mn^{3+}–NOL complexes.[10] In addition, amino acids and peptides (*e.g.*, siderophores) provide suitable binding sites for Mn^{3+}.[28,29] NOLs are the key component because stable Mn^{3+} can only be formed in the presence of ligands.[30] Nevertheless, the molecular complexity of DOM makes it challenging to predict the formation of Mn^{3+}–NOL complexes.

In soils, the principle mechanisms for Mn release[3] are (i) proton (H^+)-promoted dissolution,[31] (ii) biological reduction (dissimilatory reductive dissolution),[32–34] (iii) abiotic reduction (reductive dissolution), and (iv) ligand-promoted dissolution of Mn oxides.[26]

In this study, the examined abiotic mechanisms for Mn oxide dissolution are defined as (i) H^+-promoted dissolution ($Mn^{IV}O_2 + 4H^+ + 2e^- \rightarrow Mn^{2+} + 2H_2O$), (ii) ligand-promoted reductive dissolution (*e.g.*, $Mn^{IV} + NOL + 2e^- \rightarrow Mn^{2+} + NOL_{ox}$), (iii) ligand-promoted non-reductive dissolution ($Mn^{III} + NOL \rightarrow Mn^{3+}$–NOL), and (iv) ligand exchange (Mn^{III}–OH + $NOL^- \rightarrow Mn^{III}$–NOL + $OH^- \rightarrow Mn^{3+} + NOL \rightarrow Mn^{3+}$–NOL). Because H^+-promoted dissolution of both Mn oxides begins at pH ≤ 5, background dissolution rates were quantified in this study in the absence of NOLs to determine NOL-induced dissolution. The gradual H^+-promoted release of Mn^{2+} is assumed to occur in parallel in the presence of NOLs. Looking at ligand-promoted reductive dissolution, if the NOL has reductive properties, surface-bound Mn^{IV} and Mn^{III} are converted to Mn^{3+} and Mn^{2+}. These reduced Mn species may be complexed by the same NOL or by additional NOLs, forming either Mn^{3+}–NOL or more soluble Mn^{2+}–NOL complexes,[26] with or without subsequent oxidation. The formation rate of Mn^{3+}–NOL complexes by abiotic oxidation rate is strongly dependent to the pH of the solution and the properties and concentrations of NOLs.[30] Alternatively, after adsorption onto the surface of the Mn oxides, NOLs may non-reductively detach surface-bound Mn^{III} as Mn^{3+}–NOL complexes. We assume that these mechanisms affect the formation of Mn^{3+}–NOL complexes.

Various studies have investigated the interactions between Mn oxides and NOLs including model ligands, focusing on (i) H^+- and ligand-promoted reductive dissolution of Mn oxides,[26,28,29,31,35–37] or (ii) oxidative degradation of organic pollutants.[38] However, a quantitative speciation analysis of the resulting total dissolved Mn (Mn_T) pool is absent from the literature.

Our main objectives were (i) to determine Mn_T solution speciation, including Mn^{2+} (sum of Mn^{2+} and Mn^{2+}–NOL complexes) and Mn^{3+}–NOL complex (sum of Mn^{3+}–NOL_{weak} and Mn^{3+}–NOL_{strong}) concentrations, and (ii) to elucidate the principles of the Mn^{3+}–NOL complex formation as a result of the abiotic dissolution of Mn oxides. A thorough understanding of the Mn^{3+}–NOL complex formation in soil solutions is highly relevant, as the strong oxidant Mn^{3+} affects the decomposition of organic matter (OM) and the associated release of carbon dioxide (CO_2).[39–44] Furthermore, it contributes to the degradation of organic pollutants,[45,46] such as methylmercury,[38] and is redox-active in water treatment works.[6]

In order to address these issues, a spectrophotometric method (porphyrin method), employing α,β,γ,δ-tetrakis(4-carboxyphenyl)porphine (T(4-CP)P), was applied.[7] This analysis enables direct qualification and quantification of the dissolved Mn species by kinetic modeling. The principal mechanism behind the porphyrin method is a metal substitution reaction. Divalent cadmium (Cd^{2+}) bound to the porphyrin (Cd^{2+}–T(4-CP)P) is replaced by free or NOL-bound Mn^{2+} and Mn^{3+} present in the sample. Thus, the method allows differentiation of the dissolved Mn_T pool based on ligand binding affinities and strengths to Mn^{2+} and Mn^{3+}.[7,8,10] From this, the proportions of Mn^{2+}, Mn^{3+}–NOL_{weak} complexes and Mn^{3+}–NOL_{strong} complexes are derived by fitting the experimental data using kinetic modeling equations. Two series of batch operations were conducted under oxidizing conditions to evaluate the influences of pH and time on NOL–Mn oxide interactions. A normalized, “native” Mn and (trace) metal cation free, DOM-stock solution from an acidic spruce site was extracted and freshly prepared for each batch experiment. Subsequently, the extract was reacted with either birnessite or manganite. The synthesized Mn oxides offer the possibility of studying different dissolution mechanisms that can be accessed by Mn speciation analysis.

3.2 Materials and Methods

3.2.1 Sampling of the forest floor

Forest floor samples were collected at the permanent environmental monitoring station #101 at Idar-Oberstein (49°44′33.38″ N, 7°11′47.61″ E), Rhineland-Palatinate, Germany, which is managed by the federal state authority Research Institute for Forest Ecology and

Forestry of the state of Rhineland-Palatinate in Trippstadt.[47] The soil is classified as a Dystric Cambisol[48] and covered by stands of spruce (*Picea abies* (L.) H. Karst.).

From the Oe horizon (+5–+9 cm),[49] characterized as moder-like raw humus,[50] about 5 kg of fresh material was obtained over an area of 15 m^2. In the laboratory, the material was sieved to <2 mm and stored in polypropylene (PP) bags in the dark at 4 °C to minimize changes in composition.[51] A subsample was dried at 60 °C and finely ground in an agate ball mill (PM 400, Retsch, Haan, Germany).

3.2.2 Experimental methods

Forest floor

The pH of the Oe horizon was examined potentiometrically in a 0.01 M calcium chloride ($CaCl_2$) solution and ultrapure water using a glass electrode (SenTIX 81, WTW, Weilheim, Germany). A conductivity electrode (SevenEasy, Mettler Toledo, Giessen, Germany) was used to measure electrical conductivity (EC) in a suspension of the Oe material and deionized water (1 : 5 w : v). Total carbon (TC) and nitrogen (N) were determined in duplicate by dry combustion of ground samples using a CNS analyzer (Vario EL cube, Elementar, Hanau, Germany) equipped with a thermal conductivity conductor.

Extraction of the DOM-stock solution

A fresh DOM-stock solution (3.75 ± 0.17 mmol C L^{-1}) was obtained for each batch operation by 0.001 M $CaCl_2$ extraction of the Oe horizon. The extraction was modified on the basis of $CaCl_2$ extractions described in the literature, which employed various methodological approaches.[52–54] 40 g of forest floor material and 200 mL of a 0.001 M $CaCl_2$ solution (1 : 5 w : v) were put in a 500 mL amber glass flask. The glass was then shaken constantly at 9 rpm on an overhead shaker (Reax 20/21, Heidolph Instruments, Schwabach, Germany) for 24 h at 22 ± 1 °C. Centrifugation at 4000 *g* (Rotina 420 R, Hettich, Kirchlengern, Germany) for 10 min was followed by filtration through a <2 µm ashless blue ribbon filter (589/3, Whatman®, Maidstone, United Kingdom). Next, the extract was passed through a 0.2 µm filter (cellulose acetate, Sartorius, Göttingen, Germany) using acid-cleaned filtration units (polycarbonate, Sartorius, Göttingen, Germany). In order to remove “native” Mn and (trace) metal cations from the DOM-stock

solution, it was passed four times through a cation exchange column (2.5 x 50 cm) filled with an acidic cation exchange resin (Dowex® 50W-X8 cation exchange resin, mesh 16–50, Dow Chemical, Michigan, USA). A flow rate of 13 mL min^{-1} was applied following the protocol presented by Strobel *et al.* (2001).[55] Subsequently, the H^+ saturated extract was refiltered through 0.2 µm cellulose acetate filters in order to remove potential residues of the cation exchange resin. The removal of "native" Mn and (trace) metal cations was checked by inductively coupled plasma optical emission spectrometry (ICP OES). Sodium azide (NaN_3) was added at a concentration of 0.01 M to the DOM-stock solution in order to suppress biological activities.[56]

To determine the total dissolved organic C (DOC) concentration in the DOM-stock solution, a sample volume of 100 µL was injected into a small glass tube and subjected to high-temperature catalytic oxidation to CO_2 at 850 °C. The DOC content was quantified using a non-dispersive infrared TOC analyzer (Dimatoc 2000, Dimatec, Essen, Germany). All samples were analyzed in triplicate.

Characterization of the DOM-stock solution

Excitation-emission matrix (EEM) spectroscopy was applied on the DOM-stock solution using a fluorescence spectrometer (FLS 980, Edinburgh Instruments, Livingston, United Kingdom) equipped with a 450 W xenon lamp as the excitation source and a photomultiplier (PMT) detector (R928P, Hamamatsu Photonics, Shizuoka, Japan) at the Department of Chemistry, University of Cologne. Excitation (Ex) wavelengths (200–500 nm, 10 nm steps) and emission (Em) wavelengths (250–700 nm, 1 nm steps) were recorded in a 1 cm quartz cuvette at 22 ± 1 °C. The slits of excitation and emission were set to 2.5 nm and 3.0 nm, respectively. Before the EEM recording, all samples were checked for their absorbance at 254 nm and were diluted with ultrapure water (18.2 MΩ cm) to an absorbance of <0.3 A in order to avoid inner filter effects.[57] The dilution factor was considered in the further calculations. Subtracting the ultrapure water blank spectrum eliminated Raman scattering.[58] In order to further characterize the initial DOM pool, three indices were calculated according to literature: (i) the fluorescence index (FI),[59] (ii) the humification index (HIX),[57,60] and (iii) the biological index (BIX)[61] (see SI). Additionally, four major fluorescent DOM (FDOM) component peaks (B, T, A, C)

characterizing terrestrial FDOM were determined. Peak B is at E_x/E_m = 275/310 nm and includes tyrosine-like and protein-like signals; peak T, at E_x/E_m = 275/340 nm, indicates tryptophan-like and protein-like signals. Peak A is at E_m/E_x = 260/380–460 nm and peak C is at E_m/E_x = 350/420–480 nm – both mark humic-like FDOM components.[62] Calculating the FDOM data was done in R (version 4.2.2)[63] using RStudio (version 2022.12.0)[64] and the package *staRdom* (version 1.1.25).[65]

3.2.3 Preparation of Mn oxides

The preparation of the birnessite followed the protocol by Rabenhorst and Persing (2017).[66] Manganite synthesis was performed according to the method of Giovanoli and Leuenberger (1969),[67] modified after Lee *et al.* (1980).[68] Detailed descriptions of the syntheses are provided in the SI.

Characterization of Mn oxides

The synthesized Mn oxides were analyzed by X-ray powder diffraction (XRD), scanning electron microscopy (SEM) and the Brunauer–Emmett–Teller method (BET) at the Federal Institute for Geosciences and Natural Resources (BGR, Hannover, Germany). Additionally, attenuated total reflection Fourier-transform infrared spectroscopy (ATR FT-IR) was performed at the Department of Chemistry, University of Cologne (Cologne, Germany). The AOS and the PZC were determined at the Institute of Geography, University of Cologne. More detailed information can be found in the SI.

3.2.4 Batch experiments

Batch operations were chosen in order to investigate the effects of pH (3–7, 5 steps) and time (1–168 h, 7 steps). Initially, 20 ± 0.1 mg of Mn oxide was weighed into a 50 mL PP centrifuge tube (Sarstedt, Nürnbrecht, Germany) and covered in aluminum foil to block ambient light. Subsequently, a 30 mL aliquot of the freshly prepared DOM-stock solution (3.75 ± 0.17 mmol C L^{-1}) was adjusted with 10 M HNO_3 (≤100 µL) or 10 M NaOH (≤100 µL) based on preliminary experiments to maintain the desired pH, then added to the tube. The suspension was shaken on a horizontal shaker (GFL-3006, Lauda, Lauda-Königshofen, Germany) at 200 rpm for a predefined batch operation time at

constant atmospheric conditions (T = 20 ± 0.1 °C, p = 0.1013 MPa). The suspension was then immediately passed through a 0.2 µm cellulose acetate filter. After filtration, pH (827 pH Lab, Metrohm, Herisau, Switzerland) and EC (SevenEasy™, Mettler-Toledo, Columbus, USA) values were recorded. Experimental samples (in triplicate) were prepared for Mn speciation analysis (in triplicate for each sample), subsequent DOM measurements by UV/Vis spectroscopy (in duplicate) and determination of the DOC concentrations (in triplicate). The H^+-promoted background dissolution rates were separately determined in the absence of NOLs at pH 3, 4, and 5. Total Mn concentrations in this experiment were quantified by ICP OES.

3.2.5 Mn speciation analysis by kinetic modeling

Dissolved Mn speciation analysis was performed using the spectrophotometric porphyrin method, following the protocols outlined in Madison *et al.* (2011)[7] and Oldham *et al.* (2015).[10] The extended protocol for acidic forest soil solutions and soil solutions was applied as described in Lux and Mansfeldt (2023).[9] In summary, the spectrophotometric analyses included the determination of Mn^{2+}, Mn^{3+}–NOL_{weak} complexes, Mn^{3+}–NOL_{strong} complexes, and Mn_T based on kinetic modeling. They were conducted at a specific Soret band (468 nm) using (T(4-CP)P). All absorbance measurements were performed on a Lambda 25™ spectrophotometer (PerkinElmer®, Rodgau, Germany) using a 1 cm pathlength glass cuvette with 3 mL of total volume. Prior to the analyses, the absorption coefficient (ε = 95 340 M^{-1} cm^{-1}) for the Mn^{3+}–T(4-CP)P complex was determined using manganese chloride tetrahydrate ($MnCl_2 \cdot 4H_2O$) standards (0.1–10 µM). The concentrations of T(4-CP)P and cadmium chloride ($CdCl_2$) in the cuvettes were 24 µM each, as proposed by Madison *et al.* (2011).[7] The method requires a controlled pH range of 7.5–8 to facilitate the metal substitution reaction between Cd^{2+}–T(4-CP)P and Mn^{2+} or Mn^{3+}–NOL_{weak} complexes. In order to maintain this pH range, a borate buffer mix was used.

The pipetting volumes of the samples were adapted to the expected Mn_T concentrations in the cuvette and ranged from 50 to 2360 µL to comply with the method's detection range. Subsequently, the absorption was recorded every 5 seconds over a period of 10 minutes. The recording was stopped earlier depending on kinetics and the formation

of a sufficient plateau, which indicated that the absorbance maximum was reached and the metal substitution reaction had ended.

In DOM-rich solutions, inherent coloration can interfere with the Soret band at 468 nm. Therefore, a background correction was performed.[9] The same sample quantity used in the porphyrin method was placed in a cuvette and diluted with ultrapure water to a final volume of 3 mL. Absorbance was measured against 3 mL of ultrapure water at 468 nm for the same duration as the corresponding Mn speciation analysis. The resulting background absorbance was then subtracted from the Mn absorbance measurement to correct for interference.

For each sample, a 10 mL aliquot was mixed with 10 µL of concentrated HNO_3 (suprapur®, 65%) for subsequent ICP OES analysis. It should be noted that acidification of humic-rich samples to a pH value <2 leads to precipitation of humic substances and thus to an underestimation of metal concentrations.[12]

As described by Madison *et al.* (2011),[7] the kinetic modeling approach was tested on several Mn^{2+}/Mn^{3+}–pyrophosphate mixtures with varying species concentrations. Initial Mn^{2+} and Mn^{3+} concentrations were predicted within 0.4–2% of their known values. These results suggest that the method can be a reliable tool for Mn speciation analysis. However, it must be considered that unknown environmental samples contain a diverse DOM pool and a complex solution matrix, characterizing them a as ‘black box’.

The kinetic modeling of the dissolved Mn_T pool was carried out as outlined in Lux and Mansfeldt (2023).[9] In order to determine the dissolved Mn_T pool, two separate measurements were performed: one in the absence (non-reduced samples) and one in the presence of the strong reducing agent hydroxylamine (reduced samples). The modeling equations proposed by Madison *et al.* (2011)[7] were extended by introducing an additional parameter (t_0) to estimate the reaction start time, as it did not coincide with the first absorbance measurement due to manual operation [eqn (1) and (2)]. Initially, kinetic modeling of the non-reduced samples provides the concentrations of Mn^{2+} and Mn^{3+}–NOL_{weak} complexes [eqn (1)], where Mn^{2+}, Mn^{3+}–NOL_{weak} complexes, k_1, k_2 and t_0 are parameterized. Mn^{3+}–NOL_{weak} complexes comprise NOLs with different binding affinities and strengths, which most strongly influence the reaction kinetics and thus the recorded absorbance curves. In order to clearly differentiate Mn^{3+}–NOL_{weak} complexes from Mn^{2+}, the condition $k_1 \geq 3*k_2$ has to be satisfied.[14]

In the second modeling step, the concentration of $Mn_{T(hydroxylamine)}$, representing Mn^{2+} and all forms of Mn^{3+}–NOL complexes, was determined by parameterizing Mn^{2+}, k_1, and t_0 [eqn (2)]. The addition of the reducing agent was necessary to model the concentration of Mn^{3+}, which is methodically defined as Mn^{3+}–NOL_{strong} complexes, since the ligand-bound Mn^{3+} cannot be outcompeted by T(4-CP)P.[10] The concentration of Mn^{3+}–NOL_{strong} complexes was determined by calculating the difference between the reduced and the non-reduced sample [eqn (3)]. Together, the modeling equations require the estimation of eight parameters for each speciation analysis.

Five-parameter equation:

$$Mn_T = (Mn^{3+}\text{–}T(4\text{-}CP)P)_T = Mn^{2+}\cdot(1 - e^{-k_1\cdot(t - t_0)}) + Mn^{3+}\text{–}NOL_{weak}\cdot(1 - e^{-k_2\cdot(t - t_0)}) \quad (1)$$

where Mn^{2+} = Mn^{2+} concentration (µmol L^{-1}); Mn^{3+}–NOL_{weak} = Mn^{3+}–NOL_{weak} concentration (µmol L^{-1}); k_1 = Mn^{2+} rate constant (s^{-1}); k_2 = Mn^{3+}–NOL_{weak} rate constant (s^{-1}); t = reaction time (s); and t_0 = reaction start (s).

Three-parameter equation:

$$Mn_{T(hydroxylamine)} = Mn^{2+}\cdot(1 - e^{-k_1\cdot(t - t_0)}) \quad (2)$$

where Mn^{2+} = Mn^{2+} concentration (µmol L^{-1}); k_1 = Mn^{2+} rate constant (s^{-1}); t = reaction time (s); and t_0 = reaction start (s).

$$Mn^{3+}\text{–}NOL_{strong} = Mn_{T(hydroxylamine)} - (Mn^{2+} + Mn^{3+}\text{–}NOL_{weak}) \quad (3)$$

An R code written in RStudio (version 2022.12.0)[63] using R (version 4.2.2)[62] and the *nlmrt* package (version 2016.3.2)[69] was executed. The initial parameter estimation [eqn (1) and (2)] was performed using the *wrapnls* method, which attempts to solve the nonlinear sum of squares problem by employing the *nlxb* algorithm and introducing predefined lower and upper limits for each parameter. Thereafter, the nonlinear least squares (*nls*) method based on the *stats* package (version 4.2.2)[63,70] was executed in order to estimate the parameters more precisely. To verify the goodness of fit to the recorded data, the root mean square error (RMSE) was determined. As reported by Johnson *et al.* (2018)[6] and by Lux and Mansfeldt (2023),[9] smaller rate constants for the $MnCl_2 \cdot 4H_2O$

standards (reaction end in approximately 90 s) were determined in contrast to Madison *et al.* (2011),[7] and considered in the modeling process.

3.2.6 Characterization of DOM-stock and DOM-batch solutions

The pH- and time-dependent, qualitative and quantitative, changes of the batch DOM pool in relation to the DOM-stock solution after interaction with the Mn oxides were investigated. Prior to the experiments, the DOM-stock solution was adjusted to a DOC concentration of 3.75 ± 0.17 mmol C L^{-1} using a 0.01 M $CaCl_2$ solution as a background electrolyte. Various parameters, including the DOC concentration, the molar absorption (MA), the absorption ratio (A), the spectral slope (S), and the spectral slope ratio (S_R) were determined for reacted DOM-batch samples using a TOC analyzer and UV/Vis spectroscopy. UV/Vis spectra were collected for samples using an UV/Vis spectrometer (Lambda 25™, PerkinElmer®, Rodgau, Germany). Scans were performed from 800 to 200 nm with a 1 nm decrement to prevent UV-induced DOM degradation. All samples were analyzed in a 1 cm pathlength cuvette against a 3 mL ultrapure water (18.2 MΩ cm) reagent blank at 20.0 ± 0.1 °C.[71] Molar absorptions at 254, 280, and 350 nm were calculated in order to elucidate the aromaticity of DOM, *e.g.*, humic substance aromaticity[71–73] and relations to molecular weight (MW).[74] The absorbance ratio A_{280}/A_{350} is reported as a well correlating parameter for both aromaticity and MW.[73] Spectral slopes were determined over the wavelength ranges 275–295 nm ($S_{275–295}$), 290–350 nm ($S_{290–350}$), and 350–400 nm ($S_{350–400}$). These are related to phototransformation of low molecular weight (LMW) material to more humic-like material as well as information about LMW material and aromaticity.[72,75,76] Finally, the S_R ($S_{275–295}/S_{350–400}$) was calculated as a proxy of DOM MW and photobleaching.[76] Calculations of the DOM parameters were performed using the R package *staRdom*.[65]

3.3 Results

3.3.1 Forest floor

The Oe horizon showed a strongly acidic pH of 3.6 ± 0.008 in 0.01 M $CaCl_2$ and 4.7 ± 0.006 in ultrapure water. An EC of 153 ± 11.2 µS cm^{-1} was determined. Elemental

analysis revealed proportions of 47.0 ± 0.8% C and 1.7 ± 0.0% N resulting in a C/N ratio of 27.1 ± 0.3, indicating a moder-like raw humus.[50]

3.3.2 Characterization of the DOM-stock solution

The DOM-stock solution had a strongly acidic pH of 2–3 and the ICP OES analysis revealed Mn concentrations <0.182 µmol L^{-1}. DOC concentrations averaged 3.75 ± 0.17 mmol C L^{-1} after protonation by the cation exchange resin, which is similar to forest floor solutions reported in the literature.[77] A substantial loss of DOC was not observed. Further analysis by EEM spectroscopy revealed humic-like peaks (denoted as A and C), while distinct protein-like (B and T) and fulvic-like (D and E) FDOM peaks were absent (Figure 3.S4). An A/C peak ratio of 1.83 confirmed a blue-shifted humic-like FDOM. Additionally, calculated values for the BIX (0.400), FI (1.58), and HIX (0.966) were derived from the 3D scan.

3.3.3 Batch experiments

Total manganese concentrations

Figure 3.1 shows the development of the dissolved Mn_T concentrations as a function of pH and time analyzed by ICP OES (see Tables 3.S2 and 3.S3). The H^+-promoted background dissolution (pH ≤ 5) of the Mn oxides was subtracted in order to determine the exclusively NOL-induced dissolution ($Mn_{T(NOL)}$).

For birnessite (Figure 3.1a), the following general trends were observed: (i) a decrease in pH results in higher Mn concentrations, (ii) a longer reaction times promote an increased Mn release, and (iii) the lower the pH the lower the NOL-induced dissolution relative to the H^+-promoted dissolution. Mean $Mn_{T(NOL)}$ concentrations ranged from 0.884 ± 0.212 to 899 ± 108 µmol L^{-1} (Table 3.S2) and peaked at pH 3 after 168 h (Figure 3.1a). The largest proportions of $Mn_{T(NOL)}$ (100%) were revealed at pH 6 and 7 (Table 3.S2). By contrast, the lowest proportions were observed at pH 4 ranging between 37.8 ± 3.9% and 73.9 ± 0.1% with an overall mean of 58.5 ± 10.7% (Table 3.S2). The highest dissolution rates were identified within the first 24 h. Prolonged batch operations revealed considerably slower dissolution kinetics.

Manganite showed similar general trends to birnessite (Figure 3.1b). In comparison, the mean $Mn_{T(NOL)}$ concentrations ranged from 13.6 ± 0.675 to 567 ± 22.4 µmol L^{-1} (Table 3.S3) and revealed an almost halved maximum concentration at pH 3 after 48 h. The highest proportions (100%) of NOL-induced dissolution were observed at pH 6 and 7 (Table 3.S3). On the other hand, the lowest means were recorded at pH 3 ranging from 20.9 ± 4.3 to 47.1 ± 1.1% with an overall mean of 38.1 ± 9.2% (Table 3.S3). This indicates a further significant reduction in NOL-induced dissolution under strongly acidic conditions compared to the birnessite batch experiments. Particularly noteworthy is the increased release of Mn at pH 6 and 7. Equally, the manganite batch experiments showed that increasing acidic conditions and a prolonged batch operation contributed to an increased dissolution. Looking at the dissolution kinetics, the dissolution of manganite was most rapid in the first 12 h, in particular with decreasing pH. Subsequently, the dissolution decreased sharply.

Considering the additional H^+-promoted dissolution, mean Mn_T concentrations during the birnessite batch experiments ranged from 0.884 ± 0.212 to 1418 ± 108 µmol L^{-1} (Table 3.S2) and revealed a higher solubility of birnessite compared to manganite. The $Mn_{T(Porph)}/Mn_{T(ICP\ OES)}$ ratio for birnessite ranged from 0.87 to 1.27 with a mean of 1.03 ± 0.08 (n = 35, r = 0.996, R^2 = 0.991, p < 0.001). The manganite batch experiments revealed a narrower range of mean Mn_T concentrations (13.6 ± 0.675 to 1338 ± 77.4 µmol L^{-1}) (Table 3.S3). For manganite, the $Mn_{T(Porph)}/Mn_{T(ICP\ OES)}$ ratio ranged from 0.85 to 1.17 with a mean of 1.02 ± 0.06 (n = 35, r = 0.998, R^2 = 0.995, p < 0.001).

The results show that NOL-induced dissolution (pH ≤ 5) appears to be an important process. However, the relative contribution to the overall dissolution decreased with decreasing pH, rendering H^+-promoted dissolution more effective especially during manganite batch experiments. Based on these findings, possible abiotic dissolution mechanisms are outlined in section 3.4.1.

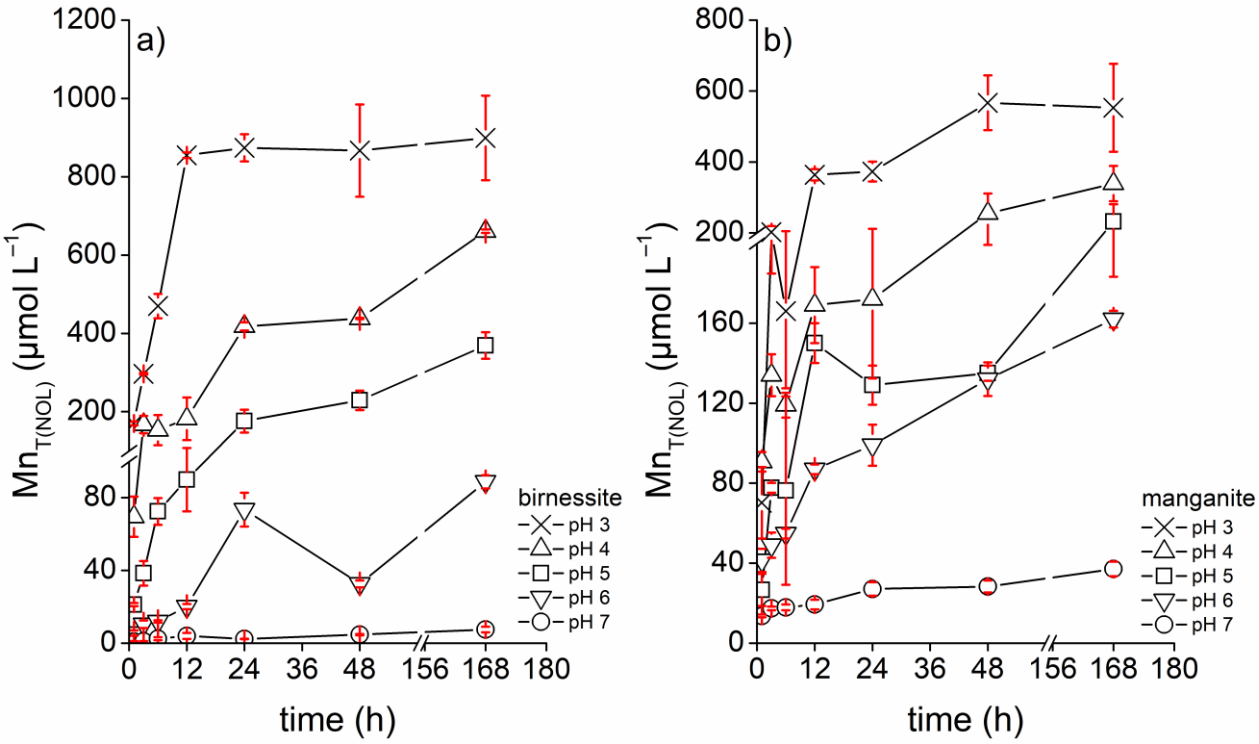

Figure 3.1 $Mn_{T(NOL)}$ concentrations of pH-dependent and NOL-induced Mn oxide dissolution over time for (a) birnessite, and (b) manganite. H^+-promoted background dissolution was subtracted. Each experiment was conducted in triplicate and analyzed by ICP OES. $Mn_{T(NOL)}$ = total dissolved Mn by NOL-induced dissolution; NOL = natural organic ligand.

Kinetic modeling

Figure 3.2 presents experimental data from the Mn speciation analysis of a single birnessite (non-reduced) and a single manganite (non-reduced) sample in the presence of NOL at pH 7 after 1 h. For each sample, two representative analytical measurements (A and B) are depicted in order to highlight clear differences in reaction kinetics. Kinetic modeling was conducted to fit the data including Mn^{2+} and Mn^{3+}–NOL_{weak} complexes [eqn (1)]. For clarity, the modeled Mn^{3+}–NOL_{strong} complexes are not shown, as weakly binding ligands primarily influence the reaction kinetics when employing the porphyrin method. Figure 3.3 depicts the modeled proportions of Mn^{2+}, Mn^{3+}–NOL_{weak} and Mn^{3+}–NOL_{strong} complexes relative to Mn_T for both samples. Notable differences in the reaction kinetics between the Mn oxides were observed, as indicated by distinct curve shapes (Figure 3.2) and substantial variations in the modeled Mn^{3+}–NOL_{weak} complex proportions (Figure 3.3).

In particular, the recorded curves for the NOL–birnessite interactions appear flattened (Figure 3.2a) compared to those for manganite (Figure 3.2b), indicating slower reaction kinetics. Kinetic modeling of the analytical replicates A and B revealed sample-specific dominant proportions of Mn^{3+}–NOL_{weak} complexes, accounting for 73.9 and 77.2% relative to Mn_T (Figure 3.3). Proportions of Mn^{2+} contributed 26.1 and 8.6%, while Mn^{3+}–NOL_{strong} complexes accounted for 0 and 14.2%, respectively (Figure 3.3).

Manganite, in contrast, exhibited faster reaction kinetics (Figure 3.2b), as the curves plateaued more quickly. After 1 h, only minor traces of Mn^{3+}–NOL_{weak} complexes (16.2 and 5.6%) were detected, while Mn^{2+} was the dominant species (74.3 and 86.9%) (Figure 3.3). The sample-specific proportions of Mn^{3+}–NOL_{strong} complexes were 8.5 and 10.3% (Figure 3.3). Notably, the k_2 values were an order of magnitude lower than the k_1 values, confirming distinct kinetic behavior (Figure 3.2b).

For both NOL–Mn oxide interactions, the modeled Mn species proportions vary across individual measurements (Figure 3.3). Additionally, the modeled rate constants satisfied the condition $k_1 \geq 3k_2$, which is used to differentiate ligands based on their binding affinities and strengths.[14]

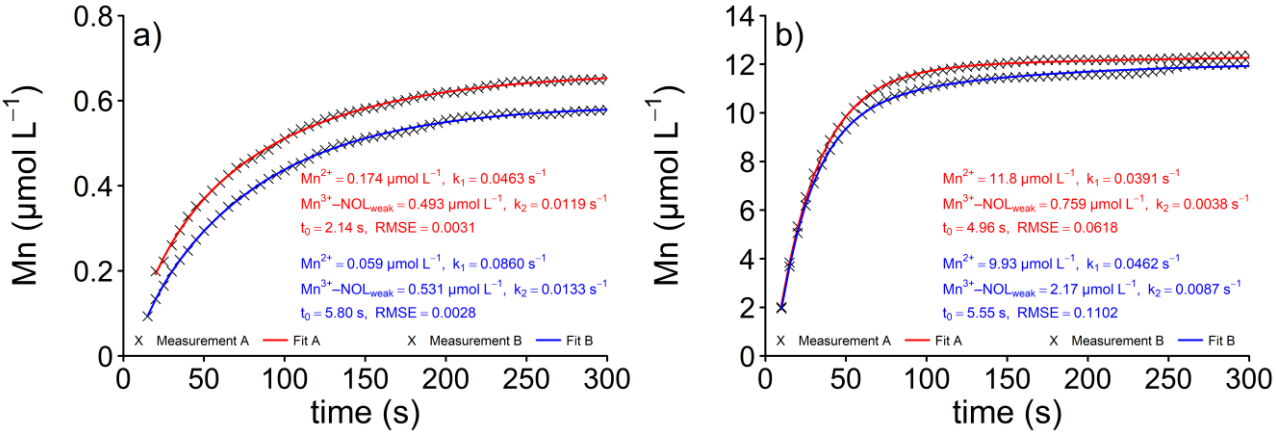

Figure 3.2 Kinetic modeling of (a) a single birnessite (non-reduced) and (b) a single manganite sample (non-reduced) at pH 7 after 1 h. The analysis of the non-reduced sample represents the Mn speciation analysis without the hydroxylamine treatment. The modeling includes complexes of Mn^{2+} and Mn^{3+}–NOL_{weak} (Tables 3.S2 and 3.S3), excluding Mn^{3+}–NOL_{strong} complexes. Two analytical measurements (A and B) are demonstrated for each sample, along with the corresponding fits: measurement A (black crosses) with fit A (red line), and measurement B (black crosses) with fit B (blue line)). NOL = natural organic ligand; Mn^{3+}–NOL_{weak} = weakly bound Mn^{3+}; Mn^{3+}–NOL_{strong} = strongly bound Mn^{3+}.

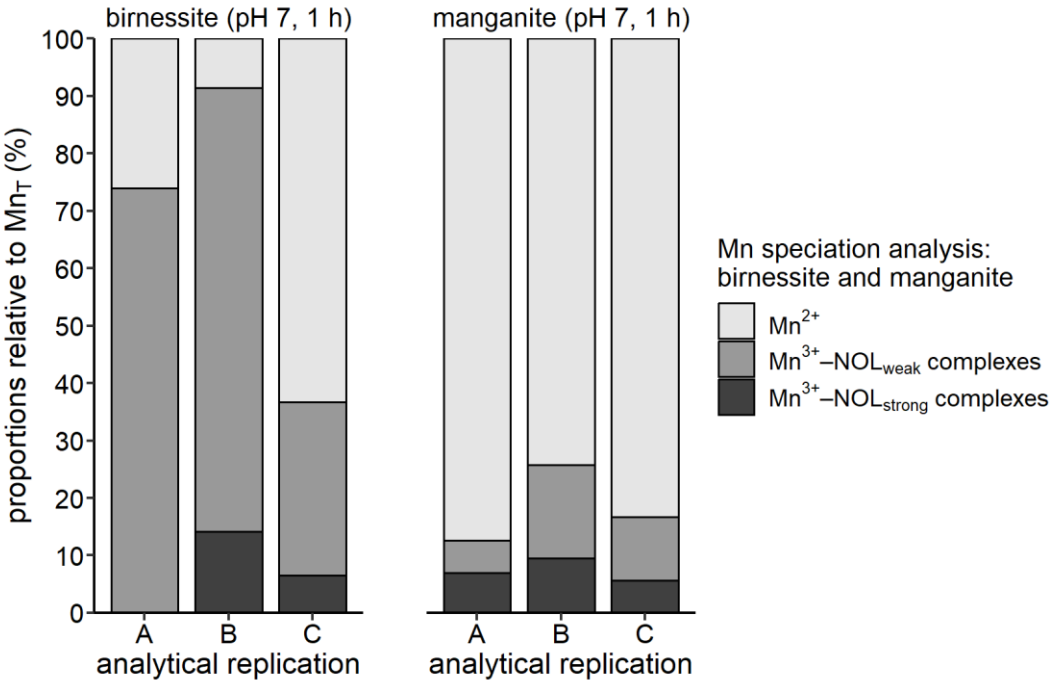

Figure 3.3 Mn speciation analysis in triplicate (A–C) of a single birnessite and manganite sample at pH 7 after 1 h. Mn_T = total dissolved Mn; Mn^{3+}–NOL_{weak} = weakly bound Mn^{3+}; Mn^{3+}–NOL_{strong} = strongly bound Mn^{3+}.

Manganese speciation analysis

In this study, the speciation analysis of Mn_T was performed including Mn^{2+}, Mn^{3+}–NOL_{weak} complexes, and Mn^{3+}–NOL_{strong} complexes. Figure 3.4 shows the percentage of Mn_T that are Mn^{3+}–NOL complexes (sum of Mn^{3+}–NOL_{weak} and Mn^{3+}–NOL_{strong} complexes) for the NOL–birnessite and the NOL–manganite interaction as a function of pH (3–7) and time (1–168 h). The formation and stabilization of Mn^{3+}–NOL complexes was dependent on the individual Mn oxide, showing sharp decreases with lowering pH and increasing reaction time (strongly acidic conditions) (Figure 3.4). Notably, our analysis of molar Mn_T : DOC ratios indicates that values ≥0.08 resulted in a sharp decrease in Mn^{3+}–NOL complex proportions (Tables 3.S4 and 3.S5). The molar ratios exceeded this threshold multiple times, especially under strongly acidic conditions and reaction times ≥6 h.

For the birnessite batch experiments, the Mn^{3+}–NOL complex proportions ranged from 0 to 87 ± 18% across all pH and time steps (Figure 3.4a). The highest proportion of Mn^{3+}–NOL complexes was observed at pH 7 after 24 h. Under circumneutral conditions, Mn^{3+}–NOL complexes predominated at all time steps ranging from 68 ± 9 to 87 ± 18%. A

strong contrast with low Mn^{3+}–NOL complex proportions (6 ± 4 to 11 ± 7%) was observed at pH 5 between 1 and 6 h. The sharp decrease in Mn^{3+}–NOL complexes within the NOL–birnessite interactions resulted from the modeling process. The parameterization of the rate constants narrowly missed the condition $k_1 \geq 3k_2$ (Table 3.S2). The Mn^{3+}–NOL_{weak} complexes could not, therefore, be modeled. Subsequently, the proportions (35 ± 4 to 86 ± 5%) increased sharply from 12 h onwards. An opposite pattern was identified under strongly acidic conditions. Mn^{3+}–NOL complexes dominated at pH 4 from 1 to 6 h; and at pH 3 only at 1 h but with a high proportion of 85 ± 9%. Remarkably, Mn^{3+}–NOL complexes decreased with decreasing pH and increasing time, becoming negligible after 6 h (pH 3 and 4). Interestingly, the proportions of Mn^{3+}–NOL complexes were mainly assigned to the Mn^{3+}–NOL_{weak} complexes, as shown in Table 3.S3, which is in contrast to the NOL–manganite interaction.

In summary, birnessite batch experiments indicate that Mn^{3+}–NOL complexes can be predominant under all pH conditions, but the formation and stability is strongly dependent on the reaction time under strongly acidic conditions.

Figure 3.4b shows the proportions of Mn_T that are Mn^{3+}–NOL complexes observed in the manganite batch experiments. Overall, the Mn^{3+}–NOL complex proportions ranged from 0 to 69 ± 14%. Looking closely at the pH steps, a different pattern of the Mn^{3+}–NOL complex distribution becomes apparent. The highest Mn^{3+}–NOL complex proportions were detected at circumneutral pH. A pH ≤ 6 already leads to a sharp decrease in the Mn^{3+}–NOL complex proportions. Similar to birnessite, the proportions decreased with time. In particular, the maximum proportion of Mn^{3+}–NOL complexes (69 ± 14%) was recorded at pH 7 after 12 h. Furthermore, a consistent but decreasing dominance of Mn^{3+}–NOL complexes was observed only at pH 7 from 12 to 48 h (69 ± 14 to 65 ± 7%). Under both moderately and strongly acidic conditions, the Mn^{3+}–NOL complex proportions decreased drastically, ranging between 0 and 21 ± 7% (pH 6, 1 h). Exceptions were observed at pH 4 after 3 h (39 ± 6%) and at pH 3 after 1 h (57 ± 4%). All modeled proportions of Mn^{3+}–NOL complexes were predominantly attributed to Mn^{3+}–NOL_{strong} complexes (Table 3.S3).

To sum up, the results of the manganite batch experiments show that pH is undoubtedly the critical parameter, while the influence of time is only assumed for strongly acidic conditions and a reaction time >3 h.

For all samples in both series of batch experiments, the condition $k_1 \geq 3*k_2$ was fulfilled in the modeling process.[14] This provides evidence for the presence of Mn^{3+}–NOL_{weak} complexes, in addition to dissolved Mn^{2+} (Tables 3.S2 and 3.S3).

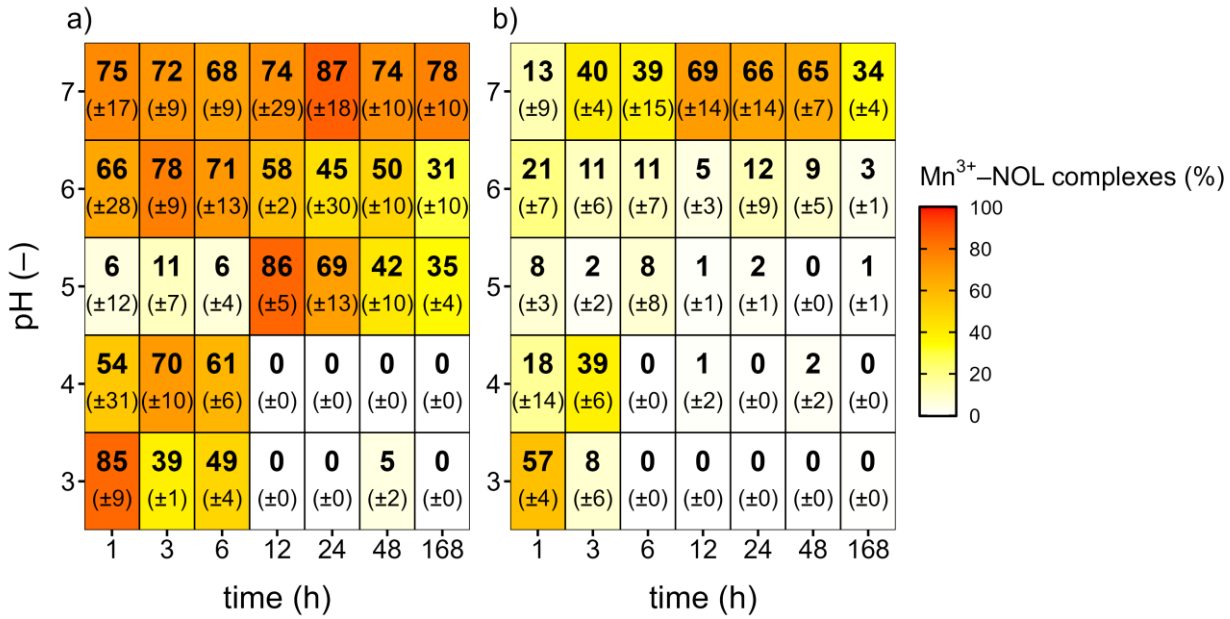

Figure 3.4 Proportions of Mn^{3+}–NOL complexes (%) (sum of Mn^{3+}–NOL_{weak} and Mn^{3+}–NOL_{strong} complexes) for (a) the NOL–birnessite and (b) the NOL–manganite interaction as a function of pH (–) and time (h) relative to Mn_T. NOL = natural organic ligand; Mn^{3+}–NOL_{weak} = weakly bound Mn^{3+}; Mn^{3+}–NOL_{strong} = strongly bound Mn^{3+}.

Concentrations and properties of the natural organic ligands

Here, we briefly outline trends that affect the formation of Mn^{3+}–NOL complexes. All DOM-batch solutions were within ±0.2 of the target pH after the batch experiments. Accordingly, the initial acid/base additions compensated for a possible pH increase induced by sorption processes (*e.g.*, ligand exchange), dissolution processes (*e.g.*, NOL-induced or H^+-promoted) and redox reactions.

For both Mn oxides, we observed that (i) strongly acidic conditions (pH 3 and 4) particularly promoted a loss in DOC (DOC_{loss}) (Table 3.S4 and 3.S5), while (ii) reaction time exclusively mattered in the birnessite batch experiments for pH 3–6 at 168 h (Table 3.S4).

During the birnessite batch experiments, mean values of DOC_{loss} ranged from 2.3 ± 1.8 to 38.4 ± 2.1% with an overall mean of 15.5 ± 11.2%. At pH 7, consistently low mean DOC_{loss} proportions (7.3 ± 4.0%) were recorded, ranging from 4.3 ± 1.4 to

9.8 ± 2.1%. In contrast, sharp increases were observed at pH 3 (29.4 ± 4.5%) between 24.0 ± 3.0% and 32.9 ± 3.9%. Strikingly, mean DOC_{loss} proportions (≥29.8 ± 1.7%) at pH 4–6 increased significantly at 168 h (Table 3.S4). Overall, a DOC_{loss} was identified with increasing time relative to the initial DOC concentrations of the DOM-batch solution for each of the five pH steps (Table 3.S4).

DOC_{loss} proportions observed in manganite batch experiments showed a narrower range from 3.2 ± 0.6 to 22.9 ± 4.1% (Table 3.S5) over all pH steps but a similar overall mean of 13.1 ± 7.0%. Consistently low mean DOC_{loss} proportions were recorded at pH 7 (5.6 ± 4.0%), ranging from 3.2 ± 0.6 to 10.3 ± 4.7%. Similar to birnessite, the loss of DOC was promoted under strongly acidic conditions. The highest average amounts were found at pH 4 (18.5 ± 5.4%) between 11.7 ± 0.5 and 21.6 ± 5.3%, and mean proportions at pH 3 (18.3 ± 5.4%) were nearly identical, ranging from 11.9 ± 6.3 to 22.9 ± 4.1%. However, a DOC loss promoted by increasing reaction time was not observed. Remarkably, the highest mean DOC_{loss} amounts recorded during manganite batch experiments were almost half as high (59.6%) as during the birnessite batch experiments.

UV/Vis spectroscopy analysis revealed a pH dependence for the Ss and S_Rs data in the birnessite batch experiments (Table 3.S4). Under strongly acidic conditions, the parameters showed increased values compared to moderately and circumneutral conditions, peaking at 168 h.

Similar trends were detected in the manganite batch experiments (Table 3.S5). Though, the differences are not so pronounced and only the Ss showed clear maxima after 168 h. Additionally, MA_{254} and MA_{350} values were relatively decreased under strongly acidic conditions compared to moderately acidic conditions and circumneutral conditions.

3.4 Discussion

3.4.1 Possible dissolution mechanisms

Figures 3.5 and 3.6 summarize the possible abiotic pathways enabling the Mn^{3+}–NOL complex formation during our batch experiments, while biological reduction was excluded.

Biotic processes are mostly inactivated by NaN_3 but the activity of Gram-positive bacteria such as actinomycetes is only partially suppressed or even not affected.[78] Therefore, microbially-mediated processes like DOC degradation, resynthesis, and

transformation cannot be completely excluded. Nevertheless, microbial activity should be largely restricted in this study and we focus solely on abiotic processes. These abiotic NOL–Mn oxide interactions can be categorized into four possible dissolution mechanisms (Figures 3.5 and 3.6):

(1) Ligand-promoted non-reductive dissolution, (2) ligand-promoted reductive dissolution, (3) H^+-promoted dissolution, and (4) ligand exchange.

Looking at the NOL–birnessite interactions (Figure 3.5), ligand-promoted non-reductive dissolution is a possible mechanism under circumneutral and moderately acidic conditions. Surface-bound Mn^{III} is dissolved by the adsorption of a near-associated NOL and released as a Mn^{3+}–NOL complex,[12] while the NOL is neither oxidized nor reduced [eqn (4)]. Because the AOS of the birnessite used in this study clearly indicates an increased proportion of Mn^{III}, we expect the mechanism to support the Mn^{3+}–NOL complex formation (Table 3.S1).

$$Mn^{III}\ (s) + NOL\ (aq) \rightarrow Mn^{3+}\text{–}NOL\ (aq) \qquad (4)$$

The second mechanism involves ligand-promoted reductive dissolution (1-e^- or 2-e^- transfer) of mineral-bound Mn^{III} and Mn^{IV} by a directly associated NOL. Consequently, Mn oxide reduction and NOL oxidation proceed in parallel [eqn (5), (6) and (7)] and the same NOL forms either a Mn^{3+}–NOL complex or a Mn^{2+}–NOL complex. Alternatively, the NOL detaches Mn^{2+} or Mn^{3+} as it is oxidized, and another NOL from the solution may form a Mn^{3+}–NOL complex or a Mn^{2+}–NOL complex [eqn (5), (6) and (7)]. Banerjee and Nesbitt (1999, 2001)[22,79] stated that the reduction of birnessite is controlled by a 1-e^- transfer reaction from Mn^{IV} to Mn^{III}, forming a strong Mn^{3+} carboxyl surface complex.

$$Mn^{IV}\ (s) + NOL\ (aq) + e^- \rightarrow Mn^{3+}\text{–}NOL_{ox}\ (aq) \qquad (5)$$

$$Mn^{IV}\ (s) + NOL\ (aq) + 2e^- \rightarrow Mn^{2+}\text{–}NOL_{ox}\ (aq) \qquad (6)$$

$$Mn^{III}\ (s) + NOL\ (aq) + e^- \rightarrow Mn^{2+}\text{–}NOL_{ox}\ (aq) \qquad (7)$$

EEM spectroscopy revealed humic proportions containing hydroquinones and thus phenolic groups. We assume that these functional groups contribute to homolytic 1-e^- transfers mediated by the formation of radical semiquinones in the hydroquinone/quinone system, or by intermediate phenoxy radicals. Ligand-promoted

reductive dissolution is surface-controlled, requiring close association of NOLs with surface sites prior to e^- transfer and metal ion release.[80] Released Mn^{2+} and Mn^{3+} may subsequently be complexed by additional NOLs [eqn (8)–(10)]. Terrestrial NOLs are known to inhibit the complete oxidation of Mn^{2+} to Mn^{IV} oxides,[11,26] by stabilizing the Mn^{3+} intermediate through ligand-promoted oxidation, complexation, and simultaneous NOL reduction [eqn (9)]. Following reductive dissolution, Mn^{3+}–NOL complex formation can occur *via* ligand-promoted oxidative complexation similar to eqn (9). Released Mn^{2+} is complexed by NOL. The intermediate Mn^{2+}–NOL complex is then oxidized during a dark reaction promoted by reactive oxygen species, namely superoxide ($O_2^{\bullet-}$) [eqn (11)].[11–13,81] This H^+-consuming reaction is favored under moderately to strongly acidic conditions, where high Mn oxide dissolution rates, excessive H^+ concentrations and dissolved O_2 are present.

$$Mn^{3+}\ (aq) + NOL\ (aq) \rightarrow Mn^{3+}\text{–}NOL\ (aq) \quad (8)$$

$$Mn^{2+}\ (aq) + NOL\ (aq) \rightarrow Mn^{3+}\text{–}NOL_{red}\ (aq) \quad (9)$$

$$Mn^{2+}\ (aq) + NOL\ (aq) \rightarrow Mn^{2+}\text{–}NOL\ (aq) \quad (10)$$

$$Mn^{2+}\ (aq) + O_2^{\bullet-} + 2H^+ + NOL\ (aq) \rightarrow Mn^{3+}\text{–}NOL\ (aq) + H_2O_2\ (aq) \quad (11)$$

Under increasing acidic conditions, we propose H^+-promoted dissolution as the third mechanism. The observed increase in H^+-promoted background dissolution (Table 3.S2) combined with the increasing NOL-induced dissolution (Figure 3.1a) results in a decrease in Mn^{3+}–NOL complex formation. Consequently, Mn^{2+} concentrations increase, suggesting that H^+-promoted dissolution of Mn^{IV} and Mn^{III} to Mn^{2+} proceeds *via* a 2-e^- or a 1-e^- transfer mediated by inorganic or organic reductants [eqn (12) and (13)]. McKendry *et al.* (2015)[82] outlined that Mn^{III}-enriched active sites promote water oxidation and subsequent H^+ generation, which intensifies H^+-promoted background dissolution [eqn (12) and (13)]. The low AOS of our triclinic birnessite renders enhanced H^+-promoted dissolution plausible, as supported by increased initial dissolution rates and a corresponding decrease in pH.

$$Mn^{IV}O_2\ (s) + 4H^+ + 2e^- \rightarrow Mn^{2+}\ (aq) + 2H_2O \quad (12)$$

$$Mn^{III}O(OH)\ (s) + 3H^+ + e^- \rightarrow Mn^{2+}\ (aq) + 2H_2O \quad (13)$$

In addition to the mechanisms presented in [eqn (6), (7), (12) and (13)], the sharp decrease in Mn^{3+}–NOL complex proportions (Figure 3.4a) with decreasing pH and longer batch operation (>6 h) necessitates the consideration of additional mechanisms. The decay of Mn^{3+}–NOL complexes might result from internal redox reactions of organic molecules, as observed for Mn^{3+}–catechol or Mn^{3+}–citrate, leading to Mn^{2+} formation.[10,25] It is conceivable that a reduction of Mn^{3+}–NOL complexes, coupled with oxidation of ambient NOLs (1-e^- transfer) [eqn (14)], similar to the transformation of organic pollutants,[45,46] contributes to the decrease in Mn^{3+}–NOL complex proportions relative to Mn_T with increasing reaction time.

$$Mn^{3+}\text{–NOL (aq)} + \text{NOL (aq)} + e^- \rightarrow Mn^{2+}\text{–NOL (aq)} + NOL_{ox}\text{ (aq)} \quad (14)$$

Ligand exchange, the forth possible mechanism, involves the substitution of surface hydroxyl groups (–OH) by carboxyl or phenolic groups of DOM.[3] Initial acid/base additions stabilized the pH and compensated for –OH release. NOLs adsorb to Mn centers, replacing –OH groups, weakening Mn–OH bonds,[3,83] and altering surface coordination, promoting the release of Mn^{3+}, which is subsequently complexed by additional NOLs [eqn (15)]. This mechanism is favored by NOLs with high molecular weight (HMW), acidity, and aromaticity,[3] and likely contributes to Mn^{3+}–NOL complex formation under circumneutral conditions. As noted by Stuckey *et al.* (2018),[83] ligand exchange may be particularly relevant under moderately to strongly acidic conditions, supporting Mn^{3+}–NOL complex formation in the early stages of the NOL–Mn oxide interactions.

$$Mn^{III}\text{–OH (s)} + NOL^-\text{ (aq)} \rightarrow Mn^{III}\text{–NOL (aq)} + OH^- \rightarrow$$

$$Mn^{3+}\text{ (aq)} + \text{NOL (aq)} \rightarrow Mn^{3+}\text{–NOL (aq)} \quad (15)$$

Complementary to the mechanisms discussed above, Mn^{3+}–NOL complexes may be formed or degraded by additional reactions. Disproportionation of Mn^{3+}–NOL complexes [eqn (16)], as proposed for neutral pH and citrate as the chelator, may explain the small Mn^{2+} proportions at circumneutral pH (Figure 3.4a).[24]

$$2Mn^{3+}\text{–NOL (aq)} + 2H_2O \rightarrow Mn^{2+}\text{–}NOL_{ox}\text{ (aq)} + Mn^{IV}O_2\text{ (s)} + NOL_{ox}\text{ (aq)} + 4H^+ \quad (16)$$

Surface-catalyzed oxidation of Mn^{2+} to Mn^{3+}, followed by complexation through additional ligands, promotes Mn^{3+}–NOL complex formation [eqn (17)].[11] In combination

with eqn (11) and (15), Mn^{3+}–NOL complex concentrations increase, consistent with the rise observed at pH 5 after 12 h (Figure 3.4a).

$$Mn^{2+}\ (aq) + surface\ (s) + NOL\ (aq) \rightarrow Mn^{3+}–NOL_{red}\ (aq) \quad (17)$$

We conclude that (i) ligand-promoted non-reductive dissolution, (ii) ligand-promoted reductive dissolution either directly or followed by subsequent complexation with and without oxidation, (iii) ligand exchange, and apart from these mechanisms (iv) the observed molar Mn_T : DOC ratio ≤0.08 (Table 3.S4) promote the formation of Mn^{3+}–NOL complexes under circumneutral and moderately acidic conditions. The relatively small Mn^{2+} proportions resulted from reductive degradation of Mn^{3+}–NOL complexes, for example through redox-active transformation of additional NOLs. Contrastingly, under strongly acidic conditions (pH 3–4, >6 h), decreased Mn^{3+}–NOL complex concentrations (Figure 3.4a) result from (i) lesser ligand-promoted non-reductive dissolution, (ii) dominant ligand-promoted or H^+-promoted dissolution, followed by complexation without oxidation, (iii) progressive reduction of Mn^{3+}–NOL complexes by additional NOLs, and besides these mechanisms (iv) the observed molar Mn_T : DOC ratio ≥0.08 (Table 3.S4). Since the experimental setup provides only a temporary, limited insight into the ongoing solution chemistry, considerable variations in the Mn^{3+}–NOL complex concentrations are expected. Overall, Mn^{3+}–NOL complexes appear to be metastable under strongly acidic conditions.

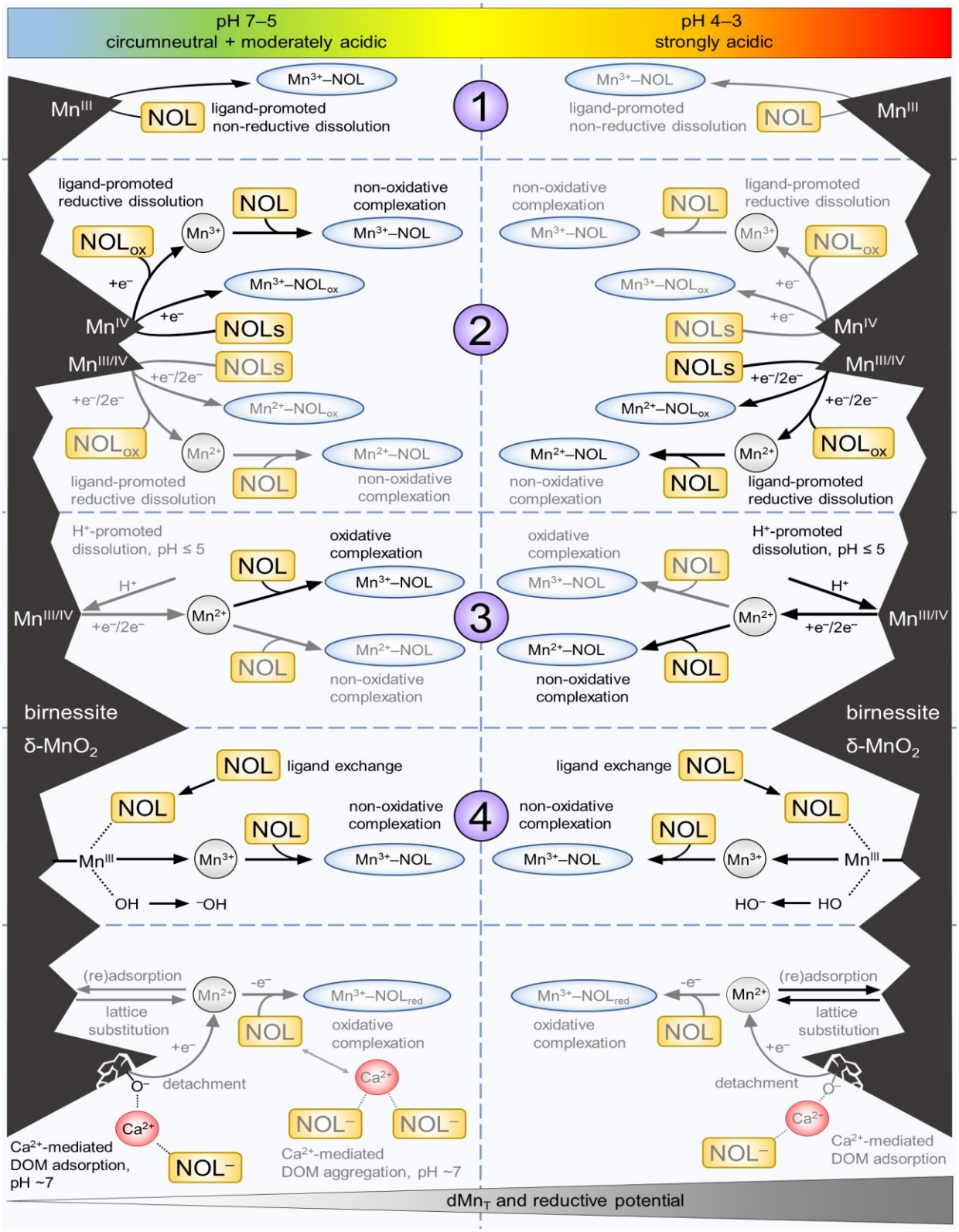

Figure 3.5 Schematic illustration of the assumed essential (black) and side (gray) NOL–birnessite interactions and the proposed parallel main (black) and minor (grey) ad-/desorption processes that lead to the formation of Mn^{3+}–NOL complexes. NOL = natural organic ligand; Mn^{3+}–NOL_{weak} = weakly bound Mn^{3+}; Mn^{3+}–NOL_{strong} = strongly bound Mn^{3+}.

Focusing on NOL–manganite interactions (Figure 3.6), (i) ligand-promoted non-reductive dissolution [eqn (4)], (ii) ligand-promoted reductive dissolution by direct complexation (1-e^- transfer) or detachment of Mn^{2+} [eqn (7)] with subsequent oxidation [eqn (9) and (11)], and (iii) ligand exchange [eqn (15)] are assumed to promote the formation of Mn^{3+}–NOL complexes under circumneutral conditions (Figure 3.4b). Similar to birnessite, the observed pH drift caused by –OH release could be initialized by ligand exchange [eqn (12)].[84]

At pH ≤ 6, the strong decrease in Mn^{3+}–NOL complexes indicates a change in the predominating mechanisms. As pH decreases, the synergy between H^+-promoted and ligand-promoted reductive dissolution of surface-coordinated Mn^{III} increases.[36] Similar to birnessite, solid Mn^{III} is reductively dissolved and the corresponding NOLs are simultaneously oxidized [eqn (7)]. Additional NOLs then complex Mn^{2+} without oxidation [eqn (10)]. Manganite provides a higher E_H (1.51 V) than Mn^{IV} oxides (1.23 V) and thus, an increased potential to oxidize DOM and to be reduced.[85] Various studies have shown that manganite is reductively dissolved by a myriad of organic compounds.[26–29] The negligible traces of Mn^{3+}–NOL_{weak} complexes and the small proportions of Mn^{3+}–NOL_{strong} complexes are consistent with the findings by McArdell *et al.* (1998),[35] who studied the dissolution of $Mn^{III}O(OH)$ interacting with ligands such as aminocarboxylates.

Another reductive dissolution mechanism that increases the Mn^{2+} concentration is the H^+-promoted disproportionation (pH < 6) of Mn^{III} [eqn (18)].[29,31] The precipitated MnO_2 is susceptible to reductive dissolution, potentially further increasing Mn^{2+} concentration.

$$2Mn^{III}O(OH)\,(s) + 2H^+ \rightarrow Mn^{2+}\,(aq) + Mn^{IV}O_2\,(s) + 2H_2O \qquad (18)$$

Under strongly acidic conditions, the higher proportions of Mn^{3+}–NOL complexes observed during the first 3 h can be attributed to synergistic effects of the four possible dissolution mechanisms. The variability in Mn^{3+}–NOL complex proportions highlights the unstable nature of these complexes, which are susceptible to disproportionation at low pH. Additionally, they are prone to degradation *via* intramolecular or intermolecular e^- transfer reactions.[10,30,45,46]

In contrast to birnessite, NOL–manganite interactions favor the formation of Mn^{3+}–NOL_{strong} complexes (Table 3.S3). Whether the high Mn^{3+}–NOL_{strong} complex proportions result from the individual E_H of the manganite, its predominant valence state, low

SSA, surface charge, or selective NOL adsorption remains uncertain and warrants further investigation.

The formation and stabilization of Mn^{3+}–NOL complexes primarily depends on pH (key parameter), as well as on reaction time and the properties of both Mn oxides and NOLs. We assume that the predominant Mn valence of the Mn oxide governs the preferential dissolution mechanisms as a function of solution pH. However, further studies are required to qualify and quantify the influence of the dominant Mn valence.

Similar to the findings on Mn^{3+}–NOM complexes,[3] it can be confirmed from our data that lower molar Mn_T : DOC ratios (≤0.08) support the formation of Mn^{3+}–NOL complexes (Tables 3.S4 and 3.S5). We therefore hypothesize that NOL availability is a decisive factor. The range of Mn^{3+}–NOL complex proportions (Figure 3.4) determined in this study (0 to 87 ± 18%), particularly under strongly acidic conditions during the first 6 h (0 to 85 ± 9%), aligns with our previous analyses of *in situ* sampled non-limed (11 to 79%) and formerly limed (10 to 87%) forest floor solutions and soil solutions.[9]

Although Mn^{2+} was the predominant species under strongly acidic conditions, Mn^{3+}–NOL complexes remain a non-negligible compound in NOL-enriched topsoil layers at the acidic forest site. However, the formation and stabilization of Mn^{3+}–NOL complexes are evidently restricted, characterizing them metastable under natural acidic conditions.

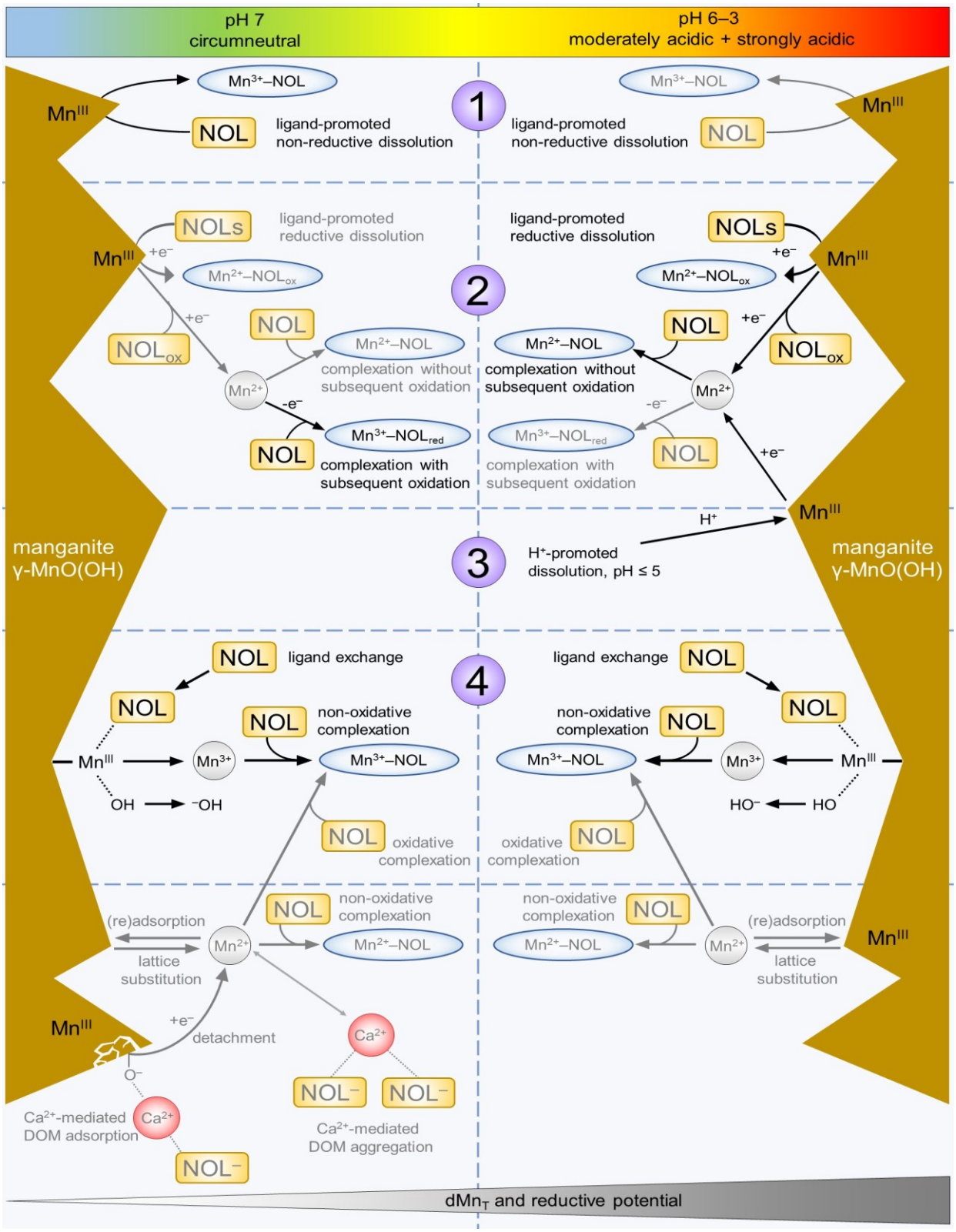

Figure 3.6 Schematic illustration of the assumed essential (black) and side (gray) NOL–manganite interactions and the proposed parallel main (black) and minor (grey) ad-/desorption processes that lead to the formation of Mn^{3+}–NOL complexes. NOL = natural organic ligand; Mn^{3+}–NOL_{weak} = weakly bound Mn^{3+}; Mn^{3+}–NOL_{strong} = strongly bound Mn^{3+}.

Possible side mechanisms

Parallel side mechanisms occur during NOL–Mn oxide interactions (Figures 3.5 and 3.6) and affect the Mn speciation analysis.

Adsorption of released Mn^{2+} was neither qualitatively nor quantitatively assessed in this study, but it should be considered. Mn^{2+} adsorption is particularly favored by negatively charged mineral surfaces and high SSA. This surface-catalyzed process can occur under strongly to moderately acidic conditions, particularly for the synthesized birnessite, as well as under circumneutral conditions (Figure 3.5). Upon adsorption onto the mineral surface, Mn^{2+} may participate in redox interactions, leading to the formation of various Mn^{3+}-containing mineral phases through comproportionation.[86,87] Alternatively, Mn^{2+} may undergo oxidation followed by precipitation, however, this process is strongly pH-dependent and thermodynamically unfavorable below pH 8.[88]

Any addition of salts to the DOM-stock solution increases the ionic strength, influences the solubility of (trace) metals, affects the binding affinity of DOM to the surfaces of the Mn oxides, and thus the dissolution kinetics and Mn speciation analysis.[89,90]

During our batch operations, the mean molarities for Ca^{2+} ranged from 0.0003 to 0.001 M (Tables 3.S6 and 3.S7). This cation mediates interactions between negatively charged NOLs, in particular carboxyl groups, and negatively charged Mn oxide surfaces by the formation of inner- and outer-sphere surface complexes and/or electrostatic attraction.[90] Experimental indications of this side mechanism were found during the NOL–Mn oxide interactions at pH 7 for birnessite at all time steps and more limited for manganite at ≥12 h (Figures 3.5 and 3.6). By this mechanism, the NOLs are (temporarily) removed from the solution and are not available for, amongst others, the complexation of dissolved Mn^{2+} with or without oxidation [eqn (8)–(10)]. This effect was indicated by a distinct decrease in the Ca^{2+} concentrations (Tables 3.S6 and 3.S7). However, the experimental data do not provide conclusive evidence for this mechanism and further studies are needed. By contrast, this mechanism did not occur reliably under strongly acidic conditions, since Ca^{2+} then has a lower sorption affinity towards Mn oxides[91,92] and is displaced by (excessively) released Mn^{2+} and H^{+}.[93] Looking at manganite, its high PZC and smaller SSA limit the readsorption rate.

Another possible side mechanism involves the formation of Ca^{2+}-mediated DOM aggregates, leading to HMW organic molecules.[94] It occurs preferentially under circumneutral conditions, as carboxyl groups are mainly deprotonated. Although HMW NOLs are more prevalent under circumneutral conditions, this process cannot be conclusively verified by the data. Similar effects do not occur in Na^+ and Mg^{2+} solutions.[95] For mechanisms such as cation bridging and aggregate formation, the influence of NaN_3 and NaOH which were used in our experiments is negligible. However, NaN_3 can act as both an oxidant and a reductant, potentially altering DOM molecules (*e.g.*, quinones and phenols) by rapidly reducing redox-active functional groups, thereby decreasing their overall reducing capacity.[96] Since a control experiment without NaN_3 was not performed, a potential influence of NaN_3 on the reducing capacity of DOM or the EEM spectroscopy analysis cannot be excluded.

Interactions of the natural organic ligands

During the batch experiments, the observed DOC_{loss} proportions may result from (i) adsorption onto mineral surfaces, (ii) surface-catalyzed degradation to CO_2,[97] and (iii) the formation and precipitation of non-filter-passing $Mn^{2+/3+}$ colloids stabilized by humic acids.[3,97] These processes alter the DOM composition, thereby influencing Mn^{3+}–NOL complex formation and, consequently, Mn speciation analysis.

For birnessite, increased DOC_{loss} proportions (pH ≤ 4) are attributed to its high SSA and surface charge, which promote adsorption, higher sorption capacities (*e.g.*, Mn^{2+}, DOM),[83,98] dissolution kinetics,[31] and oxidation of many polar organic compounds.[85] Protonated functional groups like carboxyl (pK_a 3–6)[99] and phenolic groups (pK_a 8–11)[100] are less repelled by the negatively charged surface. Adsorption is largely governed by carboxyl groups, which are abundant alongside hydroxylic groups in terrestrial DOM.[101] These groups initiate bridging and/or the mono-/bidentate bonds that bind DOM to birnessite.[102] Once adsorbed, DOM is prone to surface-catalyzed oxidation, as indicated by increased Ss and S_R values (Table 3.S4). Birnessite is known for its ability to oxidize organic molecules such as catechol to CO_2, releasing Mn^{2+}. This process contributes to a progressive DOC loss over time, which further shifts the Mn_T : DOC ratio, preventing the formation of Mn^{3+}–NOL complexes.

For manganite, the almost halved DOC_{loss} (pH ≤ 4) compared to birnessite results from its small SSA and repelled functional groups due to the mineral surface charge. Decreased MA_{254} and MA_{350} values, along with increased Ss and S_Rs, suggest shrinking aromaticity and a predominance of LMW NOLs (Table 3.S5). This aligns with the preferential adsorption of molecules with HMW, high(er) aromaticity, high content of oxygen, nitrogen and carbohydrates, while unsaturated LMW molecules, defined by less oxygen-containing functional groups, remain dissolved.[3,97,103] Ongoing oxidation of DOM, driven by the strong oxidative potential of manganite as well as the higher reductive potential of the solution, leads to its degradation. Consequently, terrestrial LMW NOLs complex Mn^{3+} only to a limited extent and the resulting Mn^{3+}–NOL complexes are metastable, particularly under strongly acidic conditions.

Considering the general binding affinity of NOLs under strongly acidic conditions, Mn^{2+} and H^+ are assumed to compete for binding sites on NOLs, such as humic acids.[104] This competitive binding, resulted by reductive dissolution mechanisms and a molar Mn_T : DOC ratio ≥0.08, strongly hinders Mn^{3+}–NOL complex formation.

In summary, concentration, availability, composition (*e.g.*, functional groups, charge) and potential transformation of DOM during NOL–Mn oxide interactions are crucial for Mn^{3+}–NOL complex formation.

3.4.2 Method criticism

The extraction protocol for the forest floor solution affects the duration of extraction, the dissolution ratio,[105] the concentration of the background electrolyte,[77,106] and the intensity of rewetting of the dried forest soil sample.[107] Consequently, the protocol for the extraction of NOLs has a decisive influence on the NOL concentration, composition, and reactivity.[108] In addition, micro- and nano-sized Mn oxides that surpass the filtration steps cannot be completely excluded and might lead to an overestimation of Mn^{3+}–NOL_{strong} complexes.[30]

Looking at the kinetic modeling process, unknown environmental samples with their individual reaction kinetics are challenging. In particular, a large number of unknown NOLs complicate the modeling and parameterization.[9,109] The equations used for modeling [eqn (1) and (2)] are simplified and represent the diversity of the NOL pool only to a limited extent. More precise kinetic modeling would require extending these equations to account

for the individual number of NOLs, as suggested by Kim *et al.* (2022).[109] Furthermore, due to the largy variety of NOLs, it remains unclear whether certain NOLs withstand competition from T(4-CP)P[30] or hydroxylamine. Consequently, it is impossible to fully incorporate the variability of unknown NOLs into the modeling process.

Additionally, the use of experimental and analytical triplicates introduces further variability into the Mn_T pool data. This variability arises from (i) the individual DOM composition of each replicate, (ii) minor inconsistencies in manual procedures (*e.g.*, pipetting) and (iii) the process of fitting experimental data to the model equations.

We are critically aware that, in particular, the removal of Al^{3+} and Fe^{3+} species by the cation exchange resin excluded prominent binding partners for NOLs. Under natural conditions, these cations form stable complexes with the NOLs of the soil solution[110] and thus compete with dissolved Mn species. It is, therefore, obvious that natural soil solutions exhibit a more variable cation pool. We conclude that additional competitive side reactions potentially decrease Mn^{3+}–NOL complex concentrations, resulting in increased Mn^{2+} proportions.

3.5 Conclusions

Our results demonstrate that Mn^{3+}–NOL complexes are important constituents of the Mn_T pool in forest floor solutions. We further outline fundamental abiotic mechanisms that are assumed to contribute to the formation of Mn^{3+}–NOL complexes in terrestrial environments. Since its formation and stability are particularly limited under strongly acidic conditions, it is a metastable species that is subject to a continuous cycle of formation and decay. However, Mn^{3+}–NOL complexes remain a non-negligible compound. It is likely that high amounts of reactive Mn^{3+}–NOL complexes promote the oxidative degradation of organic compounds as well as altering the acidity and redox capacity of forest floor solutions. Consequently, the role of Mn^{3+}–NOL complexes in terrestrial environments has been underestimated. Based on our findings, we hypothesize that different types of Mn oxides react with NOLs to enable the formation of Mn^{3+}–NOL complexes over a wide pH range in forest floor solutions, even under oxidizing conditions. Further research should investigate more complex forest floor and soil solution matrices as well as different Mn oxides, and follow the trace of Mn^{3+}–NOL complexes.

Conflicts of interest

The authors declare that there are no conflicts of interest.

Data availability

The data supporting this article have been included as part of the SI. See DOI: https://doi.org/10.1039/d5em00388a.

Acknowledgements

Financial support was provided by the Deutsche Forschungsgemeinschaft (DFG, German Research Foundation) under the contract number Ma 2143/17-1 and is gratefully acknowledged. We thank Dr. Martin Greve, Research Institute for Forest Ecology and Forestry (FAWF) of the State of Rhineland-Palatinate, Trippstadt, Germany, for providing access to the study area. Special thanks to the AG Wickleder and AG Mathur, Department of Chemistry, University of Cologne, Germany, for support with EEM spectroscopy and ATR FT-IR spectroscopy. Additionally, we extend our thanks to Jana Glombitza, Karin Greef and Nicole Mantke for their assistance with the laboratory work.

References

1 Z. L. He, J. Shentu and X. E. Yang, in *Trace Elements in Soils*, ed. P. S. Hooda, Wiley, West Sussex, 1st edn., 2010, ch. 20, pp. 481–495.

2 N. Wiberg, E. Wiberg and A. F. Hollemann, in *Anorganische Chemie, Band 2*, ed. N. Wiberg, de Gruyter, Berlin, 103rd edn., 2017, ch. XXVIII, pp. 1899–1933.

3 H. Li, F. Santos, K. Butler and E. Herndon, A Critical Review on the Multiple Roles of Manganese in Stabilizing and Destabilizing Soil Organic Matter, *Environ. Sci. Technol.*, 2021, **55**, 12136–12152.

4 G. Biedermann and R. Palombari, On the Hydrolysis of Manganese(III) Ion, *Acta Chem. Scand. A*, 1978, **32**, 381–390.

5 G. Davies, Some Aspects of Chemistry of Manganese(III) in Aqueous Solution, *Coordin. Chem. Rev.*, 1969, **4**, 199–224.

6 K. L. Johnson, C. M. McCann, J.-L. Wilkinson, M. Jones, B. M. Tebo, M. West, C. Elgy, C. E. Clarke, C. Gowdy and K. A. Hudson-Edwards, Dissolved Mn(III) in water treatment works: Prevalence and significance, *Water Res.*, 2018, **140**, 181–190.

7 A. S. Madison, B. M. Tebo and G. W. Luther, 3rd, Simultaneous determination of soluble manganese(III), manganese(II) and total manganese in natural (pore)waters, *Talanta*, 2011, **84**, 374–381.

8 G. W. Luther, 3rd, A. S. Madison, A. Mucci, B. Sundby and V. E. Oldham, A kinetic approach to assess the strengths of ligands bound to soluble Mn(III), *Mar. Chem.*, 2015, **173**, 93–99.

9 C. Lux and T. Mansfeldt, Evidence of dissolved trivalent manganese in acidic forest soils, *J. Plant Nutr. Soil Sci.*, 2023, **186**, 321–329.

10 V. E. Oldham, S. M. Owings, M. R. Jones, B. M. Tebo and G. W. Luther, 3rd, Evidence for the presence of strong Mn(III)-binding ligands in the water column of the Chesapeake Bay, *Mar. Chem.*, 2015, **171**, 58–66.

11 V. E. Oldham, A. Mucci, B. M. Tebo and G. W. Luther, 3rd, Soluble Mn(III)–L complexes are abundant in oxygenated waters and stabilized by humic ligands, *Geochim. Cosmochim. Acta*, 2017, **199**, 238–246.

12 V. E. Oldham, M. T. Miller, L. T. Jensen and G. W. Luther, 3rd, Revisiting Mn and Fe removal in humic rich estuaries, *Geochim. Cosmochim. Acta*, 2017, **209**, 267–283.

13 V. E. Oldham, M. R. Jones, B. M. Tebo and G. W. Luther, 3rd, Oxidative and reductive processes contributing to manganese cycling at oxic-anoxic interfaces, *Mar. Chem.*, 2017, **195**, 122–128.

14 A. Thibault de Chanvalon and G. W. Luther, 3rd, Mn speciation at nanomolar concentrations with a porphyrin competitive ligand and UV-vis measurements, *Talanta*, 2019, **200**, 15–21.

15 L. A. Sparrow and N. C. Uren, Manganese oxidation and reduction in soils: effects of temperature, water potential, pH and their interactions, *Soil Res.*, 2014, **52**, 483–494.

16 X. H. Feng, L. M. Zhai, W. F. Tan, F. Liu and J. Z. He, Adsorption and redox reactions of heavy metals on synthesized Mn oxide minerals, *Environ. Pollut.*, 2007, **147**, 366–373.

17 J. E. Post, Manganese oxide minerals: Crystal structures and economic and environmental significance, *Proc. Natl. Acad. Sci. USA*, 1999, **96**, 3447–3454.

18 S. T. Martin, in *Environmental Catalysis*, ed. V. H. Grassian, CRC Press, New York, 1st edn., 2005, ch. 3, pp. 61–82.

19 B. M. Tebo, J. R. Bargar, B. G. Clement, G. J. Dick, K. J. Murray, D. Parker, R. Verity and S. M. Webb, BIOGENIC MANGANESE OXIDES: Properties and Mechanisms of Formation, Annu. Rev. Earth Planet. Sci., 2004, **32**, 287–328.

20 A.-C. Gaillot, V. A. Drits, A. Manceau and B. Lanson, Structure of the synthetic K-rich phyllomanganate birnessite obtained by high-temperature decomposition of $KMnO_4$: Substructures of K-rich birnessite from 1000 °C experiment, *Micropor. Mesopor. Mat.*, 2007, **98**, 267–282.

21 D. C. Golden, J. B. Dixon and C. C. Chen, Ion Exchange, Thermal Transformations, and Oxidizing Properties of Birnessite, *Clay Clay Miner.*, 1986, **34**, 511–520.

22 D. Banerjee and H. W. Nesbitt, XPS study of reductive dissolution of birnessite by oxalate: Rates and mechanistic aspects of dissolution and redox processes, *Geochim. Cosmochim. Acta*, 1999, **63**, 3025–3038.

23 G. R. Aiken, H. Hsu-Kim and J. N. Ryan, Influence of dissolved organic matter on the environmental fate of metals, nanoparticles, and colloids, *Environ. Sci. Technol.*, 2011, **45**, 3196–3201.

24 J. K. Klewicki and J. J. Morgan, Kinetic behavior of Mn(III) complexes of pyrophosphate, EDTA, and citrate, *Environ. Sci. Technol.*, 1998, **32**, 2916–2922.

25 J. K. Klewicki and J. J. Morgan, Dissolution of β-MnOOH particles by ligands: Pyrophosphate, ethylenediaminetetraacetate, and citrate, *Geochim. Cosmochim. Acta*, 1999, **63**, 3017–3024.

26 Y. Wang and A. T. Stone, Reaction of $Mn^{III,IV}$ (hydr)oxides with oxalic acid, glyoxylic acid, phosphonoformic acid, and structurally-related organic compounds, *Geochim. Cosmochim. Acta*, 2006, **70**, 4477–4490.

27 Y. Wang and A. T. Stone, Phosphonate- and carboxylate-based chelating agents that solubilize (hydr)oxide-bound Mn^{III}, *Environ. Sci. Technol.*, 2008, **42**, 4397–4403.

28 O. W. Duckworth and G. Sposito, Siderophore–manganese(III) interactions. I. Air-oxidation of manganese(II) promoted by desferrioxamine B, *Environ. Sci. Technol.*, 2005, **39**, 6037–6044.

29 O. W. Duckworth and G. Sposito, Siderophore–manganese(III) interactions II. Manganite dissolution promoted by desferrioxamine B, *Environ. Sci. Technol.*, 2005, **39**, 6045–6051.

30 X. Wang, M. R. Jones, Z. Pan, X. Lu, Y. Deng, M. Zhu and Z. Wang, Trivalent manganese in dissolved forms: Occurrence, speciation, reactivity and environmental geochemical impact, *Water Res.*, 2024, **263**, 122198.

31 M. Ramstedt and S. Sjöberg, Phase Transformations and Proton Promoted Dissolution of Hydrous Manganite (γ-MnOOH), *Aquat. Geochem.*, 2005, **11**, 413–431.

32 D. R. Lovley and E. J. P. Phillips, Novel Mode of Microbial Energy Metabolism: Organic Carbon Oxidation Coupled to Dissimilatory Reduction of Iron or Manganese, *Appl. Environ. Microb.*, 1988, **54**, 1472–1480.

33 C. R. Myers and K. H. Nealson, Bacterial Manganese Reduction and Growth with Manganese Oxide as the Sole Electron Acceptor, *Science*, 1988, **240**, 1319–1321.

34 J. E. Johnson, P. Savalia, R. Davis, B. D. Kocar, S. M. Webb, K. H. Nealson and W. W. Fischer, Real-Time Manganese Phase Dynamics during Biological and Abiotic Manganese Oxide Reduction, *Environ. Sci. Technol.*, 2016, **50**, 4248–4258.

35 C. S. McArdell, A. T. Stone and J. Tian, Reaction of EDTA and related aminocarboxylate chelating agents with Co(III)OOH (heterogenite) and Mn(III)OOH (manganite), *Environ. Sci. Technol.*, 1998, **32**, 2923–2930.

36 A. T. Stone and J. J. Morgan, Reduction and Dissolution of Manganese(III) and Manganese(IV) Oxides by Organics. 1. Reaction with Hydroquinone, *Environ. Sci. Technol.*, 1984, **18**, 450–456.

37 A. G. Xyla, B. Sulzberger, G. W. Luther, 3rd, J. G. Hering, P. Van Cappellen and W. Stumm, Reductive Dissolution of Manganese(III,IV) (Hydr)oxides by Oxalate: The Effect of pH and Light, *Langmuir*, 1992, **8**, 95–103.

38 S. Zhang, B. Li, Y. Chen, M. Zhu, J. A. Pedersen, B. Gu, Z. Wang, H. Li, J. Liu, X.-Q. Zhou, Y.-Y. Hao, H. Jiang, F. Liu, Y.-R. Liu and H. Yin, Methylmercury Degradation by Trivalent Manganese, *Environ. Sci. Technol.*, 2023, **57**, 5988–5998.

39 B. Berg, K. T. Steffen and C. McClaugherty, Litter decomposition rate is dependent on litter Mn concentrations, *Biogeochem.*, 2007, **82**, 29–39.

40 M. Hofrichter, Review: lignin conversion by manganese peroxidase (MnP), *Enzyme Microb. Technol.*, 2002, **30**, 454–466.

41 M. E. Jones, P. S. Nico, S. Ying, T. Regier, J. Thieme and M. Keiluweit, Manganese-Driven Carbon Oxidation at Oxic–Anoxic Interfaces, *Environ. Sci. Technol.*, 2018, **52**, 12349–12357.

42 M. E. Jones, R. E. LaCroix, J. Zeigler, S. C. Ying, P. S. Nico and M. Keiluweit, Enzymes, Manganese, or Iron? Drivers of Oxidative Organic Matter Decomposition in Soils, *Environ. Sci. Technol.*, 2020, **54**, 14114–14123.

43 M. Keiluweit, P. Nico, M. E. Harmon, J. Mao, J. Pett-Ridge and M. Kleber, Long-term litter decomposition controlled by manganese redox cycling, *Proc. Natl. Acad. Sci. USA*, 2015, **112**, E5253–5260.

44 J. Stendahl, B. Berg and B. D. Lindahl, Manganese availability is negatively associated with carbon storage in northern coniferous forest humus layers, *Sci. Rep.*, 2017, **7**, 15487.

45 E. Hu, Y. Zhang, S. Wu, J. Wu, L. Liang and F. He, Role of dissolved Mn(III) in transformation of organic contaminants: Non-oxidative versus oxidative mechanisms, *Water Res.*, 2017, **111**, 234–243.

46 X. Wang, J. Yao, S. Wang, X. Pan, R. Xiao, Q. Huang, Z. Wang and R. Qu, Phototransformation of estrogens mediated by Mn(III), not by reactive oxygen species, in the presence of humic acids, *Chemosphere*, 2018, **201**, 224–233.

47 Forschungsanstalt für Waldökologie und Forstwirtschaft Rheinland-Pfalz (FAWF), Dauerbeobachtungsfläche 101: Idar-Oberstein (Umweltkontrollstation), https://fawf.wald.rlp.de/indexphp?id=12306, accessed May 2025.

48 IUSS Working Group WRB. 2022. World Reference Base for Soil Resources. International soil classification system for naming soils and creating legends for soil maps. 4th edn., International Union of Soil Sciences (IUSS), Vienna, Austria https://www.isric.org/sites/default/files/WRB_fourth_edition_2022-12-18.pdf, accessed May 2025.

49 Soil Science Division Staff, Examination and Description of Soil Profiles, in *Soil Survey Manual*, eds. C. Ditzler, K. Scheffe and H. C. Monger, USDA Handbook 18, 2018, ch. 3, pp. 83–233.

50 Ad-hoc-Arbeitsgruppe Boden, Bodenkundliche Kartieranleitung (KA5), Bundesanstalt für Geowissenschaften und Rohstoffe, Hannover, 6th edn., 2025.

51 GAFA, *Handbuch Forstliche Analytik (HFA), 1. - 6. Ergänzung des Gutachterausschuss Forstliche Analytik*, Bundesministerium für Ernährung, Landwirtschaft und Verbraucherschutz (BMELV) & Nordwestdeutsche Forstliche Versuchsanstalt (NWFVA), https://blumwald.thuenen.de/fileadmin/blumwald/BZE/HFA_Gesamtdatei_2022.pdf, accessed May 2025.

52 F. Amery, F. Degryse, W. Degeling, E. Smolders and R. Merckx, The Copper-Mobilizing-Potential of Dissolved Organic Matter in Soils Varies 10-Fold Depending on Soil Incubation and Extraction Procedures, *Environ. Sci. Technol.*, 2007, **41**, 2277–2281.

53 V. J. G. Houba, I. Novozamsky, Th. M. Lexmond and J. J. van der Lee, Applicability of 0.01 M $CaCl_2$ as a single extraction solution for the assessment of the nutrient status of soils and other diagnostic purposes, *Commun. Soil Sci. Plan.*,1990, **21**, 2281–2290.

54 M. R. Provenzano, P. Caricasole, G. Brunetti and N. Senesi, Dissolved Organic Matter Extracted With Water and a Saline Solution From Different Soil Profiles, *Soil Sci.*, 2010, **175**, 255–262.

55 B. W. Strobel, H. C. B. Hansen, O. K. Borggaard, M. K. Andersen and K. Raulund-Rasmussen, Composition and reactivity of DOC in forest floor soil solutions in relation to tree species and soil type, *Biogeochem.*, 2001, **56**, 1–26.

56 P. G.-J. de Maagd, T. L. Sinnige, S. M. Schrap, A. Opperhuizen and D. T. H. M. Sijm, Sorption coefficients of polycyclic aromatic hydrocarbons for two lake sediments: Influence of the bactericide sodium azide, *Environ. Toxicol. Chem.*, 1998, **17**, 1899–1907.

57 T. Ohno, Fluorescence inner-filtering correction for determining the humification index of dissolved organic matter, *Environ. Sci. Technol.*, 2002, **36**, 742–746.

58 C. A. Stedmon, S. Markager and R. Bro, Tracing dissolved organic matter in aquatic environments using a new approach to fluorescence spectroscopy, *Mar. Chem.*, 2003, **82**, 239–254.

59 D. M. McKnight, E. W. Boyer, P. K. Westerhoff, P. T. Doran, T. Kulbe and D. T. Andersen, Spectrofluorometric characterization of dissolved organic matter for indication of precursor organic material and aromaticity, *Limnol. Oceanogr.*, 2001, **46**, 38–48.

60 A. Zsolnay, E. Baigar, M. Jimenez, B. Steinweg and F. Saccomandi, Differentiating with fluorescence spectroscopy the sources of dissolved organic matter in soils subjected to drying, *Chemosphere*, 1999, **38**, 45–50.

61 A. Huguet, L. Vacher, S. Relexans, S. Saubusse, J. M. Froidefond and E. Parlanti, Properties of fluorescent dissolved organic matter in the Gironde Estuary, *Org. Geochem.*, 2009, **40**, 706–719.

62 P. G. Coble, Characterization of marine and terrestrial DOM in seawater using excitation–emission matrix spectroscopy, *Mar. Chem.*, 1996, **51**, 325–346.

63 R Core Team, R: A Language and Environment for Statistical Computing, version 4.2.2, Vienna, Austria, 2022.

64 Posit team, RStudio: Integrated Development Environment for R, version 2022.12.0, Posit Software, PBC, Boston, MA, 2022.

65 M. Pucher, U. Wünsch, G. Weigelhofer, K. Murphy, T. Hein and D. Graeber, staRdom: Versatile Software for Analyzing Spectroscopic Data of Dissolved Organic Matter in R, *Water*, 2019, **11**, 2366.

66 M. C. Rabenhorst and K. A. Persing, A Synthesized Manganese Oxide for Easily Making Durable Manganese-Coated IRIS Tubes, *Soil Sci. Soc. Am. J.*, 2017, **81**, 233–239.

67 R. Giovanoli and U. Leuenberger, 233. Über die Oxydation von Manganoxidhydroxid, *Helv. Chim. Acta*, 1969, **52**, 2333–2347.

68 J. A. Lee, C. E. Newnham, F. S. Stone and F. L. Tye, Thermal Decomposition of Manganese Oxyhydroxide, *J. Solid State Chem.*, 1980, **31**, 81–93.

69 J. C. Nash, nlmrt: Functions for Nonlinear Least Squares Solutions, https://cran.r-project.org/web/packages/nlmrt/index.html, accessed May 2025.

70 J. C. Nash, *Compact numerical methods for computers: Linear algebra and function minimisation*, Adam Hilger Ltd., Bristol, 2nd edn., 1990.

71 J. L. Weishaar, G. R. Aiken, B. A. Bergamaschi, M. S. Fram, R. Fujii and K. Mopper, Evaluation of specific ultraviolet absorbance as an indicator of the chemical composition and reactivity of dissolved organic carbon, *Environ. Sci. Technol.*, 2003, **37**, 4702–4708.

72 A. M. Hansen, T. E. C. Kraus, B. A. Pellerin, J. A. Fleck, B. D. Downing and B. A. Bergamaschi, Optical properties of dissolved organic matter (DOM): Effects of biological and photolytic degradation, *Limnol. Oceanogr.*, 2016, **61**, 1015–1032.

73 F. J. Rodríguez, P. Schlenger and M. García-Valverde, Monitoring changes in the structure and properties of humic substances following ozonation using UV-Vis, FTIR and ^{1}H NMR techniques, *Sci. Total Environ.*, 2016, **541**, 623–637.

74 S. Chowdhury, Trihalomethanes in drinking water: Effect of natural organic matter distribution, *Water SA*, 2013, **39**, 1–8.

75 H. De Haan and T. De Boer, Applicability of Light Absorbance and Fluorescence as Measures of Concentration and Molecular Size of Dissolved Organic Carbon in Humic Lake Tjeukemeer, *Water Res.*, 1987, **21**, 731–734.

76 J. R. Helms, A. Stubbins, J. D. Ritchie, E. C. Minor, D. J. Kieber and K. Mopper, Absorption spectral slopes and slope ratios as indicators of molecular weight,

source, and photobleaching of chromophoric dissolved organic matter, *Limnol. Oceanogr.*, 2008, **53**, 955–969.

77 A. T.-S. Chow, Y. Ulus, G. Huang, M. A. Kline and W.-Y. Cheah, Challenges in quantifying and characterizing dissolved organic carbon: Sampling, isolation, storage, and analysis, *J. Environ. Qual.*, 2022, **51**, 837–871.

78 M. S. Aulakh and D. A. Rennie, Azide Effects Upon N_2O Emission and Transformations of N in Soils, *Can. J. Soil Sci.*, 1985, **65**, 205–212.

79 D. Banerjee and H. W. Nesbitt, XPS study of dissolution of birnessite by humate with constraints on reaction mechanism, *Geochim. Cosmochim. Acta*, 2001, **65**, 1703–1714.

80 A. T. Stone, Microbial metabolites and the reductive dissolution of manganese oxides: Oxalate and pyruvate, *Geochim. Cosmochim. Acta*, 1987, **51**, 919–925.

81 S. P. Hansard, H. D. Easter and B. M. Voelker, Rapid reaction of nanomolar Mn(II) with superoxide radical in seawater and simulated freshwater, *Environ. Sci. Technol.*, 2011, **45**, 2811–2817.

82 I. G. McKendry, S. K. Kondaveeti, S. L. Shumlas, D. R. Strongin and M. J. Zdilla, Decoration of the layered manganese oxide birnessite with Mn(II/III) gives a new water oxidation catalyst with fifty-fold turnover number enhancement, *Dalton Trans.*, 2015, **44**, 12981–12984.

83 J. W. Stuckey, C. Goodwin, J. Wang, L. A. Kaplan, P. Vidal-Esquivel, T. P. Beebe, Jr. and D. L. Sparks, Impacts of hydrous manganese oxide on the retention and lability of dissolved organic matter, *Geochem. Trans.*, 2018, **19**, 6.

84 J. Chorover and M. K. Amistadi, Reaction of forest floor organic matter at goethite, birnessite and smectite surfaces, *Geochim. Cosmochim. Acta*, 2001, **65**, 95–109.

85 J. A. Greathouse, K. L. Johnson and H. C. Greenwell, Interaction of Natural Organic Matter with Layered Minerals: Recent Developments in Computational Methods at the Nanoscale, *Minerals*, 2014, **4**, 519–540.

86 S. Tu, G. J. Racz and T. B. Goh, Transformation of Synthetic Birnessite as Affected by pH and Manganese Concentration, *Clay Clay Miner.*, 1994, **42**, 321–330.

87 E. J. Elzinga, Reductive Transformation of Birnessite by Aqueous Mn(II), *Envrion. Sci. Technol.*, **45**, 6366–6372.

88 G. W. Luther, 3rd, The Role of One- and Two-Electron Transfer Reactions in Forming Thermodynamically Unstable Intermediates as Barriers in Multi-Electron Redox Reactions, *Aquat. Geochem.*, 2010, **16**, 395–420.

89 J. A. Acosta, B. Jansen, K. Kalbitz, A. Faz and S. Martínez-Martínez, Salinity increases mobility of heavy metals in soils, *Chemosphere*, 2011, **85**, 1318–1324.

90 H. Cheng, J. Ma, J. Jiang, S.-Y. Pang, T. Yang and P. Wang, Aggregation Kinetics of Manganese Oxides Formed from permanganate activated by (Bi)sulfite: Dual Role of Ca^{2+} and $Mn^{II/III}$, *Water Res.*, 2019, **159**, 454–463.

91 J. J. Morgan and W. Stumm, Colloid-Chemical Properties of Manganese Dioxide, *J. Colloid Sci.*, 1964, **19**, 347–359.

92 J. W. Tonkin, L. S. Balistrieri and J. W. Murray, Modeling sorption of divalent metal cations on hydrous manganese oxide using the diffuse double layer model, *Appl. Geochem.*, 2004, **19**, 29–53.

93 H. S. Posselt, F. J. Aderson and W. J. Weber, Cation sorption on colloidal hydrous manganese dioxide, *Environ. Sci. Technol.*, 1968, **2**, 1087–1093.

94 A. G. Kalinichev, E. Iskrenova-Tchoukova, W.-Y. Ahn, M. M. Clark and R. J. Kirkpatrick, Effects of Ca^{2+} on supramolecular aggregation of natural organic matter in aqueous solutions: A comparison of molecular modeling approaches, *Geoderma*, 2011, **169**, 27–32.

95 E. Iskrenova-Tchoukova, A. G. Kalinichev and R. J. Kirkpatrick, Metal cation complexation with natural organic matter in aqueous solutions: molecular dynamics simulations and potentials of mean force, *Langmuir*, 2010, **26**, 15909–15919.

96 K. Hendrix, N. Bleyen, T. Mennecart, C. Bruggeman and E. Valcke, Sodium azide used as a microbial inhibitor caused unwanted by-products in anaerobic geochemical studies, *Appl. Geochem.*, 2019, **107**, 120–130.

97 E. L. Trainer, M. Ginder-Vogel and C. K. Remucal, Selective Reactivity and Oxidation of Dissolved Organic Matter by Manganese Oxides, *Environ. Sci. Technol.*, 2021, **55**, 12084–12094.

98 C. K. Remucal and M. Ginder-Vogel, A critical review of the reactivity of manganese oxides with organic contaminants, *Environ. Sci. Process Impacts*, 2014, **16**, 1247–1266.

99 K. Nambu and K. Yonebayashi, Acidic properties of dissolved organic matter leached from organic layers in temperate forests, *Soil Sci. Plant Nutr.*, 1999, **45**, 65–77.

100 S. Sagbas, C. Kantar and N. Sahiner, Preparation of Poly(Humic Acid) Particles and Their Use in Toxic Organo-Phenolic Compound Removal from Aqueous Environments, *Water Air Soil Pollut.*, 2013, **225**, 1809.

101 M. Zark and T. Dittmar, Universal molecular structures in natural dissolved organic matter, *Nat. Commun.*, 2018, **9**, 3178.

102 K. Johnson, G. Purvis, E. Lopez-Capel, C. Peacock, N. Gray, T. Wagner, C. März, L. Bowen, J. Ojeda, N. Finlay, S. Robertson, F. Worrall and C. Greenwell, Towards a mechanistic understanding of carbon stabilization in manganese oxides, *Nat. Commun.*, 2015, **6**, 7628.

103 Z. Ding, Y. Ding, F. Liu, J. Yang, R. Li, Z. Dang and Z. Shi, Coupled Sorption and Oxidation of Soil Dissolved Organic Matter on Manganese Oxides: Nano/Sub-nanoscale Distribution and Molecular Transformation, *Environ. Sci. Technol.*, 2022, **56**, 2783–2793.

104 S. Paul, T. Sharma, D. Saikia, P. P. Saikia, D. Borah and M. K. Baruah, Evaluation of pKa Values of Soil Humic Acids and their Complexation Properties, *Int. J. Plant Soil Sci.*, 2015, **6**, 218–228.

105 E. P. M. J. Fest, E. J. M. Temminghoff, R. N. J. Comans and W. H. van Riemsdijk, Partitioning of organic matter and heavy metals in a sandy soil: Effects of extracting solution, solid to liquid ratio and pH, *Geoderma*, 2008, **146**, 66–74.

106 A. T. Chow, K. K. Tanji and S. Gao, Production of dissolved organic carbon (DOC) and trihalomethane (THM) precursor from peat soils, *Water Res.*, 2003, **37**, 4475–4485.

107 G. F. Koopmans and J. E. Groenenberg, Effects of soil oven-drying on concentrations and speciation of trace metals and dissolved organic matter in soil solution extracts of sandy soils, *Geoderma*, 2011, **161**, 147–158.

108 A. R. Schneider, M. Ponthieu, B. Cancès, A. Conreux, X. Morvan, M. Gommeaux, B. Marin and M. F. Benedetti, Influence of dissolved organic matter and manganese oxides on metal speciation in soil solution: A modelling approach, *Environ. Pollut.*, 2016, **213**, 618–627.

109 B. Kim, U. F. Lingappa, J. Magyar, D. Monteverde, J. S. Valentine, J. Cho and W. Fischer, Challenges of Measuring Soluble Mn(III) Species in Natural Samples, *Molecules*, 2022, **27**, 1661.

110 D. Kupka and P. Gruba, Effect of pH on the sorption of dissolved organic carbon derived from six tree species in forest soils, *Ecol. Indic.*, 2022, **140**, 108975.

Electronic Supplementary Information (ESI)

for

Dissolved trivalent manganese in forest soils – interactions of natural organic ligands with manganese oxides

Preparation of Mn oxides

Birnessite:

A mixture of 10 mL sodium lactate (60%) and 100 mL 0.063 M potassium permanganate ($KMnO_4$) was reacted for 2 h under stirring and then allowed to stand for further 2 h before the supernatant was decanted. The residue was added in 250 mL Nalgene® bottles (Thermo Fisher Scientific, Waltham, USA), centrifuged for 10 min at 3300 *g* (Rotina 420 R, Hettich, Kirchlengern, Germany) and washed 5 times. Thereafter, the residue was transferred into molecular-porous membrane dialysis tubes (12,000–14,000 Da, Spectrum™, Thermo Fisher Scientific, Waltham, USA). These tubes were placed in a large vessel (5 L, PP) filled with ultrapure water to remove any remaining salts by osmosis. After freeze-drying (Alpha 1–4 LO plus, Christ, Osterode am Harz, Germany), a fine, homogeneous powder was made using an agate mortar.

Manganite:

Initially, 75 mL of 0.2 M ammonium hydroxide (NH_4OH) was slowly added to a stirred solution of 250 mL manganese(II) sulfate monohydrate (0.06 M) containing 5.1 mL H_2O_2 (30%) at room temperature. This caused the immediate formation of a brown precipitate, which was then heated to 100 °C under reflux for 26 h. The finely-dispersed, yellow-brown precipitate was centrifuge-washed and filtered off by 0.2 µm filtration (cellulose acetate, Sartorius, Göttingen, Germany). Finally, the solid was dried in a drying cabinet (UF55, Memmert, Schwabach, Germany) at 80 °C for 24 h.

Characterization of Mn oxides

X-ray powder diffraction patterns were recorded using a PANalytical X'Pert PRO MPD Θ-Θ diffractometer (Co-Kα radiation generated at 40 kV and 40 mA), equipped with a variable divergence slit (20 mm irradiated length), primary and secondary Soller, diffracted beam monochromator, point detector, and a sample changer (sample diameter

28 mm). The samples were investigated from 1° to 80° 2Θ with a step size of 0.03° 2Θ and a measuring time of 15 sec per step. For specimen preparation the back loading technique was used.

ATR FT-IR mid infrared spectra (4,000–400 cm^{-1}) running 4 scan cycles were obtained using a Spectrum™ 400 unit (PerkinElmer, Rodgau, Germany) equipped with a zinc selenide thallium bromo-iodide (KRS5) crystal. All spectra were interpreted with reference to various publications.

Scanning electron microscopy (Sigma 300 VP FEG SEM, Zeiss, Oberkochen, Germany) was used to study the particle morphologies of the Mn oxides. Imaging was performed at an accelerating voltage of 20 kV in high-definition backscattered electron detector (HDBSD) mode. The working distance was set at 9.7 mm for birnessite and 9.9 mm for manganite. In order to characterize the morphology of the mineral, magnifications of 1,760x (birnessite) and 7,240x (manganite) were applied.

The SSA was determined using the BET method (DIN ISO 9277:2022)[1]. This is based on a five-point N_2 adsorption measurement using a surface analyzer (Gemini VII 2390, Micromeritics Instrument Corporation, Norcross, USA) and a sample quantity of 300 mg. Prior to measurement, the samples were prepared under vacuum for 12 h at a temperature of 105 °C. Furthermore, the AOS of the Mn oxides was determined by iodometric titration and subsequent calculation as proposed by Murray *et al.* (1984).[2]

The determination of the PZC was done by a salt addition method described by Mustafa *et al.* (2002).[3] For this purpose, 20 mL sodium nitrate ($NaNO_3$) (0.01 mol L^{-1}) were added to 50 mL PP centrifuge tubes (Sarstedt, Nürnbrecht, Germany) and the initial pH value in the tubes was adjusted to cover a pH range from 2 to 11 using nitric acid (HNO_3, suprapur®, 65%), or sodium hydroxide (NaOH). Then, 0.1 g of Mn oxide was added to the prepared PP centrifuge tubes and the samples were shaken for 24 h. The final pH was measured (827 pH Lab, Metrohm, Herisau, Switzerland) and the PZC determined from ΔpH (difference between initial and final pH) versus pH plots, as pH at which ΔpH = 0.

Characterization of Mn oxides (results)

XRD patterns of both birnessite and manganite revealed peak patterns in good agreement with the reference patterns (Figure 3.S1). For birnessite, small traces of the mineral

feitknechtite (β-$Mn^{III}OOH$) were found, but they could not be verified. For manganite, proven traces of the mixed-valence Mn oxide hausmannite ($Mn^{II}Mn^{III}_2O_4$) were detected.

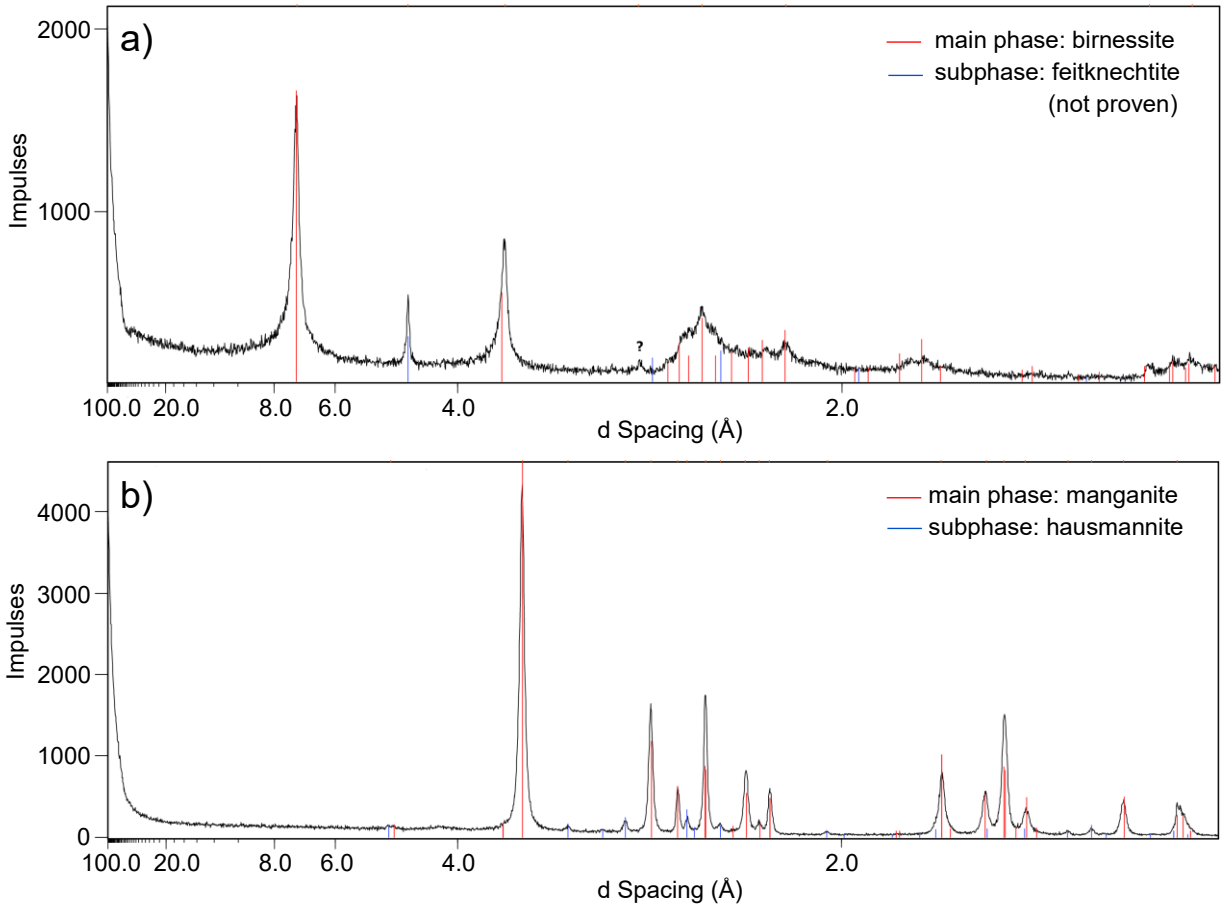

Figure 3.S1 Powder X-ray diffraction patterns of synthetic a) birnessite and b) manganite.

Multiple IR bands and peaks for birnessite and manganite were identified by ATR FT-IR spectroscopy (Figure 3.S2). Both Mn oxides showed individual distributed IR patterns. For birnessite, IR peaks at lower wavenumbers (471 and 507 cm^{-1}), narrow bands at 735, 947 and 1067 cm^{-1} and more prominent ones at 1635 and 3350–3450 cm^{-1} were detected. Similarly, the IR spectrum of manganite showed bands and peaks in the lower wavenumber region (409, 439, 483, 589 and 641–643 cm^{-1}). A triplet of narrow IR bands was recorded at 1083, 1117, and 1152 cm^{-1}. In addition, a distinct band at ~1630 cm^{-1} was observed and two broader bands were determined at higher wavenumbers (~2070 cm^{-1} and 2600–2700 cm^{-1}).

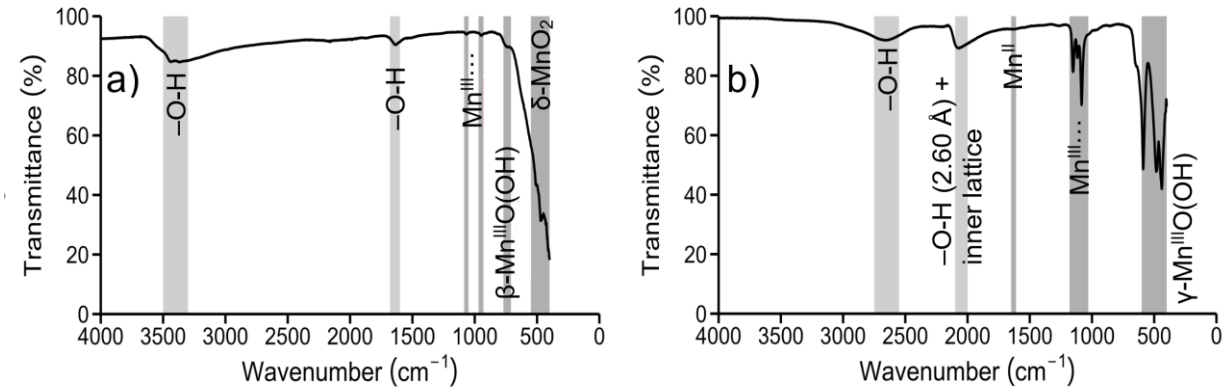

Figure 3.S2 Attenuated total reflection *Fourier transform* infrared spectra (ATR FT-IR) of the synthetic a) birnessite and b) manganite.

Scanning electron microscopy indicated the individual morphologies of the Mn oxides and emphasized clear structural differences between them (Figure 3.S3). Birnessite showed a microporous, flake-like, and fine-grained morphology (Figure 3.S3a). In contrast, manganite showed a structure of randomly distributed fine needles (Figure 3.S3b).

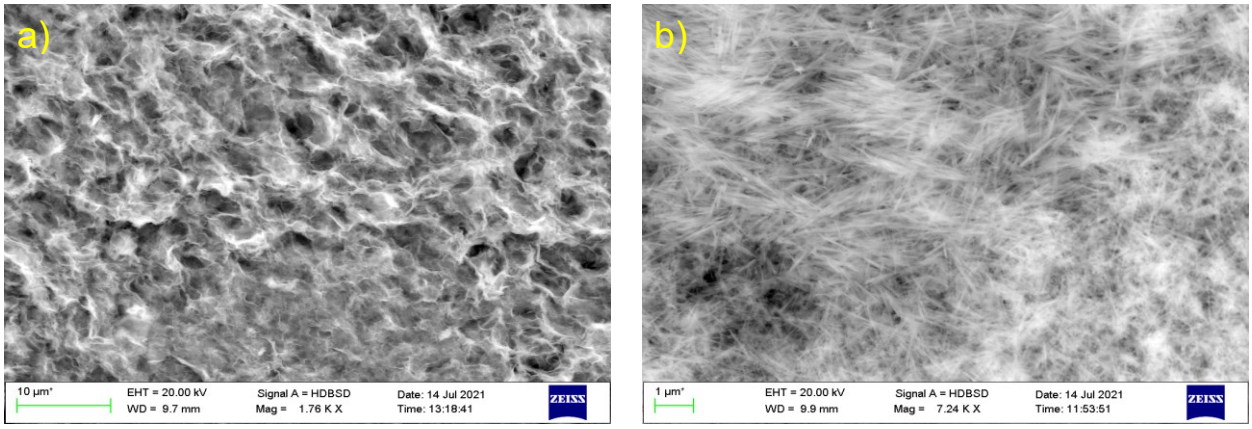

Figure 3.S3 Scanning electron microscopy images of the synthetic a) birnessite and b) manganite.

Table 3.S1 compares the properties of the synthetic Mn oxides used in this study with those reported in the literature. As a result of the BET analyses, the SSA of birnessite (140 $m^2\ g^{-1}$) exceeded that of manganite (28.5 $m^2\ g^{-1}$) fivefold. Both synthetic Mn oxides showed SSAs in agreement with the literature. Additionally, the AOS calculations revealed a higher value for birnessite (3.68) compared to manganite (2.94). The low AOS of manganite can be explained by the detected subphase of hausmannite (Figure 3.S1b) and thus additional proportions of Mn^{II}. The PZC of birnessite was 2.40 but manganite

was higher at 6.65. For the PZCs, manganite agrees well with the data in the literature, but higher values are given for alkaline birnessites. This discrepancy can be explained by the salt addition method used, which yields lower PZC for birnessite. However, the PZC of the birnessite should be lower than 3 and therefore the mineral surface is negatively charged about the entire pH range investigated in this study.

Table 3.S1 Comparison of the properties determined for the synthetic Mn oxides used in this study with data reported in the literature.

Properties	synthetic birnessite	birnessite literature	synthetic manganite	manganite literature
SSA (m^2 g^{-1})	140	10.0–280; mostly ranging between 100–200[4–7]	28.5	8.90–75.0[8–10]
AOS (–)	3.68	3.42–3.96[5,11–13]	2.94	2.98–3.07[14,15]
PZC (–)	2.10	1.40–3.00[16]	6.65	6.20–8.50[17]

EEM spectroscopy

The calculations of the fluorescence indices were conducted as described below.

Biological index (BIX): An indicator for autotrophic productivity.[18] Low values (< 0.6) denote terrestrial DOM originated from low microbial activity.[19] The index was calculated at Ex = 310 nm following Huguet *et al.* (2009).[19]

$$\mathrm{BIX} = \frac{\mathrm{I(Ex = 310,\ Em = 380)}}{\mathrm{I(Ex = 310,\ Em = 430)}}$$

with

I = fluorescence intensity at each wavelength

Fluorescence index (FI): Values ranging from 1.4 to 1.9 represent contributions of terrestrial plants as well as microbial origin and are typical for natural waters.[18,20] The FI was calculated at Ex = 370 nm as proposed by McKnight *et al.* (2001).[21]

$$\mathrm{FI} = \frac{\mathrm{I(Ex = 370,\ Em = 450)}}{\mathrm{I(Ex = 370,\ Em = 500)}}$$

with

I = fluorescence intensity at each wavelength

Humification index (HIX): The HIX describes the degree of humification of soluble organic matter (Zsolnay *et al.* 1999).[22] A value > 0.9 is assumed to be more humified organic material rather than fresh input from plants.[18] HIX has been calculated at Ex = 254 nm according to Ohno (2002).[23]

$$HIX = \frac{\sum I_{435 \rightarrow 480}}{(\sum I_{300 \rightarrow 345} + \sum I_{435 \rightarrow 480})}$$

with

I = fluorescence intensity at each wavelength

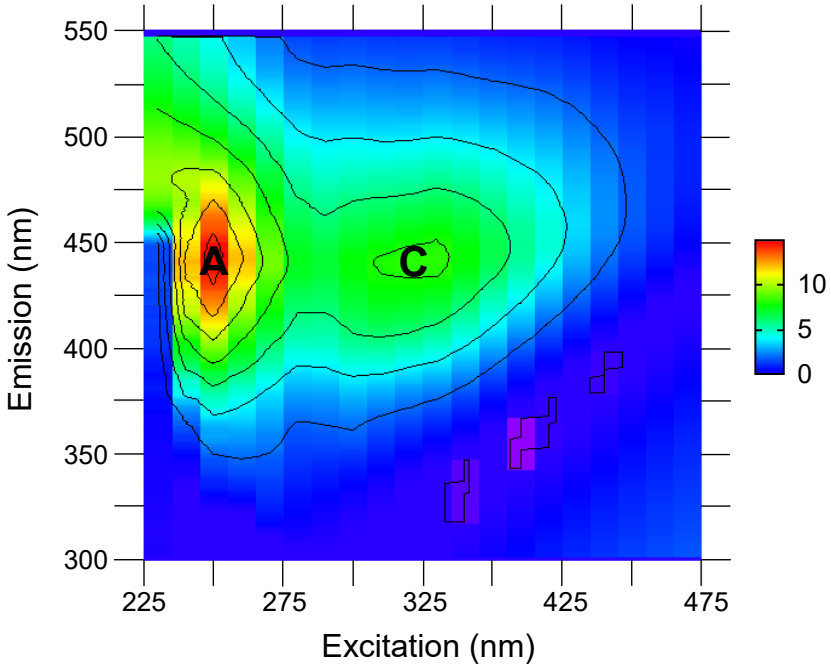

Figure 3.S4 EEM spectrum of the filtered (0.2 µm) DOM-stock solution with labeled Coble peaks (A and C).

Table 3.S2 Spectrophotometric speciation data including Mn_T, Mn^{2+}, Mn^{3+}–NOL complexes and k-values and ICP OES data (Mn_T) of the NOL–birnessite batch experiments.

pH (–)	time (h)	$Mn_{T(ICP)}$ Range (µmol L^{-1})	$Mn_{T(ICP)}$ Mean (µmol L^{-1})	$Mn_{NOL(ICP)}$ Range (µmol L^{-1})	$Mn_{NOL(ICP)}$ Mean (µmol L^{-1})	$Mn_{NOL(ICP)}$ Range (%)	$Mn_{NOL(ICP)}$ Mean (%)	$Mn_{T(Porph)}$ Range (µmol L^{-1})	$Mn_{T(Porph)}$ Mean (µmol L^{-1})
7	1	0.626–1.14	0.884±0.212	0.626–1.14	0.884±0.212	–	100±0	0.651–0.933	0.814±0.107
6	1	4.48–7.68	5.59±1.48	4.48–7.68	5.59±1.48	–	100±0	4.99–8.58	6.24±1.60
5	1	72.8–74.8	73.6±0.871	20.4–22.4	21.2±0.871	28.0–29.9	28.8±0.8	74.5–78.8	77.1±1.33
4	1	168–194	183±11.1	54.4–81.0	69.5±11.1	32.4–41.7	37.8±3.9	177–204	191±9.64
3	1	382–393	387±4.54	166–177	170±4.54	43.3–44.9	44.0±0.7	435–457	449±9.22
7	3	0.965–1.15	1.07±0.076	0.965–1.15	1.07±0.076	–	100±0	0.892–1.18	1.05±0.093
6	3	7.88–12.9	10.4±2.07	7.88–12.9	10.4±2.07	–	100±0	8.20–14.0	11.1±2.33
5	3	83.0–98.8	89.6±6.75	31.9–47.7	38.4±6.75	38.4–48.3	42.6±4.2	84.2–89.8	87.6±2.40
4	3	223–274	254±22.1	137–191	167±22.7	53.0–61.2	57.6±3.4	276–337	310±25.4
3	3	541–545	544±2.06	294–298	297±2.06	54.3–54.7	57.6±3.4	540–545	542±2.20
7	6	1.45–3.39	2.45±0.794	1.45–3.39	2.45±0.794	–	100±0	1.84–3.01	2.53±0.433
6	6	11.1–12.7	11.9±0.643	11.1–12.7	11.9±0.643	–	100±0	10.3–11.8	11.0±0.578
5	6	112–130	119±7.39	65.5–82.6	72.4±7.39	58.3–63.8	60.5±2.4	102–120	112±8.96
4	6	252–345	295±38.7	109–203	153±38.7	43.5–58.9	50.9±6.3	255–347	297±37.3
3	6	694–764	737±31.2	426–497	470±31.2	61.5–65.1	63.7±1.6	746–763	747±0.708
7	12	1.72–5.57	4.00±1.65	1.72–5.57	4.00±1.65	–	100±0	2.10–7.31	5.06±2.11
6	12	18.1–21.1	20.1±1.38	18.1–21.1	20.1±1.38	–	100±0	19.8–23.3	21.6±1.39
5	12	131–171	147±17.4	73.9–114	89.9±17.4	56.3–66.6	60.5±4.4	133–192	152±22.1
4	12	313–433	357±54.2	139–259	182±54.2	44.2–59.7	50.0±6.9	304–428	377±57.6
3	12	1331–1347	1340±7.02	705–938	855±106	68.3–74.1	72.1±2.7	1127–1313	1163±56.9
7	24	2.13–2.42	2.32±0.133	2.13–2.42	2.32±0.133	–	100±0	2.36–3.01	2.73±0.221
6	24	60.2–80.3	73.4±9.31	60.2–80.3	73.4±9.31	–	100±0	63.3–86.3	77.7±10.6
5	24	201–267	242±29.4	135–201	176±29.4	67.1–75.3	72.2±3.7	202–167	246±25.9
4	24	599–624	612±10.4	405–430	418±10.4	67.6–68.9	68.3±0.5	575–601	588±7.48
3	24	1127–1210	1173±34.9	827–911	874±34.9	73.4–75.2	74.4±0.8	1050–1323	1180±79.9
7	48	4.37–5.17	4.70±0.340	4.37–5.17	4.70±0.340	–	100±0	4.32–5.36	4.89±0.360
6	48	30.3–35.0	32.6±1.90	30.3–35.0	32.6±1.90	–	100±0	29.6–34.4	32.4±1.81
5	48	275–329	310±24.8	194–248	229±24.8	70.4–75.2	73.6±2.2	283–337	314±19.5
4	48	613–617	615±1.72	437–440	438±1.72	71.2–71.4	71.2±0.1	568–590	585±7.19
3	48	1198–1449	1282±118	783–1034	867±118	65.3–71.4	71.2±0.1	1190–1466	1281±121
7	168	5.39–8.74	7.49±1.50	5.39–8.74	7.49±1.50	–	100±0	5.69–8.78	7.09±1.25
6	168	85.0–93.7	88.7±3.69	85.0–93.7	88.7±3.69	–	100±0	80.4–96.9	88.3±4.49
5	168	391–471	425±33.9	335–416	369±33.9	85.7–88.1	86.8±1.0	371–407	387±14.7
4	168	888–899	894±4.46	655–666	661±4.46	73.8–74.1	73.9±0.1	890–925	911±11.4
3	168	1269–1518	1418±108	750–999	899±108	59.1–65.8	63.2±2.9	1420–1519	1496±35.5

Table 3.S2 (continued)

pH (–)	time (h)	Mn^{2+} Range (µmol L^{-1})	Mn^{2+} Mean (µmol L^{-1})	Mn^{2+} Range (%)	Mn^{2+} Mean (%)	Mn^{3+}–NOL_{weak} Range (µmol L^{-1})	Mn^{3+}–NOL_{weak} Mean (µmol L^{-1})	Mn^{3+}–NOL_{weak} Range (%)	Mn^{3+}–NOL_{weak} Mean (%)
7	1	0.059–0.412	0.814±0.107	8.0–63.2	24.7±17.8	0.197–0.776	0.564±0.161	30.2–83.2	68.5±16.0
6	1	0.814–5.97	2.24±1.58	15.6–69.6	33.7±17.3	2.09–5.89	3.70±1.13	25.7–84.4	61.4±17.5
5	1	47.1–78.5	73.0±9.21	59.9–100	94.5±12.3	0–30.8	34.2±9.67	0–39.1	4.3±12.3
4	1	15.1–175	86.2±58.1	7.4–91.1	46.1±31.6	17.2–181	102±61.6	8.9–88.9	52.7±30.8
3	1	2.18–139	67.1±44.9	0.5–31.6	15.1±10.2	301–430	363±41.1	68.4–94.2	80.9±8.3
7	3	0.182–0.400	0.293±0.065	15.4–36.4	28.4±7.0	0.510–0.801	0.669±0.107	52.7–77.2	63.8±7.0
6	3	0.910–5.11	2.50±1.33	11.1–46.2	21.7±10.3	5.73–10.9	7.85±1.89	51.9–78.4	70.8±7.4
5	3	68.9–84.6	77.8±6.58	76.7–95.4	89.0±8.7	0–7.13	3.24±2.95	0–7.9	3.7±3.3
4	3	45.9–153	93.1±34.3	14.1–46.6	29.8±9.8	170–272	212±33.8	51.7–83.4	68.6±9.9
3	3	326–335	331±3.74	60.3–62.0	61.0±0.7	191–193	192±1.13	35.1–35.8	35.4±0.3
7	6	0.506–1.16	0.819±0.241	19.8–38.7	32.5±7.7	0.977–1.85	1.19±0.630	49.5–66.0	57.5±6.5
6	6	1.96–5.64	3.17±1.29	18.7–54.0	29.2±12.7	4.81–9.10	7.28±1.51	46.0–80.0	66.5±12.6
5	6	96.7–116	105±8.25	84.1–96.5	93.6±3.7	1.12–2.60	1.65±0.428	0.9–2.5	1.5±0.4
4	6	81.5–169	118±31.2	31.9–48.8	39.2±5.7	161–195	178±11.4	51.2–68.1	60.6±5.6
3	6	330–429	386±26.4	44.1–56.8	51.3±3.5	316–418	358±26.4	41.8–55.9	47.6±3.6
7	12	0.205–2.98	1.44±0.944	9.4–48.2	26.5±11.8	0.850–4.68	2.32±1.44	13.7–80.1	51.3±24.4
6	12	8.50–10.0	9.19±0.449	41.1–45.0	42.2±2.0	10.3–13.3	21.1±1.05	52.0–57.7	55.5±1.8
5	12	11.5–29.8	21.1±5.65	8.2–19.3	14.1±3.0	112–150	125±14.1	78.0–91.8	84.3±4.0
4	12	304–428	377±57.6	–	100±0	n.d.	n.d.	n.d.	n.d.
3	12	1127–1313	1163±56.9	–	100±0	n.d.	n.d.	n.d.	n.d.
7	24	0.045–0.645	0.351±0.316	1.8–33.2	12.6±11.3	1.42–2.48	2.10±0.360	51.8–98.2	77.8±16.2
6	24	12.7–81.0	44.2±27.5	15.1–96.4	54.7±29.9	0–71.2	31.5±23.1	0–84.9	42.5±30.1
5	24	22.9–135	77.6±36.5	9.0–50.6	31.1±13.4	122–226	167±32.4	49.4–88.7	68.1±13.1
4	24	575–601	588±7.48	–	100±0	n.d.	n.d.	n.d.	n.d.
3	24	1050–1323	1180±79.9	–	100±0	n.d.	n.d.	n.d.	n.d.
7	48	0.319–2.55	1.29±0.675	6.6–47.6	25.9±12.1	2.71–3.88	3.22±0.338	52.4–79.8	66.0±7.4
6	48	10.2–21.5	16.3±3.01	31.0–63.5	50.4±10.1	10.8–22.7	16.0±2.64	36.5–69.0	49.0±9.8
5	48	117–224	182±34.9	41.2–75.9	57.9±10.0	71.3–167	129±28.5	24.1–58.8	41.3±9.9
4	48	568–590	585±7.19	–	100±0	n.d.	n.d.	n.d.	n.d.
3	48	1093–1417	1216±129	91.8–96.7	94.9±1.6	48.9–98.3	64.7±16.5	3.3–8.2	5.1±1.6
7	168	0.622–2.23	1.58±0.504	10.9–33.8	22.1±5.9	3.67–6.83	5.17±1.13	55.6–87.4	72.9±8.5
6	168	47.8–74.3	61.3±9.75	52.0–84.3	69.4±10.2	13.5–44.2	27.0±9.14	15.7–48.0	30.6±10.2
5	168	224–305	252±26.6	58.0–74.9	64.9±5.0	102–143	129±12.5	25.1–38.3	33.6±3.8
4	168	890–925	911±11.4	–	100±0	n.d.	n.d.	n.d.	n.d.
3	168	1420–1519	1496±35.5	–	100±0	n.d.	n.d.	n.d.	n.d.

Table 3.S2 (continued)

pH (–)	time (h)	Mn^{3+}–NOL_{strong} Range (µmol L^{-1})	Mn^{3+}–NOL_{strong} Mean (µmol L^{-1})	Mn^{3+}–NOL_{strong} Range (%)	Mn^{3+}–NOL_{strong} Mean (%)
7	1	0–0.097	0.055±0.034	0–14.1	6.8±4.4
6	1	0–0.435	0.299±0.136	0–8.5	4.9±2.4
5	1	0.018–1.58	0.910±0.528	0–2.0	1.2±0.7
4	1	0–3.73	2.33±2.43	0–3.7	1.2±1.2
3	1	0–41.4	18.3±16.1	0–9.1	4.0±3.5
7	3	0.019–0.237	0.083±0.064	1.7–20.0	7.8±5.4
6	3	0.211–1.19	0.744±0.335	1.9–14.5	7.5±4.8
5	3	1.72–13.8	6.51±5.21	2.0–15.3	7.3±5.8
4	3	0–8.11	4.86±3.03	0–2.6	1.6±1.0
3	3	12.2–23.3	19.3±5.03	2.3–4.3	3.6±0.9
7	6	0–2.73	0.248±0.185	8.1–17.5	10.0±6.7
6	6	0.004–0.855	0.476±0.313	0–7.9	4.3±2.8
5	6	2.47–17.9	5.73±4.85	2.1–15.0	5.0±4.0
4	6	0–2.26	0.377±0.753	0–0.8	0.1±0.3
3	6	0–1.12	8.53±5.76	0–2.6	1.1±0.8
7	12	0.207–3.24	1.31±1.16	4.5–47.0	22.2±15.4
6	12	0.182–0.801	0.512±0.190	0.9–3.5	2.3±0.8
5	12	0–16.3	2.82±5.27	0–8.5	1.6±2.8
4	12	n.d.	n.d.	n.d.	n.d.
3	12	n.d.	n.d.	n.d.	n.d.
7	24	0–0.502	0.276±0.200	0–16.7	9.6±6.9
6	24	0–4.91	2.04±1.40	0–7.9	2.8±2.2
5	24	0–6.37	1.89±2.46	0–2.5	0.7±1.0
4	24	n.d.	n.d.	n.d.	n.d.
3	24	n.d.	n.d.	n.d.	n.d.
7	48	0–0.730	0.385±0.287	0–14.8	8.1±6.0
6	48	0–0.889	0.190±0.299	0–2.7	0.6±0.9
5	48	0–16.4	2.52±5.27	0–4.9	0.8±1.6
4	48	n.d.	n.d.	n.d.	n.d.
3	48	n.d.	n.d.	n.d.	n.d.
7	168	0–0.991	0.340±0.402	0–14.4	5.0±5.9
6	168	n.d.	n.d.	n.d.	n.d.
5	168	0–23.9	5.63±8.70	0–6.2	1.5±2.3
4	168	n.d.	n.d.	n.d.	n.d.
3	168	n.d.	n.d.	n.d.	n.d.

Table 3.S2 (continued)

pH (–)	time (h)	k_1 Range (s^{-1})	k_1 Mean (s^{-1})	k_2 Range (s^{-1})	k_2 Mean (s^{-1})
7	1	0.0178–0.0860	0.0378±0.0216	0.0089–0.0134	0.0117±0.0013
6	1	0.0336–0.0485	0.0419±0.0056	0.0020–0.0178	0.0134±0.0047
5	1	0.0432–0.0635	0.0529±0.0061	0.0191–0.0191	0.0191±0.0000
4	1	0.0425–0.1582	0.0867±0.0381	0.0164–0.0309	0.0276±0.0047
3	1	0.0394–0.1199	0.0916±0.0319	0.0055–0.0397	0.0267±0.0114
7	3	0.0606–0.0820	0.0666±0.0066	0.0035–0.0158	0.0099±0.0041
6	3	0.0337–0.0636	0.0437±0.0100	0.0109–0.0160	0.0135±0.0019
5	3	0.0374–0.0466	0.0420±0.0201	0.0125–0.0127	0.0126±0.0001
4	3	0.0361–0.0882	0.0584±0.0157	0.0111–0.0250	0.0177±0.0039
3	3	0.0445–0.0471	0.0459±0.0010	0.0114–0.0116	0.0115±0.0001
7	6	0.0267–0.0458	0.0316±0.0078	0.0075–0.0136	0.0103±0.0028
6	6	0.0333–0.0711	0.0527±0.0148	0.0097–0.0167	0.0147±0.0022
5	6	0.0424–0.0526	0.0469±0.0033	0.0141–0.0175	0.0156±0.0011
4	6	0.0576–0.0874	0.0679±0.0081	0.0181–0.0278	0.0227±0.0033
3	6	0.0618–0.0874	0.0723±0.0081	0.0176–0.0222	0.0194±0.0014
7	12	0.0167–0.0442	0.0267±0.0088	0.0037–0.0148	0.0090±0.0032
6	12	0.0534–0.0789	0.0659±0.0089	0.0089–0.0245	0.0175±0.0052
5	12	0.0928–0.1240	0.1132±0.0097	0.0333–0.0393	0.0365±0.0019
4	12	0.0398–0.0487	0.0435±0.0030	n.d.	n.d.
3	12	0.0461–0.0515	0.0489±0.0016	n.d.	n.d.
7	24	0.0430–0.0918	0.0613±0.0223	0.0156–0.0201	0.0185±0.0016
6	24	0.0539–0.1368	0.0790±0.0263	0.0167–0.0453	0.0263±0.0095
5	24	0.0500–0.0896	0.0651±0.0137	0.0115–0.0291	0.0200±0.0058
4	24	0.0269–0.0302	0.0280±0.0010	n.d.	n.d.
3	24	0.0626–0.0729	0.0676±0.0030	n.d.	n.d.
7	48	0.0246–0.0330	0.0273±0.0028	0.0042–0.0146	0.0092±0.0028
6	48	0.0276–0.0790	0.0358±0.0155	0.0070–0.0097	0.0085±0.0009
5	48	0.0390–0.0808	0.0646±0.0138	0.0121–0.0260	0.0192±0.0041
4	48	0.0220–0.0357	0.0284±0.0036	n.d.	n.d.
3	48	0.0746–0.1115	0.0925±0.0114	0.0097–0.0196	0.0134±0.0030
7	168	0.0230–0.0354	0.0279±0.0043	0.0074–0.0111	0.0093±0.0014
6	168	0.0238–0.0402	0.0286±0.0053	0.0045–0.0138	0.0091±0.0034
5	168	0.0437–0.0526	0.0499±0.0028	0.0122–0.0167	0.0141±0.0016
4	168	0.0489–0.0569	0.0516±0.0025	n.d.	n.d.
3	168	0.0458–0.0509	0.0477±0.0016	n.d.	n.d.

Table 3.S3 Spectrophotometric speciation data including Mn_T, Mn^{2+}, Mn^{3+} and k-values and ICP OES data (Mn_T) of the NOL–manganite batch experiments.

pH (–)	time (h)	$Mn_{T(ICP)}$ Range (µmol L^{-1})	$Mn_{T(ICP)}$ Mean (µmol L^{-1})	$Mn_{NOL(ICP)}$ Range (µmol L^{-1})	$Mn_{NOL(ICP)}$ Mean (µmol L^{-1})	$Mn_{NOL(ICP)}$ Range (%)	$Mn_{NOL(ICP)}$ Mean (%)	$Mn_{T(Porph)}$ Range (µmol L^{-1})	$Mn_{T(Porph)}$ Mean (µmol L^{-1})
7	1	12.7–14.3	13.6±0.675	12.7–14.3	13.6±0.675	–	100±0	12.1–13.5	13.0±0.480
6	1	37.3–49.5	41.4±5.75	37.3–49.5	41.4±5.75	–	100±0	36.8–48.0	43.2±4.31
5	1	123–142	131±8.04	18.4–37.5	26.6±8.04	14.9–26.4	20.0±4.8	125–142	131±6.25
4	1	269–280	275±4.84	84.1–95.6	90.7±4.84	31.3–34.1	32.9±1.2	266–270	267±1.13
3	1	309–353	332±17.9	47.1–90.8	70.2±17.9	15.2–25.7	20.9±4.3	339–368	356±11.8
7	3	16.3–18.5	17.4±0.922	16.3–18.5	17.4±0.922	–	100±0	19.3–22.2	20.3±0.955
6	3	44.4–57.9	49.0±6.31	44.4–57.9	49.0±6.31	–	100±0	43.9–59.5	50.7±6.09
5	3	202–210	207±2.45	72.8–80.5	77.7±3.45	36.1–38.4	37.6±1.1	206–214	210±2.50
4	3	329–353	344±10.5	120–143	134±10.5	36.3–40.5	39.0±1.9	330–349	343±6.94
3	3	488–530	510±17.2	179–221	202±17.2	36.7–41.7	39.4±2.1	506–529	516±9.71
7	6	16.5–19.8	17.9±1.40	16.5–19.8	17.9±1.40	–	100±0	16.3–21.2	18.1±2.14
6	6	51.5–57.5	54.8±2.48	51.5–57.5	54.8±2.48	–	100±0	54.6–54.9	58.4±2.61
5	6	179–289	225±47.1	30.8–141	76.3±47.1	17.2–48.7	31.2±13.1	199–301	242±42.2
4	6	320–335	326±6.19	113–127	119±6.19	35.2–38.0	36.4±1.2	333–353	339±5.66
3	6	450–541	502±38.6	113–204	166±38.6	25.1–37.7	32.6±5.4	441–443	496±38.3
7	12	15.9–21.5	19.3±2.44	15.9–21.5	19.3±2.44	–	100±0	13.8–20.8	18.3±3.16
6	12	85.0–90.3	86.9±2.41	85.0–90.3	86.9±2.41	–	100±0	83.5–92.2	87.1±3.52
5	12	293–317	306±9.96	137–161	150±10.0	46.6–50.7	48.9±1.7	292–319	303±8.29
4	12	395–440	420±19.0	143–189	169±19.0	36.3–42.9	40.0±2.8	418–473	444±21.2
3	12	755–794	772±16.1	348–386	364±16.1	46.0–48.6	47.1±1.1	827–830	842±11.5
7	24	22.3–29.5	27.1±3.41	22.3–29.5	27.1±3.41	–	100±0	23.2–29.2	26.7±2.52
6	24	85.4–110	99.0±10.3	85.4–110	99.0±10.3	–	100±0	91.7–118	105±10.4
5	24	293–317	306±9.75	116–140	129±9.75	39.6–44.1	42.0±1.9	294–312	303±7.00
4	24	411–499	443±39.6	141–228	172±39.6	34.2–45.7	38.4±5.2	404–489	445±32.5
3	24	854–916	893±28.0	333–395	373±28.0	39.0–43.1	41.7±1.9	902–947	934±28.5
7	48	24.2–31.1	28.3±2.98	24.2–31.1	28.3±2.98	–	100±0	24.9–31.4	28.9±2.78
6	48	124–144	132±8.37	124–144	132±8.37	–	100±0	132–149	139±7.16
5	48	293–302	296±3.76	131–140	135±3.76	44.7–46.3	45.4±0.7	315–327	321±5.73
4	48	519–641	598±55.9	176–298	255±55.9	34.0–46.6	42.2±5.8	513–663	589±54.5
3	48	1247–1436	1338±77.4	539–593	567±22.4	42.5–44.9	43.8±1.0	1320–1337	1331±5.13
7	168	33.6–42.2	37.1±3.68	33.6–42.2	37.1±3.68	–	100±0	39.2–43.9	41.4±1.54
6	168	156–166	162±4.15	156–166	162±4.15	–	100±0	162–172	167±3.59
5	168	384–501	450±48.8	166–282	232±48.8	43.1–56.4	50.9±5.6	380–381	381±0.485
4	168	775–892	823±49.7	291–408	339±49.7	37.6–45.7	41.0±3.5	747–777	766±13.2
3	168	1201–1487	1315±124	439–724	553±124	36.5–48.7	41.5±5.2	1154–1456	1278±109

Table 3.S3 (continued)

pH (–)	time (h)	Mn^{2+} Range (µmol L^{-1})	Mn^{2+} Mean (µmol L^{-1})	Mn^{2+} Range (%)	Mn^{2+} Mean (%)	Mn^{3+}–NOL_{weak} Range (µmol L^{-1})	Mn^{3+}–NOL_{weak} Mean (µmol L^{-1})	Mn^{3+}–NOL_{weak} Range (%)	Mn^{3+}–NOL_{weak} Mean (%)
7	1	8.74–12.4	11.4±1.17	74.3–98.1	87.2±8.4	0–2.79	0.719±1.00	0–23.1	5.6±8.0
6	1	29.4–35.8	33.7±1.87	61.2–89.1	78.9±8.4	0–4.19	0.570±1.29	0–8.7	1.2±2.7
5	1	110–132	121±8.05	86.0–95.9	92.3±3.3	n.d.	n.d.	n.d.	n.d.
4	1	171–266	220±36.0	64.0–99.5	82.3±13.6	0–96.5	44.4±37.9	0–36.0	16.6±14.1
3	1	132–185	153±15.2	35.8–50.4	43.0±3.9	173–223	199±14.4	47.1–60.6	55.8±4.1
7	3	11.5–12.9	12.1±0.580	54.4–65.9	59.8±4.2	n.d.	n.d.	n.d.	n.d.
6	3	37.0–54.4	45.3±6.75	76.2–100	89.1±6.2	n.d.	n.d.	n.d.	n.d.
5	3	198–214	207±5.46	95.6–100	98.4±1.5	n.d.	n.d.	n.d.	n.d.
4	3	185–265	210±22.4	53.0–76.1	61.2±6.6	79–153	129±21.6	22.7–43.8	37.8±6.1
3	3	450–506	474±23.7	85.0–100	91.9±6.2	0–79.5	42.1±32.6	0–15.0	8.1±6.2
7	6	8.43–13.5	10.9±1.74	40.0–82.3	61.4±13.8	1.40–6.67	3.97±1.72	8.5–39.5	22.0±9.8
6	6	49.2–56.6	52.1±2.53	81.4–100	89.4±7.5	0–2.91	0.323±0.915	0–4.8	0.5±1.5
5	6	195–242	220±19.2	80.3–99.3	92.3±8.3	n.d.	n.d.	n.d.	n.d.
4	6	333–353	339±5.66	–	100±0	n.d.	n.d.	n.d.	n.d.
3	6	441–443	496±38.3	–	100±0	n.d.	n.d.	n.d.	n.d.
7	12	1.87–11.7	5.64±2.83	9.0–56.2	30.6±12.9	7.27–17.4	11.4±3.03	34.9–83.9	62.8±13.7
6	12	80.7–84.6	82.9±1.42	89.6–100	95.3±3.4	n.d.	n.d.	n.d.	n.d.
5	12	283–319	300±11.3	96.4–100	98.9±1.3	n.d.	n.d.	n.d.	n.d.
4	12	418–473	440±20.9	95.0–100	99.1±1.8	n.d.	n.d.	n.d.	n.d.
3	12	827–830	842±11.5	–	100±0	n.d.	n.d.	n.d.	n.d.
7	24	4.89–10.7	9.03±1.64	17.0–41.7	34.1±6.7	9.41–14.7	11.4±1.76	33.8–57.8	43.3±9.3
6	24	81.7–105	91.5±8.86	77.3–99.0	87.6±8.1	0–8.31	1.29±2.69	0–7.1	1.2±2.4
5	24	290–306	299±5.81	96.5–99.5	98.4±1.1	n.d.	n.d.	n.d.	n.d.
4	24	409–489	444±32.7	98.3–100	99.8±0.5	0–7.71	0.857±2.42	0–1.7	0.2±0.5
3	24	902–947	934±28.5	–	100±0	n.d.	n.d.	n.d.	n.d.
7	48	6.37–12.9	10.2±2.24	25.5–41.6	35.0±5.2	11.1–17.3	14.8±2.02	44.5–56.8	51.0±3.8
6	48	122–132	127±2.62	83.3–98.3	91.3±4.7	n.d.	n.d.	n.d.	n.d.
5	48	315–327	321±5.73	–	100±0	n.d.	n.d.	n.d.	n.d.
4	48	513–663	580±54.4	94.0–100	98.5±2.1	n.d.	n.d.	n.d.	n.d.
3	48	1320–1337	1331±5.13	–	100±0	n.d.	n.d.	n.d.	n.d.
7	168	25.5–28.7	27.3±1.02	59.3–71.5	66.0±4.5	n.d.	n.d.	n.d.	n.d.
6	168	156–169	162±3.91	94.1–98.0	97.0±1.1	n.d.	n.d.	n.d.	n.d.
5	168	374–381	378±3.11	98.4–100	99.4±0.7	n.d.	n.d.	n.d.	n.d.
4	168	747–777	766±13.2	–	100±0	n.d.	n.d.	n.d.	n.d.
3	168	1154–1456	1278±109	99.5–100	99.9±0.1	n.d.	n.d.	n.d.	n.d.

Table 3.S3 (continued)

pH (–)	time (h)	Mn^{3+}–NOL_{strong} Range (µmol L^{-1})	Mn^{3+}–NOL_{strong} Mean (µmol L^{-1})	Mn^{3+}–NOL_{strong} Range (%)	Mn^{3+}–NOL_{strong} Mean (%)
7	1	0.240–1.50	0.948±0.389	1.9–11.1	7.2±2.8
6	1	3.77–14.4	8.90±2.63	10.2–30.0	19.9±6.7
5	1	5.15–17.9	10.1±4.08	4.1–14.0	7.7±3.3
4	1	0–8.91	2.99±3.39	0–3.3	1.1±1.3
3	1	0–15.7	4.23±6.18	0–4.3	1.2±1.7
7	3	6.58–10.1	8.2±1.18	34.1–45.6	40.2±4.2
6	3	0–11.8	5.45±2.93	0–23.8	10.9±6.2
5	3	0–9.17	3.38±3.12	0–4.4	1.6±1.5
4	3	0–11.8	3.39±4.45	0–3.4	1.0±1.3
3	3	n.d.	n.d.	n.d.	n.d.
7	6	1.22–6.98	3.25±2.48	7.5–32.9	16.6±10.8
6	6	0–10.6	6.04±4.29	1.4–17.4	10.1±7.0
5	6	1.68–59.5	21.9±25.6	0.7–19.7	7.7±8.3
4	6	n.d.	n.d.	n.d.	n.d.
3	6	n.d.	n.d.	n.d.	n.d.
7	12	0.150–2.04	1.29±0.710	1.1–10.0	6.6±3.2
6	12	0–9.67	4.21±3.12	0–10.4	4.7±3.4
5	12	0–10.4	3.18±3.70	0–3.6	1.1±1.3
4	12	0–22.7	4.19±8.04	0–5.0	0.9±1.8
3	12	n.d.	n.d.	n.d.	n.d.
7	24	1.58–9.25	6.29±3.25	6.8–32.1	22.6±10.7
6	24	0.495–24.0	12.1±8.95	0.5–22.7	11.2±8.5
5	24	1.44–11.0	4.84±3.39	0.5–3.5	1.6±1.1
4	24	n.d.	n.d.	n.d.	n.d.
3	24	n.d.	n.d.	n.d.	n.d.
7	48	2.19–5.64	3.90±1.32	7.2–22.5	14.0±5.9
6	48	2.34–25.0	12.4±7.29	1.7–16.7	8.7±4.7
5	48	n.d.	n.d.	n.d.	n.d.
4	48	0–35.3	9.21±12.7	0–6.0	1.5±2.1
3	48	n.d.	n.d.	n.d.	n.d.
7	168	11.2–17.7	14.1±2.39	28.5–40.7	34.0±4.5
6	168	3.38–10.1	5.05±1.96	2.0–5.9	3.0±1.1
5	168	0–6.11	2.19±2.78	0–1.6	0.6±0.7
4	168	n.d.	n.d.	n.d.	n.d.
3	168	0–6.40	213±3.02	0–0.5	0.1±0.1

Table 3.S3 (continued)

pH (–)	time (h)	k_1 range (s^{-1})	k_1 mean (s^{-1})	k_2 range (s^{-1})	k_2 mean (s^{-1})
7	1	0.0276–0.0462	0.0337±0.0064	0.0038–0.0135	0.0086±0.0040
6	1	0.0629–0.0979	0.0776±0.0107	0.0030–0.0280	0.0125±0.0110
5	1	0.0453–0.0548	0.0502±0.0029	n.d.	n.d.
4	1	0.0428–0.0906	0.0596±0.0146	0.0148–0.0268	0.0196±0.0042
3	1	0.0671–0.0894	0.0783±0.0063	0.0204–0.0251	0.0204±0.0015
7	3	0.0518–0.1017	0.0804±0.0154	n.d.	n.d.
6	3	0.0613–0.0781	0.0718±0.0046	n.d.	n.d.
5	3	0.0494–0.0533	0.0514±0.0015	n.d.	n.d.
4	3	0.521–0.1125	0.0813±0.0168	0.0155–0.0326	0.0267±0.0046
3	3	0.0499–0.0620	0.0562±0.0050	0.0152–0.0160	0.0156±0.0004
7	6	0.0338–0.1068	0.0502±0.0206	0.0067–0.0302	0.0167±0.0063
6	6	0.0625–0.0706	0.0657±0.0026	0.0012–0.0012	0.0012±0
5	6	0.0507–0.0614	0.0541±0.0029	n.d.	n.d.
4	6	0.0406–0.0469	0.0438±0.0021	n.d.	n.d.
3	6	0.0613–0.0815	0.0690±0.0059	n.d.	n.d.
7	12	0.0342–0.1381	0.0912±0.0362	0.0059–0.0284	0.0208±0.0062
6	12	0.0719–0.0766	0.0740±0.0018	n.d.	n.d.
5	12	0.0618–0.1016	0.0741±0.0127	n.d.	n.d.
4	12	0.0557–0.0690	0.0646±0.0037	n.d.	n.d.
3	12	0.0548–0.0715	0.0604±0.0050	n.d.	n.d.
7	24	0.0344–0.0637	0.0457±0.0076	0.0105–0.0211	0.0148±0.0026
6	24	0.0531–0.0616	0.0574±0.0029	0.0137–0.0142	0.0140±0.0003
5	24	0.0378–0.0427	0.0400±0.0013	n.d.	n.d.
4	24	0.0469–0.0628	0.0552±0.0052	0.0033–0.0033	0.0033±0.0000
3	24	0.0371–0.0593	0.0458±0.0064	n.d.	n.d.
7	48	0.0374–0.0537	0.0435±0.0058	0.0106–0.0169	0.0136±0.0023
6	48	0.0462–0.0827	0.0527±0.0107	n.d.	n.d.
5	48	0.0523–0.0657	0.0572±0.0041	n.d.	n.d.
4	48	0.0541–0.0796	0.0647±0.0077	n.d.	n.d.
3	48	0.0356–0.0500	0.0402±0.0041	n.d.	n.d.
7	168	0.0612–0.0749	0.0663±0.0035	n.d.	n.d.
6	168	0.0514–0.0552	0.0533±0.0011	n.d.	n.d.
5	168	0.0259–0.0352	0.0297±0.0028	n.d.	n.d.
4	168	0.0293–0.0391	0.0347±0.0041	n.d.	n.d.
3	168	0.0389–0.0553	0.0472±0.0055	n.d.	n.d.

Table 3.S4 Characterization of the DOM-batch solutions (NOL–birnessite interactions) after batch operation.

pH (–)	time (h)	DOC Range (mmol L^{-1})	DOC Mean (mmol L^{-1})	$Mn_{T(ICP)}$:DOC (–)	DOC_{loss} Range (%)	DOC_{loss} Mean (%)
7	1	3.46–3.90	3.66±0.182	0.0002	0.2–11.5	6.3±4.7
6	1	3.45–3.64	3.51±0.090	0.0016	6.8–11.7	10.0±2.3
5	1	3.31–3.56	3.47±0.117	0.0212	8.7–15.4	11.1±3.0
4	1	3.22–3.60	3.43±0.158	0.0534	7.7–17.5	12.1±4.0
3	1	2.64–3.17	2.85±0.227	0.1358	18.9–32.3	27.0±5.8
7	3	3.67–3.81	3.74±0.055	0.0003	2.6–6.0	4.3±1.4
6	3	3.38–3.85	3.64±0.192	0.0029	1.5–13.3	6.9±4.9
5	3	3.48–3.80	3.61±0.134	0.0248	2.6–10.8	7.3±3.4
4	3	3.12–3.20	3.17±0.035	0.0801	18.1–20.0	18.8±0.9
3	3	2.58–2.87	2.73±0.119	0.1993	26.4–33.9	30.1±3.0
7	6	3.57–3.76	3.66±0.075	0.0007	3.8–8.5	6.2±1.9
6	6	3.56–3.67	3.61±0.045	0.0033	6.0–8.7	7.5±1.2
5	6	3.45–3.49	3.47±0.017	0.0343	10.7–11.7	11.2±0.4
4	6	3.42–3.43	3.42±0.004	0.0863	12.2–12.4	12.3±0.1
3	6	2.52–2.76	2.66±0.102	0.2771	29.4–35.4	31.8±2.6
7	12	3.32–3.96	3.55±0.293	0.0011	0–14.9	9.6±6.8
6	12	3.71–3.86	3.81±0.071	0.0053	1.1–4.9	2.3±1.8
5	12	3.60–3.87	3.75±0.114	0.0392	0.9–7.9	4.0±2.9
4	12	3.46–3.60	3.53±0.054	0.1011	7.9–11.3	9.6±1.4
3	12	2.62–2.69	2.66±0.027	0.5038	31.1–32.8	32.0±0.7
7	24	3.49–3.75	3.59±0.114	0.0006	4.0–10.6	8.2±2.9
6	24	3.57–3.62	3.60±0.020	0.0204	7.2–8.5	7.8±0.5
5	24	3.50–3.66	3.56±0.070	0.0680	6.3–10.4	8.8±1.8
4	24	3.04–3.32	3.19±0.115	0.1918	15.0–22.2	18.4±2.9
3	24	2.76–2.95	2.81±0.091	0.4174	24.5–29.5	27.8±2.3
7	48	3.56–3.75	3.65±0.077	0.0013	4.0–8.8	6.5±2.0
6	48	2.48–3.87	3.40±0.654	0.0096	0.9–36.6	12.9±16.8
5	48	3.65–3.88	3.75±0.092	0.0827	0.8–6.4	3.9±2.4
4	48	3.11–3.16	3.13±0.018	0.1965	19.2–20.3	19.8±0.5
3	48	2.81–3.08	2.96±0.117	0.4331	21.2–28.2	24.0±3.0
7	168	3.46–3.64	3.52±0.082	0.0021	6.8–11.3	9.8±2.1
6	168	2.65–2.80	2.74±0.067	0.0324	28.4–32.2	29.8±1.7
5	168	2.54–2.80	2.66±0.106	0.1598	28.4–35.0	31.9±2.7
4	168	2.32–2.51	2.41±0.080	0.3710	35.6–40.5	38.4±2.1
3	168	2.47–2.83	2.62±0.153	0.5412	27.5–36.7	32.9±3.9

Table 3.S4 (continued)

pH	time	MA_{254} Range	MA_{254} Mean	MA_{280} Range	MA_{280} Mean	MA_{350} Range	MA_{350} Mean
(–)	(h)	(L mg^{-1}-C m^{-1})	(L mg^{-1}-C m^{-1})	(L mg^{-1}-C m^{-1})	(L mg^{-1}-C m^{-1})	(L mg^{-1}-C m^{-1})	(L mg^{-1}-C m^{-1})
7	1	444–526	478±34.8	255–297	271±18.5	75.2–94.2	81.8±8.76
6	1	489–499	493±4.40	267–279	275±5.41	84.2–88.6	86.9±1.92
5	1	451–461	456±5.21	270–281	275±5.64	81.4–82.2	81.8±0.392
4	1	447–464	456±8.64	299–316	307±8.46	83.8–86.2	85.0±1.17
3	1	472–525	506±24.2	334–368	354±14.8	75.8–94.2	86.0±7.67
7	3	460–511	484±20.9	317–335	329±8.25	88.6–96.0	93.0±3.14
6	3	447–486	462±17.4	252–274	260±10.1	78.2–91.1	84.2±5.28
5	3	441–457	450±6.78	278–284	281±2.55	77.7–85.1	82.2±3.23
4	3	421–465	444±18.0	231–281	261±19.1	77.6–85.2	82.6±3.57
3	3	304–344	329±18.0	161–180	173±8.01	55.7–71.2	64.2±6.42
7	6	422–491	466±31.1	191–212	201±8.81	76.0–82.3	79.9±2.81
6	6	491–538	507±21.7	268–310	283±19.0	102–105	103±1.40
5	6	472–532	497±25.5	289–341	309±22.7	93.2–116	104±9.32
4	6	327–395	361±27.7	202–256	225±22.5	75.5–89.3	82.7±5.65
3	6	452–495	465±20.9	199–233	212±15.5	70.7–80.2	74.0±4.36
7	12	456–548	517±43.0	254–314	294±28.0	88.4–115	105±11.7
6	12	478–492	486±6.09	274–284	280±4.52	89.8–101	94.8±4.53
5	12	445–488	461±19.3	269–311	284±18.9	83.5–103	91.2±8.43
4	12	439–481	455±18.2	294–325	305±14.1	66.7–79.9	75.0±5.85
3	12	490–570	532±32.8	322–390	357±27.9	64.3–73.5	68.7±3.75
7	24	470–504	490±14.4	264–278	272±5.94	90.7–96.4	94.3±2.61
6	24	458–474	465±6.65	254–264	259±4.26	82.2–87.3	84.1±2.27
5	24	427–481	448±23.6	245–301	266±24.7	69.5–84.9	75.7±1.55
4	24	396–430	410±14.5	243–278	261±14.2	54.2–60.2	57.9±2.68
3	24	388–454	425±27.8	238–297	272±25.3	52.8–58.2	55.0±2.35
7	48	413–457	437±18.2	211–254	234±17.7	85.2–86.5	86.0±0.596
6	48	434–712	541±122	252–433	326±77.5	83.2–120	97.6±16.3
5	48	375–433	410±25.3	215–266	243±21.0	64.6–81.1	72.3±6.77
4	48	407–504	375±32.3	212–273	241±24.6	54.7–56.3	55.7±0.694
3	48	401–436	416±14.7	249–282	265±13.9	49.5–62.5	56.5±5.34
7	168	486–506	493±9.34	262–292	273±13.6	86.4–90.0	88.5±1.52
6	168	489–580	522±41.3	264–328	287±29.3	74.4–77.9	75.7±1.62
5	168	493–590	529±42.9	264–336	289±33.2	70.3–101	81.1±13.9
4	168	412–578	499±67.9	222–273	262±29.5	43.3–65.3	52.6±9.31
3	168	342–479	403±57.1	196–310	244±47.9	30.1–56.5	40.7±11.4

Table 3.S4 (continued)

pH (–)	time (h)	$A_{280/350}$ Range (–)	$A_{280/350}$ Mean (–)	$S_{275–295}$ Range (nm^{-1})	$S_{275–295}$ Mean (nm^{-1})	$S_{290–350}$ Range (nm^{-1})	$S_{290–350}$ Mean (nm^{-1})
7	1	3.12–3.54	3.31±0.167	0.013–0.017	0.015±0.002	0.016–0.018	0.017±0.001
6	1	3.01–3.32	3.16±0.121	0.013–0.016	0.015±0.001	0.016–0.017	0.016±0.001
5	1	3.24–3.45	3.34±0.085	0.016–0.018	0.016±0.001	0.017–0.018	0.017±0.000
4	1	3.46–3.81	3.59±0.143	0.019–0.022	0.020±0.001	0.018–0.020	0.019±0.001
3	1	3.87–4.40	4.14±0.206	0.020–0.023	0.022±0.001	0.019–0.021	0.020±0.001
7	3	3.48–3.71	3.57±0.078	0.015–0.016	0.015±0.000	0.018–0.019	0.018±0.000
6	3	2.98–3.25	3.09±0.110	0.013–0.016	0.014±0.001	0.016–0.017	0.016±0.001
5	3	3.34–3.60	3.43±0.107	0.017–0.020	0.018±0.001	0.017–0.019	0.018±0.001
4	3	3.04–3.30	3.16±0.106	0.019–0.021	0.020±0.001	0.018–0.022	0.020±0.002
3	3	2.48–2.89	2.70±0.171	0.023–0.023	0.023±0.000	0.021–0.024	0.023±0.001
7	6	2.34–2.64	2.52±0.129	0.015–0.018	0.016±0.001	0.013–0.016	0.014±0.001
6	6	2.65–2.99	2.77±0.143	0.009–0.014	0.011±0.002	0.014–0.016	0.015±0.001
5	6	2.59–3.33	2.99±0.303	0.012–0.018	0.015±0.003	0.013–0.018	0.016±0.002
4	6	2.44–3.07	2.73±0.259	0.021–0.023	0.022±0.001	0.019–0.021	0.020±0.001
3	6	2.81–2.91	2.85±0.039	0.022–0.025	0.024±0.001	0.023–0.025	0.024±0.001
7	12	2.75–2.88	2.81±0.054	0.012–0.013	0.013±0.000	0.014–0.015	0.015±0.000
6	12	2.84–3.06	2.98±0.088	0.013–0.015	0.014±0.001	0.015–0.016	0.016±0.000
5	12	2.65–3.59	3.18±0.391	0.012–0.020	0.016±0.003	0.014–0.019	0.017±0.002
4	12	3.67–4.38	4.05±0.273	0.020–0.024	0.023±0.002	0.018–0.022	0.021±0.002
3	12	4.88–5.71	5.20±0.364	0.026–0.029	0.027±0.002	0.023–0.027	0.024±0.002
7	24	2.86–2.94	2.90±0.027	0.013–0.014	0.013±0.000	0.015–0.015	0.015±0.000
6	24	2.98–3.22	3.09±0.097	0.013–0.016	0.014±0.001	0.015–0.017	0.016±0.000
5	24	3.40–3.66	3.54±0.110	0.017–0.021	0.019±0.001	0.017–0.019	0.018±0.001
4	24	4.09–4.82	4.51±0.306	0.022–0.026	0.024±0.002	0.019–0.023	0.022±0.002
3	24	4.51–5.51	4.95±0.417	0.025–0.030	0.028±0.002	0.021–0.027	0.024±0.002
7	48	2.51–2.97	2.76±0.173	0.007–0.013	0.010±0.003	0.013–0.015	0.014±0.001
6	48	3.08–3.61	3.33±0.212	0.014–0.020	0.017±0.002	0.016–0.020	0.018±0.001
5	48	3.25–3.50	3.38±0.101	0.017–0.019	0.017±0.001	0.017–0.018	0.017±0.000
4	48	3.88–4.86	4.32±0.407	0.020–0.027	0.024±0.003	0.019–0.025	0.022±0.003
3	48	4.53–5.04	4.75±0.207	0.026–0.028	0.027±0.001	0.022–0.024	0.023±0.001
7	168	2.94–3.40	3.10±0.209	0.013–0.019	0.015±0.003	0.015–0.019	0.017±0.002
6	168	3.37–4.40	3.79±0.429	0.017–0.025	0.020±0.003	0.017–0.024	0.020±0.003
5	168	3.34–3.88	3.65±0.210	0.019–0.020	0.019±0.000	0.018–0.019	0.018±0.000
4	168	4.52–6.30	5.09±0.856	0.027–0.039	0.031±0.005	0.022–0.039	0.028±0.008
3	168	5.49–6.51	6.13±0.456	0.033–0.035	0.034±0.001	0.029–0.030	0.029±0.001

Table 3.S4 (continued)

pH (–)	time (h)	$S_{350–400}$ Range (nm^{-1})	$S_{350–400}$ Mean (nm^{-1})	S_R Range (–)	S_R Mean (–)
7	1	0.023–0.024	0.024±0.000	0.536–0.705	0.636±0.058
6	1	0.022–0.023	0.022±0.000	0.592–0.692	0.654±0.042
5	1	0.023–0.024	0.023±0.000	0.673–0.763	0.707±0.039
4	1	0.023–0.023	0.023±0.000	0.826–0.980	0.886±0.065
3	1	0.023–0.026	0.025±0.001	0.851–0.908	0.870±0.020
7	3	0.022–0.023	0.022±0.001	0.645–0.735	0.685±0.034
6	3	0.021–0.022	0.022±0.000	0.604–0.763	0.664±0.068
5	3	0.022–0.023	0.023±0.000	0.729–0.873	0.786±0.079
4	3	0.021–0.024	0.023±0.001	0.888–0.930	0.905±0.017
3	3	0.024–0.024	0.024±0.000	0.947–0.967	0.977±0.041
7	6	0.020–0.022	0.021±0.001	0.701–0.859	0.784±0.060
6	6	0.020–0.021	0.020±0.000	0.447–0.698	0.544±0.103
5	6	0.017–0.023	0.020±0.002	0.614–0.910	0.740±0.123
4	6	0.022–0.024	0.023±0.001	0.912–1.09	0.949±0.031
3	6	0.026–0.027	0.026±0.000	0.846–0.961	0.910±0.036
7	12	0.019–0.020	0.019±0.001	0.635–0.651	0.643±0.006
6	12	0.020–0.021	0.020±0.000	0.631–0.722	0.685±0.038
5	12	0.018–0.023	0.021±0.002	0.667–0.886	0.761±0.089
4	12	0.023–0.024	0.024±0.000	0.876–1.02	0.956±0.058
3	12	0.023–0.026	0.025±0.001	0.978–1.20	1.10±0.088
7	24	0.020–0.021	0.020±0.000	0.619–0.686	0.649±0.026
6	24	0.022–0.022	0.022±0.000	0.614–0.714	0.657±0.041
5	24	0.021–0.025	0.023±0.002	0.727–0.998	0.835±0.117
4	24	0.027–0.033	0.030±0.002	0.710–0.953	0.808±0.101
3	24	0.027–0.030	0.028±0.001	0.865–1.05	0.977±0.065
7	48	0.021–0.022	0.022±0.000	0.307–0.601	0.457±0.116
6	48	0.021–0.022	0.022±0.000	0.656–0.876	0.776±0.089
5	48	0.022–0.024	0.023±0.001	0.723–0.797	0.761±0.029
4	48	0.025–0.026	0.025±0.001	0.818–1.04	0.940±0.089
3	48	0.025–0.028	0.026±0.001	1.00–1.05	1.02±0.015
7	168	0.018–0.020	0.019±0.001	0.667–1.05	0.796±0.173
6	168	0.022–0.023	0.023±0.001	0.793–1.06	0.889±0.120
5	168	0.019–0.027	0.023±0.003	0.701–1.04	0.853±0.135
4	168	0.024–0.031	0.027±0.002	1.13–1.40	1.28±0.118
3	168	0.026–0.029	0.028±0.001	1.24–1.58	1.37±0.141

Table 3.S5 Characterization of the DOM-batch solutions (NOL–manganite interactions) after batch operation.

pH (–)	time (h)	DOC Range (mmol L^{-1})	DOC Mean (mmol L^{-1})	$Mn_{T(ICP)}$:DOC (–)	DOC_{loss} Range (%)	DOC_{loss} Mean (%)
7	1	3.45–3.48	3.47±0.018	0.0039	4.5–5.5	4.9±0.5
6	1	3.31–3.48	3.40±0.073	0.0122	4.5–9.4	6.8±2.0
5	1	3.29–3.47	3.38±0.075	0.0388	4.8–9.8	7.4±2.0
4	1	3.20–3.23	3.22±0.017	0.0854	11.4–12.4	11.7±0.5
3	1	3.09–3.18	3.13±0.037	0.1061	12.8–15.3	14.0±1.0
7	3	3.37–3.59	3.49±0.088	0.0050	1.7–7.5	4.2±2.4
6	3	3.17–3.18	3.17±0.007	0.0155	12.8–13.2	13.0±0.2
5	3	3.01–3.06	3.04±0.021	0.0681	16.0–17.4	16.7±0.6
4	3	2.58–2.76	2.98±0.084	0.1154	15.0–20.1	18.3±2.3
3	3	2.65–2.98	2.86±0.156	0.1783	18.2–27.5	21.4±4.3
7	6	3.36–3.66	3.51±0.121	0.0051	0–7.7	3.9±3.2
6	6	3.32–3.74	3.46±0.195	0.0158	0–9.0	5.9±4.2
5	6	3.21–3.36	3.29±0.071	0.0684	7.9–9.9	9.9±1.9
4	6	2.78–3.20	2.95±0.180	0.1105	12.4–23.7	19.2±4.9
3	6	2.87–2.92	2.90±0.021	0.1731	20.0–21.3	20.5±0.6
7	12	3.51–3.55	3.53±0.022	0.0055	2.6–3.8	3.2±0.6
6	12	3.31–3.46	3.39±0.061	0.0256	5.2–9.2	7.1±1.7
5	12	3.31–3.60	3.42±0.130	0.0895	1.3–9.1	6.3±3.6
4	12	2.93–3.06	2.98±0.056	0.1409	16.1–19.6	18.2±1.5
3	12	2.66–2.96	2.81±0.149	0.2747	18.8–27.0	22.9±4.1
7	24	3.03–3.43	3.27±0.171	0.0083	6.1–16.8	10.3±4.7
6	24	2.92–3.08	3.02±0.070	0.0328	15.6–19.9	17.2±1.9
5	24	2.88–3.26	3.04±0.164	0.1007	10.5–21.0	16.6±4.5
4	24	2.59–3.04	2.86±0.193	0.1549	16.6–29.0	21.6±5.3
3	24	3.05–3.54	3.21±0.231	0.2782	3.0–16.5	11.9±6.3
7	48	3.33–3.71	3.54±0.158	0.0080	0–8.7	3.5±3.7
6	48	3.28–3.46	3.36±0.075	0.0393	5.1–10.2	7.8±2.1
5	48	2.97–3.24	3.15±0.124	0.0940	11.1–18.4	13.7±3.4
4	48	2.52–3.04	2.87±0.248	0.2084	16.6–31.0	21.4±6.8
3	48	2.75–3.05	2.88±0.125	0.4646	16.5–24.6	21.1±3.4
7	168	3.26–3.34	3.30±0.039	0.0112	8.5–10.6	9.6±1.1
6	168	3.08–3.27	3.20±0.082	0.0506	10.3–15.4	12.3±2.2
5	168	2.95–2.97	2.96±0.006	0.1520	18.7–19.1	18.9±0.2
4	168	2.65–3.10	2.94±0.210	0.2799	15.0–27.5	19.3±5.7
3	168	2.91–3.15	3.02±0.120	0.4354	13.8–20.4	17.1±3.3

Table 3.S5 (continued)

pH	time	MA_{254} Range	MA_{254} Mean	MA_{280} Range	MA_{280} Mean	MA_{350} Range	MA_{350} Mean
(–)	(h)	(L mg^{-1}-C m^{-1})	(L mg^{-1}-C m^{-1})	(L mg^{-1}-C m^{-1})	(L mg^{-1}-C m^{-1})	(L mg^{-1}-C m^{-1})	(L mg^{-1}-C m^{-1})
7	1	462–478	470±6.72	233–266	252±13.9	80.9–84.5	83.1±1.54
6	1	455–482	470±11.0	250–267	258±7.25	77.8–85.1	82.0±3.09
5	1	434–443	438±3.65	242–251	247±4.21	69.3–78.0	73.7±3.53
4	1	383–396	391±5.81	247–256	252±3.97	67.0–75.8	70.9±3.63
3	1	385–428	407±17.3	267–300	283±13.3	63.4–72.1	68.2±3.63
7	3	485–536	516±22.1	265–303	286±15.8	88.6–94.5	90.8±2.65
6	3	526–582	545±26.6	281–333	298±24.3	92.1–94.3	93.5±1.00
5	3	425–527	476±41.3	225–306	266±32.9	78.2–81.8	80.4±1.62
4	3	370–472	415±42.3	253–308	277±22.9	75.7–77.8	77.1±0.930
3	3	404–480	441±31.2	274–327	301±21.5	67.0–75.9	70.7±3.80
7	6	445–472	460±11.0	242–255	250±5.65	83.2–86.0	84.5±1.14
6	6	445–477	465±13.9	249–254	251±2.06	72.9–86.0	81.4±6.03
5	6	470–503	486±16.9	281–316	298±17.5	72.2–99.8	86.0±13.8
4	6	428–509	464±34.0	282–347	310±27.5	66.3–100	72.7±4.57
3	6	408–428	419±7.88	278–296	287±7.29	61.6–69.7	64.4±3.74
7	12	471–499	485±13.7	268–291	280±11.4	83.0–83.5	83.3±0.261
6	12	474–518	497±18.1	256–286	272±12.1	81.1–82.6	81.8±0.613
5	12	403–458	434±23.3	228–271	251±17.5	68.1–75.0	72.0±2.87
4	12	411–427	420±6.92	263–273	269±4.82	54.7–63.4	59.6±3.63
3	12	387–449	418±31.2	262–291	376±14.8	60.6–60.7	60.6±0.079
7	24	496–577	531±33.8	273–322	296±20.3	90.5–108	97.4±7.76
6	24	504–605	545±43.2	259–339	296±32.7	91.7–96.8	95.0±2.36
5	24	427–490	451±27.8	238–283	255±20.2	63.5–68.1	66.5±2.09
4	24	417–581	479±73.0	266–392	312±56.4	64.0–93.3	75.2±12.9
3	24	375–395	387±8.47	245–271	260±10.6	52.4–55.7	54.4±1.40
7	48	448–546	500±40.2	249–320	287±29.6	91.2–95.5	92.7±1.95
6	48	536–667	596±54.0	312–422	360±46.3	87.7–101	92.5±6.03
5	48	435–459	449±9.71	254–275	267±9.21	78.3–81.5	80.4±1.48
4	48	398–610	483±91.8	243–408	311±70.6	66.4–111	83.7±19.8
3	48	360–423	390±25.7	231–281	254±20.6	44.1–48.5	46.2±1.80
7	168	485–490	488±2.46	262–270	266±3.90	87.4–92.4	89.9±2.54
6	168	465–531	497±26.9	247–286	267±15.9	80.1–91.2	85.6±4.56
5	168	469–569	514±41.5	265–344	298±33.2	68.0–80.3	72.5±5.53
4	168	445–529	477±37.2	282–334	302±22.9	46.8–57.1	52.6±4.30
3	168	320–389	354±34.3	191–246	219±27.4	41.0–48.7	44.9±3.86

Table 3.S5 (continued)

pH (–)	time (h)	$A_{280/350}$ Range (–)	$A_{280/350}$ Mean (–)	$S_{275–295}$ Range (nm^{-1})	$S_{275–295}$ Mean (nm^{-1})	$S_{290–350}$ Range (nm^{-1})	$S_{290–350}$ Mean (nm^{-1})
7	1	2.88–3.15	3.03±0.112	0.013–0.017	0.015±0.002	0.015–0.017	0.016±0.001
6	1	3.12–3.21	3.16±0.042	0.015–0.016	0.016±0.000	0.016–0.017	0.017±0.000
5	1	3.09–3.60	3.37±0.204	0.015–0.019	0.017±0.002	0.016–0.019	0.018±0.001
4	1	3.08–3.99	3.57±0.288	0.019–0.023	0.021±0.002	0.016–0.021	0.018±0.002
3	1	4.07–4.22	4.15±0.054	0.024–0.025	0.025±0.000	0.022–0.022	0.022±0.000
7	3	2.96–3.43	3.15±0.198	0.015–0.020	0.017±0.002	0.016–0.020	0.017±0.002
6	3	2.98–3.55	3.19±0.242	0.014–0.021	0.017±0.003	0.016–0.020	0.017±0.002
5	3	2.88–3.84	3.31±0.363	0.013–0.022	0.017±0.003	0.015–0.021	0.017±0.002
4	3	3.25–3.96	3.59±0.287	0.017–0.022	0.019±0.002	0.017–0.020	0.019±0.001
3	3	3.96–4.54	4.26±0.224	0.021–0.024	0.023±0.001	0.020–0.022	0.021±0.001
7	6	2.90–3.10	2.96±0.038	0.013–0.015	0.013±0.001	0.015–0.016	0.015±0.000
6	6	2.89–3.43	3.10±0.224	0.013–0.018	0.015±0.002	0.015–0.019	0.016±0.002
5	6	3.16–3.89	3.53±0.362	0.020–0.023	0.021±0.001	0.018–0.021	0.020±0.001
4	6	3.90–4.65	4.27±0.297	0.020–0.026	0.023±0.002	0.019–0.024	0.021±0.002
3	6	4.23–4.64	4.46±0.162	0.023–0.026	0.024±0.001	0.021–0.023	0.022±0.001
7	12	3.23–3.52	3.36±0.129	0.016–0.020	0.018±0.002	0.017–0.020	0.018±0.001
6	12	3.14–3.52	3.32±0.141	0.016–0.019	0.017±0.001	0.017–0.019	0.018±0.001
5	12	3.34–3.63	3.48±0.109	0.018–0.020	0.019±0.001	0.017–0.019	0.018±0.001
4	12	4.14–4.99	4.54±0.347	0.022–0.025	0.023±0.001	0.020–0.023	0.022±0.001
3	12	4.32–4.79	4.56±0.235	0.018–0.025	0.023±0.003	0.020–0.022	0.021±0.001
7	24	2.91–3.24	3.04±0.132	0.013–0.016	0.015±0.001	0.015–0.017	0.016±0.001
6	24	2.82–3.53	3.11±0.286	0.012–0.020	0.016±0.003	0.015–0.020	0.017±0.002
5	24	3.49–4.20	3.83±0.277	0.018–0.023	0.020±0.002	0.017–0.022	0.020±0.002
4	24	3.86–4.40	4.15±0.204	0.022–0.026	0.024±0.002	0.020–0.023	0.022±0.001
3	24	4.66–4.91	4.77±0.089	0.025–0.027	0.026±0.001	0.022–0.025	0.023±0.001
7	48	2.73–3.38	3.09±0.267	0.012–0.019	0.016±0.003	0.014–0.019	0.017±0.002
6	48	3.38–4.82	3.91±0.641	0.019–0.019	0.019±0.000	0.019–0.029	0.022±0.005
5	48	3.11–3.80	3.33±0.231	0.015–0.022	0.017±0.002	0.016–0.019	0.017±0.001
4	48	3.64–3.86	3.73±0.093	0.021–0.024	0.022±0.001	0.018–0.021	0.019±0.001
3	48	5.23–5.80	5.48±0.247	0.025–0.028	0.027±0.001	0.023–0.026	0.024±0.001
7	168	2.91–3.01	2.96±0.042	0.014–0.014	0.014±0.000	0.015–0.016	0.016±0.000
6	168	3.07–3.14	3.11±0.025	0.014–0.015	0.015±0.000	0.016–0.016	0.016±0.000
5	168	3.29–4.97	4.16±0.681	0.016–0.029	0.023±0.005	0.017–0.027	0.022±0.004
4	168	5.16–6.25	5.77±0.407	0.030–0.031	0.031±0.001	0.027–0.031	0.029±0.001
3	168	4.63–5.09	4.86±0.196	0.026–0.026	0.026±0.000	0.021–0.023	0.022±0.001

Table 3.S5 (continued)

pH (–)	time (h)	$S_{350–400}$ Range (nm^{-1})	$S_{350–400}$ Mean (nm^{-1})	S_R Range (–)	S_R Mean (–)
7	1	0.019–0.020	0.020±0.000	0.647–0.840	0.767±0.085
6	1	0.019–0.021	0.020±0.001	0.739–0.829	0.774±0.033
5	1	0.021–0.023	0.022±0.001	0.681–0.829	0.776±0.063
4	1	0.020–0.025	0.023±0.002	0.785–1.03	0.891±0.096
3	1	0.023–0.024	0.023±0.000	1.04–1.09	1.06±0.017
7	3	0.019–0.020	0.019±0.000	0.780–1.01	0.881±0.093
6	3	0.019–0.021	0.020±0.001	0.706–1.06	0.829±0.160
5	3	0.023–0.024	0.023±0.000	0.540–0.928	0.732±0.150
4	3	0.022–0.023	0.023±0.001	0.753–0.929	0.843±0.069
3	3	0.023–0.024	0.024±0.000	0.892–0.990	0.943±0.039
7	6	0.020–0.021	0.020±0.000	0.621–0.727	0.649±0.036
6	6	0.020–0.021	0.021±0.000	0.633–0.882	0.718±0.111
5	6	0.016–0.023	0.019±0.004	0.957–1.29	1.12±0.151
4	6	0.022–0.024	0.024±0.001	0.872–1.15	0.969±0.107
3	6	0.025–0.028	0.026±0.001	0.881–0.973	0.925±0.031
7	12	0.020–0.021	0.021±0.000	0.774–0.946	0.861±0.085
6	12	0.021–0.022	0.021±0.001	0.751–0.848	0.804±0.038
5	12	0.023–0.024	0.023±0.000	0.771–0.893	0.824±0.045
4	12	0.027–0.033	0.030±0.002	0.754–0.813	0.774±0.021
3	12	0.026–0.028	0.027±0.001	0.699–0.898	0.838±0.081
7	24	0.020–0.022	0.021±0.001	0.649–0.752	0.700±0.040
6	24	0.018–0.021	0.020±0.001	0.564–0.979	0.799±0.171
5	24	0.025–0.026	0.025±0.001	0.699–0.873	0.806±0.076
4	24	0.021–0.024	0.023±0.001	0.921–1.18	1.06±0.098
3	24	0.023–0.029	0.026±0.002	0.878–1.20	0.997±0.140
7	48	0.019–0.020	0.019±0.000	0.608–0.936	0.806±0.140
6	48	0.019–0.021	0.020±0.001	0.925–1.37	1.09±0.192
5	48	0.023–0.026	0.024±0.001	0.655–0.851	0.728±0.067
4	48	0.022–0.026	0.024±0.002	0.790–1.38	1.01±0.253
3	48	0.029–0.033	0.031±0.001	0.810–0.927	0.871±0.045
7	168	0.018–0.020	0.019±0.001	0.697–0.776	0.737±0.037
6	168	0.020–0.021	0.021±0.000	0.628–0.764	0.723±0.030
5	168	0.022–0.026	0.024±0.001	0.730–1.19	0.944±0.186
4	168	0.023–0.030	0.028±0.003	1.03–1.31	1.15±0.112
3	168	0.024–0.030	0.027±0.003	0.872–1.07	0.976±0.092

Table 3.S6 ICP OES data of mono, di and trivalent cations after batch operations (NOL–birnessite interactions).

pH	time	K^+ Range	K^+ Mean	Na^+ Range	Na^+ Mean	Ca^{2+} Range	Ca^{2+} Mean
(–)	(h)	(µmol L^{-1})	(µmol L^{-1})	(mmol L^{-1})	(mmol L^{-1})	(mmol L^{-1})	(mmol L^{-1})
7	1	117–128	122±5.61	10.6–10.9	10.7±0.175	0.399–0.427	0.413±0.014
6	1	91.8–131	118±18.3	10.0–11.6	10.8±0.663	0.287–0.526	0.405±0.098
5	1	128–133	131±2.07	8.51–8.66	8.60±0.065	0.519–0.546	0.533±0.011
4	1	110–121	117±4.97	5.69–5.79	5.75±0.042	0.609–0.614	0.612±0.002
3	1	136–139	138±1.22	5.54–5.61	5.57±0.031	0.729–0.751	0.738±0.010
7	3	126–128	128±1.41	9.48–9.61	9.56±0.059	0.439–0.457	0.447±0.007
6	3	110–138	126±11.6	9.86–10.3	10.0±0.181	0.644–0.694	0.666±0.021
5	3	118–122	121±1.62	6.66–6.76	6.73±0.047	0.649–0.659	0.653±0.004
4	3	123–132	128±3.98	5.76–5.86	5.80±0.047	0.719–0.783	0.742±0.029
3	3	149–158	152±3.93	3.34–5.74	4.90±1.10	0.761–0.766	0.764±0.002
7	6	122–158	139±15.0	9.36–10.3	9.72±0.416	0.776–0.936	0.878±0.073
6	6	119–128	124±4.01	6.39–7.16	6.68±0.344	0.609–0.711	0.661±0.042
5	6	127–132	130±2.12	6.51–6.59	6.55±0.031	0.621–0.691	0.654±0.029
4	6	129–133	131±1.96	5.39–5.44	5.41±0.020	0.721–0.818	0.769±0.040
3	6	163–165	164±1.02	5.44–5.59	5.52±0.062	0.783–0.953	0.843±0.078
7	12	124–136	130±5.20	9.11–9.26	9.18±0.061	0.409–0.604	0.481±0.087
6	12	128–143	135±6.22	8.56–8.81	8.70±0.105	0.549–0.788	0.629±0.113
5	12	124–135	129±4.72	6.59–6.66	6.62±0.031	0.639–0.686	0.666±0.020
4	12	136–144	139±3.51	5.41–5.51	5.46±0.041	0.696–0.719	0.704±0.010
3	12	127–173	156±20.5	5.54–5.66	5.60±0.051	0.691–0.991	0.816±0.127
7	24	145–152	149±3.29	16.4–16.6	16.5±0.065	0.387–0.432	0.404±0.020
6	24	157–157	157±0.118	15.6–16.7	16.0±0.463	0.529–0.596	0.555±0.030
5	24	159–165	162±2.76	13.6–15.0	14.1±0.655	0.616–0.734	0.661±0.052
4	24	155–163	159±2.98	8.38–8.43	8.41±0.020	0.674–0.691	0.680±0.008
3	24	180–186	182±2.47	8.03–9.38	8.76±0.555	0.744–0.911	0.831±0.068
7	48	163–168	165±2.20	14.9–16.8	15.8±0.807	0.314–0.472	0.379±0.067
6	48	153–157	154±1.88	13.0–14.4	13.6±0.585	0.447–0.546	0.486±0.044
5	48	165–179	170±6.25	11.6–11.9	11.8±0.147	0.609–0.634	0.620±0.010
4	48	164–179	170±6.64	9.81–9.88	9.85±0.031	0.694–0.704	0.699±0.004
3	48	184–190	186±2.78	6.99–7.09	7.02±0.047	0.746–0.759	0.751±0.005
7	168	151–156	154±2.18	15.5–15.7	15.6±0.071	0.544–0.566	0.556±0.009
6	168	153–170	162±7.13	12.1–12.2	12.2±0.042	0.664–0.873	0.736±0.097
5	168	165–185	176±8.33	10.6–10.8	10.7±0.092	0.841–0.848	0.844±0.003
4	168	175–184	180±3.59	8.08–8.11	8.10±0.012	0.901–0.903	0.902±0.001
3	168	178–202	194±10.9	6.21–6.26	6.24±0.020	0.931–0.991	0.951±0.028

Table 3.S6 (continued)

pH (–)	time (h)	Mg^{2+} Range (µmol L^{-1})	Mg^{2+} Mean (µmol L^{-1})	Al^{3+} Range (µmol L^{-1})	Al^{3+} Mean (µmol L^{-1})	Fe^{3+} Range (µmol L^{-1})	Fe^{3+} Mean (µmol L^{-1})
7	1	2.64–3.17	2.98±0.238	1.73–1.98	1.83±0.108	n.d.	< 0.358
6	1	2.42–2.58	2.49±0.063	1.73–1.99	1.85±0.104	n.d.	< 0.358
5	1	2.86–2.97	2.92±0.044	1.75–1.88	1.82±0.057	n.d.	< 0.358
4	1	2.71–3.08	2.86±0.157	1.59–1.66	1.62±0.029	n.d.	< 0.358
3	1	2.91–2.93	2.91±0.008	1.52–1.58	1.56±0.026	n.d.	< 0.358
7	3	2.08–2.25	2.15±0.076	1.65–1.79	1.72±0.061	n.d.	< 0.358
6	3	2.72–3.25	2.96±0.218	2.07–2.12	2.11±0.026	n.d.	< 0.358
5	3	2.32–3.42	2.78±0.468	1.71–1.89	1.78±0.080	n.d.	< 0.358
4	3	2.69–4.11	3.18±0.660	1.77–1.82	1.80±0.020	n.d.	< 0.358
3	3	2.53–2.81	2.64±0.119	1.71–1.80	1.74±0.038	n.d.	< 0.358
7	6	2.39–2.66	2.54±0.115	1.60–1.82	1.73±0.094	n.d.	< 0.358
6	6	2.45–2.65	2.56±0.082	1.68–1.82	1.74±0.057	n.d.	< 0.358
5	6	2.60–2.68	2.63±0.036	1.70–1.90	1.81±0.080	n.d.	< 0.358
4	6	2.85–2.97	2.90±0.056	1.61–1.78	1.70±0.068	n.d.	< 0.358
3	6	3.08–3.31	3.21±0.096	1.72–1.78	1.74±0.026	n.d.	< 0.358
7	12	2.62–2.90	2.72±0.132	1.37–1.82	1.64±0.189	n.d.	< 0.358
6	12	2.88–3.07	3.00±0.086	1.55–1.92	1.74±0.151	n.d.	< 0.358
5	12	2.71–2.83	2.77±0.051	1.73–1.78	1.76±0.020	n.d.	< 0.358
4	12	2.86–2.89	2.87±0.014	1.51–1.68	1.61±0.073	n.d.	< 0.358
3	12	3.01–3.04	3.03±0.016	1.67–1.74	1.71±0.029	n.d.	< 0.358
7	24	2.53–3.42	2.90±0.379	2.33–2.42	2.37±0.042	n.d.	< 0.358
6	24	2.60–2.68	2.65±0.032	2.09–2.52	2.26±0.186	n.d.	< 0.358
5	24	2.76–3.03	2.87±0.115	2.34–2.82	2.53±0.212	n.d.	< 0.358
4	24	2.87–3.01	2.95±0.056	2.26–2.35	2.31±0.038	n.d.	< 0.358
3	24	2.86–3.02	2.92±0.074	2.08–2.19	2.12±0.047	n.d.	< 0.358
7	48	2.30–2.41	2.37±0.049	1.59–1.86	1.75±0.112	n.d.	< 0.358
6	48	2.67–3.07	2.81±0.185	1.63–2.34	1.90±0.316	n.d.	< 0.358
5	48	2.84–3.18	2.99±0.139	1.87–2.38	2.05±0.235	n.d.	< 0.358
4	48	3.06–3.46	3.22±0.170	1.88–2.03	1.95±0.064	n.d.	< 0.358
3	48	3.04–3.23	3.15±0.079	2.23–2.48	2.32±0.110	n.d.	< 0.358
7	168	2.62–3.18	2.84±0.248	1.25–1.47	1.37±0.093	n.d.	< 0.358
6	168	3.08–3.26	3.19±0.076	1.36–1.58	1.44±0.100	n.d.	< 0.358
5	168	3.36–3.57	3.48±0.086	1.83–2.38	2.15±0.235	n.d.	< 0.358
4	168	3.58–3.67	3.62±0.037	2.76–2.82	2.79±0.024	n.d.	< 0.358
3	168	3.50–3.76	3.65±0.110	4.00–4.78	4.44±0.324	n.d.	< 0.358

Table 3.S7 ICP OES data of mono, di and trivalent cations after batch operations (NOL–manganite interactions).

pH	time	K^+ Range	K^+ Mean	Na^+ Range	Na^+ Mean	Ca^{2+} Range	Ca^{2+} Mean
(–)	(h)	(µmol L^{-1})	(µmol L^{-1})	(mmol L^{-1})	(mmol L^{-1})	(mmol L^{-1})	(mmol L^{-1})
7	1	2.06–5.24	4.08±1.43	8.88–9.26	9.12±0.171	0.881–0.933	0.915±0.024
6	1	1.92–6.69	4.43±1.95	8.26–8.83	8.47±0.260	0.821–0.908	0.853±0.040
5	1	4.52–6.99	5.93±1.04	7.36–8.18	7.69±0.358	0.863–1.00	0.928±0.057
4	1	2.45–7.39	4.16±2.28	10.7–12.0	11.5±0.555	0.901–1.01	0.973±0.051
3	1	5.14–7.11	6.01±0.820	8.36–8.66	8.47±0.136	0.823–0.853	0.835±0.013
7	3	5.36–7.01	6.13±0.677	8.21–8.38	8.30±0.072	0.856–0.901	0.871±0.021
6	3	3.49–5.02	4.37±0.641	8.73–8.91	8.84±0.077	0.811–0.836	0.823±0.010
5	3	2.36–3.34	2.71±0.446	6.79–6.84	6.82±0.024	0.846–0.858	0.850±0.006
4	3	2.12–2.77	2.41±0.269	5.49–5.59	5.52±0.042	0.833–0.881	0.854±0.020
3	3	2.55–3.04	2.73±0.224	5.56–5.71	5.62±0.065	0.851–0.953	0.891±0.045
7	6	9.31–13.9	11.4±1.92	9.03–9.41	9.22±0.017	0.741–0.771	0.756±0.012
6	6	2.87–3.94	3.23±0.506	9.41–10.7	10.3±0.612	0.896–1.06	1.00±0.076
5	6	5.71–8.16	7.02±1.01	6.89–7.36	7.15±0.198	0.978–0.998	0.989±0.008
4	6	2.62–5.14	3.58±1.11	6.61–7.01	6.75±0.188	0.883–0.908	0.899±0.011
3	6	2.82–4.79	3.71±0.816	4.77–5.14	4.90±0.171	0.766–0.776	0.773±0.005
7	12	3.19–4.29	3.66±0.463	8.03–8.21	8.10±0.077	0.619–0.651	0.636±0.013
6	12	4.11–4.33	4.22±0.090	8.76–8.86	8.80±0.042	0.604–0.801	0.724±0.086
5	12	2.69–11.5	6.65±3.63	6.49–6.54	6.52±0.024	0.796–0.806	0.801±0.004
4	12	2.20–2.69	2.42±0.207	5.24–5.34	5.29±0.041	0.783–0.806	0.798±0.010
3	12	2.87–5.56	3.88±1.20	5.24–5.24	5.30±0.042	0.803–0.848	0.823±0.019
7	24	5.35–6.19	5.65±0.383	9.48–10.3	9.78±0.372	0.656–0.731	0.692±0.031
6	24	2.89–8.68	4.90±2.68	10.1–10.5	10.3±0.176	0.898–1.02	0.949±0.049
5	24	2.82–5.02	3.73±0.936	7.46–8.08	7.69±0.283	0.958–1.00	0.985±0.019
4	24	1.26–2.82	1.96±0.646	5.24–5.36	5.29±0.054	0.926–0.993	0.966±0.029
3	24	3.84–4.84	4.28±0.416	4.79–4.89	4.86±0.047	0.736–0.769	0.750±0.014
7	48	6.36–7.24	6.75±0.365	12.6–14.2	13.5±0.698	0.644–0.704	0.681±0.027
6	48	5.99–6.26	6.15±0.119	11.3–12.1	11.6±0.367	0.614–0.654	0.632±0.016
5	48	4.99–7.41	5.90±1.08	8.28–8.73	8.49±0.185	0.674–0.886	0.764±0.090
4	48	4.27–5.71	4.79±0.655	5.94–6.86	6.32±0.393	0.918–0.966	0.941±0.019
3	48	3.77–4.79	4.32±0.423	4.79–4.89	4.84±0.041	0.754–0.771	0.764±0.008
7	168	0.936–1.56	1.33±0.280	9.68–11.0	10.2±0.555	0.626–0.811	0.705±0.078
6	168	0.793–0.963	0.873±0.070	9.56–9.71	9.65±0.065	0.724–0.846	0.769±0.055
5	168	3.14–3.52	3.28±0.171	7.26–7.29	7.27±0.012	0.956–1.00	0.973±0.020
4	168	3.92–9.61	7.56±2.58	5.07–5.16	5.12±0.041	0.981–0.991	0.984±0.005
3	168	7.01–8.06	7.58±0.432	5.04–5.19	5.12±0.062	0.986–0.993	0.989±0.003

Table 3.S7 (continued)

pH (–)	time (h)	Mg^{2+} Range (µmol L^{-1})	Mg^{2+} Mean (µmol L^{-1})	Al^{3+} Range (µmol L^{-1})	Al^{3+} Mean (µmol L^{-1})	Fe^{3+} Range (µmol L^{-1})	Fe^{3+} Mean (µmol L^{-1})
7	1	2.78–2.79	2.79±0.008	1.55–1.63	1.59±0.030	n.d.	< 0.179
6	1	2.62–3.03	2.78±0.181	1.66–1.74	1.70±0.031	n.d.	< 0.179
5	1	3.09–3.23	3.16±0.058	1.78–1.85	1.81±0.030	n.d.	< 0.179
4	1	2.59–2.67	2.62±0.039	1.89–1.96	1.91±0.033	n.d.	< 0.179
3	1	2.90–2.93	2.89±0.027	2.00–2.07	2.03±0.030	n.d.	< 0.179
7	3	2.87–3.51	3.19±0.319	2.24–2.33	2.29±0.036	n.d.	< 0.179
6	3	2.83–3.04	2.91±0.091	2.10–3.41	2.62±0.572	n.d.	< 0.179
5	3	2.76–2.97	2.89±0.095	2.08–2.19	2.13±0.046	n.d.	< 0.179
4	3	2.98–3.06	3.02±0.034	1.93–1.96	1.95±0.014	n.d.	< 0.179
3	3	3.00–3.48	3.18±0.214	3.15–3.28	3.22±0.055	n.d.	< 0.179
7	6	3.07–3.18	3.12±0.043	1.11–1.13	1.12±0.009	n.d.	< 0.179
6	6	2.46–2.51	2.48±0.022	1.77–1.96	1.89±0.087	n.d.	< 0.179
5	6	2.46–2.54	2.51±0.034	1.96–2.55	2.17±0.267	n.d.	< 0.179
4	6	2.52–2.90	2.67±0.167	2.29–2.79	2.57±0.210	n.d.	< 0.179
3	6	2.02–2.26	2.14±0.098	3.63–4.00	3.78±0.162	n.d.	< 0.179
7	12	2.49–2.72	2.60±0.094	1.74–2.35	1.97±0.266	n.d.	< 0.179
6	12	2.65–2.97	2.84±0.136	2.29–2.43	2.35±0.062	n.d.	< 0.179
5	12	2.89–3.15	3.00±0.111	1.73–1.75	1.74±0.012	n.d.	< 0.179
4	12	2.77–3.06	2.92±0.118	2.26–2.32	2.30±0.026	n.d.	< 0.179
3	12	3.08–3.13	3.10±0.019	3.82–4.00	3.93±0.080	n.d.	< 0.179
7	24	2.73–3.14	2.91±0.172	1.39–1.49	1.45±0.044	n.d.	< 0.179
6	24	2.46–2.56	2.51±0.044	1.29–1.51	1.38±0.092	n.d.	< 0.179
5	24	2.49–2.56	2.51±0.032	1.81–2.48	2.11±0.279	n.d.	< 0.179
4	24	2.48–2.88	2.63±0.180	2.18–2.60	2.44±0.187	n.d.	< 0.179
3	24	2.81–2.85	2.84±0.017	4.37–4.60	4.48±0.091	n.d.	< 0.179
7	48	2.55–2.69	2.61±0.060	1.24–1.29	1.26±0.024	n.d.	< 0.179
6	48	2.68–2.91	2.76±0.107	1.43–1.45	1.44±0.009	n.d.	< 0.179
5	48	2.44–2.67	2.59±0.106	1.93–1.96	1.94±0.011	n.d.	< 0.179
4	48	2.69–2.88	2.78±0.076	2.62–2.92	2.79±0.128	n.d.	< 0.179
3	48	2.82–3.25	3.03±0.175	5.37–5.49	5.42±0.046	n.d.	< 0.179
7	168	3.02–4.32	3.53±0.565	1.19–1.25	1.22±0.023	n.d.	< 0.179
6	168	2.69–3.37	2.95±0.302	1.52–1.97	1.81±0.201	n.d.	< 0.179
5	168	2.51–2.66	2.57±0.065	1.76–1.87	1.83±0.051	n.d.	< 0.179
4	168	2.65–2.83	2.75±0.077	2.95–3.08	3.00±0.059	n.d.	< 0.179
3	168	3.80–4.07	3.94±0.138	4.71–4.97	4.79±0.122	n.d.	< 0.179

References

1 International Organization for Standardization (ed.), (ISO 9277:2022), Determination of the specific surface area of solids by gas adsorption – BET method, 3rd edn., https://www.iso.org/standard/71014.html (accessed May 2025).

2 J. W. Murray, L. S. Balistrieri and B. Paul, The oxidation state of manganese in marine sediments and ferromanganese nodules, *Geochim. Cosmochim. Acta*, 1984, **48**, 1237–1247.

3 S. Mustafa, B. Dilara, K. Nargis, A. Naeem and P. Shahida, Surface properties of the mixed oxides of iron and silica, *Colloid. Surface. A*, 2002, **205**, 273–282.

4 H. Li, F. Santos, K. Butler and E. Herndon, A Critical Review on the Multiple Roles of Manganese in Stabilizing and Destabilizing Soil Organic Matter, *Environ. Sci. Technol.*, 2021, **55**, 12136–12152.

5 C. S. Liu, L. J. Zhang, C. H. Feng, C. A. Wu, F. B. Li and X. Z. Li, Relationship between oxidative degradation of 2-mercaptobenzothiazole and physicochemical properties of manganese (hydro)oxides, *Environ. Chem.*, 2009, **6**, 83–92.

6 C. K. Remucal and M. Ginder-Vogel, A critical review of the reactivity of manganese oxides with organic contaminants, *Environ. Sci. Process Impacts*, 2014, **16**, 1247–1266.

7 H. Shindo and P. M. Huang, Catalytic Effects of Manganese(IV), Iron(III), Aluminum, and Silicon Oxides on the Formation of Phenolic Polymers, *Soil Sci. Soc. Am. J.*, **48**, 927–934.

8 D. A. Shaughnessy, H. Nitsche, C. H. Booth, D. K. Shuh, G. A. Waychunas, R. E. Wilson, H. Gill, K. J. Cantrell and R. J. Serne, Molecular Interfacial Reactions between Pu(VI) and Manganese Oxide Minerals Manganite and Hausmanite, *Environ. Sci. Technol.*, 2003, **37**, 3367–3374.

9 L. Ukrainczyk and M. B. McBride, Oxidation of Phenol in Acidic Aqueous Suspensions of Manganese Oxides, *Clay Clay Miner.*, 1992, **40**, 157–166.

10 R. M. Weaver, M. F. Hochella, Jr. and E. S. Ilton, Dynamic processes occurring at the Cr^{III}_{aq}-manganite (γ-MnOOH) interface: Simultaneous adsorption, microprecipitation, oxidation/reduction, and dissolution, *Geochim. Cosmochim. Acta*, 2002, **66**, 4119–4132.

11 H. Cui, G. Qiu, X. Feng, W. Tan and F. Liu, Birnessites with Different Average Manganese Oxidation States Synthesized, Characterized, and Transformed to Todorokite at Atmospheric Pressure, *Clay Clay Miner.*, 2009, **57**, 715–724.

12 X. H. Feng, L. M. Zhai, W. F. Tan, F. Liu and J. Z. He, Adsorption and redox reactions of heavy metals on synthesized Mn oxide minerals, *Environ. Pollut.*, 2007, **147**, 366–373.

13 W. Zhao, F. Liu, X. Feng, W. Tan, G. Qiu and X. Chen, Fourier transform infrared spectroscopy study of acid birnessites before and after Pb^{2+} adsorption, *Clay Miner.*, 2012, **47**, 191–204.

14 Y. Luo, J. Ding, J. Hai, W. Tan, R. Hao and G. Qiu, Interaction mechanism of dissolved Cr(VI) and manganite in the presence of goethite coating, *Environ. Pollut.*, 2020, **260**, 114046.

15 T. Zahoransky, A. V. Wegorzewski, W. Huong and C. Mikutta, X-ray absorption spectroscopy study of Mn reference compounds for Mn speciation in terrestrial surface environments, *Am. Mineral.*, 2023, **108**, 847–864.

16 W.-F. Tan, S.-J. Lu, F. Liu, X.-H. Feng, J.-Z. He and L. K. Koopal, Determination of the Point-Of-Zero Charge of Manganese Oxides with Different Methods Including an Improved Salt Titration Method, *Soil Sci.*, 2008, **173**, 277–286.

17 M. Ramstedt, B. M. Andersson, A. Shchukarev and S. Sjöberg, Surface Properties of Hydrous Manganite (γ-MnOOH). A Potentiometric, Electroacoustic, and X-ray Photoelectron Spectroscopy Study, *Langmuir*, 2004, **20**, 8224–8229.

18 A. M. Hansen, T. E. C. Kraus, B. A. Pellerin, J. A. Fleck, B. D. Downing and B. A. Bergamaschi, Optical properties of dissolved organic matter (DOM): Effects of biological and photolytic degradation, *Limnol. Oceanogr.*, 2016, **61**, 1015–1032.

19 A. Huguet, L. Vacher, S. Relexans, S. Saubusse, J. M. Froidefond and E. Parlanti, Properties of fluorescent dissolved organic matter in the Gironde Estuary, *Org. Geochem.*, 2009, **40**, 706–719.

20 J. Li, L. Zhao, M. Li, Y. Min, F. Zhan, Y. Wang, L. Sheng and H. Bian, Changes in soil dissolved organic matter optical properties during peatland succession, *Ecol. Indic.*, 2022, **143**, 109386.

21 D. M. McKnight, E. W. Boyer, P. K. Westerhoff, P. T. Doran, T. Kulbe and D. T. Andersen, Spectrofluorometric characterization of dissolved organic matter for indication of precursor organic material and aromaticity, *Limnol. Oceanogr.*, 2001, **46**, 38–48.

22 A. Zsolnay, E. Baigar, M. Jimenez, B. Steinweg and F. Saccomandi, Differentiating with fluorescence spectroscopy the sources of dissolved organic matter in soils subjected to drying, *Chemosphere*, 1999, **38**, 45–50.

23 T. Ohno, Fluorescence inner-filtering correction for determining the humification index of dissolved organic matter, *Environ. Sci. Technol.*, 2002, **36**, 742–746.

Chapter 4: Dissolved trivalent manganese under defined redox conditions in redoximorphic soils: laboratory and field evidence

Manuscript

Author: Constantin Lux[1] (CL)

Co-author: Tim Mansfeldt[1] (TM)

Formatting and orthography are adapted to the dissertation style.

This study extends the previous work by applying the porphyrin method to redoximorphic soils under defined redox conditions, ranging from oxidizing to strongly reducing conditions, both in the laboratory and *in situ*. Mn^{3+}–NOL complexes were detected across all investigated redox conditions, providing further insights for the final interpretation of Mn^{3+} chemistry in soils within this dissertation.

Author contributions are presented by category, including conceptualization and methodology, sample acquisition, sample preparation, formal analysis, software and data curation, investigation, visualization, writing – original draft, writing – review and editing, validation, supervision, project administration and funding acquisition. Within each category, authors are listed in order of their initials to indicate their respective contributions.

Conceptualization and methodology: CL and TM; sample acquisition: CL and TM; sample preparation: CL; formal analysis: CL; software and data curation: CL; investigation: CL; visualization: CL; writing – original draft: CL; writing – review and editing: CL and TM; validation: TM; supervision: TM; project administration: TM; funding acquisition: TM.

The manuscript was submitted to the “European Journal of Soil Science (EJSS)” on 17 November 2025. A revised version was accepted for publication in EJSS on 20 May 2026.

[1] Institute of Geography, Faculty of Mathematics and Natural Sciences, Department of Geosciences, University of Cologne, Albertus-Magnus-Platz, D-50923 Cologne, Germany.

Research Highlights:

- Mn^{3+}–NOL complexes are part of the Mn_T pool under defined redox conditions.
- Intermediate Mn^{3+}–NOL complexes are temporarily resistant against oxidation.
- Redox fluctuations induced by waterlogging–aeration cycles promote Mn^{3+}–NOL complex formation.
- Mn^{3+}–NOL complexes are evident under field conditions.

Abstract

The reduction-oxidation (redox) cycling of manganese (Mn) regulates biogeochemical element cycles, including the carbon cycle, in soils. Dissolved trivalent Mn (Mn^{3+}), stabilized by complexation with natural organic ligands (NOLs), is a key component mediating these processes. Accurate quantification of this species is therefore needed. Our objectives were to (i) speciate the total dissolved Mn (Mn_T) pool under defined redox conditions, (ii) elucidate possible biotic and abiotic pathways of Mn^{3+}–NOL complex formation, and (iii) provide evidence for Mn^{3+}–NOL complexes under field conditions. Bulk soil from two horizons (AhBg and Bg) of a Calcaric Gleysol was incubated in a microcosm, running two redox cycles (I: oxidizing → weakly reducing → moderately reducing → reoxidizing; II: oxidizing → strongly reducing → reoxidizing) as expressed by the redox potential (E_H) to simulate typical redox fluctuations driven by waterlogging–aeration cycles. In addition, soil solutions were collected *in situ* from the Calcaric Gleysol and a nearby Salic Tidalic Fluvisol. Mn speciation analysis was conducted following a spectrophotometric protocol based on kinetic modeling. During microcosm experiments, Mn_T was absent under the initial oxidation conditions, while Mn^{2+} dominated subsequent reducing regimes. During redox cycle I, mean Mn^{3+}–NOL complex proportions increased from weakly reducing conditions (AhBg: 8.5 ± 7.8%, Bg: 4.0 ± 4.8%) to moderately reducing conditions (AhBg: 10.8 ± 12.3%, Bg: 25.3 ± 24.2%). Reoxidizing conditions showed contrasting trends for each suspension (AhBg: 12.2 ± 12.6%, Bg: 3.6 ± 3.5%). In redox cycle II, mean Mn^{3+}–NOL complex proportions were lower under strongly reducing conditions (AhBg: 4.2 ± 4.3%, Bg: 15.5 ± 5.5%) than under moderately reducing conditions in redox cycle I. Under reoxidizing conditions, Mn^{3+}–NOL complexes increased (AhBg: 36.4 ± 29.8%, Bg: 30.0 ± 6.4%), indicating stabilization against oxidation. The results demonstrate that Mn^{3+}–NOL complexes form under both oxidizing and reducing conditions through biotic and abiotic pathways. Field data confirmed the occurrence of these complexes in the Calcaric Gleysol (≤52.5 ± 2.7%) and Salic Tidalic Fluvisol (≤90.0 ± 0.9%). These findings highlight that redox fluctuations induced by waterlogging–aeration cycles are a key driver of Mn^{3+}–NOL complex formation and stabilization.

Keywords: dissolved organic matter, manganese cycle, manganese speciation analysis, microcosm, natural organic ligands, redox cycle, wetland

4.1 Introduction

Manganese (Mn) is a ubiquitous trace element and a key component of biogeochemical processes, including the cycling of carbon (C), nutrients, and trace elements (Li et al. 2021). Released through mineral weathering, Mn accumulates in sediments and soils at concentrations ranging from 20–6,000 mg kg^{-1} (Reddy et al. 2023).

In soils, Mn biogeochemistry is governed by three oxidation states. The most soluble form, dissolved divalent Mn (Mn^{2+}), can be oxidized biotically and abiotically to poorly crystalline Mn^{IV} oxides (Li et al. 2021). During this process, dissolved trivalent Mn (Mn^{3+}) may be stabilized by natural organic ligands (NOLs). These Mn^{3+}–NOL complexes constitute up to 100% of the total dissolved Mn (Mn_T) pool in marine sediments, stratified water columns, and water treatment works under oxic to anoxic conditions (Madison et al. 2011, 2013; Oldham et al. 2017a–c; Johnson et al. 2018). More recently, Mn^{3+}–NOL complexes have been detected in acidic forest floor solutions, soil solutions, and soil extracts (Lux and Mansfeldt 2023; Lux et al. 2025).

The solubility and bioavailability of Mn are strongly influenced by the soil redox potential (E_H), pH, temperature, and soil organic matter (SOM) content (Sparrow and Uren 2014; Reddy et al. 2023). In redoximorphic soils, a broad spectrum of redox conditions occur (Reddy et al. 2023), induced by alternating periods of waterlogging and aeration. Following the classification system of Reddy et al. (2023), soil redox conditions can be categorized depending on the preferential electron acceptor: oxidizing (> +300 mV, O_2 reduction); weakly reducing (+100 to +300 mV, $Mn^{III/IV}$ and nitrate (NO_3^-) reduction); moderately reducing (+100 to –100 mV, Fe^{III} reduction); and strongly reducing (< –100 mV, sulfate (SO_4^{2-}) and carbon dioxide (CO_2) reduction). Waterlogging–aeration cycles promote fluctuations in E_H and consequently drive both biotic and abiotic transformations between Mn^{2+} and Mn^{IV}, with the transient formation of Mn^{3+}–NOL complexes. Manganese dynamics in waterlogged soils have been extensively studied with respect to E_H and pH (Patrick and Turner 1968; Gotoh and Patrick 1972; Schwab and Lindsay 1983). In the Calcaric Gleysol examined here, dissolved Mn_T was previously assumed to consist solely of Mn^{2+} (Mansfeldt 2003, 2004) due to methodological limitations. To date, Mn speciation under defined redox conditions has not been conducted, representing a knowledge gap.

Accurate Mn speciation, however, is essential for elucidating Mn-driven soil processes and refining biogeochemical models.

To address this knowledge gap, we conducted Mn speciation analysis on soil suspensions from two horizons (AhBg and Bg) of the Calcaric Gleysol incubated in a microcosm system. The Calcaric Gleysol is characterized by pronounced, groundwater-induced seasonal E_H fluctuations (Dorau and Mansfeldt 2016). These E_H fluctuations strongly influence the Mn solubility, with concentrations ranging from below the detection limit under oxidizing conditions (10 and 60 cm depth) to 7.64 µmol L^{-1} under moderately reducing conditions (60 cm depth) (Mansfeldt 2004). Consequently, this soil type is ideal for studying E_H-dependent processes, such as the formation of Mn^{3+}–NOL complexes. Microcosms enable the controlled study of redox-dependent processes that are difficult to resolve *in situ* (Abril et al. 2010; Anschutz et al. 2019). Two redox cycles (I: oxidizing → weakly reducing → moderately reducing → reoxidizing; II: oxidizing → strongly reducing → reoxidizing) were applied to each suspension to simulate the natural, study site-specific E_H fluctuations induced by waterlogging–aeration cycles that influence Mn speciation. Both cycles were conducted with an emphasis on weakly to strongly reducing conditions, where inorganic reductants such as ferrous iron (Fe^{2+}) and sulfides (e.g. HS^-) can occur. Strongly reducing conditions are common in this soil and are relic in deeper subsoil horizons, as indicated by the presence of Fe sulfides (FeS) (Mansfeldt 2003).

A complementary small-scale field campaign assessed Mn^{3+}–NOL complex formation under natural conditions in the Calcaric Gleysol (AhBg: 10–20 cm; Bg: 50–60 cm; Bg2: 90–100 cm) and a nearby Salic Tidalic Fluvisol (zFo: 0–10 cm; zFr: 25–35 cm).

The speciation of the Mn_T pool (including Mn^{2+}, Mn^{3+}–NOL_{weak} complexes, and Mn^{3+}–NOL_{strong} complexes) was determined using a spectrophotometric method, namely the porphyrin method (Madison et al. 2011; Oldham et al. 2015; Lux and Mansfeldt 2023). This approach employs α,β,γ,δ-tetrakis(4-carboxyphenyl)porphine (T(4-CP)P) and is based on a metal substitution reaction in which Cd^{2+}, initially complexed with the porphyrin (Cd^{2+}–T(4-CP)P), is replaced by free or NOL-bound Mn^{2+} or Mn^{3+}. The differing substitution kinetics allow the differentiation of the dissolved Mn_T pool, based on the varying ligand binding affinities and strengths to Mn^{2+} and Mn^{3+} (Madison et al. 2011; Luther et al. 2015; Oldham et al. 2015). Subsequently, the concentrations of Mn^{2+},

Mn^{3+}–NOL_{weak} complexes, and Mn^{3+}–NOL_{strong} complexes are determined by fitting the experimental data using kinetic modeling equations (Lux et al. 2025).

In natural ecosystems, Mn^{3+}–NOL complexes act as strong oxidants, supporting the depolymerization of lignin-like substances and the degradation of organic compounds, including organic pollutants such as methylmercury. Reactive Mn^{3+}–NOL complexes play a critical role in SOM decomposition and C cycling (Hofrichter 2002; Berg et al. 2007; Stendahl et al. 2017; Zhang et al. 2023). As highly redox-active intermediates, Mn^{3+}–NOL complexes mediate element cycles. This highlights the environmental significance of Mn^{3+} in biogeochemical element cycling.

The objectives of this study were to (i) speciate the Mn_T pool under defined redox conditions, (ii) elucidate possible biotic and abiotic pathways of Mn^{3+}–NOL complex formation, and (iii) provide evidence for Mn^{3+}–NOL complexes under field conditions.

4.2 Material and Methods

4.2.1 Study site, sampling

Study site A is located in the Polder Speicherkoog, Schleswig-Holstein, Northern Germany (54°8′1″ N, 8°58′28″ E; 0.5 m a.s.l.), 30 km north of the Elbe estuary and 3 km inland from the shoreline (Figure 4.1). The site, influenced by groundwater, is in a non-cultivated field within an agrarian landscape. The soil, classified as a Calcaric Gleysol (IUSS 2022), developed from Holocene calcareous marine sediments (Hoffmann 1991). For microcosm experiments, ~20 kg of moist soil was collected from the AhBg (10–20 cm) and Bg (40–60 cm) horizons, placed into polyamide (PA) bags, respectively, and transported to the laboratory for processing.

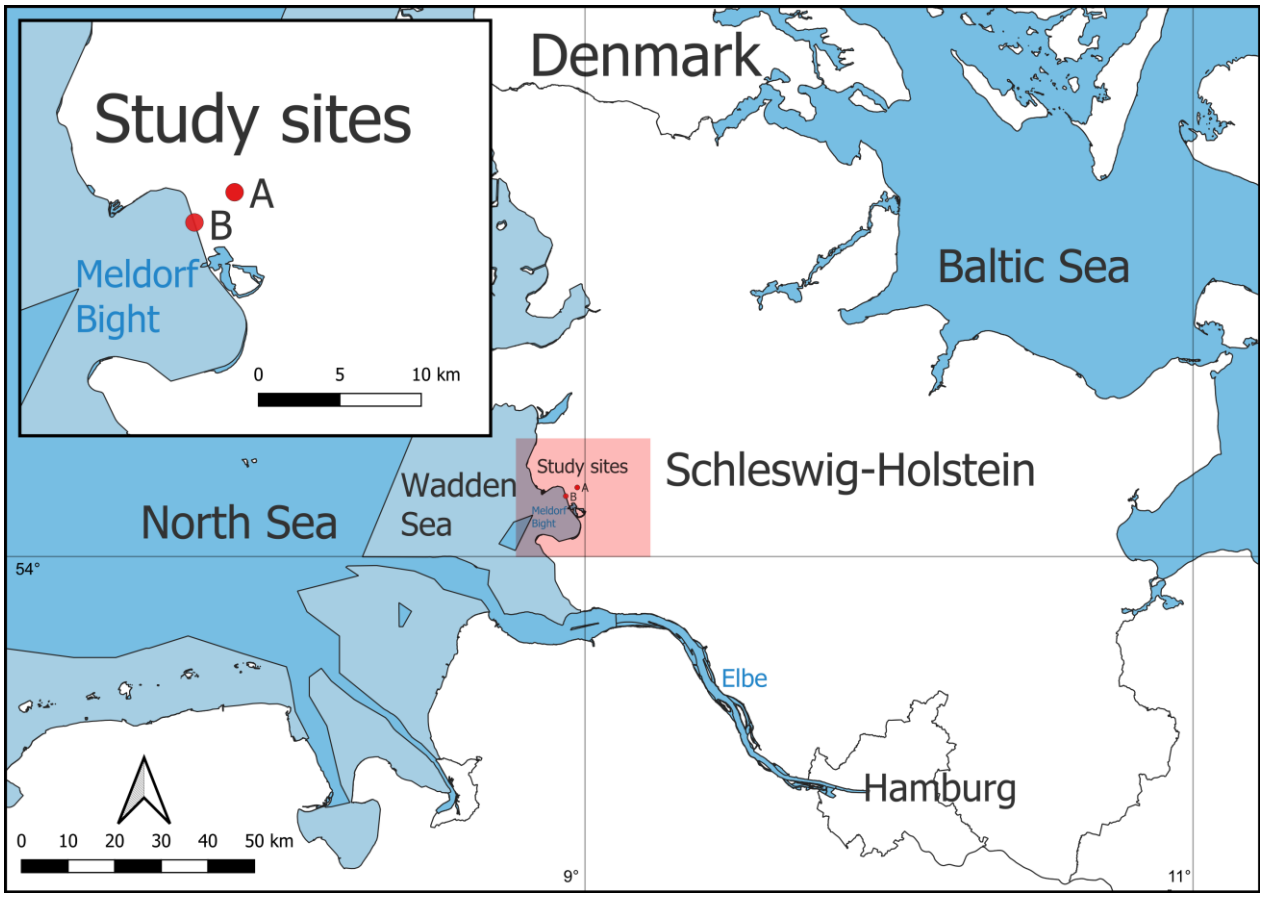

Figure 4.1 The study sites located in the Marsh (A) and the Wadden Sea (B), Schleswig-Holstein, Northern Germany. Coordinate reference system: World Geodetic System 1984 (WGS 84) (EPSG:4326).

4.2.2 Soil characterization

All soil samples were air-dried at 25 °C, manually homogenized, sieved to ≤2 mm, and stored at 4 °C in the dark prior to microcosm experiments. The particle-size distribution was determined by wet sieving and sedimentation. The soil pH was measured potentiometrically in ultrapure water and 0.01 M $CaCl_2$ using a glass electrode (SenTIX 81, WTW, Weilheim, Germany), and electrical conductivity (EC) was determined with a conductivity electrode (SevenEasy, Mettler Toledo, Giessen, Germany) in a suspension of soil material and deionized water (1:5, w:v). Dithionite-extractable Fe (Fe_d) and oxalate-extractable Fe (Fe_o) were determined (Mehra and Jackson 1958; Schwertmann 1964). The Fe_d fraction represents the total Fe oxide pool, while the Fe_o fraction reflects the short-range ordered Fe oxides.

Subsamples were ground using an agate ball mill. The total C (TC) and nitrogen (N) were determined in duplicate by dry combustion using a CNS analyzer (Vario EL cube,

Elementar, Hanau, Germany) with a thermal conductivity detector. For samples containing inorganic C (IC), carbonates were removed by acid pretreatment; organic C (OC) was then determined by dry combustion, and IC was calculated as the difference between the TC and OC. Total metal contents were determined by X-ray fluorescence spectroscopy (XRF).

4.2.3 Microcosm experiments

Microcosm experiments were carried out in a custom-designed unit (Applikon Biotechnology BV, Delft, Netherlands; see Figure 4.2 and supporting information (SI) for details).

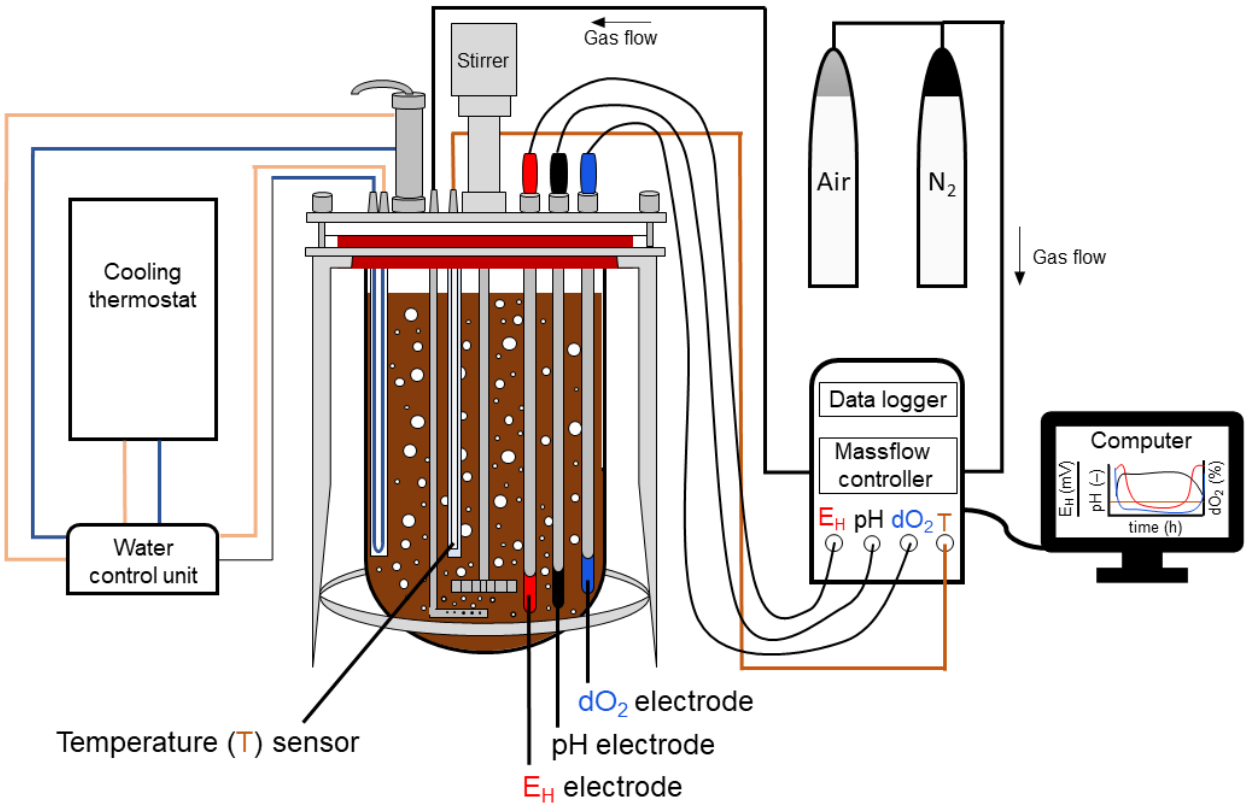

Figure 4.2 Schematic representation of both the microcosm and the control unit.

For each incubation, 250 g of air-dried, sieved soil (≤2 mm) was mixed with 1.25 L of 0.001 M $CaCl_2$ solution (1:5, w:v). Suspensions were stirred at 500 rpm under controlled conditions (T = 20 ± 0.1 °C, p = 0.1013 MPa). To minimize evaporative losses, gas inflows were humidified, and the outflow was passed through an Allihn condenser at 5 °C. The E_H, pH, dissolved O_2 (dO_2), and temperature were continuously recorded. Target E_H values were established by precise inflows of filtered ambient air and O_2-free N_2 via mass

flow controllers. All E_H values were converted in reference to the standard hydrogen electrode by adding +207 mV to the Ag/AgCl potentials and normalized to pH 7 ($E_{H(pH\ 7)}$) [Eq. 1]:

$$E_{H(pH\ 7)} = E_H + (pH - 7) \cdot 59\ mV. \quad [Eq.\ 1]$$

No acids or bases were added; thus, pH changes reflected redox-related chemical processes (e.g. mineral dissolution, sorption, and redox reactions). Photochemical reactions were suppressed by wrapping the reactor vessel in aluminum foil. To establish strongly reducing conditions in both horizon suspensions, 5 g of Wadden Sea sediment was added as an inoculum.

Redox cycles

Two redox cycles were applied to soil suspensions from the AhBg and Bg horizons of the Calcaric Gleysol. Redox cycle I progressed from oxidizing (+450 mV) to weakly reducing (+175 mV), then to moderately reducing (±0 mV), and finally to reoxidizing conditions. This sequence simulated the typical E_H dynamics at study site A. Each microcosm subjected to cycle I included 13 samples, resulting in 26 samples in total.

Redox cycle II involved a transition from oxidizing (+450 mV) to strongly reducing conditions (–175 mV) and back, resulting in 10 samples per microcosm experiment and 20 in total. This treatment aimed to evaluate the influence of strong inorganic reductants, particularly Fe^{2+} and reduced sulfur species (e.g. HS^-), on Mn^{3+}–NOL complex formation.

The actual establishment of target E_H conditions depended on the soil's intrinsic buffer capacity, which required adjustments to the initial sampling schedule (see SI).

Speciation of the Mn_T pool by kinetic modeling

The Mn speciation analysis was conducted using the porphyrin method, following established protocols (Madison et al. 2011; Oldham et al. 2015), with modifications for dissolved organic C (DOC)-rich soil solutions (Lux and Mansfeldt 2023). This method enables the speciation of the Mn_T pool, including Mn^{2+}, Mn^{3+}–NOL_{weak} complexes, and Mn^{3+}–NOL_{strong} complexes, based on kinetic modeling. Spectrophotometric measurements were performed on a Lambda 25™ spectrophotometer (PerkinElmer®,

Rodgau, Germany) using a 1 cm pathlength glass cuvette with a total volume of 3 mL. Measurements were executed at the Soret band (468 nm) using T(4-CP)P. In advance of the analyses, the molar absorption coefficient (ε = 95,340 M^{-1} cm^{-1}) of the Mn^{3+}–T(4-CP)P complex was determined using a standard series of manganese(II) chloride tetrahydrate solutions ($MnCl_2 \cdot 4H_2O$) (0.1–10 µM). Reagent concentrations were prepared according to Madison et al. (2011) and Oldham et al. (2015). Since the porphyrin method requires a stable pH of 7.5 to 8 for efficient metal substitution, a borate buffer mixture was added to maintain the desired pH. Sample pipetting volumes (100–2360 µL) were adjusted to the expected Mn_T concentrations in the cuvette to comply with the method's detection range. Absorbance was recorded at 5-second intervals for up to 10 minutes. Measurements were stopped earlier if the recorded kinetic curves sufficiently plateaued at the absorbance maximum, indicating the completion of the metal substitution reaction.

For cross-validation, a 10 mL aliquot of each sample was acidified with 10 µL of concentrated nitric acid (HNO_3, suprapur®, 65%) for subsequent inductively coupled plasma optical emission spectrometry (ICP OES) analysis. The excessive acidification (pH < 2) of humic-rich samples causes the precipitation of humic substances and associated metals, leading to the underestimation of trace metal concentrations (Oldham et al. 2017b).

In summary, Mn speciation was determined in two separate measurements with subsequent kinetic modeling: one measurement in the absence (non-reduced samples) and one measurement in the presence (reduced samples) of the strong reducing agent hydroxylamine, as described by Lux et al. (2025). Further details are provided in the SI.

Analyses of aqueous solutions

Prior to aqueous analyses, soil suspensions were extracted using a 60 mL syringe and filtered through ≤0.2 µm cellulose acetate membranes (Sartorius, Göttingen, Germany). Samples collected under reducing conditions were immediately transferred into a vinyl anaerobic chamber (Coy Laboratory Products Inc., Michigan, USA) and processed under O_2-free conditions (<5 ppm).

For elemental analysis, 10 mL aliquots were acidified with 10 µL of concentrated HNO_3 (suprapur®, 65%) prior to ICP OES analysis.

Unacidified samples were analyzed for DOC and dissolved inorganic C (DIC). A 100 µL sample volume was injected into a glass tube and subjected to high-temperature catalytic oxidation to CO_2 at 850 °C, with the DOC and DIC quantified using a non-dispersive infrared TOC analyzer (Dimatoc 2000, Dimatec, Essen, Germany). All samples were analyzed in triplicate. In addition, UV/Vis absorbance spectra were recorded from 800–200 nm to calculate molar absorptivities at 254 nm (MA_{254}), 280 nm (MA_{280}), and 350 nm (MA_{350}). These parameters are commonly associated with the aromaticity and molecular weight of dissolved organic matter (DOM) (Weishaar et al. 2003; Rodríguez et al. 2016). Iron speciation was determined using the ferrozine method (Viollier et al. 2000), with Fe^{2+} and Fe^{3+} quantified spectrophotometrically at 562 nm. Sulfide species (H_2S, HS^-, and S^{2-}) under strongly reducing conditions were analyzed at 660 nm using a modified Cline assay (Engelbrektson et al. 2014).

4.2.4 Field campaign

Study sites and sampling

Study site A was the Calcaric Gleysol (see Section 4.2.1). Soil solutions were sampled in triplicate from the AhBg (10–20 cm), Bg (50–60 cm), and Bg2 (90–100 cm) horizons using pre-installed PA suction cups with a 0.45 µm pore size (Ecotech, Bonn, Germany). Before sampling, 1 L acid-cleaned amber glass flasks (Ecotech, Bonn, Germany) were rinsed with fresh soil solution. Suction (–60 kPa) was maintained using a manual vacuum pump (Ecotech, Bonn, Germany). Samples were collected in amber glass flasks and sealed with Parafilm® (PM-992, Bemis, Sheboygan Falls, Wisconsin, USA).

Study site B was located in a tidally influenced area ~3 km west of site A (Figure 4.1), within the Wadden Sea (UNESCO World Heritage Site) in the Meldorf Bight, about 30 m from the shoreline (54°7′3″ N, 8°56′7″ E; 0 m a.s.l.). The soil was classified as a Salic Tidalic Fluvisol (IUSS 2022). Here, PA suction cups were temporarily installed to collect soil solution from the zFo (0–10 cm) and zFr (25–35 cm) horizons. Sampling followed the same protocol as for the Calcaric Gleysol but was restricted to low tide.

Samples were transported immediately to a nearby facility for Mn speciation analysis and further processing. Supporting data on *in situ* E_H conditions in the Calcaric Gleysol were obtained from a nearby monitoring station (Dorau and Mansfeldt 2016).

Mn speciation and solution analyses

Soil solutions were passed through 0.2 µm syringe filters (cellulose acetate, VWR, Radnor, PA, USA). Subsequently, Mn speciation analysis (Section 4.2.3 *Speciation of the Mn_T pool by kinetic modeling*) was performed using a portable VIS spectrometer (DR 1900, HACH, Loveland, CO, USA). For elemental analysis, 10 mL aliquots were acidified with 10 µL concentrated HNO_3 (suprapur®, 65%) and analyzed by ICP OES. Non-acidified 10 mL aliquots were used for DOC and ion chromatography analyses.

4.3 Results

4.3.1 Soil properties

Table 4.1 summarizes the physico-chemical soil properties of the AhBg (10–20 cm) and Bg (40–60 cm) horizons of the Calcaric Gleysol. Soil texture was a silt loam (IUSS 2022). Due to the calcareous marine parent material, pH was circumneutral in the AhBg horizon ($pH_{(H_2O)}$ = 7.13; $pH_{(CaCl_2)}$ = 6.94) and weakly alkaline in the Bg horizon ($pH_{(H_2O)}$ = 7.99; $pH_{(CaCl_2)}$ = 7.54).

The TC decreased from 33.3 g kg^{-1} (AhBg) to 15.7 g kg^{-1} (Bg), mainly due to a threefold decrease in OC (32.1 versus 9.20 g kg^{-1}), while IC increased (1.20 versus 6.45 g kg^{-1}) with depth. The C:N ratio increased from 9.94 to 13.0.

Manganese concentrations decreased sharply from 767 mg kg^{-1} (AhBg) to 294 mg kg^{-1} (Bg). Iron concentrations slightly increased from 21.9–23.4 g kg^{-1} with depth. A strong decrease in the Mn:Fe ratio from 0.035 to 0.013 was observed. The Fe_o/Fe_d ratio also decreased with depth (0.89–0.78), indicating the dominance of short-range ordered Fe oxides. Calcium tripled (8.30–24.0 g kg^{-1}), suggesting carbonate accumulation in the Bg horizon, while sodium (Na) concentrations (5.64 g kg^{-1}) remained constant. With depth, Cl^- and SO_4^{2-} concentrations decreased, while NO_2^- and PO_4^{3-} were not detectable.

Table 4.1 Physico-chemical soil properties of the AhBg and Bg horizons of the Calcaric Gleysol, Speicherkoog, Schleswig-Holstein, Germany.

Soil properties	AhBg	Bg
Bulk soil		
Depth (cm)	10–20	40–60
Parent material	Calcareous marine sediments	Calcareous marine sediments
Sand (g kg^{-1})	265	190
Silt (g kg^{-1})	530	565
Loam (g kg^{-1})	210	240
Texture	Silt loam[a]	Silt loam[a]
pH in H_2O (–)	7.13	7.99
pH in $CaCl_2$ (–)	6.94	7.54
EC (µS cm^{-1})	139	108
C_{total} (g kg^{-1})	33.2	15.7
C_{org} (g kg^{-1})	32.1	9.20
C_{inorg} (g kg^{-1})	1.20	6.45
N_{total} (g kg^{-1})	3.35	1.20
C:N (–)	9.94	13.0
Mn (mg kg^{-1})	767	294
Fe (g kg^{-1})	21.9	23.4
Fe_{ox} (g kg^{-1})	4.96[b]	4.65[b]
Fe_d (g kg^{-1})	5.57[c]	5.96[c]
Fe_o/Fe_d (–)	0.89	0.78
Al (g kg^{-1})	42.3	45.3
Ca (g kg^{-1})	8.30	24.0
K (g kg^{-1})	15.3	16.0
Mg (g kg^{-1})	6.39	7.66
Na (g kg^{-1})	5.64	5.64
Si (g kg^{-1})	336	335
Soil solution		
Cl^- (mg L^{-1})	4.58	2.04
F^- (mg L^{-1})	0.058	0.232
NO_3^- (mg L^{-1})	1.89	0.560
NO_2^- (mg L^{-1})	n.d.*	n.d.
PO_4^{3-} (mg L^{-1})	n.d.	n.d.
SO_4^{2-} (mg L^{-1})	4.34	2.93

[a] according to FAO

[b] oxalate-extractable Fe

[c] dithionite-extractable Fe

* n.d. = not detectable

4.3.2 Laboratory studies

In the following sections, samples obtained during the microcosm experiments are assigned to redox conditions as follows: initially oxidizing (OX 1–3), weakly reducing (WR 1–3), moderately reducing (MR 1–3), strongly reducing (SR 1–3), and reoxidizing (OX 4–7).

Microcosm redox cycles

Figure 4.3 shows redox cycles conducted on the suspensions from the AhBg and Bg horizons of the Calcaric Gleysol, with E_H, pH, and dO_2 plotted over time. Sampling events are indicated by black triangles.

During redox cycle I, the defined redox conditions were successfully achieved in both soil suspensions. In redox cycle II, however, the objectives were only partially met. Although strongly reducing conditions were reached, the E_H values remained close to the threshold of moderately reducing conditions. This made it difficult to precisely evaluate the influence of sulfides on Mn^{3+}–NOL complex formation.

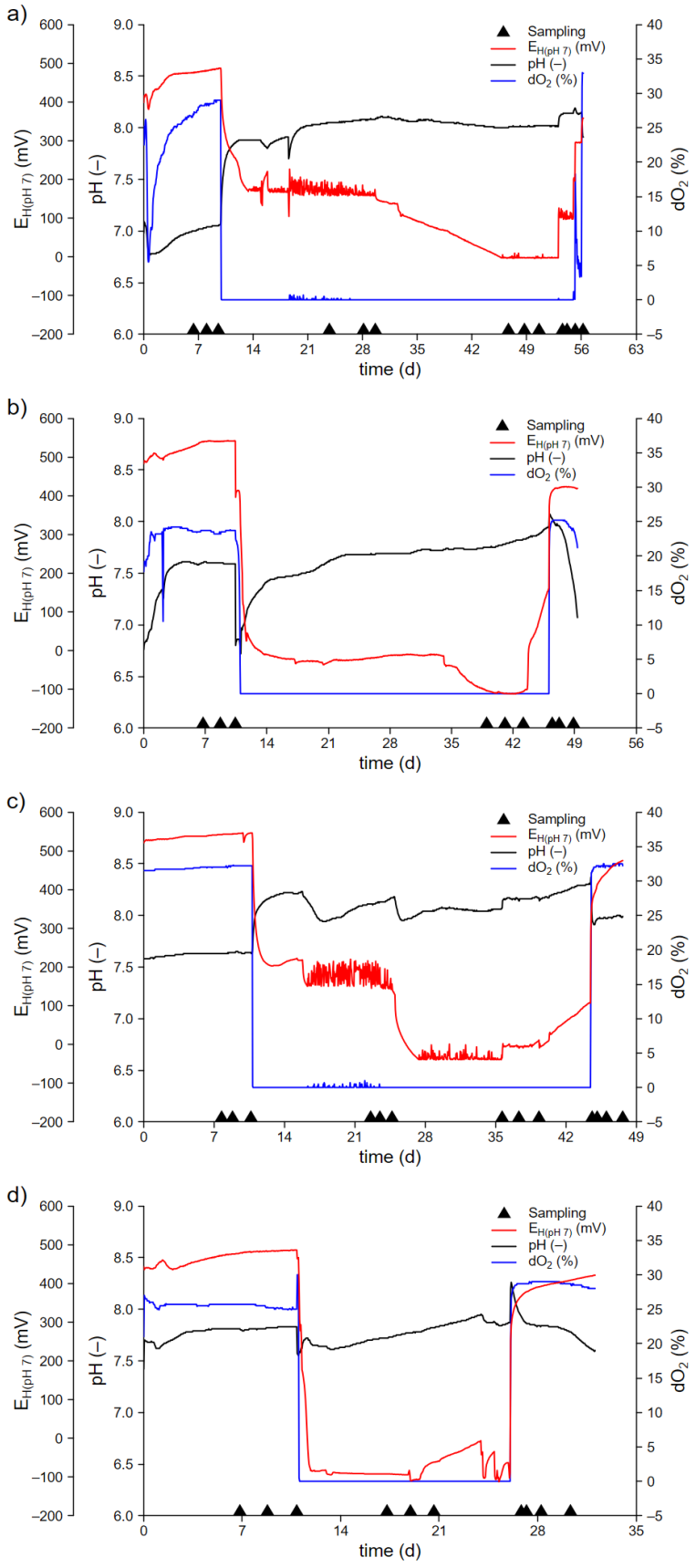

Figure 4.3 Time series of redox potential (E_H) (red line), pH (black line), and dissolved O_2 (dO_2) (blue line), comprising sampling events (black triangles), for a) the AhBg suspension during redox cycle I (oxidizing → weakly reducing → moderately reducing → reoxidizing), b) the AhBg suspension during redox cycle II (oxidizing → strongly reducing → reoxidizing), c) the Bg suspension during redox cycle I, and d) the Bg suspension during redox cycle II.

Mn speciation under defined redox conditions

Figure 4.4 presents Mn speciation data from the kinetic modeling of Mn_T, including Mn^{2+}, Mn^{3+}–NOL_{weak} complexes, and Mn^{3+}–NOL_{strong} complexes for all microcosm experiments: AhBg suspension during redox cycles I and II (Figures 4.4a, b) and Bg suspension during redox cycles I and II (Figures 4.4c, d). Speciation was not possible under initial oxidizing conditions because Mn_T was not detectable. Three trends emerged: (i) Mn^{2+} dominated; (ii) reducing conditions promoted Mn^{3+}–NOL complex formation, particularly under moderately reducing conditions; and (iii) reoxidizing conditions favored their formation and transient stabilization. Tables 4.S1–4.S4 present the proportions.

In the AhBg suspension (redox cycle I; Figure 4.4a), Mn^{2+} dominated across all redox conditions. The strongest increase in Mn^{3+}–NOL_{weak} complexes occurred during the shift from weakly to moderately reducing conditions, with mean proportions rising from 1.4 ± 1.7% (0–0.513 µmol L^{-1}, mean: 0.173 ± 0.203 µmol L^{-1}) to 8.9 ± 12.3% (0–7.87 µmol L^{-1}, mean: 2.11 ± 2.94 µmol L^{-1}) of Mn_T. In contrast, Mn^{3+}–NOL_{strong} complexes decreased from 7.1 ± 7.6% (0.063–2.67 µmol L^{-1}, mean: 0.943 ± 1.03 µmol L^{-1}) to 1.9 ± 0.5% (0.270–0.561 µmol L^{-1}, mean: 0.439 ± 0.106 µmol L^{-1}). Overall, Mn^{3+}–NOL complexes accounted for 10.8% of Mn_T under moderately reducing conditions. During reoxidizing conditions (OX 4–OX 6), Mn^{3+}–NOL_{weak} complexes initially decreased slightly and then sharply increased, peaking at OX 6 (22.1 ± 14.5%). On average, Mn^{3+}–NOL_{weak} and Mn^{3+}–NOL_{strong} complexes represented 9.3 ± 12.6% (0–8.70 µmol L^{-1}; mean: 1.85 ± 2.51 µmol L^{-1}) and 2.9 ± 1.0% (0.230–1.02 µmol L^{-1}; mean: 0.624 ± 0.244 µmol L^{-1}) of Mn_T, respectively, summing to 12.2% of Mn_T.

During redox cycle II (Figure 4.4b), Mn^{2+} also dominated under strongly reducing conditions. The mean Mn^{3+}–NOL_{weak} complex proportions were 3.6 ± 4.2% (0–4.53 µmol L^{-1}, mean: 1.58 ± 1.82 µmol L^{-1}), lower than under moderately reducing conditions. Mn^{3+}–NOL_{strong} complexes were only detected in SR 2, averaging 0.6 ± 1.1%. Mn^{3+}–NOL complex proportions accounted for 4.2% of Mn_T under strongly reducing conditions. Reoxidizing conditions substantially increased Mn^{3+}–NOL_{weak} complexes to 30.7 ± 29.4% (0–22.3 µmol L^{-1}, mean: 9.25 ± 9.24 µmol L^{-1}), peaking at OX 4 (57.1 ± 0.4%) and OX 5 (61.9 ± 9.8%), temporarily surpassing Mn^{2+}. Mn^{3+}–NOL_{strong}

complexes averaged 5.7 ± 4.9% (0–0.879 µmol L^{-1}, mean: 0.457 ± 0.272 µmol L^{-1}). Combined, Mn^{3+}–NOL complexes comprised 36.4% of Mn_T during reoxidizing conditions.

In the Bg suspension (redox cycle I; Figure 4.4c), Mn^{2+} was most abundant. Similar to the AhBg suspension, mean Mn^{3+}–NOL_{weak} complex proportions increased from 2.9 ± 4.0% (0–0.104 µmol L^{-1}, mean: 0.032 ± 0.045 µmol L^{-1}) under weakly reducing conditions to 10.0 ± 10.8% (0–0.378 µmol L^{-1}, mean: 0.122 ± 0.122 µmol L^{-1}) under moderately reducing conditions. Concurrently, Mn^{3+}–NOL_{strong} complex proportions increased from 1.1 ± 2.7% (0–0.096 µmol L^{-1}, mean: 0.012 ± 0.030 µmol L^{-1}) to 15.3 ± 21.7% (0–0.797 µmol L^{-1}, mean: 0.250 ± 0.355 µmol L^{-1}). Mn^{3+}–NOL complexes comprised 25.3% of Mn_T, more than twice the proportion observed in the AhBg suspension under moderately reducing conditions. Both species decreased to a combined 3.6% of Mn_T under reoxidizing conditions.

During redox cycle II (Figure 4.4d), Mn^{2+} remained dominant. Under strongly reducing conditions, Mn^{3+}–NOL_{weak} complexes contributed 2.7 ± 4.1% (0–0.601 µmol L^{-1}, mean: 0.137 ± 0.209 µmol L^{-1}), while Mn^{3+}–NOL_{strong} complexes comprised 12.8 ± 3.7% (0.280–0.831 µmol L^{-1}, mean: 0.644 ± 0.197 µmol L^{-1}). Thus, Mn^{3+}–NOL complexes accounted for 15.5% of Mn_T, considerably less than under moderately reducing conditions. During reoxidizing conditions, Mn^{3+}–NOL_{weak} complexes remained low at 2.1 ± 2.8% (0–0.103 µmol L^{-1}, mean: 0.028 ± 0.037 µmol L^{-1}), whereas Mn^{3+}–NOL_{strong} complexes increased to 27.9 ± 5.7% (0.353–0.501 µmol L^{-1}, mean: 0.439 ± 0.047 µmol L^{-1}). Under reoxidizing conditions, both complex species accounted for 30.0% of Mn_T.

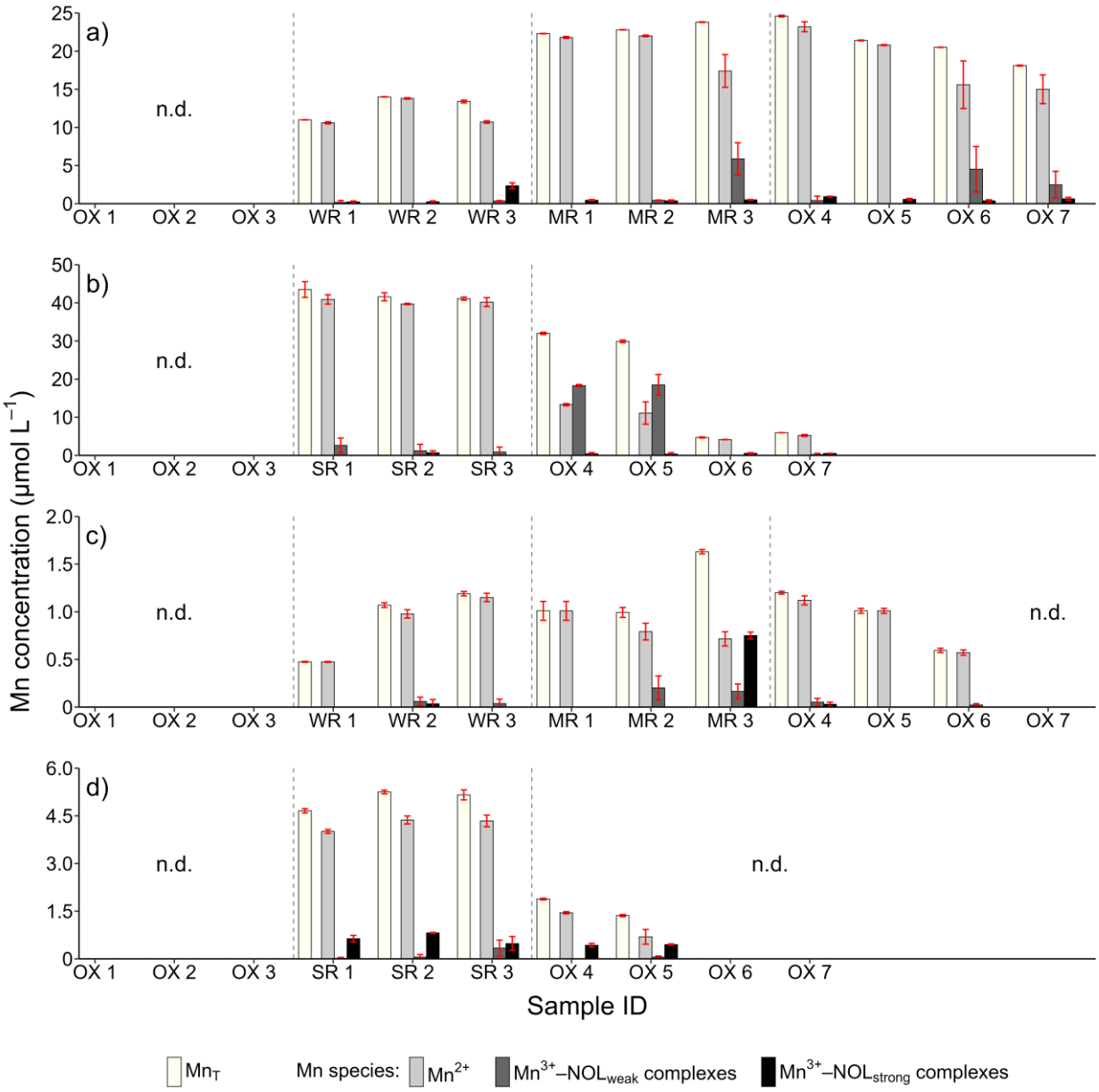

Figure 4.4 Results of Mn speciation analysis by kinetic modeling, consisting of total dissolved manganese concentrations (Mn_T, yellowish bar), and the Mn species concentrations of Mn^{2+} (light grey bar), Mn^{3+}–NOL_{weak} complexes (grey bar), and Mn^{3+}–NOL_{strong} complexes (black bar) contained therein, for a) the AhBg suspension during redox cycle I (oxidizing → weakly reducing → moderately reducing → reoxidizing), b) the AhBg suspension during redox cycle II (oxidizing → strongly reducing → reoxidizing), c) the Bg suspension during redox cycle I, and d) the Bg suspension during redox cycle II. All samples were measured in triplicate. n.d. = not detectable; OX = oxidizing conditions; WR = weakly reducing conditions; MR = moderately reducing conditions; SR = strongly reducing conditions.

Analyses of supporting parameters

Because NOLs govern Mn^{3+}–NOL complex formation, DOC and DIC dynamics were monitored, and DOC optical properties and Mn_T/DOC ratios were calculated during the microcosm experiments (Tables 4.S5–4.S8). Two consistent patterns emerged: (i) the mean DOC increased, and (ii) molar absorptivities (MA_{254}, MA_{280}, MA_{350}) declined under progressively reducing conditions and longer incubation times.

In the AhBg suspension (redox cycle I; Table 4.S5), mean DOC concentrations increased from initial oxidizing conditions (3.49 ± 0.339 mmol L^{-1}) to weakly reducing conditions (8.93 ± 0.896 mmol L^{-1}) and peaked under moderately reducing conditions (13.0 ± 1.60 mmol L^{-1}). During reoxidizing conditions, DOC decreased to 11.4 ± 1.89 mmol L^{-1}. In contrast, DIC showed an inverse pattern, with the highest mean concentration under initial oxidizing conditions (1.93 ± 0.202 mmol L^{-1}) and the lowest under moderately oxidizing conditions (0.097 ± 0.050 mmol L^{-1}). Reflecting DOC compositional changes, MAs decreased with decreasing E_H and over time.

During redox cycle II (Table 4.S6), mean DOC concentrations rose strongly from initial oxidizing conditions (3.82 ± 0.450 mmol L^{-1}) to strongly reducing conditions (18.0 ± 0.309 mmol L^{-1}) and decreased to 13.9 ± 1.14 mmol L^{-1} under reoxidizing conditions, remaining above the values in the initial oxidizing phase. The mean DIC concentration decreased from initial oxidizing conditions (1.81 ± 0.103 mmol L^{-1}) to strongly reducing conditions (0.981 ± 0.070 mmol L^{-1}) and then recovered during reoxidizing conditions (1.76 ± 0.464 mmol L^{-1}). As in redox cycle I, MAs decreased steadily with decreasing E_H and increasing incubation time.

In the Bg suspension (redox cycle I; Table 4.S7), the mean DOC concentration (1.99 ± 0.017 mmol L^{-1}) was approximately half that in the AhBg suspension (cycle I) during the initial oxidizing phase. DOC increased to 3.60 ± 0.147 mmol L^{-1} under weakly reducing conditions and further increased to 4.91 ± 0.037 mmol L^{-1} under moderately reducing conditions. Notably, the DOC increase was less pronounced than that in the AhBg suspension. During reoxidizing conditions, the DOC concentration peaked at 4.93 ± 0.437 mmol L^{-1}. DIC mean concentrations followed an inverse pattern, with a maximum under initial oxidizing conditions (0.850 ± 0.024 mmol L^{-1}), a minimum under

moderately reducing conditions (0.263 ± 0.044 mmol L^{-1}), and recovery during reoxidizing conditions (0.922 ± 0.432 mmol L^{-1}). As in AhBg, MAs decreased consistently.

In redox cycle II (Table 4.S8), the mean DOC concentration increased from initial oxidizing conditions (2.26 ± 0.533 mmol L^{-1}) to strongly reducing conditions (4.48 ± 0.102 mmol L^{-1}) and then stabilized during reoxidizing conditions (4.38 ± 0.892 mmol L^{-1}). The mean DIC concentration was 0.785 ± 0.045 mmol L^{-1} during the initial oxidizing phase, followed by a decrease under strongly reducing conditions (0.482 ± 0.041 mmol L^{-1}) and a notable increase under reoxidizing conditions (1.17 ± 0.114 mmol L^{-1}). MAs showed the same pattern and decreased stepwise. Across all experiments, Mn_T/DOC ratios remained ≤0.0023 (Tables 4.S5–4.S8).

The Ca^{2+} concentrations (Tables 4.S9–4.S12) revealed three trends: (i) concentrations were lowest under initial oxidizing conditions, (ii) concentrations gradually increased from weakly reducing to strongly reducing conditions, and (iii) concentrations exhibited a minor decline during reoxidizing conditions.

Fe and sulfide speciation

Total dissolved Fe (Fe_T) speciation revealed three main trends (Tables 4.S9–4.S12): (i) Fe_T increased with decreasing E_H, (ii) Fe_T concentrations were higher in the AhBg suspension than in the Bg suspension, and (iii) Fe^{2+} dominated under reducing conditions but rapidly disappeared under reoxidizing conditions.

In the AhBg suspensions, the highest mean Fe_T concentration occurred under moderately reducing conditions (10.5 ± 1.89 mmol L^{-1}) during redox cycle I, exceeded by strongly reducing conditions (15.3 ± 0.074 mmol L^{-1}) in redox cycle II. Under moderately reducing conditions, mean Fe^{2+} concentrations (10.3 ± 1.92 mmol L^{-1}) accounted for most of Fe_T. However, Fe^{2+} rapidly decreased during reoxidizing conditions and was only detectable in OX 4 (2.31 mmol L^{-1}). Similarly, Fe^{2+} peaked under strongly reducing conditions (15.2 ± 0.105 mmol L^{-1}) and was also not detectable during reoxidizing conditions, except for OX 4 (2.02 mmol L^{-1}).

In contrast, the Bg suspensions revealed lower Fe_T concentrations under moderately reducing conditions (4.12 ± 0.441 mmol L^{-1}) and strongly reducing conditions (9.79 ± 0.397 mmol L^{-1}). Ferrous iron was abundant under moderately reducing

conditions (3.82 ± 0.447 mmol L^{-1}) but absent under reoxidizing conditions. Under strongly reducing conditions, Fe^{2+} peaked (9.68 ± 0.445 mmol L^{-1}) and then strongly decreased under reoxidizing conditions, remaining detectable only in OX 4 (1.81 mmol L^{-1}).

Sulfides were not detectable under strongly reducing conditions during redox cycle II (Tables 4.S9–4.S12). Thus, a precise evaluation of their impact on Mn speciation, particularly the Mn^{3+}–NOL complex formation, was not possible.

4.3.3 Field measurements

Aqueous solution analysis of field samples

In the Calcaric Gleysol, soil solutions were obtained only from the Bg2 horizon at 90 cm depth (Tables 4.S13 and 4.S14), as the low groundwater level and the absence of precipitation prevented sampling from the upper horizons. Conditions that were weakly reducing (E_H = +210 mV) and weakly alkaline (pH = 7.58) prevailed. The mean DOC and DIC concentrations were 0.954 ± 0.151 mmol L^{-1} and 7.02 ± 0.188 mmol L^{-1}, respectively. Chloride remained at <0.2 mol L^{-1}, thus not interfering with the porphyrin method (Madison et al. 2011).

In the Salic Tidalic Fluvisol, soil solutions were sampled from the zFo and zFr horizons (Tables 4.S13 and 4.S14). Weakly alkaline conditions prevailed, with mean pH values of 7.47 (zFo) and 7.62 (zFr). The EC indicated high salinity, and the mean salinity values decreased from 42.8 ± 0.100 mS cm^{-1} (zFo) to 32.5 ± 8.80 mS cm^{-1} (zFr). DOC concentrations varied spatially: 0.794–2.62 mmol L^{-1} (mean: 1.71 ± 0.915 mmol L^{-1}) in zFo solutions, and 0.510–0.618 mmol L^{-1} (mean: 0.564 ± 0.054 mmol L^{-1}) in zFr solutions. In all Fluvisol samples, Cl^- concentrations exceeded the 0.2 mol L^{-1} threshold. Therefore, Mn speciation analysis was conducted on diluted solutions.

Total dissolved Mn under field conditions

The total dissolved Mn was determined by ICP OES (Table 4.S13). In the Calcaric Gleysol, Mn_T concentrations ranged from 19.8–28.1 mmol L^{-1} (mean: 22.8 ± 3.81 mmol L^{-1}) in the Bg2 soil solutions. In contrast, the Salic Tidalic Fluvisol

revealed higher Mn_T concentrations of 37.1 and 65.0 mmol L^{-1} (mean: 51.1 ± 14.0 mmol L^{-1}) in the zFo soil solutions and lower values of 4.11 and 21.2 mmol L^{-1} (mean: 11.7 ± 7.63 mmol L^{-1}) in the zFr soil solutions. Cross-validation between the porphyrin method and ICP OES showed good agreement, with an overall mean of 1.02 ± 0.03 (n = 7, r = 0.999, R^2 = 0.999, p < 0.001) (Figure 4.S2).

In situ Mn speciation analysis

The field application of the porphyrin method revealed that reaction kinetics were highly sensitive to the soil solution temperature and ambient temperature fluctuations, making reliable *in situ* Mn speciation unfeasible. Consequently, all samples were analyzed immediately under controlled conditions (T = 20 ± 1 °C, p = 0.1013 MPa) at a nearby facility. Figure 4.5 presents Mn speciation results from these soil solutions, which exhibited high variability in Mn^{3+}–NOL complex concentrations.

In the Calcaric Gleysol (Bg2), Mn^{3+}–NOL_{weak} complexes accounted for up to 17.4 ± 24.7% (0 to 15.9 mmol L^{-1}, mean: 5.09 ± 7.21 mmol L^{-1}) of Mn_T, whereas Mn^{3+}–NOL_{strong} complexes contributed 0.7 ± 0.8% (0 to 0.394 mmol L^{-1}, mean: 0.143 ± 0.169 mmol L^{-1}). Both species were nearly absent in samples A and C (Table 4.S13).

In the Salic Tidalic Fluvisol, Mn^{3+}–NOL complexes occurred only in zFo sample A, with Mn^{3+}–NOL_{weak} and Mn^{3+}–NOL_{strong} complexes averaging 1.7 ± 1.9% (0–3.50 mmol L^{-1}; mean: 1.16 ± 1.32 mmol L^{-1}) and 0.4 ± 0.9% (0–1.63 mmol L^{-1}; mean: 0.272 ± 0.609 mmol L^{-1}), respectively. In contrast, the zFr soil solutions exhibited higher proportions, with Mn^{3+}–NOL_{weak} at 44.2 ± 44.2% (0–3.62 mmol L^{-1}; mean: 1.79 ± 1.79 mmol L^{-1}) and Mn^{3+}–NOL_{strong} at 2.2 ± 1.7% (0–1.07 mmol L^{-1}; mean: 0.316 ± 0.401 mmol L^{-1}).

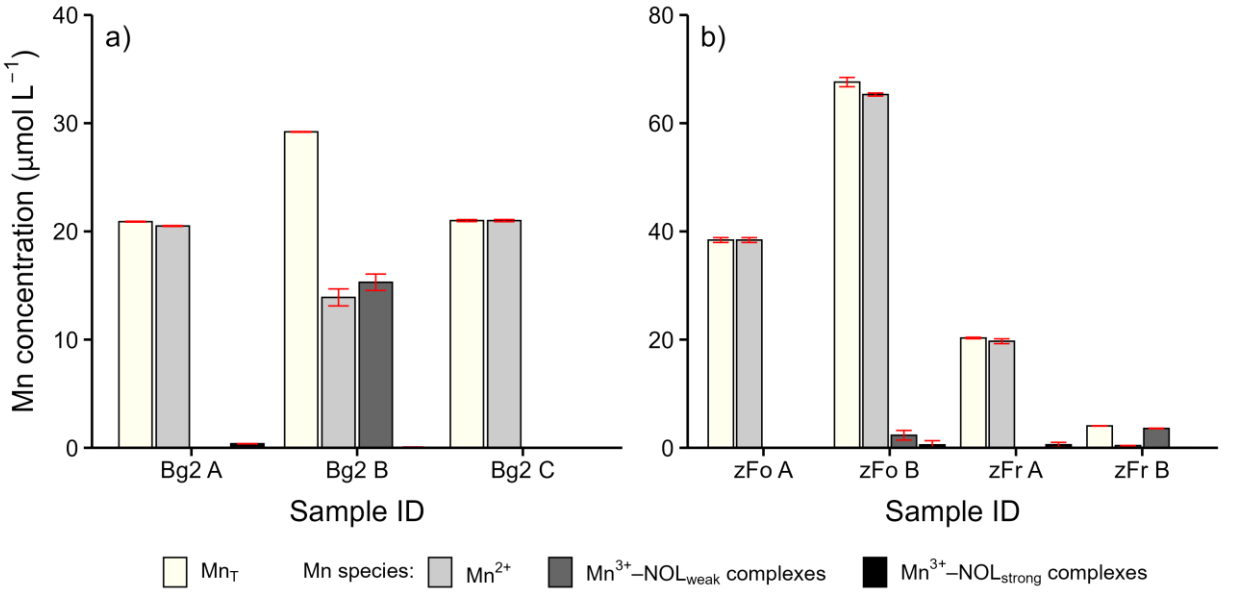

Figure 4.5 Results of Mn speciation by kinetic modeling on in situ soil solutions of a) the Calcaric Gleysol (Bg2 horizon, 3 samples) and b) the Salic Tidalic Fluvisol (zFo and zFr horizons, 2 samples each). Samples were measured in triplicate. The Mn speciation comprised total dissolved manganese concentrations (Mn_T, yellowish bar), including Mn^{2+} (light grey bar), Mn^{3+}–NOL_{weak} complexes (grey bar), and Mn^{3+}–NOL_{strong} complexes (black bar).

4.4 Discussion

4.4.1 Mn cycling

The solubility, mobility, and speciation of Mn are mainly controlled by E_H, pH, temperature, NOL availability, and closely related element cycles (Patrick and Turner 1968; Sparrow and Uren 2014; Wang et al. 2024). These parameters drive both reductive and oxidative pathways of abiotic and biotic origin (Section 4.4.3), contributing to Mn^{3+}–NOL complex formation (Li et al. 2021). Photochemical reactions were minimized in the microcosm experiments and are therefore not considered.

4.4.2 Mn speciation

Figure 4.6 shows the proposed Mn cycle focusing on the formation of Mn^{3+}–NOL complexes during the microcosm experiments in the Calcaric Gleysol. Although Mn speciation data revealed variability during the incubation experiments, we assume the following: (i) Mn^{2+} dominates across all redox conditions, (ii) Mn^{3+}–NOL complexes form under both

oxidizing and reducing conditions through biotic and abiotic pathways, and (iii) these complexes act as reactive intermediates during the oxidation of Mn^{2+} to Mn^{IV}.

During initial oxidizing conditions, Mn^{3+}–NOL complexes were not detectable because dissolved Mn_T was removed by adsorption and precipitation (Figure 4.6, Tables 4.S1–4.S4), consistent with oxidizing soil conditions (E_H > +300 mV) (Mansfeldt 2004; Patrick and Jugsujinda 1992). Under gradually increasing reducing conditions, dissolved Mn_T increased due to biotic and abiotic (non)-reductive dissolution processes, promoting Mn^{3+}–NOL complex formation (Li et al. 2021) (Figure 4.6). Notably, reoxidizing conditions lead to temporarily high Mn^{3+}–NOL proportions (up to 63%), but prolonged aeration caused the complete degradation of Mn^{3+}–NOL complexes and the depletion of the Mn_T pool (Table 4.S2). We propose that waterlogging–aeration cycles are critical for both the formation and stabilization of Mn^{3+}–NOL complexes. These cycles drive the Mn^{2+}–Mn^{IV} “redox wheel”, enabling transient Mn^{3+}–NOL complex formation (Figure 4.6).

Previous studies assumed that Mn^{2+} was the predominant Mn species in the investigated Calcaric Gleysol (Mansfeldt 2003, 2004), consistent with our findings. However, Mn^{3+}–NOL complexes were detected as a persistent, albeit minor, component of the dissolved Mn_T. The dominance of Mn^{2+} contrasts with previous reports of Mn^{3+}–NOL proportions up to 87% of Mn_T in acidic forest soils, including forest floor solutions, soil solutions, and soil extracts (Lux and Mansfeldt 2023; Lux et al. 2025). This discrepancy likely reflects site-specific factors in the Calcaric Gleysol, including (i) circumneutral to weakly alkaline pH, (ii) elevated native Ca^{2+} and competing cations (e.g. $Fe^{2+/3+}$), and (iii) soil mineral composition, including Mn oxides and rhodochrosite ($Mn^{II}CO_3$).

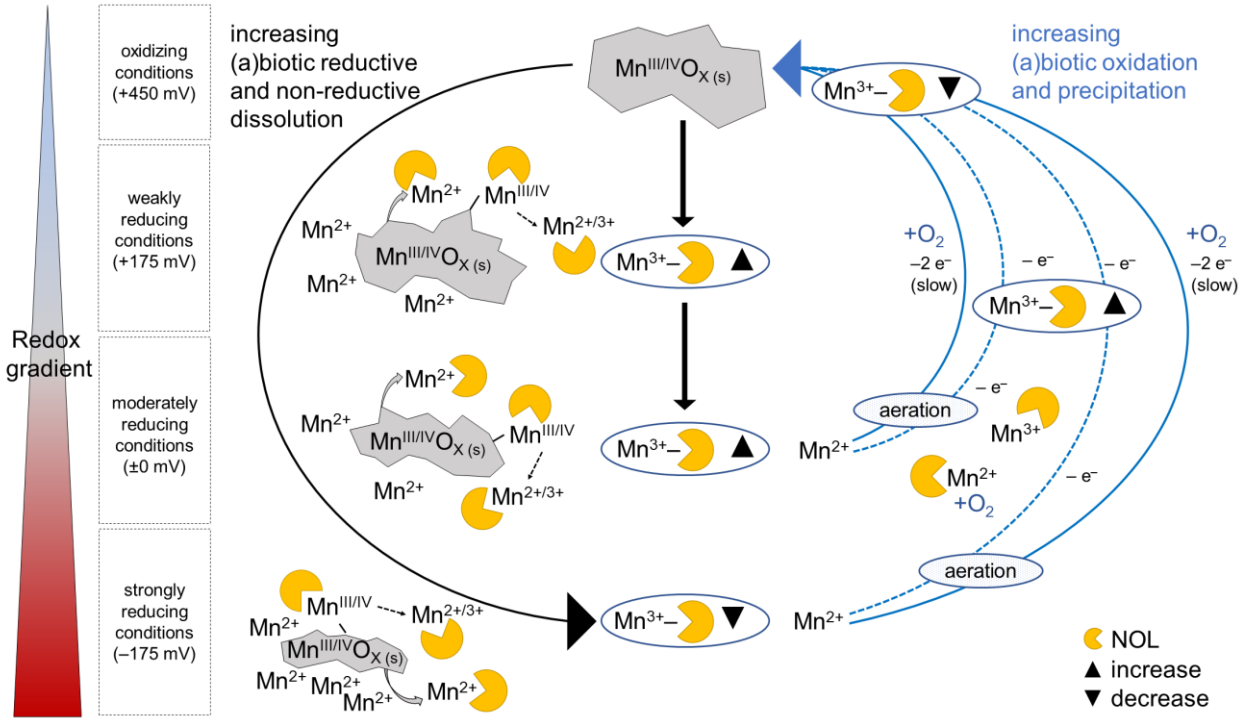

Figure 4.6 Schematic of the proposed Mn cycle and the formation of Mn^{3+}–NOL complexes during redox cycle experiments in the Calcaric Gleysol.

4.4.3 Biotic and abiotic pathways along defined redox conditions

Our results provide first insights into Mn speciation in a Calcaric Gleysol under defined redox conditions. Under reducing and reoxidizing conditions, Mn^{3+}–NOL complexes were detected, suggesting that both biotic and abiotic processes contribute to their formation and degradation via reductive and oxidative pathways, with NOLs stabilizing intermediate Mn^{3+} species.

Under initially oxidizing, circumneutral to weakly alkaline conditions, the already advanced biotic and abiotic oxidation of the Mn_T pool results in the precipitation of Mn^{IV} oxides. This process is coupled with DOC removal through adsorption and its subsequent transformation (Oldham et al. 2017b; Ma et al. 2020). The depletion of Mn^{2+} and Mn^{3+}–NOL complexes is typically driven by microbial oxidation, which can be several orders of magnitude faster (~10^3 at pH 8) than uncatalysed abiotic oxidation (Morgan 2005; Learman et al. 2011; Sparrow and Uren 2014). However, abiotic Mn^{2+} oxidation may become significant under circumneutral to alkaline conditions (Wang et al. 2024), particularly in the presence of catalytic mineral surfaces (Davies and Morgan 1989; Lan et al. 2017)

or when dissimilatory reduction is inhibited (Ma et al. 2020). Consequently, already advanced biotic and abiotic oxidation immobilizes Mn and suppresses Mn^{3+}–NOL complex formation.

Weakly reducing conditions and an increase in pH lead to an increase in Mn_T concentrations and initiate Mn^{3+}–NOL complex formation. Mn oxide reduction is often driven by a decrease in soil E_H induced by bacterial metabolic activities (Sparrow and Uren 2014). Dissimilatory reduction using NOLs as electron donors drives the dissolution of Mn oxides and Mn^{3+}–NOL complex formation via a one-electron transfer reaction (Oldham et al. 2017c; Li et al. 2021) [Eq. 2]:

$$Mn^{IV}O_2\,(s) + 4H^+ + e^- + NOL\,(aq) + bacteria_{(cat.)} \rightarrow Mn^{3+}\text{–}NOL\,(aq) + 2H_2O. \quad \text{[Eq. 2]}$$

Abiotic ligand-promoted reductive dissolution requires mineral surface-associated NOLs with reducing properties. Surface-bound Mn^{III} and Mn^{IV} are reduced via one- or two-electron transfer reactions, while NOLs are simultaneously oxidized. Subsequently, either the same NOLs form Mn^{2+}–NOL or Mn^{3+}–NOL complexes [Eqs. 3 and 4] or reductively released Mn^{2+} and Mn^{3+} are complexed by other NOLs without oxidation [Eqs. 5 and 6] (Lux et al. 2025):

$$Mn^{III}\,(s) + NOL\,(aq) + e^- \rightarrow Mn^{2+}\text{–}NOL\,(aq), \quad \text{[Eq. 3]}$$

$$Mn^{IV}\,(s) + NOL\,(aq) + e^- \rightarrow Mn^{3+}\text{–}NOL\,(aq), \quad \text{[Eq. 4]}$$

$$Mn^{2+}\,(aq) + NOL\,(aq) \rightarrow Mn^{2+}\text{–}NOL\,(aq), \quad \text{[Eq. 5]}$$

$$Mn^{3+}\,(aq) + NOL\,(aq) \rightarrow Mn^{3+}\text{–}NOL\,(aq). \quad \text{[Eq. 6]}$$

The stepwise biotic and abiotic reduction of Mn oxides thus produces transient Mn^{3+}–NOL complexes (Li et al. 2021), temporarily stabilizing Mn^{3+} and preventing immediate disproportionation [Eq. 7]:

$$2Mn^{3+}\text{–}NOL\,(aq) + 2H_2O \rightarrow Mn^{2+}\text{–}NOL_{ox}\,(aq) + Mn^{IV}O_2\,(s) + NOL_{ox}\,(aq) + 4H^+. \quad \text{[Eq. 7]}$$

Under moderately reducing conditions, increasing Mn_T concentrations indicate that $Mn^{III,IV}$ oxides act as electron acceptors and that reductive dissolution promotes Mn^{3+}–NOL complex formation and accumulation [Eqs. 2–6].

At strongly reducing conditions, the increasing reductive potential may promote the degradation of Mn^{3+}–NOL complexes through disproportionation [Eq. 7] or breakdown through reductants (Section 4.4.4). Reductive pathways dominate, rendering strongly reducing conditions unfavorable for Mn^{3+}–NOL stabilization, consistent with their low observed concentrations.

Under reoxidizing conditions, microbial catalysis (bacteria) accelerates Mn^{2+} oxidation. In the presence of NOLs (e.g. pyrophosphate), the first one-electron transfer forms Mn^{3+}–NOL complexes [Eq. 8] (Webb et al. 2005a). With continued reaeration, microbes further oxidize both free and complexed Mn^{3+} to poorly crystalline phyllomanganate phases (Webb et al. 2005a; Madison et al. 2013; Li et al. 2021) [Eq. 9]. However, the final mineral phase depends on geochemical conditions during and after oxidation (Webb et al. 2005b):

$$Mn^{2+}\ (aq) + O_2 + NOL\ (aq) + e^- + bacteria_{(cat.)} \rightarrow Mn^{3+}\text{–}NOL\ (aq), \qquad [Eq.\ 8]$$

$$Mn^{3+}\text{–}NOL\ (aq) + O_2 + e^- + bacteria_{(cat.)} \rightarrow Mn^{IV}O_2\ (s) + NOL^-\ (aq). \qquad [Eq.\ 9]$$

Morgan et al. (2021) propose three potential effects of abiotic ligand-promoted Mn^{2+} oxidation in the presence of O_2: i) Mn^{2+}–NOL complex formation, ii) Mn^{3+}–NOL complex formation, and iii) ligand adsorption onto Mn oxide surfaces.

Strongly binding NOLs form Mn^{2+}–NOL complexes that lower the availability of O_2-reactive species ($MnOH^+$, $Mn(OH)_2^0$), thereby inhibiting further oxidation to solid $Mn^{III/IV}$ phases (Morgan et al. 2021). These complexes can subsequently be oxidized to Mn^{3+}–NOL complexes. Additional Mn^{3+}–NOL formation pathways include ligand-promoted oxidation [Eq. 10] and superoxide-mediated oxidation during dark reactions [Eq. 11] (Oldham et al. 2017c). When Mn^{2+} and NOLs are adsorbed onto mineral surfaces, the surface-catalyzed oxidation of Mn^{2+} can take place, followed by Mn^{3+}–NOL complex formation [Eq. 12]:

$$Mn^{2+}\ (aq) + NOL \rightarrow Mn^{3+}\text{–}NOL_{red}\ (aq), \qquad [Eq.\ 10]$$

$$Mn^{2+}\ (aq) + O_2^{\bullet -} + 2H^+ + NOL\ (aq) \rightarrow Mn^{3+}\text{–}NOL\ (aq) + H_2O_2\ (aq), \qquad [Eq.\ 11]$$

Mn^{2+} (aq) + surface (s) + NOL (aq) → Mn^{3+}–NOL (aq). [Eq. 12]

Further abiotic, reductive dissolution mechanisms yielding Mn^{3+}–NOL complexes under oxidizing conditions include (i) ligand-promoted non-reductive dissolution [Eq. 13], (ii) ligand-promoted reductive dissolution [Eq. 14], and (iii) ligand exchange [Eq. 15] (Lux et al. 2025):

Mn^{III} (s) + NOL (aq) → Mn^{3+}–NOL (aq), [Eq. 13]

Mn^{IV} (s) + NOL (aq) + e^- → Mn^{3+}–NOL (aq), [Eq. 14]

Mn^{III}–OH (s) + NOL^- (aq) → Mn^{III}–NOL (aq) + OH^-
→ Mn^{3+} (aq) + NOL (aq) → Mn^{3+}–NOL (aq). [Eq. 15]

Mn^{3+}–NOL complexes have been shown to be relatively stable under oxic conditions, given sufficient ligand concentrations and appropriate pH, resisting rapid disproportionation or further oxidation (Oldham et al. 2017b, 2021; Lux and Mansfeldt 2023; Lux et al. 2025). Couture et al. (2015) reported that dissolved Mn is rapidly removed upon O_2 reintroduction, which is supported by our data (Figure 4.4, Tables 4.S1–4.S4), as abiotic oxidation is catalyzed by mineral surfaces such as ferrihydrite (Lan et al. 2017). Consequently, dissolved Mn species, including intermediate Mn^{3+}–NOL complexes, are immobilized through adsorption or precipitation.

Overall, biotic and abiotic redox transformations governing the Mn^{2+}–Mn^{IV} redox cycle frequently produce intermediate Mn^{3+}–NOL complexes via one-electron transfer reactions. Molecular orbital theory and experimental data (Luther 2005) confirm that one-electron transfer is thermodynamically and kinetically favored over two-electron transfer.

4.4.4 $Fe^{2+/3+}$ and sulfide–cycle interactions

In redoximorphic soils experiencing fluctuating redox conditions, Fe undergoes continuous redox-driven transformations, including the recurring formation and dissolution of Fe oxides (Yu et al. 2021).

Under initially oxidizing conditions, Fe predominantly occurs as Fe oxides that adsorb Mn^{2+} and catalyze its oxidation (Lan et al. 2017; Hu et al. 2023) while also partially

stabilizing NOLs against microbial degradation (Li et al. 2023). This immobilization of Mn^{2+} and NOLs restricts Mn^{3+}–NOL complex formation and contributes to Mn deficiency in the soil suspensions (Figure 4.4).

Under reducing conditions, Fe^{III} reduction begins at an E_H of approximately +100 mV (Patrick and Jugsujinda 1992). Once O_2 is depleted, oxide-bound Fe^{3+} serves as a terminal electron acceptor, driving the reductive dissolution of Fe^{3+} oxides (e.g. ferrihydrite, goethite) and Fe^{3+}–NOL complexes (Huang et al. 2021; Yu et al. 2021). This releases Fe^{2+} and NOLs into the suspension (Li et al. 2023) [Eq. 16], increasing the pool of reactive ligands:

$$4Fe^{III}(OH)_3\ (s) + CH_2O + 8H^+ \rightarrow 4Fe^{2+}\ (aq) + CO_2\ (g) + 11H_2O. \quad \text{[Eq. 16]}$$

Although Fe^{2+} could theoretically reduce Mn^{3+}–NOL complexes [Eq. 17], our results, consistent with Oldham et al. (2017b), indicate that these complexes resist reduction:

$$Mn^{3+}\text{–NOL}\ (aq) + Fe^{2+}\ (aq) \rightarrow Mn^{2+}\ (aq) + Fe^{3+}\text{–NOL}\ (aq). \quad \text{[Eq. 17]}$$

Ferrous iron can also reductively dissolve Mn oxides [Eq. 18] (Reddy et al. 2023), releasing Mn^{2+} into solution and supplying the Mn_T pool:

$$2MnO_2\ (s) + 2Fe^{2+}\ (aq) + 4H_2O \rightarrow 2Mn^{2+}\ (aq) + 2Fe(OH)_3\ (s) + 2H^+. \quad \text{[Eq. 18]}$$

During reoxidizing conditions, Fe^{2+} is rapidly oxidized (Mansfeldt et al. 2012), leading to the precipitation of poorly soluble short-range ordered Fe^{III} oxides (Huang et al. 2021) [Eq. 19]. This appears to be a recurrent process, as indicated by the Fe_o/Fe_d ratios in both soil horizons of the Calcaric Gleysol (Table 4.1). Subsequently, Fe oxides adsorb Fe^{2+} and Mn^{2+} and provide catalytic surfaces for rapid abiotic oxidation (Huang et al. 2021; Li et al. 2021), effectively immobilizing both metals:

$$4Fe^{2+}\ (aq) + O_2 + 10H_2O \rightarrow 4Fe^{III}(OH)_3\ (s) + 8H^+. \quad \text{[Eq. 19]}$$

The absence of detectable sulfides in our study can be attributed to (i) the unabated availability of Mn and Fe oxides as electron acceptors, delaying sulfate reduction (Yu et al. 2021); (ii) the reaction of sulfides with Mn and Fe oxides to form transient MnS and FeS (mackinawite) [Eqs. 20 and 21], followed by transformation to pyrite (FeS_2) (Huang et al. 2021); and (iii) the rapid oxidation of sulfides by Mn^{3+}–NOL complexes (Oldham et al. 2015, 2017a), preventing sulfide accumulation. The latter could explain the decrease in

overall Mn^{3+}–NOL complex proportions, particularly in Mn^{3+}–NOL_{weak} complexes, under strongly reducing conditions:

$$Mn^{IV}O_2\,(s) + 2HS^-\,(aq) \rightarrow Mn^{II}S\,(s) + 1/8S_8^0\,(s) + 2OH^-, \quad \text{[Eq. 20]}$$

$$2Fe^{III}(OH)_3\,(s) + 3HS^-\,(aq) \rightarrow 2Fe^{II}S\,(s) + 1/8S_8^0\,(s) + 3OH^- + 3H_2O. \quad \text{[Eq. 21]}$$

4.4.5 DOC interactions

DOC concentrations decreased slightly under initially oxidizing conditions due to adsorption onto Mn and Fe oxides and subsequent transformation to CO_2 (Li et al. 2021), which limited Mn^{3+}–NOL complex formation. Under reducing conditions, DOC increased as the reductive dissolution of Mn and Fe oxides released adsorbed DOC. Concurrently, the rise in pH enhanced DOM solubility (Grybos et al. 2009), increasing NOL availability and promoting Mn^{3+}–NOL complex formation. Under reoxidizing conditions, the precipitation of Fe and Mn oxides restored effective DOC adsorbents, scavenging DOC and limiting further Mn^{3+}–NOL complex formation. The analysis of MAs revealed a continuous decrease from initially oxidizing to reducing conditions and then to reoxidizing conditions, reflecting compositional changes in the DOC pool driven by (i) NOL–mineral interactions and associated adsorption/desorption processes, (ii) progressive DOC degradation via intermolecular redox reactions, and (iii) DOC transformation and mineralization to CO_2 (e.g. $CH_2O + O_2 \rightarrow CO_2 + H_2O$) (Trainer et al. 2021).

As reported previously (Lux et al. 2025), Mn_T:DOC ratios of ≥0.08 may suppress Mn^{3+}–NOL complex formation. In this study, however, values never exceeded this threshold (Tables 4.S5–4.S8), excluding Mn_T:DOC ratios as a critical factor.

4.4.6 The special role of calcium

The Calcaric Gleysol, developed from marine deposits, is high in Ca^{2+}. Under reducing conditions, Mn^{IV} and Fe^{III} oxides are reduced, while calcium carbonate ($Ca^{II}CO_3$) buffers the carbonate system. The resulting Fe^{2+} and Mn^{2+} may react with CO_3^{2-} to precipitate $MnCO_3$ and siderite ($Fe^{II}CO_3$), carbonate minerals that are characteristic of circumneutral to alkaline anoxic environments (Lebron and Suarez 1999; Koo and Kim 2020) [Eqs. 22 and 23]. The observed decrease in DIC concentrations under reducing conditions aligns

with carbonate precipitation (Tables 4.S5–4.S8), although other processes (e.g. respiration or degassing) may also contribute:

$$Mn^{2+}\,(aq) + CO_3^{2-}\,(aq) \rightarrow Mn^{II}CO_3\,(s), \qquad \text{[Eq. 22]}$$

$$Fe^{2+}\,(aq) + CO_3^{2-}\,(aq) \rightarrow Fe^{II}CO_3\,(s). \qquad \text{[Eq. 23]}$$

During reoxidizing conditions, carbonate minerals can dissolve (the reverse of Eqs. 22 and 23), increasing DIC, while Fe^{2+} and Mn^{2+} are oxidized biotically and abiotically [Eqs. 24 and 25]; for Mn, this likely involves transient Mn^{3+}–NOL complex formation:

$$Mn^{2+}\,(aq) + 2H_2O \rightarrow Mn^{IV}O_2\,(s) + 4H^+, \qquad \text{[Eq. 24]}$$

$$Fe^{2+}\,(aq) + 3H_2O \rightarrow Fe^{III}(OH)_3\,(s) + 3H^+. \qquad \text{[Eq. 25]}$$

The release of H^+ during Fe and Mn oxidation lowers pH and promotes $CaCO_3$ dissolution [Eq. 26], explaining the relatively stable Ca^{2+} concentrations observed during reoxidizing conditions (Tables 4.S9–4.S12):

$$CaCO_3\,(s) + 2H^+ \rightarrow Ca^{2+}\,(aq) + CO_2\,(aq) + H_2O. \qquad \text{[Eq. 26]}$$

Additionally, Ca^{2+} can act as a bridging ion between negatively charged NOLs and Mn oxide surfaces, promoting inner- and outer-sphere complexation as well as electrostatic interactions (Cheng et al. 2019). This immobilizes NOLs, limiting Mn^{2+} or Mn^{3+} complexation. Furthermore, Ca^{2+} facilitates the formation of height molecular weight DOM aggregates under circumneutral conditions (Kalinichev et al. 2011), possibly explaining the MA increase at the end of the incubation experiments. Similar effects were not present in Na^+ and Mg^{2+} solutions (Iskrenova-Tchoukova et al. 2010).

4.4.7 Trivalent manganese under field conditions

Our results provide clear evidence for Mn^{3+}–NOL complexes under natural conditions at both study sites (A and B), with (i) pronounced heterogeneity within the horizons and (ii) high proportions relative to Mn_T in individual samples.

In the Calcaric Gleysol, weakly reducing conditions induced by groundwater promote Mn^{3+}–NOL formation, likely via pathways similar to those observed in microcosm experiments [Eqs. 2–6]. In the Salic Tidal Fluvisol, Mn^{3+}–NOL complexes may represent

a considerable portion of the Mn_T pool in the transition zone between terrestrial and marine ecosystems.

Spatial and temporal E_H zonation in soils drives heterogeneity in physico-chemical processes (e.g. sorption, redox reactions) and biological processes (e.g. microbial community structure, microbial activity, and metabolic pathways), as well as broader gradients in E_H, pH, and dissolved O_2 due to aerobic and anaerobic microsites over short distances (Zhang and Furman 2021; Lacroix et al. 2023). Consequently, natural soil solutions exhibit greater E_H variability than incubated soil suspensions under defined E_H conditions. Fluctuating groundwater levels and O_2 diffusion further influence these dynamics, indicating that Mn^{3+}–NOL formation *in situ* is governed by (microscale) processes not captured in controlled experiments.

These findings highlight Mn^{3+}–NOL complexes as an important component of the soil Mn_T pool. However, the conclusions are limited to the studied horizons and represent an initial step toward understanding their formation under natural conditions.

4.4.8 Environmental implications

Despite the dominance of Mn^{2+} across all redox conditions in the microcosm experiments, we provide evidence for the formation of Mn^{3+}–NOL complexes. Although they are minor in concentration, these complexes represent a non-negligible component of the Mn_T pool, often not covered in conventional Mn speciation analysis.

Strongly coupled to the presence and composition of NOLs, Mn^{3+}–NOL complexes link C dynamics, including lignin decomposition and organic pollutant degradation, to Mn cycling. Once complexed, Mn^{3+} resists immediate degradation, even in the presence of reductants like Fe^{2+}.

Field observations in the Calcaric Gleysol and the Salic Tidalic Fluvisol demonstrate that fluctuating redox conditions, induced by variable groundwater tables, regulate both Mn mobilization and Mn^{3+}–NOL complex dynamics. Future hydrological changes (e.g. more frequent drought–rainfall cycles, sea-level rise) will likely modify redox cycles, affecting Mn mobilization and species distribution. Reactive Mn^{3+}–NOL intermediates may influence redox buffering, microbial activity, plant nutrient availability, Mn leaching, and trace element cycling.

These insights demonstrate that precise Mn speciation is more relevant than previously assumed. Recognizing Mn^{3+}–NOL complexes as both redox-active and persistent redefines our understanding of Mn cycling in terrestrial environments. Their implementation in geochemical models is essential for accurately predicting Mn species dynamics in soils.

4.5 Conclusions

Mn^{3+}–NOL complexes, although they are less abundant than Mn^{2+}, constitute a non-negligible component of the Mn_T pool in redoximorphic soils under defined redox conditions. We hypothesize that waterlogging–aeration cycles promote transient Mn^{3+}–NOL complex formation, potentially influencing the following soil biogeochemical processes, e.g., nutrient cycling and plant availability; DOM decomposition, modulating C turnover and storage; microbial activity, by serving as alternative electron acceptors under strongly reducing conditions; and Mn mobility and leaching. Field observations confirm Mn^{3+}–NOL complexes in soils with temporarily reducing conditions. Compared with previous findings in an acidic forest soil, our findings highlight the role of site-specific physico-chemical properties (e.g. E_H, pH, and NOL composition) in controlling Mn^{3+}–NOL complex formation, stabilization, and degradation. Within the scope of this study, it was not possible to conduct a detailed investigation of the influence of sulfides on Mn speciation, particularly regarding the formation of Mn^{3+}–NOL complexes. Future research should address this aspect in order to clarify the role of sulfides more precisely. In addition, we recommend *in situ* monitoring of Mn^{3+}–NOL complex dynamics in soils, especially in transition zones with waterlogging–aeration cycles.

Author contributions

Constantin Lux: investigation, formal analysis, writing – review and editing, visualization, validation, methodology, writing – original draft, conceptualization, data curation.

Tim Mansfeldt: resources, supervision, funding acquisition, project administration, writing – review and editing, validation.

Acknowledgements

Financial support was provided by the Deutsche Forschungsgemeinschaft (DFG) (German Research Foundation) under the contract number Ma 2143/17-1 and is gratefully acknowledged. The authors thank Jana Glombitza, Karin Greef, and Nicole Mantke for technical assistance in the laboratory and field.

Conflicts of Interest

The authors declare no conflicts of interest.

Data Availability Statement

The data that support the findings of this study are available from the corresponding author upon reasonable request.

References

Abril, G., Commarieu, M.-V., Etcheber, H., Deborde, J., Deflandre, B., Zivadinovic, M. K., Chaillou, G. and Anschutz, P. 2010. “In vitro simulation of oxic/suboxic diagenesis in an estuarine fluid mud subjected to redox oscillations.” *Estuarine Coastal and Shelf Science*, 88, no. 2: 279–291. https://doi.org/10.1016/j.ecss.2010.04.00

Anschutz, P., Bouchet, S., Abril, G., Bridou, R., Tessier, E. and Amouroux, D. 2019. “In vitro simulation of oscillatory redox conditions in intertidal sediments: N, Mn, Fe, and P coupling.” *Continental Shelf Research*, 177: 33–41. https://doi.org/10.1016/j.csr.2019.03.007

Berg, B., Steffen, K. T. and McClaugherty, C. 2007. “Litter decomposition rate is dependent on litter Mn concentrations.” *Biogeochemistry*, 82: 29–39. https://doi.org/10.1007/s10533-006-9050-6

Cheng, H., Ma, J., Jiang, J., Pang, S.-Y., Yang, T. and Wang, P. 2019. “Aggregation kinetics of manganese oxides formed from permanganate activated by (Bi)sulfite: Dual role of Ca^{2+} and $Mn^{II/III}$.” *Water Research*, 159: 454–463. https://doi.org/10.1016/j.watres.2019.05.033

Couture, R.-M., Laurent, C., Markelova, E., Madé, B. and Parsons, C. T. 2015. “On–off mobilization of contaminants in soils during redox oscillations.” *Environmental Science & Technology*, 49, no. 5: 3015–3023. https://doi.org/10.1021/es5061879

Davies, S. H. R. and Morgan, J. J. 1989. “Manganese(II) oxidation-kinetics on metal oxide surfaces.” *Journal of Colloid and Interface Science*, 129, no. 1: 63–77. https://doi.org/10.1016/0021-9797(89)90416-5

Dorau, K. and Mansfeldt, T. 2016. “Comparison of redox potential dynamics in a diked marsh soil: 1990 to 1993 versus 2011 to 2014.” *Journal of Plant Nutrition and Soil Science*, 179, no. 5: 641–651.

Engelbrektson, A., Hubbard, C. G., Tom, L. M., Boussina, A., Jin, Y. T., Wong, H., Piceno, Y. M., Carlson, H. K., Conrad, M. E., Anderson, G. and Coates, J. D. 2014. “Inhibition of microbial sulfate reduction in a flow-through column system by (per)chlorate treatment.” *Frontiers in Microbiology*, 5: 315. https://doi.org/10.3389/fmicb.2014.00315

Gotoh, S. and Patrick Jr., W. H. 1972. “Transformation of manganese in a waterlogged soil as affected by redox potential and pH.” *Soil Science Society of America Proceedings*, 36, no. 5: 738–742. https://doi.org/10.2136/sssaj1972.03615995003600050018x

Grybos, M., Davranche, M., Gruau, G., Petitjean, P. and Pédrot, M. 2009. “Increasing pH drives organic matter solubilization from wetland soils under reducing conditions.” *Geoderma*, 154, no. 1–2: 13–19. https://doi.org/10.1016/j.geoderma.2009.09.001

Hoffmann, D. 1991. “Sea level changes at the Schleswig-Holsteinian North sea coast during the last 3000 years.” *Quarternary International*, 9: 61–65. https://doi.org/10.1016/1040-6182(91)90064-U

Hofrichter, M. 2002. “Review: Lignin conversion by manganese peroxidase (MnP).” *Enzyme and Microbial Technology*, 30, no. 4: 454–466. https://doi.org/10.1016/S0141-0229(01)00528-2

Hu, S., Zheng, L., Zhang, H., Chen, G., Yang, Y., Ouyang, Z., Chen, S., Gao, K., Liu, C., Wang, Q. and Liu, T. 2023. “Hematite-mediated Mn(II) abiotic oxidation under oxic conditions: pH effect and mineralization.” *Journal of Colloid and Interface Science*, 636: 267–278. https://doi.org/10.1016/j.jcis.2023.01.034

Huang, J., Jones, A., Waite, T. D., Chen, Y., Huang, X., Rosso, K. M., Kappler, A., Mansor, M., Tratnyek, P. G. and Zhang, H. 2021. “Fe(II) redox chemistry in the environment.” *Chemical Reviews*, 121, no. 13: 8161–8233. https://doi.org/10.1021/acs.chemrev.0c01286

Iskrenova-Tchoukova, E., Kalinichev, A. G. and Kirkpatrick, R. J. 2010. “Metal cation complexation with natural organic matter in aqueous solutions: Molecular dynamics simulations and potentials of mean force.” *Langmuir*, 26, no. 10: 15909–15919. https://doi.org/10.1021/la102535n

IUSS Working Group WRB. 2022. “*World Reference Base for Soil Resources. International soil classification system for naming soils and creating legends for soil maps.*” 4th edition. International Union of Soil Sciences (IUSS), Vienna, Austria. https://files.isric.org/public/documents/WRB_fourth_edition_2022-12-18.pdf, accessed October 2025.

Johnson, K. L., McCann, C. M., Wilkinson, J.-L., Jones, M., Tebo, B. M., West, M., Elgy, C., Clarke, C. E., Gowdy, C. and Hudson-Edwards, K. A. 2018. “Dissolved Mn(III) in water treatment works: Prevalence and significance.” *Water Research*, 140: 181–190. https://doi.org/10.1016/j.watres.2018.04.038

Kalinichev, A. G., Iskrenova-Tchoukova, E., Ahn, W.-Y., Clark, M. M. and Kirkpatrick, R. J. 2011. “Effects of Ca^{2+} on supramolecular aggregation of natural organic matter in aqueous solutions: A comparison of molecular modeling approaches.” *Geoderma*, 169: 27–32. https://doi.org/10.1016/j.geoderma.2010.09.002

Koo, T.-h. and Kim, J. 2020. “Controls on the formation and stability of siderite ($FeCO_3$) and chukanovite ($Fe_2(CO_3)(OH)_2$) in reducing environment.” *Minerals*, 10, no. 2: 156. https://doi.org/10.3390/min10020156

Lacroix, E. M., Aeppli, M., Boye, K., Brodie, E., Fendorf, S., Keiluweit, M., Naughton, H. R., Noël, V. and Sihi, D. 2023. “Consider the anoxic microsite: Acknowledging and appreciating spatiotemporal redox heterogeneity in soils and sediments.” *ACS Earth and Space Chemistry*, 7, no. 9: 1592–1609. https://doi.org/10.1021/acsearthspacechem.3c00032

Lan, S., Wang, X., Xiang, Q., Yin, H., Tan, W., Qiu, G., Liu, F., Zhang, J. and Feng, X. 2017. “Mechanisms of Mn(II) catalytic oxidation on ferrihydrite surfaces and the formation of manganese (oxyhydr)oxides.” *Geochimica et Cosmochimica Acta*, 211: 79–96. https://doi.org/10.1016/j.gca.2017.04.044

Learman, D. R., Voelker, B. M., Vazquez-Rodriguez, A. I. and Hansel, C.M. 2011. “Formation of manganese oxides by bacterially generated superoxide.” *Nature Geoscience*, 4: 95–98. https://doi.org/10.1038/ngeo1055

Lebron, I. and Suarez, D. L. 1999. “Mechanisms and precipitation rate of rhodochrosite at 25°C as affected by PCO2 and organic ligands.” *Soil Science Society of America Journal*, 63, no. 3: 561–568. https://doi.org/10.2136/sssaj1999.03615995006300030019x

Li, H., Santos, F., Butler, K. and Herndon, E. 2021. “A critical review on the multiple roles of manganese in stabilizing and destabilizing soil organic matter.” *Environmental Science & Technology*, 55, no. 18: 12136–12152. https://doi.org/10.1021/acs.est.1c00299

Li, Q., Hu, W., Li, L. and Li, Y. 2023. “Interactions between organic matter and Fe oxides at soil micro-interfaces: Quantification, associations, and influencing factors.” *Science of the Total Environment*, 855: 158710. https://doi.org/10.1016/j.scitotenv.2022.158710

Luther 3rd, G. W. 2005. “Manganese(II) oxidation and Mn(IV) reduction in the environment - Two one-electron transfer steps versus a single two-electron step.” *Geomicrobiology Journal*, 22, no. 3–4: 195–203. https://doi.org/10.1080/01490450590946022

Luther 3rd, G. W., Madison, A. S., Mucci, A., Sundby, B. and Oldham, V. E. 2015. “A kinetic approach to assess the strengths of ligands bound to soluble Mn(III).” *Marine Chemistry*, 173: 93–99. https://doi.org/10.1016/j.marchem.2014.09.006

Lux, C. and Mansfeldt, T. 2023. “Evidence of dissolved trivalent manganese in acidic forest soils.” *Journal of Plant Nutrition and Soil Science*, 186, no. 3: 321–329. https://doi.org/10.1002/jpln.202200271

Lux, C., Ufer, K. and Mansfeldt, T. 2025. “Dissolved trivalent manganese in forest soils - Interactions of natural organic ligands with manganese oxides.” *Environmental Science: Processes & Impacts*, 27, no. 9: 2875–2893. https://doi.org/10.1039/D5EM00388A

Ma, D., Wu, J., Yang, P. and Zhu, M. 2020. “Coupled manganese redox cycling and organic carbon degradation on mineral surfaces.” *Environmental Science & Technology*, 54, no. 14: 8801–8810. https://doi.org/10.1021/acs.est.0c02065

Madison, A. S., Tebo, B. M. and Luther 3rd, G. W. 2011. “Simultaneous determination of soluble manganese(III), manganese(II) and total manganese in natural (pore)waters.” *Talanta*, 84, no. 2: 374–381. https://doi.org/10.1016/j.talanta.2011.01.025

Madison, A. S., Tebo, B. M., Mucci, A., Sundby, B. and Luther 3rd, G. W. 2013. “Abundant porewater Mn(III) Is a major component of the sedimentary redox system.” *Science*, 341, no. 6148: 875–878. https://doi.org/10.1126/science.1241396

Mansfeldt, T. 2003. “In situ long-term redox potential measurements in a dyked marsh soil.” *Journal of Plant Nutrition and Soil Science*, 166, no. 2: 210–219. https://doi.org/10.1002/jpln.200390031

Mansfeldt, T. 2004. “Redox potential of bulk soil and soil solution concentration of nitrate, manganese, iron, and sulfate in two Gleysols.” *Journal of Plant Nutrition and Soil Science*, 167, no. 1: 7–16. https://doi.org/10.1002/jpln.200321204

Mansfeldt, T., Schuth, S., Häusler, W., Wagner, F. E., Kaufhold, S. and Overesch, M. 2012. “Iron oxide mineralogy and stable iron isotope composition in a Gleysol with petrogleyic properties.” *Journal of Soils and Sediments*, 12: 97–114. https://doi.org/10.1007/s11368-011-0402-z

Mehra, O. P. and Jackson, M. L. 1958. “Iron oxide removal from soils and clays by a dithionite-citrate system buffered with sodium bicarbonate.” *Clays and Clay Minerals*, 7: 317–327. https://doi.org/10.1346/CCMN.1958.0070122

Morgan, J. J. 2005. “Kinetics of reaction between O_2 and Mn(II) species in aqueous solutions.” *Geochimica et Cosmochimica Acta*, 69, no. 1: 35–48. https://doi.org/10.1016/j.gca.2004.06.013

Morgan, J. J., Schlautman, M. A. and Bilinski, H. 2021. “Rates of abiotic Mn^{II} oxidation by O_2: Influence of various multidentate ligands at high pH.” *Environmental Science & Technology*, 55, no. 21: 14426–14435. https://doi.org/10.1021/acs.est.1c01795

Oldham, V. E., Chmiel, R., Hansel, C. M., DiTullio, G. R., Rao, D. and Saito, M. 2021. “Inhibited manganese oxide formation hinders cobalt scavenging in the Ross Sea.” *Global Biogeochemical Cycles*, 35, no. 5: e2020GB006706. https://doi.org/10.1029/2020GB006706

Oldham, V. E., Jones, M. R., Tebo, B. M. and Luther 3rd, G. W. 2017a. “Oxidative and reductive processes contributing to manganese cycling at oxic-anoxic interfaces.” *Marine Chemistry*, 195: 122–128. https://doi.org/10.1016/j.marchem.2017.06.002

Oldham, V. E., Miller, M. T., Jensen, L. T. and Luther 3rd, G. W. 2017b. “Revisiting Mn and Fe removal in humic rich estuaries.” *Geochimica et Cosmochimica Acta*, 209: 267–283. https://doi.org/10.1016/j.gca.2017.04.001

Oldham, V. E., Mucci, A., Tebo, B. M. and Luther 3rd, G. W. 2017c. “Soluble Mn(III)-L complexes are abundant in oxygenated waters and stabilized by humic ligands.” *Geochimica et Cosmochimica Acta*, 199: 238–246. https://doi.org/10.1016/j.gca.2016.11.043

Oldham, V. E., Owings, S. M., Jones, M. R., Tebo, B. M. and Luther 3rd, G. W. 2015. “Evidence for the presence of strong Mn(III)-binding ligands in the water column of the Chesapeake Bay.” *Marine Chemistry*, 171: 58–66. https://doi.org/10.1016/j.marchem.2015.02.008

Patrick Jr., W. H. and Jugsujinda, A. 1992. “Sequential reduction and oxidation of inorganic nitrogen, manganese, and iron in flooded soil.” *Soil Science Society of America Journal*, 56, no. 4: 1071–1073. https://doi.org/10.2136/sssaj1992.03615995005600040011x

Patrick, WM. H. and Turner, F. T. 1968. “Effect of redox potential on manganese transformation in waterlogged soil.” *Nature*, 220: 476–478. https://doi.org/10.1038/220476a0

Reddy, K. R., DeLaune, R. D. and Inglett, P. W. 2023. *Biogeochemistry of Wetlands. Science and Applications*. 2nd edition. CRC Press.

Rodríguez, F. J., Schlenger, P. and García-Valverde, M. 2016. “Monitoring changes in the structure and properties of humic substances following ozonation using UV-Vis, FTIR and ^{1}H NMR techniques.” *Science of the Total Environment*, 541: 623–637. https://doi.org/10.1016/j.scitotenv.2015.09.127

Schwab, A. P. and Lindsay, W. L. 1983. “The effect of redox on the solubility and availability of manganese in a calcareous soil.” *Soil Science Society of America Journal*, 47, no. 2: 217–220. https://doi.org/10.2136/sssaj1983.03615995004700020008x

Schwertmann, U. 1964. “Differenzierung der Eisenoxide des Bodens durch Extraktion mit Ammoniumoxalat-Lösung.” *Zeitschrift für Pflanzenernährung, Düngung, Bodenkunde*, 105, no. 3: 194–202. https://doi.org/10.1002/jpln.3591050303

Sparrow, L. A. and Uren, N. C. 2014. “Manganese oxidation and reduction in soils: Effects of temperature, water potential, pH and their interactions.” *Soil Research*, 52, no. 5: 483–494. https://doi.org/10.1071/SR13159

Stendahl, J., Berg, B. and Lindahl, B. D. 2017. “Manganese availability is negatively associated with carbon storage in northern coniferous forest humus layers.” *Scientific Reports*, 7: 15487. https://doi.org/10.1038/s41598-017-15801-y

Trainer, E. L., Ginder-Vogel, M. and Remucal, C. K. 2021. “Selective reactivity and oxidation of dissolved organic matter by manganese oxides.” *Environmental Science & Technology*, 55, no. 17: 12084–12094. https://doi.org/10.1021/acs.est.1c03972

Viollier, E., Inglett, P. W., Hunter, K., Roychoudhury, A. N. and Van Cappellen, P. 2000. “The ferrozine method revisited: Fe(II)/Fe(III) determination in natural waters.”

Applied Geochemistry, 15, no. 6: 785–790. https://doi.org/10.1016/S0883-2927(99)00097-9

Wang, X., Jones, M. R., Pan, Z., Lu, X., Deng, Y., Zhu, M. and Wang, Z. 2024."Trivalent manganese in dissolved forms: Occurrence, speciation, reactivity and environmental geochemical impact." *Water Research*, 263: 122198. https://doi.org/10.1016/j.watres.2024.122198

Webb, S. M., Dick, G. J., Bargar, J. R. and Tebo, B. M. 2005a. "Evidence for the presence of Mn(III) intermediates in the bacterial oxidation of Mn(II)." *Proceedings of the National Academy of Sciences of the United States of America*, 102, no. 15: 5558–5563. https://doi.org/10.1073/pnas.0409119102

Webb, S. M., Tebo, B. M. and Bargar, J. R. 2005b. "Structural characterization of biogenic Mn oxides produced in seawater by the marine bacillus sp. strain SG-1." *American Mineralogist*, 90, no. 8–9: 1342–1357. https://doi.org/10.2138/am.2005.1669

Weishaar, J. L., Aiken, G. R., Bergamaschi, B. A., Fram, M. S., Fujii, R. and Mopper, K. 2003. "Evaluation of specific ultraviolet absorbance as an indicator of the chemical composition and reactivity of dissolved organic carbon." *Environmental Science & Technology*, 37, no. 20: 4702–4708. https://doi.org/10.1021/es030360x

Yu, C., Xie, S., Song, Z., Xia, S. and Åström, M. E. 2021. "Biogeochemical cycling of iron (hydr-)oxides and its impact on organic carbon turnover in coastal wetlands: A global synthesis and perspective." *Earth-Science Reviews*, 218: 103658. https://doi.org/10.1016/j.earscirev.2021.103658

Zhang, S., Li, B., Chen, Y., Zhu, M., Pedersen, J. A., Gu, B., Wang, Z., Li, H., Liu, J., Zhou, X.-Q., Hao, Y.-Y., Jiang, H., Liu, F., Liu, Y.-R. and Yin, H. 2023. "Methylmercury degradation by trivalent manganese." *Environmental Science & Technology*, 57, no. 14: 5988–5998. https://doi.org/10.1021/acs.est.3c00532

Zhang, Z. and Furman, A. 2021. "Soil redox dynamics under dynamic hydrologic regimes - A review." *Science of the Total Environment*, 763: 143026. https://doi.org/10.1016/j.scitotenv.2020.143026

Supplementary Information

for

Dissolved trivalent manganese under defined redox conditions in redoximorphic soils: laboratory and field evidence

Microcosm unit and application

The microcosm unit features a reactor vessel with a working volume of 1.7 L and a headspace volume of 0.5 L. The reactor vessel was made of borosilicate glass, while all the other components were fabricated from stainless steel. This microcosm setup enabled the continuous monitoring of redox potential (E_H) (E_H electrode: Ag/AgCl, Z061023511, AppliSens, Applikon Biotechnology BV, Delft, The Netherlands), pH (pH electrode: Z001023551, AppliSens, Applikon Biotechnology BV, Delft, The Netherlands), partial pressure of O_2 (pO_2) (pO_2 polarographic sensor: Z010023525, AppliSens, Applikon Biotechnology BV, Delft, The Netherlands), and temperature (electric resistance: Pt-100). Prior to each experiment, the E_H electrode and the pH electrode were polished, checked (pH and E_H) using standard buffer solutions, and calibrated (pH) (Markelova et al., 2017).

Redox cycles

Redox cycle I:

To allow the soil suspension to equilibrate, the E_H was maintained under oxidizing conditions during the first week (t = 1–7 days). In the second week, three samples were extracted using a syringe at t = 8, 10, and 12 days. The system was then shifted to weakly reducing conditions (t = 15) and subsequently to moderately reducing conditions (t = 29). Sampling was conducted following the same scheme at t = 22, 24, and 26 days under weakly reducing conditions, and at t = 36, 38, and 40 days under moderately reducing conditions. Finally, the system was returned to reoxidizing conditions (t = 43) to simulate aeration. Because aeration is a rapid process, the sampling intervals were shortened (t = 43.5, 44, 45, and 47 days). Thus, in the ideal case, the redox cycle I had a total duration of 47 days.

Redox cycle II:

The initial phase of redox cycle II followed the same pattern as cycle I. The soil suspension was allowed one week (t = 1–7 days) to equilibrate under initial oxidizing conditions. Sampling was conducted in the second week at t = 8, 10, and 12 days. Subsequently, the system was shifted to strongly reducing conditions (t = 15). Because bioavailable Mn and Fe oxides in the soil can act as redox buffers during the reduction process, the duration of the experiment could not be predicted precisely. The main objective was therefore to achieve strongly reducing conditions within a reasonable time frame that did not exceed that of redox cycle I. At the end of redox cycle II, the system was switched back to reoxidizing conditions, and four samples were extracted by syringe following the same scheme as in cycle I to investigate the suspension under reoxidizing conditions.

Mn speciation and kinetic modeling

Kinetic modeling of the non-reduced samples [Eq. 1] allowed to determine the concentrations of Mn^{2+} and Mn^{3+}–NOL_{weak} complexes, while the reduced samples [Eq. 2] provided the combined concentrations of Mn^{2+} and all forms of Mn^{3+}–NOL complexes including Mn^{3+}–NOL_{strong} complexes. The concentration of Mn^{3+}–NOL_{strong} complexes was calculated using [Eq. 3]. For reliable differentiation of Mn^{2+} and Mn^{3+}–NOL_{weak} complexes, the kinetic constraint $k_1 \geq 3*k_2$ must be satisfied (Thibault de Chanvalon and Luther, 2019).

Five-parameter equation:

$$Mn_T = (Mn^{3+}\text{–}T(4\text{-}CP)P)_T = Mn^{2+} \cdot (1 - e^{-k_1 \cdot (t - t_0)}) + Mn^{3+}\text{–}NOL_{weak} \cdot (1 - e^{-k_2 \cdot (t - t_0)}) \quad \text{[Eq. 1]}$$

where Mn^{2+} = Mn^{2+} concentration (µmol L^{-1}); Mn^{3+}–NOL_{weak} = Mn^{3+}–NOL_{weak} concentration (µmol L^{-1}); k_1 = Mn^{2+} rate constant (s^{-1}); k_2 = Mn^{3+}–NOL_{weak} rate constant (s^{-1}); t = reaction time (s); and t_0 = reaction start (s).

Three-parameter equation:

$$Mn_{T(hydroxylamine)} = Mn^{2+} \cdot (1 - e^{-k_1 \cdot (t - t_0)}) \quad \text{[Eq. 2]}$$

where Mn^{2+} = Mn^{2+} concentration (µmol L^{-1}); k_1 = Mn^{2+} rate constant (s^{-1}); t = reaction time (s); and t_0 = reaction start (s).

$$Mn^{3+}\text{–}NOL_{strong} = Mn_{T(hydroxylamine)} - (Mn^{2+} + Mn^{3+}\text{–}NOL_{weak}) \quad \text{[Eq. 3]}$$

Kinetic modeling was performed based on a written code in R (version 4.5.1) in the RStudio environment (version 2025.05.1) employing the *nlmrt* package (version 2016.3.2). Parameter estimation proceeded by (i) employing the *wrapnls* method with the *nlxb* algorithm, applying predefined lower and upper limits for each parameter, followed by (ii) refinement using the nonlinear least squares (*nls*) method from the *stats* package (version 4.5.1). The goodness of fit was assessed through root mean square error (RMSE) analysis. As previously outlined by Johnson et al. (2018), Lux and Mansfeldt (2023), and Lux et al. (2025), smaller rate constants (k_1) for the $MnCl_2 \cdot 4H_2O$ standards were observed in contrast to Madison et al. (2011), with reaction completion typically occurring within approximately 90 s. This discrepancy was considered in the modeling process.

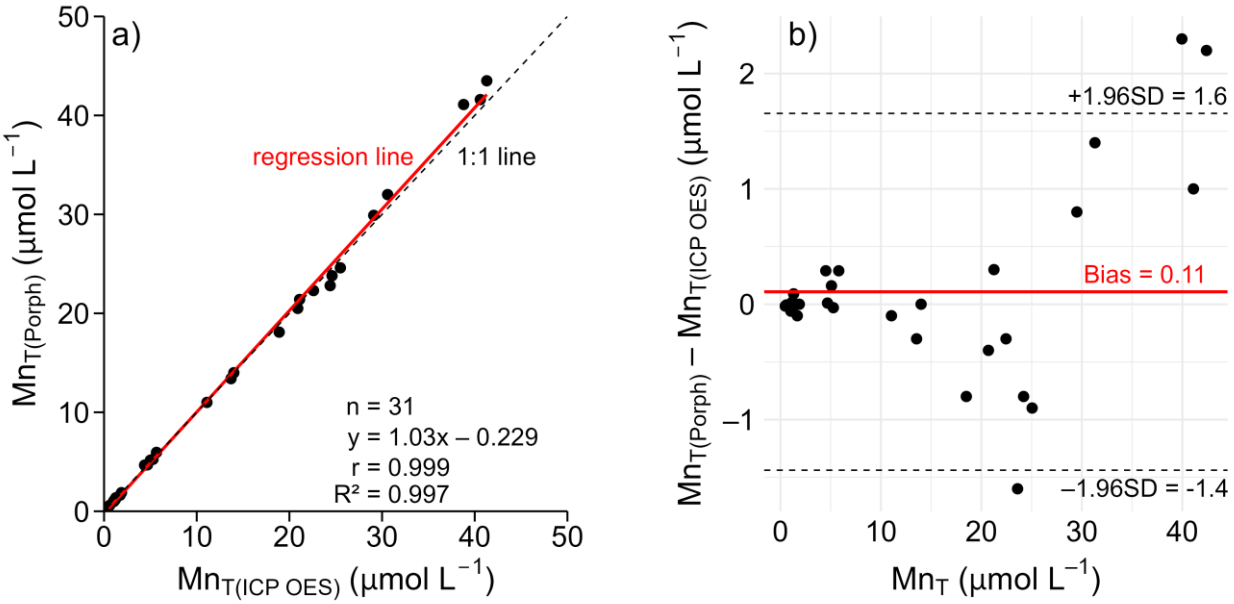

Figure 4.S1 Representation of a) the linear regression of porphyrin kinetic modeled total manganese concentrations (Mn_T) against Mn_T concentrations analyzed by inductively coupled plasma emission spectrometry (ICP OES) in soil suspensions (Calcaric Gleysol; AhBG and Bg horizons) of the microcosm experiments, and b) the Bland–Altman plot comparing the two methods for the same samples.

Table 4.S1 Dataset of the Mn speciation analysis including Mn_T, Mn^{2+}, Mn^{3+}–NOL complexes, k-values and ICP OES data (Mn_T) of the AhBg microcosm experiment (redox cycle I).

Sample ID (–)	time (d)	pH (–)	$E_{H(pH=7)}$ (mV)	dO_2 (%)	$Mn_{T(ICP)}$ (µmol L^{-1})	$Mn_{T(Porph)}$ Range (µmol L^{-1})	$Mn_{T(Porph)}$ Mean (µmol L^{-1})	$Mn_{T(Porph)}$/ $Mn_{T(ICP\ OES)}$ (–)
OX 1	6	7.00	+476	27.0	n.d.	n.d.	n.d.	n.d.
OX 2	8	7.04	+480	28.2	n.d.	n.d.	n.d.	n.d.
OX 3	9	7.05	+485	29.0	n.d.	n.d.	n.d.	n.d.
OX 1–OX 3	**–**	**7.03**	**+480 ± 3.68**	**28.1 ± 0.8**	**n.d.**	**n.d.**	**n.d.**	**n.d.**
WR 1	23	8.05	+171	0	11.1	11.0–11.0	11.0 ± 0.020	0.99
WR 2	28	8.08	+173	0	14.0	14.0–14.0	14.0 ± 0.029	1.00
WR 3	29	8.08	+162	0	13.7	13.1–13.5	13.4 ± 0.184	0.98
WR 1–WR 3	**–**	**8.07**	**+169 ± 4.78**	**0 ± 0**	**12.9 ± 1.30**	**11.0–14.0**	**12.8 ± 1.30**	**0.99 ± 0.009**
MR 1	46	8.00	–2.90	0	22.6	22.3–22.3	22.3 ± 0.029	0.99
MR 2	48	8.01	–2.90	0	24.4	22.8–22.8	22.8 ± 0.024	0.93
MR 3	50	8.02	–1.97	0	24.6	23.8–23.9	23.8 ± 0.041	0.97
MR 1–MR 3	**–**	**8.01**	**–2.59 ± 0.44**	**0 ± 0**	**23.9 ± 0.899**	**22.3–23.9**	**23.0 ± 0.635**	**0.96 ± 0.022**
OX 4	53.5	8.13	+102	0	25.5	24.4–24.7	24.6 ± 0.111	0.96
OX 5	54	8.14	+98.0	0	21.1	21.3–21.5	21.4 ± 0.056	1.01
OX 6	55	8.18	+295	18.3	20.9	20.5–20.5	20.5 ± 0.024	0.98
OX 7	56	7.91	+358	32.9	18.9	18.0–18.2	18.1 ± 0.065	0.96
OX 4–OX 7	**–**	**8.09**	**+213 ± 115**	**12.8 ± 13.8**	**21.6 ± 2.41**	**18.0–24.7**	**21.1 ± 2.30**	**0.98 ± 0.022**

Table 4.S1 (continued)

Sample ID (–)	Mn^{2+} Range (µmol L^{-1})	Mn^{2+} Mean (µmol L^{-1})	Mn^{2+} Range (%)	Mn^{2+} Mean (%)	Mn^{3+}–NOL_{weak} Range (µmol L^{-1})	Mn^{3+}–NOL_{weak} Mean (µmol L^{-1})	Mn^{3+}–NOL_{weak} Range (%)	Mn^{3+}–NOL_{weak} Mean (%)
OX 1	n.d.	n.d.	n.d.	n.d.	n.d.	n.d.	n.d.	n.d.
OX 2	n.d.	n.d.	n.d.	n.d.	n.d.	n.d.	n.d.	n.d.
OX 3	n.d.	n.d.	n.d.	n.d.	n.d.	n.d.	n.d.	n.d.
OX 1–OX 3	**n.d.**	**n.d.**	**n.d.**	**n.d.**	**n.d.**	**n.d.**	**n.d.**	**n.d.**
WR 1	10.4–10.7	10.6 ± 0.143	94.8–97.6	96.4 ± 1.2	0–0.513	0.171 ± 0.242	0–4.7	1.6 ± 2.2
WR 2	13.7–13.9	13.8 ± 0.093	97.4–99.4	98.2 ± 0.9	n.d.	n.d.	n.d.	n.d.
WR 3	10.5–10.9	10.7 ± 0.170	77.9–83.1	79.8 ± 2.4	0.249–0.409	0.347 ± 0.070	1.8–3.0	2.6 ± 0.5
WR 1–WR 3	**10.4–13.9**	**11.7 ± 1.48**	**77.9–99.4**	**91.5 ± 8.4**	**0–0.513**	**0.173 ± 0.203**	**0–4.7**	**1.4 ± 1.7**
MR 1	22.0–21.8	21.8 ± 0.120	97.6–98.6	98.0 ± 0.4	n.d.	n.d.	n.d.	n.d.
MR 2	21.9–22.1	22.0 ± 0.106	95.8–97.0	96.5 ± 0.5	0.374–0.500	0.435 ± 0.051	1.6–2.2	1.9 ± 0.2
MR 3	15.4–20.4	17.4 ± 2.15	64.8–85.7	73.2 ± 9.0	2.96–7.87	5.88 ± 2.11	12.4–33.1	24.7 ± 8.9
MR 1–MR 3	**15.4–22.1**	**20.4 ± 2.45**	**64.8–98.6**	**89.2 ± 12.5**	**0–7.87**	**2.11 ± 2.94**	**0–33.1**	**8.9 ± 12.3**
OX 4	22.3–23.8	23.2 ± 0.654	90.8–96.4	94.5 ± 2.6	0–1.24	0.413 ± 0.585	0–5.0	1.7 ± 2.4
OX 5	20.7–20.9	20.8 ± 0.068	96.6–97.9	97.4 ± 0.6	n.d.	n.d.	n.d.	n.d.
OX 6	11.2–18.1	15.6 ± 3.12	54.7–88.2	76.1 ± 15.2	2.11–8.70	4.52 ± 2.97	10.3–42.5	22.1 ± 14.5
OX 7	13.5–17.7	15.0 ± 1.89	74.3–98.0	82.9 ± 10.7	0–3.94	2.48 ± 1.76	0–21.7	13.6 ± 9.7
OX 4–OX 7	**11.2–23.8**	**18.7 ± 3.93**	**54.7–98.0**	**87.7 ± 12.7**	**0–8.70**	**1.85 ± 2.51**	**0–42.5**	**9.3 ± 12.6**

Table 4.S1 (continued)

Sample ID (–)	Mn^{3+}–NOL_{strong} Range (µmol L^{-1})	Mn^{3+}–NOL_{strong} Mean (µmol L^{-1})	Mn^{3+}–NOL_{strong} Range (%)	Mn^{3+}–NOL_{strong} Mean (%)
OX 1	n.d.	n.d.	n.d.	n.d.
OX 2	n.d.	n.d.	n.d.	n.d.
OX 3	n.d.	n.d.	n.d.	n.d.
OX 1–OX 3	**n.d.**	**n.d.**	**n.d.**	**n.d.**
WR 1	0.063–0.354	0.226 ± 0.121	0.6–3.2	2.1 ± 1.1
WR 2	0.082–0.363	0.249 ± 0.121	0.6–2.6	1.8 ± 0.9
WR 3	1.83–2.67	2.35 ± 0.376	13.9–19.8	17.6 ± 2.6
WR 1–WR 3	**0.063–2.67**	**0.943 ± 1.03**	**0.6–19.8**	**7.1 ± 7.6**
MR 1	0.313–0.529	0.445 ± 0.094	1.4–2.4	2.0 ± 0.4
MR 2	0.270–0.538	0.371 ± 0.119	1.2–2.4	1.6 ± 0.5
MR 3	0.439–0.561	0.501 ± 0.050	1.8–2.4	2.1 ± 0.2
MR 1–MR 3	**0.270–0.561**	**0.439 ± 0.106**	**1.2–2.4**	**1.9 ± 0.5**
OX 4	0.881–1.02	0.929 ± 0.061	3.6–4.1	3.8 ± 0.2
OX 5	0.453–0.731	0.565 ± 0.120	2.1–3.4	2.6 ± 0.6
OX 6	0.230–0.575	0.373 ± 0.147	1.1–2.8	1.8 ± 0.7
OX 7	0.358–0.815	0.630 ± 0.197	2.0–4.5	3.5 ± 1.1
OX 4–OX 7	**0.230–1.02**	**0.624 ± 0.244**	**1.1–4.5**	**2.9 ± 1.0**

Table 4.S1 (continued)

Sample ID (–)	k_1 range (s^{-1})	k_1 mean (s^{-1})	k_2 range (s^{-1})	k_2 mean (s^{-1})
OX 1	n.d.	n.d.	n.d.	n.d.
OX 2	n.d.	n.d.	n.d.	n.d.
OX 3	n.d.	n.d.	n.d.	n.d.
OX 1–OX 3	**n.d.**	**n.d.**	**n.d.**	**n.d.**
WR 1	0.0352–0.0360	0.0356 ± 0.0003	0.0082–0.0082	0.0082 ± 0
WR 2	0.0356–0.0415	0.0387 ± 0.0024	n.d.	n.d.
WR 3	0.0373–0.0381	0.0377 ± 0.0003	0.0020–0.0076	0.0053 ± 0.0024
WR 1–WR 3	**0.0352–0.0415**	**0.0373 ± 0.0019**	**0.0020–0.0082**	**0.0060 ± 0.0024**
MR 1	0.0217–0.0367	0.0284 ± 0.0061	n.d.	n.d.
MR 2	0.0341–0.0367	0.0354 ± 0.0011	0.0102–0.0128	0.0118 ± 0.0012
MR 3	0.0341–0.0367	0.0354 ± 0.0011	0.0102–0.0108	0.0105 ± 0.0003
MR 1–MR 3	**0.0217–0.0367**	**0.0314 ± 0.0058**	**0.0102–0.0128**	**0.0112 ± 0.0011**
OX 4	0.0256–0.0278	0.0269 ± 0.0009	0.0071–0.0071	0.0071 ± 0
OX 5	0.0284–0.0296	0.0288 ± 0.0006	n.d.	n.d.
OX 6	0.0314–0.0543	0.0398 ± 0.0103	0.0082–0.0157	0.0107 ± 0.0035
OX 7	0.0221–0.0357	0.0306 ± 0.0061	0.0107–0.0112	0.0109 ± 0.0003
OX 4–OX 7	**0.0221–0.0543**	**0.0315 ± 0.0078**	**0.0071–0.0157**	**0.102 ± 0.0028**

Table 4.S2 Dataset of the Mn speciation analysis including Mn_T, Mn^{2+}, Mn^{3+}–NOL complexes, k-values and ICP OES data (Mn_T) of the AhBg microcosm experiment (redox cycle II).

Sample ID (–)	time (d)	pH (–)	$E_{H(pH = 7)}$ (mV)	dO_2 (%)	$Mn_{T(ICP)}$ (µmol L^{-1})	$Mn_{T(Porph)}$ Range (µmol L^{-1})	$Mn_{T(Porph)}$ Mean (µmol L^{-1})	$Mn_{T(Porph)}$/ $Mn_{T(ICP\ OES)}$ (–)
OX 1	6	7.60	+539	23.7	n.d.	n.d.	n.d.	n.d.
OX 2	8	7.60	+540	23.2	n.d.	n.d.	n.d.	n.d.
OX 3	10	7.59	+541	23.7	n.d.	n.d.	n.d.	n.d.
OX 1–OX 3	**–**	**7.60**	**+540 ± 0.82**	**23.5 ± 0.2**	**n.d.**	**n.d.**	**n.d.**	**n.d.**
SR 1	39	7.75	–104	0	41.3	40.8–45.8	43.5 ± 2.06	1.05
SR 2	41	7.78	–111	0	40.6	40.9–43.1	41.6 ± 1.05	1.02
SR 3	43	7.83	–106	0	38.8	40.5–41.4	41.1 ± 0.405	1.06
SR 1–SR 3	**–**	**7.79**	**–107 ± 2.94**	**0 ± 0**	**40.2 ± 1.05**	**40.5–45.8**	**42.1 ± 1.71**	**1.05 ± 0.015**
OX 4	46	8.07	+373	20.7	30.6	31.6–32.3	32.0 ± 0.281	1.05
OX 5	46.5	8.03	+412	25.0	29.1	29.5–30.3	29.9 ± 0.339	1.03
OX 6	47	7.96	+420	23.7	4.68	4.57–4.90	4.69 ± 0.153	1.00
OX 7	49	7.40	+422	23.8	5.66	5.93–5.96	5.95 ± 0.013	1.05
OX 4–OX 7	**–**	**7.87**	**+407 ± 19.8**	**23.3 ± 1.6**	**17.5 ± 12.4**	**4.57–32.3**	**18.1 ± 12.8**	**1.03 ± 0.019**

Table 4.S2 (continued)

Sample ID (–)	Mn^{2+} Range (µmol L^{-1})	Mn^{2+} Mean (µmol L^{-1})	Mn^{2+} Range (%)	Mn^{2+} Mean (%)	Mn^{3+}–NOL_{weak} Range (µmol L^{-1})	Mn^{3+}–NOL_{weak} Mean (µmol L^{-1})	Mn^{3+}–NOL_{weak} Range (%)	Mn^{3+}–NOL_{weak} Mean (%)
OX 1	n.d.	n.d.	n.d.	n.d.	n.d.	n.d.	n.d.	n.d.
OX 2	n.d.	n.d.	n.d.	n.d.	n.d.	n.d.	n.d.	n.d.
OX 3	n.d.	n.d.	n.d.	n.d.	n.d.	n.d.	n.d.	n.d.
OX 1–OX 3	**n.d.**	**n.d.**	**n.d.**	**n.d.**	**n.d.**	**n.d.**	**n.d.**	**n.d.**
SR 1	39.4–42.4	40.9 ± 1.23	89.7–100	94.1 ± 4.3	0–4.53	2.64 ± 1.92	0–10.3	5.9 ± 4.3
SR 2	39.5–40.0	39.7 ± 0.197	91.6–97.8	95.5 ± 2.8	0–3.62	1.21 ± 1.71	0–8.4	2.8 ± 4.0
SR 3	38.6–41.4	40.2 ± 1.17	93.4–100	97.8 ± 3.1	0–2.71	0.903 ± 1.28	0–6.6	2.2 ± 3.1
SR 1–SR 3	**38.6–42.4**	**40.3 ± 1.09**	**89.7–100**	**95.8 ± 3.8**	**0–4.53**	**1.58 ± 1.82**	**0–10.3**	**3.6 ± 4.2**
OX 4	13.0–13.7	13.3 ± 0.294	40.2–42.7	41.5 ± 1.0	17.9–18.6	18.3 ± 0.294	56.6–57.6	57.1 ± 0.4
OX 5	7.00–13.8	11.1 ± 2.93	23.8–45.5	36.9 ± 9.5	16.5–22.3	18.5 ± 2.71	54.5–75.7	61.9 ± 9.8
OX 6	4.10–4.21	4.14 ± 0.045	84.0–91.6	88.5 ± 3.3	n.d.	n.d.	n.d.	n.d.
OX 7	4.86–5.40	5.22 ± 0.252	81.5–91.0	87.7 ± 4.3	0–0.660	0.220 ± 0.311	0–11.1	3.7 ± 5.2
OX 4–OX 7	**4.10–13.8**	**8.43 ± 4.13**	**23.8–91.6**	**63.6 ± 25.1**	**0–22.3**	**9.25 ± 9.24**	**0–75.7**	**30.7 ± 29.4**

Table 4.S2 (continued)

Sample ID (–)	Mn^{3+}–NOL_{strong} Range (µmol L^{-1})	Mn^{3+}–NOL_{strong} Mean (µmol L^{-1})	Mn^{3+}–NOL_{strong} Range (%)	Mn^{3+}–NOL_{strong} Mean (%)
OX 1	n.d.	n.d.	n.d.	n.d.
OX 2	n.d.	n.d.	n.d.	n.d.
OX 3	n.d.	n.d.	n.d.	n.d.
OX 1–OX 3	**n.d.**	**n.d.**	**n.d.**	**n.d.**
SR 1	n.d.	n.d.	n.d.	n.d.
SR 2	0–1.22	0.700 ± 0.514	0–3.0	1.7 ± 1.3
SR 3	n.d.	n.d.	n.d.	n.d.
SR 1–SR 3	**0–1.22**	**0.233 ± 0.444**	**0–3.0**	**0.6 ± 1.1**
OX 4	0–0.716	0.420 ± 0.305	0–2.2	1.3 ± 0.9
OX 5	0–0.879	0.349 ± 0.381	0–2.9	1.2 ± 1.3
OX 6	0.385–0.786	0.546 ± 0.173	8.4–16.0	11.5 ± 3.3
OX 7	0.441–0.571	0.515 ± 0.055	7.4–9.6	8.7 ± 0.9
OX 4–OX 7	**0–0.879**	**0.457 ± 0.272**	**0–16.0**	**5.7 ± 4.9**

Table 4.S2 (continued)

Sample ID (–)	k_1 range (s^{-1})	k_1 mean (s^{-1})	k_2 range (s^{-1})	k_2 mean (s^{-1})
OX 1	n.d.	n.d.	n.d.	n.d.
OX 2	n.d.	n.d.	n.d.	n.d.
OX 3	n.d.	n.d.	n.d.	n.d.
OX 1–OX 3	**n.d.**	**n.d.**	**n.d.**	**n.d.**
SR 1	0.0460–0.0513	0.0485 ± 0.0017	0.0071–0.0075	0.0073 ± 0.0002
SR 2	0.0482–0.0497	0.0487 ± 0.0007	0.0016–0.0016	0.0016 ± 0
SR 3	0.0471–0.0511	0.0487 ± 0.0018	0.0170–0.0170	0.0170 ± 0
SR 1–SR 3	**0.0460–0.0513**	**0.0485 ± 0.0017**	**0.0016–0.0170**	**0.0083 ± 0.0055**
OX 4	0.0437–0.0481	0.0453 ± 0.0020	0.0123–0.0146	0.0131 ± 0.0010
OX 5	0.0440–0.0689	0.0539 ± 0.0108	0.0115–0.0172	0.0147 ± 0.0024
OX 6	0.0519–0.0569	0.0551 ± 0.0022	n.d.	n.d.
OX 7	0.0526–0.0605	0.0553 ± 0.0037	0.0129–0.0129	0.0129 ± 0
OX 4–OX 7	**0.0437–0.0689**	**0.0524 ± 0.0072**	**0.0115–0.0172**	**0.0138 ± 0.0019**

Table 4.S3 Dataset of the Mn speciation analysis including Mn_T, Mn^{2+}, Mn^{3+}–NOL complexes, k-values and ICP OES data (Mn_T) of the Bg microcosm experiment (redox cycle I).

Sample ID	time	pH	$E_{H(pH = 7)}$	dO_2	$Mn_{T(ICP)}$	$Mn_{T(Porph)}$ Range	$Mn_{T(Porph)}$ Mean	$Mn_{T(Porph)}$/ $Mn_{T(ICP\ OES)}$
(–)	(d)	(–)	(mV)	(%)	(µmol L^{-1})	(µmol L^{-1})	(µmol L^{-1})	(–)
OX 1	7	7.63	+542	32.0	n.d.	n.d.	n.d.	n.d.
OX 2	9	7.64	+544	32.0	n.d.	n.d.	n.d.	n.d.
OX 3	11	7.64	+546	32.2	n.d.	n.d.	n.d.	n.d.
OX 1–OX 3	**–**	**7.64**	**+544 ± 1.63**	**32.1 ± 0.1**	**n.d.**	**n.d.**	**n.d.**	**n.d.**
WR 1	22	8.11	+187	0.5	0.491	0.467–0.480	0.475 ± 0.005	0.97
WR 2	23	8.13	+198	0	1.07	1.05–1.11	1.07 ± 0.025	1.00
WR 3	25	8.17	+156	0	1.22	1.16–1.21	1.19 ± 0.023	0.98
WR 1–WR 3	**–**	**8.14**	**+180 ± 17.8**	**0 ± 0**	**0.927 ± 0.314**	**0.467–1.21**	**0.912 ± 0.314**	**0.98 ± 0.014**
MR 1	35	8.07	–35.1	0	1.07	0.871–1.10	1.01 ± 0.099	0.94
MR 2	37	8.14	–9.20	0	1.02	0.925–1.05	0.993 ± 0.052	0.97
MR 3	39	8.17	+11.4	0	1.73	1.60–1.65	1.63 ± 0.023	0.94
MR 1–MR 3	**–**	**8.13**	**–11.0 ± 19.0**	**0 ± 0**	**1.27 ± 0.324**	**0.871–1.65**	**1.21 ± 0.305**	**0.95 ± 0.014**
OX 4	44.5	7.96	+367	31.5	1.18	1.18–1.21	1.20 ± 0.015	1.02
OX 5	45	7.96	+412	32.2	1.06	0.976–1.04	1.01 ± 0.026	0.95
OX 6	46	7.97	+443	32.2	0.601	0.565–0.612	0.595 ± 0.022	0.99
OX 7	47.5	7.99	+475	32.2	n.d.	n.d.	n.d.	n.d.
OX 4–OX 7	**–**	**7.97**	**+424 ± 39.9**	**32.0 ± 0.3**	**0.710 ± 0.464**	**0.565–1.21**	**0.934 ± 0.253**	**0.99 ± 0.026**

Table 4.S3 (continued)

Sample ID	Mn^{2+} Range	Mn^{2+} Mean	Mn^{2+} Range	Mn^{2+} Mean	Mn^{3+}–NOL_{weak} Range	Mn^{3+}–NOL_{weak} Mean	Mn^{3+}–NOL_{weak} Range	Mn^{3+}–NOL_{weak} Mean
(–)	(µmol L^{-1})	(µmol L^{-1})	(%)	(%)	(µmol L^{-1})	(µmol L^{-1})	(%)	(%)
OX 1	n.d.	n.d.	n.d.	n.d.	n.d.	n.d.	n.d.	n.d.
OX 2	n.d.	n.d.	n.d.	n.d.	n.d.	n.d.	n.d.	n.d.
OX 3	n.d.	n.d.	n.d.	n.d.	n.d.	n.d.	n.d.	n.d.
OX 1–OX 3	**n.d.**	**n.d.**	**n.d.**	**n.d.**	**n.d.**	**n.d.**	**n.d.**	**n.d.**
WR 1	0.467–0.480	0.475 ± 0.005	100–100	100 ± 0	n.d.	n.d.	n.d.	n.d.
WR 2	0.962–1.04	0.978 ± 0.044	84.4–99.3	91.3 ± 6.1	0–0.104	0.060 ± 0.044	0–9.8	5.5 ± 4.1
WR 3	1.10–1.21	1.15 ± 0.044	91.4–100	96.9 ± 3.9	0–0.103	0.037 ± 0.047	0–8.6	3.1 ± 3.9
WR 1–WR 3	**0.467–1.21**	**0.869 ± 0.290**	**84.4–100**	**96.1 ± 5.5**	**0–0.104**	**0.032 ± 0.045**	**0–9.8**	**2.9 ± 4.0**
MR 1	0.871–1.10	1.01 ± 0.099	100–100	100 ± 0	n.d.	n.d.	n.d.	n.d.
MR 2	0.673–0.879	0.792 ± 0.087	64.0–89.0	80.2 ± 11.4	0.102–0.378	0.202 ± 0.125	11.0–36.0	19.8 ± 11.4
MR 3	0.620–0.801	0.716 ± 0.074	38.7–48.8	43.8 ± 4.1	0.092–0.272	0.165 ± 0.077	5.6–17.0	10.2 ± 4.9
MR 1–MR 3	**0.620–1.10**	**0.839 ± 0.151**	**38.7–100**	**74.7 ± 24.3**	**0–0.378**	**0.122 ± 0.122**	**0–36.0**	**10.0 ± 10.8**
OX 4	1.05–1.16	1.12 ± 0.047	89.2–95.6	93.0 ± 2.8	0–0.091	0.053 ± 0.039	0–7.8	4.5 ± 3.3
OX 5	0.976–1.04	1.01 ± 0.026	100–100	100 ± 0	n.d.	n.d.	n.d.	n.d.
OX 6	0.537–0.605	0.572 ± 0.028	93.9–99.3	96.1 ± 2.3	0.004–0.037	0.023 ± 0.014	0.7–6.1	3.9 ± 2.3
OX 7	n.d.	n.d.	n.d.	n.d.	n.d.	n.d.	n.d.	n.d.
OX 4–OX 7	**0.537–1.16**	**0.899 ± 0.237**	**89.2–100**	**96.4 ± 3.5**	**0–0.091**	**0.025 ± 0.032**	**0–7.8**	**2.8 ± 3.1**

Table 4.S3 (continued)

Sample ID (–)	Mn^{3+}–NOL_{strong} Range (µmol L^{-1})	Mn^{3+}–NOL_{strong} Mean (µmol L^{-1})	Mn^{3+}–NOL_{strong} Range (%)	Mn^{3+}–NOL_{strong} Mean (%)
OX 1	n.d.	n.d.	n.d.	n.d.
OX 2	n.d.	n.d.	n.d.	n.d.
OX 3	n.d.	n.d.	n.d.	n.d.
OX 1–OX 3	**n.d.**	**n.d.**	**n.d.**	**n.d.**
WR 1	n.d.	n.d.	n.d.	n.d.
WR 2	0–0.096	0.035 ± 0.044	0–8.7	3.2 ± 3.9
WR 3	n.d.	n.d.	n.d.	n.d.
WR 1–WR 3	**0–0.096**	**0.012 ± 0.030**	**0–8.7**	**1.1 ± 2.7**
MR 1	n.d.	n.d.	n.d.	n.d.
MR 2	n.d.	n.d.	n.d.	n.d.
MR 3	0.709–0.797	0.751 ± 0.036	44.3–48.2	46.0 ± 1.6
MR 1–MR 3	**0–0.797**	**0.250 ± 0.355**	**0–48.2**	**15.3 ± 21.7**
OX 4	0–0.054	0.030 ± 0.022	0–4.4	2.5 ± 1.9
OX 5	n.d.	n.d.	n.d.	n.d.
OX 6	n.d.	n.d.	n.d.	n.d.
OX 7	n.d.	n.d.	n.d.	n.d.
OX 4–OX 7	**0–0.054**	**0.010 ± 0.019**	**0–4.4**	**0.8 ± 1.6**

Table 4.S3 (continued)

Sample ID (–)	k_1 range (s^{-1})	k_1 mean (s^{-1})	k_2 range (s^{-1})	k_2 mean (s^{-1})
OX 1	n.d.	n.d.	n.d.	n.d.
OX 2	n.d.	n.d.	n.d.	n.d.
OX 3	n.d.	n.d.	n.d.	n.d.
OX 1–OX 3	**n.d.**	**n.d.**	**n.d.**	**n.d.**
WR 1	0.0288–0.0388	0.0328 ± 0.0043	n.d.	n.d.
WR 2	0.0313–0.0407	0.0346 ± 0.0043	0.0063–0.0087	0.0075 ± 0.0012
WR 3	0.0320–0.0390	0.0355 ± 0.0028	0.0081–0.0087	0.0084 ± 0.0003
WR 1–WR 3	**0.0288–0.0407**	**0.0343 ± 0.0040**	**0.0063–0.0087**	**0.0080 ± 0.0010**
MR 1	0.0395–0.0474	0.0441 ± 0.0034	n.d.	n.d.
MR 2	0.0399–0.0459	0.0435 ± 0.0026	0.0051–0.0119	0.0089 ± 0.0028
MR 3	0.0379–0.0410	0.0399 ± 0.0014	0.0028–0.0086	0.0055 ± 0.0024
MR 1–MR 3	**0.0379–0.0474**	**0.0425 ± 0.0032**	**0.0028–0.0119**	**0.0072 ± 0.0031**
OX 4	0.0383–0.0431	0.0409 ± 0.0020	0.0076–0.0076	0.0076 ± 0
OX 5	0.0389–0.407	0.395 ± 0.0008	n.d.	n.d.
OX 6	0.0291–0.0311	0.0300 ± 0.0008	0.0015–0.0066	0.0043 ± 0.0021
OX 7	n.d.	n.d.	n.d.	n.d.
OX 4–OX 7	**0.0291–0.0431**	**0.0368 ± 0.0050**	**0.0015–0.0076**	**0.0051 ± 0.0023**

Table 4.S4 Dataset of the Mn speciation analysis including Mn_T, Mn^{2+}, Mn^{3+}–NOL complexes, k-values and ICP OES data (Mn_T) of the Bg microcosm experiment (redox cycle II).

Sample ID (–)	time (d)	pH (–)	$E_{H(pH=7)}$ (mV)	dO_2 (%)	$Mn_{T(ICP)}$ (µmol L^{-1})	$Mn_{T(Porph)}$ Range (µmol L^{-1})	$Mn_{T(Porph)}$ Mean (µmol L^{-1})	$Mn_{T(Porph)}$/ $Mn_{T(ICP\ OES)}$ (–)
OX 1	7	7.81	+478	25.7	n.d.	n.d.	n.d.	n.d.
OX 2	9	7.82	+482	25.3	n.d.	n.d.	n.d.	n.d.
OX 3	11	7.83	+486	25.0	n.d.	n.d.	n.d.	n.d.
OX 1–OX 3	**–**	**7.82**	**+482 ± 3.27**	**25.3 ± 0.3**	**n.d.**	**n.d.**	**n.d.**	**n.d.**
SR 1	17	7.72	–92.2	0	4.37	4.61–4.75	4.66 ± 0.068	1.07
SR 2	19	7.77	–109	0	5.28	5.20–5.33	5.25 ± 0.057	0.99
SR 3	20.5	7.82	–61.8	0	5.00	5.04–5.38	5.16 ± 0.157	1.03
SR 1–SR 3	**–**	**7.77**	**–87.7 ± 19.5**	**0 ± 0**	**4.88 ± 0.381**	**4.61–5.38**	**5.02 ± 0.278**	**1.03 ± 0.029**
OX 4	26.5	7.93	+367	28.7	1.88	1.85–1.91	1.88 ± 0.026	1.00
OX 5	27	7.86	+378	28.7	1.27	1.34–1.41	1.36 ± 0.033	1.07
OX 6	28	7.84	+392	29.0	n.d.	n.d.	n.d.	n.d.
OX 7	30	7.78	+408	28.7	n.d.	n.d.	n.d.	n.d.
OX 4–OX 7	**–**	**7.85**	**+386 ± 15.4**	**28.8 ± 0.1**	**1.58 ± 0.305**	**1.34–1.91**	**1.62 ± 0.260**	**1.04 ± 0.035**

Table 4.S4 (continued)

Sample ID (–)	Mn^{2+} Range (µmol L^{-1})	Mn^{2+} Mean (µmol L^{-1})	Mn^{2+} Range (%)	Mn^{2+} Mean (%)	Mn^{3+}–NOL_{weak} Range (µmol L^{-1})	Mn^{3+}–NOL_{weak} Mean (µmol L^{-1})	Mn^{3+}–NOL_{weak} Range (%)	Mn^{3+}–NOL_{weak} Mean (%)
OX 1	n.d.	n.d.	n.d.	n.d.	n.d.	n.d.	n.d.	n.d.
OX 2	n.d.	n.d.	n.d.	n.d.	n.d.	n.d.	n.d.	n.d.
OX 3	n.d.	n.d.	n.d.	n.d.	n.d.	n.d.	n.d.	n.d.
OX 1–OX 3	**n.d.**	**n.d.**	**n.d.**	**n.d.**	**n.d.**	**n.d.**	**n.d.**	**n.d.**
SR 1	3.92–4.06	4.01 ± 0.061	82.4–87.9	86.0 ± 2.5	0–0.055	0.018 ± 0.026	0–1.2	0.4 ± 0.5
SR 2	4.22–4.53	4.37 ± 0.127	81.0–85.1	83.4 ± 1.7	0–0.167	0.056 ± 0.079	0–3.2	1.1 ± 1.5
SR 3	4.16–4.59	4.34 ± 0.183	82.5–85.1	84.1 ± 1.2	0–0.601	0.337 ± 0.251	0–11.9	6.7 ± 5.0
SR 1–SR 3	**3.92–4.59**	**4.24 ± 0.213**	**81.0–87.9**	**84.5 ± 2.2**	**0–0.601**	**0.137 ± 0.209**	**0–11.9**	**2.7 ± 4.1**
OX 4	1.41–1.50	1.45 ± 0.036	73.8–81.0	77.3 ± 2.9	n.d.	n.d.	n.d.	n.d.
OX 5	0.384–0.940	0.694 ± 0.231	28.6–66.6	50.6 ± 16.1	0.021–0.103	0.056 ± 0.034	1.5–7.7	4.2 ± 2.6
OX 6	n.d.	n.d.	n.d.	n.d.	n.d.	n.d.	n.d.	n.d.
OX 7	n.d.	n.d.	n.d.	n.d.	n.d.	n.d.	n.d.	n.d.
OX 4–OX 7	**0.384–1.50**	**1.07 ± 0.413**	**28.6–81.0**	**64.0 ± 17.6**	**0–0.103**	**0.028 ± 0.037**	**0–7.7**	**2.1 ± 2.8**

Table 4.S4 (continued)

Sample ID (–)	Mn^{3+}–NOL_{strong} Range (µmol L^{-1})	Mn^{3+}–NOL_{strong} Mean (µmol L^{-1})	Mn^{3+}–NOL_{strong} Range (%)	Mn^{3+}–NOL_{strong} Mean (%)
OX 1	n.d.	n.d.	n.d.	n.d.
OX 2	n.d.	n.d.	n.d.	n.d.
OX 3	n.d.	n.d.	n.d.	n.d.
OX 1–OX 3	**n.d.**	**n.d.**	**n.d.**	**n.d.**
SR 1	0.557–0.780	0.635 ± 0.103	12.1–16.4	13.6 ± 2.0
SR 2	0.793–0.831	0.816 ± 0.016	14.9–16.0	15.6 ± 0.5
SR 3	0.280–0.789	0.481 ± 0.221	5.5–14.7	9.2 ± 3.9
SR 1–SR 3	**0.280–0.831**	**0.644 ± 0.197**	**5.5–16.4**	**12.8 ± 3.7**
OX 4	0.353–0.501	0.428 ± 0.060	19.0–26.2	22.7 ± 2.9
OX 5	0.423–0.476	0.449 ± 0.022	31.6–35.5	33.0 ± 1.8
OX 6	n.d.	n.d.	n.d.	n.d.
OX 7	n.d.	n.d.	n.d.	n.d.
OX 4–OX 7	**0.353–0.501**	**0.439 ± 0.047**	**19.0–35.5**	**27.9 ± 5.7**

Table 4.S4 (continued)

Sample ID (–)	k_1 range (s^{-1})	k_1 mean (s^{-1})	k_2 range (s^{-1})	k_2 mean (s^{-1})
OX 1	n.d.	n.d.	n.d.	n.d.
OX 2	n.d.	n.d.	n.d.	n.d.
OX 3	n.d.	n.d.	n.d.	n.d.
OX 1–OX 3	**n.d.**	**n.d.**	**n.d.**	**n.d.**
SR 1	0.0274–0.0292	0.0282 ± 0.0007	0.0048–0.0048	0.0048 ± 0
SR 2	0.0254–0.0297	0.0280 ± 0.0018	0.0086–0.0086	0.0086 ± 0
SR 3	0.0240–0.0289	0.0269 ± 0.0021	0.0044–0.0051	0.0047 ± 0.0004
SR 1–SR 3	**0.0240–0.0297**	**0.0277 ± 0.0018**	**0.0044–0.0086**	**0.0057 ± 0.0017**
OX 4	0.0237–0.0255	0.0244 ± 0.0008	n.d.	n.d.
OX 5	0.0257–0.0290	0.0268 ± 0.0015	0.0071–0.0086	0.0079 ± 0.0006
OX 6	n.d.	n.d.	n.d.	n.d.
OX 7	n.d.	n.d.	n.d.	n.d.
OX 4–OX 7	**0.0237–0.0290**	**0.0256 ± 0.0017**	**0.0071–0.0086**	**0.0079 ± 0.0006**

Table 4.S5 TOC and UV/VIS characterization of the soil solutions sampled from the incubated AhBg suspension of the Calcaric Gleysol during redox cycle I.

Sample ID (–)	DOC (mmol L^{-1})	DIC (mmol L^{-1})	MA_{254} (L mg^{-1}-C m^{-1})	MA_{280} (L mg^{-1}-C m^{-1})	MA_{350} (L mg^{-1}-C m^{-1})	$Mn_{T(ICP\ OES)}$/DOC (–)
OX 1	3.94	2.20	394	290	102	n.d.
OX 2	3.42	1.89	451	334	115	n.d.
OX 3	3.12	1.71	487	346	111	n.d.
OX 1–OX 3	**3.49 ± 0.339**	**1.93 ± 0.202**	**444 ± 38.2**	**323 ± 24.0**	**109 ± 5.39**	**n.d.**
WR 1	8.33	0.217	400	299	102	0.0013
WR 2	10.2	0.210	383	287	100	0.0014
WR 3	8.27	0.234	407	309	102	0.0017
WR 1–WR 3	**8.93 ± 0.896**	**0.220 ± 0.010**	**396 ± 10.1**	**298 ± 9.03**	**101 ± 1.18**	**0.0015 ± 0.001**
MR 1	11.5	0.161	355	266	89.4	0.0020
MR 2	12.2	0.038	370	278	92.4	0.0020
MR 3	15.2	0.092	321	240	79.5	0.0016
MR 1–MR 3	**13.0 ± 1.60**	**0.097 ± 0.050**	**349 ± 20.5**	**261 ± 15.8**	**87.1 ± 5.53**	**0.0019 ± 0.0002**
OX 4	13.8	0.546	330	246	83.3	0.0018
OX 5	12.6	0.379	328	246	79.7	0.0017
OX 6	9.74	0.673	368	280	92.8	0.0021
OX 7	9.33	0.770	332	248	84.4	0.0020
OX 4–OX 7	**11.4 ± 1.89**	**0.592 ± 0.146**	**339 ± 16.6**	**255 ± 14.2**	**85.0 ± 4.81**	**0.0019 ± 0.0002**

Table 4.S6 TOC and UV/VIS characterization of the soil solutions sampled from the incubated AhBg suspension of the Calcaric Gleysol during redox cycle II.

Sample ID (–)	DOC (mmol L^{-1})	DIC (mmol L^{-1})	MA_{254} (L mg^{-1}-C m^{-1})	MA_{280} (L mg^{-1}-C m^{-1})	MA_{350} (L mg^{-1}-C m^{-1})	$Mn_{T(ICP\ OES)}$/DOC (–)
OX 1	4.21	1.83	336	254	79.3	n.d.
OX 2	4.06	1.68	360	271	101	n.d.
OX 3	3.19	1.93	432	320	108	n.d.
OX 1–OX 3	**3.82 ± 0.450**	**1.81 ± 0.103**	**376 ± 41.1**	**282 ± 28.1**	**96.1 ± 12.3**	**n.d.**
SR 1	18.4	1.04	310	224	49.3	0.0022
SR 2	17.7	0.883	305	232	51.6	0.0023
SR 3	17.8	1.02	269	245	48.9	0.0022
SR 1–SR 3	**18.0 ± 0.309**	**0.981 ± 0.070**	**295 ± 18.3**	**234 ± 8.65**	**49.9 ± 1.19**	**0.0022 ± 0.0000**
OX 4	15.1	1.42	288	174	50.4	0.0020
OX 5	14.3	1.27	272	186	40.5	0.0020
OX 6	12.0	1.88	273	208	39.2	0.0004
OX 7	14.0	2.46	214	164	48.8	0.0004
OX 4–OX 7	**13.9 ± 1.14**	**1.76 ± 0.464**	**262 ± 28.3**	**183 ± 16.4**	**44.7 ± 4.93**	**0.0012 ± 0.0008**

Table 4.S7 TOC and UV/VIS characterization of the soil solutions sampled from the incubated Bg suspension of the Calcaric Gleysol during redox cycle I.

Sample ID (–)	DOC (mmol L^{-1})	DIC (mmol L^{-1})	MA_{254} (L mg^{-1}-C m^{-1})	MA_{280} (L mg^{-1}-C m^{-1})	MA_{350} (L mg^{-1}-C m^{-1})	$Mn_{T(ICP\ OES)}$/DOC (–)
OX 1	1.97	0.858	237	176	61.3	n.d.
OX 2	2.01	0.874	233	170	54.9	n.d.
OX 3	2.00	0.817	211	151	58.1	n.d.
OX 1–OX 3	**1.99 ± 0.017**	**0.850 ± 0.024**	**227 ± 11.5**	**166 ± 10.4**	**58.1 ± 2.61**	**n.d.**
WR 1	3.59	0.315	211	156	52.2	0.0001
WR 2	3.78	0.266	180	130	48.2	0.0003
WR 3	3.42	0.207	234	150	52.3	0.0004
WR 1–WR 3	**3.60 ± 0.147**	**0.263 ± 0.044**	**208 ± 22.1**	**145 ± 11.1**	**50.9 ± 1.93**	**0.0003 ± 0.0001**
MR 1	4.90	0.142	181	135	40.1	0.0002
MR 2	4.96	0.137	174	129	41.0	0.0002
MR 3	4.87	0.177	182	135	43.3	0.0004
MR 1–MR 3	**4.91 ± 0.037**	**1.83 ± 0.209**	**179 ± 3.79**	**133 ± 3.18**	**41.5 ± 1.36**	**0.0003 ± 0.0001**
OX 4	5.50	0.214	153	113	39.9	0.0002
OX 5	4.97	0.933	123	88	37.9	0.0002
OX 6	4.96	1.23	161	121	35.7	0.0001
OX 7	4.27	1.31	194	140	44.8	n.d.
OX 4–OX 7	**4.93 ± 0.437**	**0.922 ± 0.432**	**158 ± 25.5**	**116 ± 18.4**	**39.6 ± 3.36**	**0.0002 ± 0.0000**

Table 4.S8 TOC and UV/VIS characterization of the soil solutions sampled from the incubated Bg suspension of the Calcaric Gleysol during redox cycle II.

Sample ID (–)	DOC (mmol L^{-1})	DIC (mmol L^{-1})	MA_{254} (L mg^{-1}-C m^{-1})	MA_{280} (L mg^{-1}-C m^{-1})	MA_{350} (L mg^{-1}-C m^{-1})	$Mn_{T(ICP\ OES)}$/DOC (–)
OX 1	3.01	0.724	257	197	45.6	n.d.
OX 2	1.82	0.830	450	347	81.5	n.d.
OX 3	1.95	0.801	178	122	56.9	n.d.
OX 1–OX 3	**2.26 ± 0.533**	**0.785 ± 0.045**	**295 ± 114**	**222 ± 93.5**	**61.3 ± 15.0**	**n.d.**
SR 1	4.34	0.537	260	201	41.0	0.0010
SR 2	4.58	0.438	260	202	42.8	0.0012
SR 3	4.52	0.471	268	208	45.4	0.0011
SR 1–SR 3	**4.48 ± 0.102**	**0.482 ± 0.041**	**263 ± 3.66**	**204 ± 2.74**	**43.1 ± 1.84**	**0.0011 ± 0.0001**
OX 4	5.53	1.31	200	152	37.3	0.0003
OX 5	4.94	1.19	222	172	32.9	0.0003
OX 6	3.67	0.991	256	200	32.9	n.d.
OX 7	3.36	1.19	254	197	43.8	n.d.
OX 4–OX 7	**4.38 ± 0.892**	**1.17 ± 0.114**	**233 ± 23.1**	**180 ± 19.6**	**36.7 ± 4.47**	**0.0003 ± 0.0000**

Table 4.S9 Iron ($Fe^{2+/3+}$) and sulfide (HS^-) speciation results as well as determination of cations by ICP OES in the AhBg suspension during redox cycle I.

Sample ID (–)	Fe (µmol L^{-1})	Fe^{3+} (µmol L^{-1})	Fe^{2+} (µmol L^{-1})	HS^- (µmol L^{-1})
OX 1	1.54	1.54	n.d.	n.d.
OX 2	1.36	1.36	n.d.	n.d.
OX 3	0.931	0.931	n.d.	n.d.
OX 1–OX 3	**1.28 ± 0.255**	**1.28 ± 0.255**	**n.d.**	**n.d.**
WR 1	7.74	7.22	0.513	n.d.
WR 2	8.38	7.77	0.612	n.d.
WR 3	7.81	7.23	0.578	n.d.
WR 1–WR 3	**7.97 ± 0.288**	**7.41 ± 0.256**	**0.568 ± 0.041**	**n.d.**
MR 1	8.92	0.340	8.58	n.d.
MR 2	9.49	0.233	9.26	n.d.
MR 3	13.2	0.233	12.9	n.d.
MR 1–MR 3	**10.5 ± 1.89**	**0.269 ± 0.051**	**10.3 ± 1.92**	**n.d.**
OX 4	11.4	9.06	2.31	n.d.
OX 5	10.7	10.7	n.d.	n.d.
OX 6	6.45	6.45	n.d.	n.d.
OX 7	5.07	5.07	n.d.	n.d.
OX 4–OX 7	**8.39 ± 2.69**	**7.82 ± 2.19**	**2.31***	**n.d.**

*no standard deviation can be reported

Table 4.S9 (continued)

Sample ID (–)	Ca (mmol L^{-1})	K (mmol L^{-1})	Mg (mmol L^{-1})	Na (mmol L^{-1})
OX 1	0.798	0.583	0.662	0.254
OX 2	0.751	0.601	0.617	0.328
OX 3	0.783	0.593	0.609	0.340
OX 1–OX 3	**0.778 ± 0.020**	**0.593 ± 0.007**	**0.630 ± 0.024**	**0.307 ± 0.038**
WR 1	0.926	0.890	0.535	0.394
WR 2	1.01	0.862	0.523	0.391
WR 3	1.33	1.03	0.675	0.522
WR 1–WR 3	**1.09 ± 0.175**	**0.927 ± 0.073**	**0.577 ± 0.069**	**0.436 ± 0.061**
MR 1	1.52	1.17	0.667	0.417
MR 2	1.71	1.16	0.683	0.406
MR 3	1.76	1.47	0.798	0.474
MR 1–MR 3	**1.67 ± 0.105**	**1.27 ± 0.142**	**0.716 ± 0.059**	**0.432 ± 0.030**
OX 4	1.59	1.70	0.782	0.631
OX 5	1.48	1.53	0.667	0.535
OX 6	1.07	1.18	0.580	0.247
OX 7	1.06	1.22	0.588	0.241
OX 4–OX 7	**1.30 ± 0.238**	**1.41 ± 0.219**	**0.654 ± 0.081**	**0.414 ± 0.173**

*no standard deviation can be reported

Table 4.S10 Iron ($Fe^{2+/3+}$) and sulfide (HS^-) speciation results as well as determination of cations by ICP OES in the AhBg suspension during redox cycle II.

Sample ID (–)	Fe (µmol L^{-1})	Fe^{3+} (µmol L^{-1})	Fe^{2+} (µmol L^{-1})	HS^- (µmol L^{-1})
OX 1	0.573	0.573	n.d.	n.d.
OX 2	0.555	0.555	n.d.	n.d.
OX 3	0.591	0.591	n.d.	n.d.
OX 1–OX 3	**0.573 ± 0.015**	**0.573 ± 0.015**	**n.d.**	**n.d.**
SR 1	15.3	0.161	15.1	n.d.
SR 2	15.4	0.090	15.3	n.d.
SR 3	15.3	0.054	15.3	n.d.
SR 1–SR 3	**15.3 ± 0.074**	**0.101 ± 0.045**	**15.2 ± 0.105**	**n.d.**
OX 4	13.6	11.6	2.02	n.d.
OX 5	10.3	10.3	n.d.	n.d.
OX 6	2.61	2.61	n.d.	n.d.
OX 7	n.d.	n.d.	n.d.	n.d.
OX 4–OX 7	**8.83 ± 4.59**	**4.98 ± 3.78**	**11.5***	**n.d.**

*no standard deviation can be reported

Table 4.S10 (continued)

Sample ID (–)	Ca (mmol L^{-1})	K (mmol L^{-1})	Mg (mmol L^{-1})	Na (mmol L^{-1})
OX 1	0.778	0.604	0.695	0.234
OX 2	0.766	0.609	0.642	0.269
OX 3	0.811	0.591	0.601	0.263
OX 1–OX 3	**0.785 ± 0.019**	**0.601 ± 0.008**	**0.646 ± 0.039**	**0.255 ± 0.016**
SR 1	2.94	0.972	1.08	4.05
SR 2	3.02	0.992	1.10	4.08
SR 3	3.17	1.02	1.13	4.17
SR 1–SR 3	**3.04 ± 0.093**	**0.994 ± 0.019**	**1.10 ± 0.020**	**4.10 ± 0.048**
OX 4	3.27	1.27	1.09	4.25
OX 5	3.22	1.23	1.05	4.08
OX 6	2.57	1.09	0.893	3.58
OX 7	2.17	1.07	0.753	3.21
OX 4–OX 7	**2.81 ± 0.459**	**1.17 ± 0.085**	**0.946 ± 0.133**	**3.78 ± 0.410**

*no standard deviation can be reported

Table 4.S11 Iron ($Fe^{2+/3+}$) and sulfide (HS^-) speciation results as well as determination of cations by ICP OES in the Bg suspension during redox cycle I.

Sample ID (–)	Fe (µmol L^{-1})	Fe^{3+} (µmol L^{-1})	Fe^{2+} (µmol L^{-1})	HS^- (µmol L^{-1})
OX 1	n.d.	n.d.	n.d.	n.d.
OX 2	n.d.	n.d.	n.d.	n.d.
OX 3	n.d.	n.d.	n.d.	n.d.
OX 1–OX 3	**n.d.**	**n.d.**	**n.d.**	**n.d.**
WR 1	3.76	3.76	n.d.	n.d.
WR 2	4.66	4.66	n.d.	n.d.
WR 3	5.55	5.23	0.319	n.d.
WR 1–WR 3	**4.66 ± 0.731**	**4.55 ± 0.606**	**0.319***	**n.d.**
MR 1	4.66	0.365	4.30	n.d.
MR 2	4.12	0.180	3.94	n.d.
MR 3	3.58	0.360	3.22	n.d.
MR 1–MR 3	**4.12 ± 0.441**	**0.302 ± 0.086**	**3.82 ± 0.447**	**n.d.**
OX 4	3.22	3.22	n.d.	n.d.
OX 5	2.87	2.87	n.d.	n.d.
OX 6	n.d.	n.d.	n.d.	n.d.
OX 7	n.d.	n.d.	n.d.	n.d.
OX 4–OX 7	**3.05 ± 0.175**	**3.05 ± 0.175**	**n.d.**	**n.d.**

*no standard deviation can be reported

Table 4.S11 (continued)

Sample ID (–)	Ca (mmol L^{-1})	K (mmol L^{-1})	Mg (mmol L^{-1})	Na (mmol L^{-1})
OX 1	1.04	0.235	0.202	0.181
OX 2	1.29	0.289	0.222	0.189
OX 3	1.31	0.299	0.224	0.197
OX 1–OX 3	**1.21 ± 0.124**	**0.274 ± 0.028**	**0.216 ± 0.010**	**0.189 ± 0.007**
WR 1	1.53	0.309	0.202	0.194
WR 2	1.52	0.371	0.201	0.191
WR 3	1.53	0.366	0.207	0.192
WR 1–WR 3	**1.53 ± 0.007**	**0.349 ± 0.028**	**0.204 ± 0.003**	**0.192 ± 0.001**
MR 1	2.62	0.455	0.190	0.201
MR 2	2.69	0.504	0.190	0.216
MR 3	2.79	0.578	0.188	0.237
MR 1–MR 3	**2.70 ± 0.072**	**0.512 ± 0.050**	**0.189 ± 0.001**	**0.218 ± 0.015**
OX 4	2.69	0.616	0.240	0.204
OX 5	2.59	0.598	0.239	0.198
OX 6	2.39	0.568	0.293	0.298
OX 7	2.09	0.491	0.265	0.248
OX 4–OX 7	**2.44 ± 0.230**	**0.568 ± 0.048**	**0.260 ± 0.022**	**0.237 ± 0.040**

*no standard deviation can be reported

Table 4.S12 Iron ($Fe^{2+/3+}$) and sulfide (HS^{-}) speciation results as well as determination of cations by ICP OES in the Bg suspension during redox cycle II.

Sample ID (–)	Fe (µmol L^{-1})	Fe^{3+} (µmol L^{-1})	Fe^{2+} (µmol L^{-1})	HS^{-} (µmol L^{-1})
OX 1	n.d.	n.d.	n.d.	n.d.
OX 2	0.179	0.179	n.d.	n.d.
OX 3	n.d.	n.d.	n.d.	n.d.
OX 1–OX 3	**0.179**	**0.179**	**n.d.**	**n.d.**
SR 1	9.38	0.125	9.25	n.d.
SR 2	9.67	0.179	9.49	n.d.
SR 3	10.3	0.036	10.3	n.d.
SR 1–SR 3	**9.79 ± 0.397**	**0.113 ± 0.059**	**9.68 ± 0.445**	**n.d.**
OX 4	5.46	3.65	1.81	n.d.
OX 5	2.61	2.61	n.d.	n.d.
OX 6	n.d.	n.d.	n.d.	n.d.
OX 7	n.d.	n.d.	n.d.	n.d.
OX 4–OX 7	**4.04 ± 1.42**	**3.13 ± 0.519**	**1.81***	**n.d.**

*no standard deviation can be reported

Table 4.S12 (continued)

Sample ID (–)	Ca (mmol L^{-1})	K (mmol L^{-1})	Mg (mmol L^{-1})	Na (mmol L^{-1})
OX 1	1.32	0.307	0.213	0.181
OX 2	1.31	0.307	0.225	0.188
OX 3	1.34	0.312	0.225	0.200
OX 1–OX 3	**1.33 ± 0.015**	**0.309 ± 0.002**	**0.221 ± 0.005**	**0.189 ± 0.008**
SR 1	2.59	0.432	0.551	8.09
SR 2	2.82	0.478	0.650	9.09
SR 3	2.97	0.504	0.708	10.1
SR 1–SR 3	**2.79 ± 0.154**	**0.471 ± 0.030**	**0.636 ± 0.065**	**9.09 ± 0.817**
OX 4	4.04	0.783	0.901	10.4
OX 5	3.49	0.698	0.794	10.4
OX 6	2.89	0.547	0.679	8.66
OX 7	3.09	0.601	0.716	8.74
OX 4–OX 7	**3.38 ± 0.438**	**0.657 ± 0.090**	**0.772 ± 0.085**	**9.54 ± 0.838**

*no standard deviation can be reported

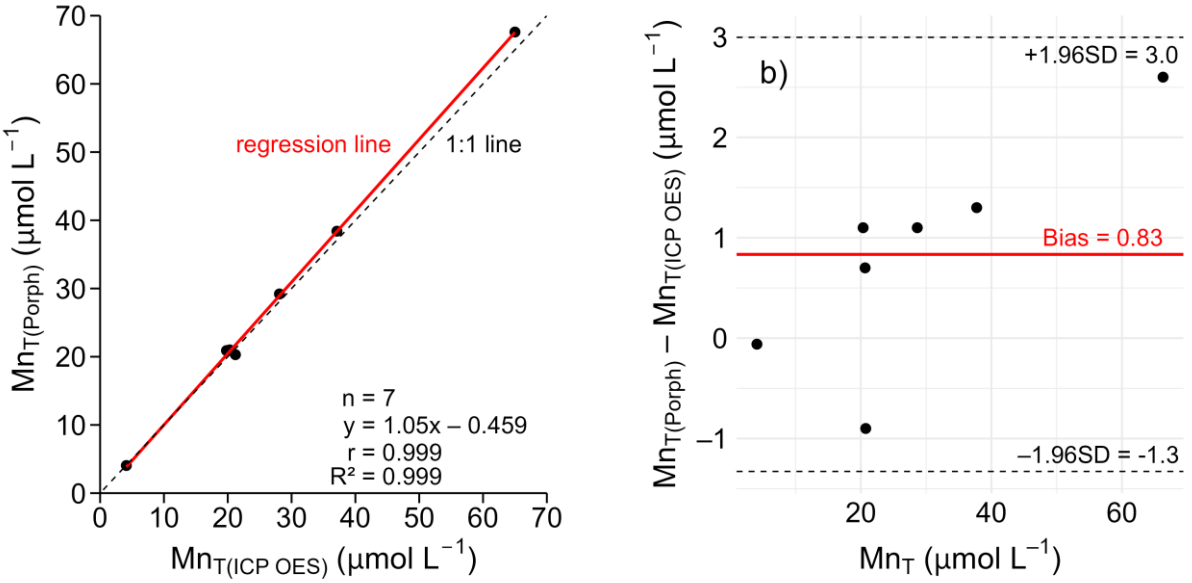

Figure 4.S2 Representation of a) the linear regression of porphyrin kinetic modeled total manganese concentrations (Mn_T) against Mn_T concentrations analyzed by inductively coupled plasma emission spectrometry (ICP OES) in soil solutions from the Calcaric Gleysol (Bg2) and the Salic Tidalic Fluvisol (zFo and zFr), and b) the Bland–Altman plot comparing the two methods for the same samples.

Table 4.S13 Dataset of the Mn speciation analysis including Mn_T, Mn^{2+}, Mn^{3+}–NOL complexes, k-values and ICP OES data (Mn_T) of the soil solutions obtained in situ from the Calcaric Gleysol (Bg2) and the Salic Tidalic Fluvisol (zFo and zFr).

Soil type (–)	Soil horizon (–)	Sample ID (–)	Depth (cm)	pH (–)	E_H (mV)	EC (mS cm^{-1})
Calcaric Gleysol	Bg2	A	90–100	7.55	+210	0.731
		B	90–100	7.56	+210	0.783
		C	90–100	7.63	+210	0.827
		A–C	**–**	**7.58**	**+210 ± 0**	**0.780 + 0.039**
Salic tidalic fluvisol	zFo	A	0–10	7.50	–	42.7
		B	0–10	7.44	–	42.9
		A–B	**–**	**7.47**	**–**	**42.8 + 0.100**
Salic tidalic fluvisol	zFr	A	25–35	7.44	–	41.3
		B	25–35	7.93	–	23.7
		A–B	**–**	**7.62**	**–**	**32.5 + 8.80**

Table 4.S13 (continued)

Soil type (–)	Soil horizon (–)	Sample ID (–)	$Mn_{T(ICP)}$ (µmol L^{-1})	$Mn_{T(Porph)}$ Range (µmol L^{-1})	$Mn_{T(Porph)}$ Mean (µmol L^{-1})	$Mn_{T(Porph)}$/ $Mn_{T(ICP\ OES)}$ (–)
Calcaric Gleysol	Bg2	A	19.8	20.8–20.9	20.9 ± 0.041	1.06
		B	28.1	29.2–29.3	29.2 ± 0.033	1.04
		C	20.3	20.9–21.1	21.0 ± 0.096	1.03
		A–C	**22.8 ± 3.81**	**20.8–29.3**	**23.7 ± 3.91**	**1.04 ± 0.01**
Salic tidalic fluvisol	zFo	A	37.1	37.8–38.9	38.4 ± 0.449	1.04
		B	65.0	67.0–68.8	67.6 ± 0.861	1.04
		A–B	**51.1 ± 14.0**	**37.8–68.8**	**53.5 ± 14.9**	**1.04 ± 0**
Salic tidalic fluvisol	zFr	A	21.2	20.1–20.4	20.3 ± 0.139	0.96
		B	4.11	4.00–4.08	4.05 ± 0.036	0.99
		A–B	**11.7 ± 7.63**	**4.00–20.4**	**12.2 ± 8.10**	**0.97 ± 0.01**

Table 4.S13 (continued)

Soil type (–)	Soil horizon (–)	Sample ID (–)	Mn^{2+} Range (µmol L^{-1})	Mn^{2+} Mean (µmol L^{-1})	Mn^{2+} Range (%)	Mn^{2+} Mean (%)
Calcaric Gleysol	Bg2	A	20.4–20.5	20.5 ± 0.041	98.1–98.2	98.2 ± 0.1
		B	13.2–15.0	13.9 ± 0.787	45.2–51.3	47.6 ± 2.6
		C	20.9–21.1	21.0 ± 0.102	99.9–100	100 ± 0.0
		A–C	**13.2–21.1**	**18.5 ± 3.26**	**45.2–100**	**81.9 ± 24.3**
Salic tidalic fluvisol	zFo	A	37.8–38.9	38.4 ± 0.449	100–100	100 ± 0
		B	64.9–65.6	65.3 ± 0.287	94.9–96.9	95.8 ± 0.8
		A–B	**37.8–65.6**	**51.8 ± 13.5**	**94.9–100**	**97.9 ± 2.2**
Salic tidalic fluvisol	zFr	A	19.3–20.3	19.7 ± 0.446	94.7–100	97.2 ± 2.2
		B	0.368–0.432	0.407 ± 0.028	9.0–10.6	10.1 ± 0.7
		A–B	**0.368–20.3**	**10.0 ± 9.64**	**9.0–100**	**53.6 ± 43.6**

Table 4.S13 (continued)

Soil type (–)	Soil horizon (–)	Sample ID (–)	Mn^{3+}–NOL_{weak} Range (µmol L^{-1})	Mn^{3+}–NOL_{weak} Mean (µmol L^{-1})	Mn^{3+}–NOL_{weak} Range (%)	Mn^{3+}–NOL_{weak} Mean (%)
Calcaric Gleysol	Bg2	A	n.d.	n.d.	n.d.	n.d.
		B	14.2–15.9	15.3 ± 0.759	48.5–54.5	52.3 ± 2.7
		C	n.d.	n.d.	n.d.	n.d.
		A–C	**0–15.9**	**5.09 ± 7.21**	**0–54.5**	**17.4 ± 24.7**
Salic tidalic fluvisol	zFo	A	n.d.	n.d.	n.d.	n.d.
		B	1.35–3.50	2.32 ± 0.891	2.0–5.1	3.4 ± 1.3
		A–B	**0–3.50**	**1.16 ± 1.32**	**0–5.1**	**1.7 ± 1.9**
Salic tidalic fluvisol	zFr	A	n.d.	n.d.	n.d.	n.d.
		B	3.51–3.62	3.58 ± 0.050	87.7–88.8	88.4 ± 0.5
		A–B	**0–3.62**	**1.79 ± 1.79**	**0–88.8**	**44.2 ± 44.2**

Table 4.S13 (continued)

Soil type (–)	Soil horizon (–)	Sample ID (–)	Mn^{3+}–NOL_{strong} Range (µmol L^{-1})	Mn^{3+}–NOL_{strong} Mean (µmol L^{-1})	Mn^{3+}–NOL_{strong} Range (%)	Mn^{3+}–NOL_{strong} Mean (%)
Calcaric Gleysol	Bg2	A	0.370–0.394	0.378 ± 0.011	1.8–1.9	1.8 ± 0.1
		B	0–0.078	0.045 ± 0.033	0–0.3	0.2 ± 0.1
		C	0–0.014	0.005 ± 0.007	0–0.1	0.0 ± 0.0
		A–C	**0–0.394**	**0.143 ± 0.169**	**0–1.9**	**0.7 ± 0.8**
Salic tidalic fluvisol	zFo	A	n.d.	n.d.	n.d.	n.d.
		B	0–1.63	0.545 ± 0.770	0–2.4	0.8 ± 1.1
		A–B	**0–1.63**	**0.272 ± 0.609**	**0–2.4**	**0.4 ± 0.9**
Salic tidalic fluvisol	zFr	A	0–1.07	0.567 ± 0.440	0–5.3	2.8 ± 2.2
		B	0.024–0.098	0.064 ± 0.030	0.6–2.4	1.6 ± 0.8
		A–B	**0–1.07**	**0.316 ± 0.401**	**0–5.3**	**2.2 ± 1.7**

Table 4.S13 (continued)

Soil type (–)	Soil horizon (–)	Sample ID (–)	k_1 range (s^{-1})	k_1 mean (s^{-1})	k_2 range (s^{-1})	k_2 mean (s^{-1})
Calcaric Gleysol	Bg2	A	0.0349–0.0444	0.0400 ± 0.0039	n.d.	n.d.
		B	0.0350–0.0381	0.0368 ± 0.0013	0.0104–0.0107	0.0106 ± 0.0001
		C	0.0371–0.0407	0.0393 ± 0.0016	n.d.	n.d.
		A–C	**0.0349–0.0444**	**0.0387 ± 0.0029**	**0.0104–0.0107**	**0.0106 ± 0.0001**
Salic tidalic fluvisol	zFo	A	0.0290–0.0341	0.0309 ± 0.0023	n.d.	n.d.
		B	0.0141–0.0146	0.0143 ± 0.0002	0.0014–0.0035	0.0026 ± 0.0009
		A–B	**0.0141–0.0341**	**0.0226 ± 0.0084**	**0.0014–0.0035**	**0.0026 ± 0.0009**
Salic tidalic fluvisol	zFr	A	0.0165–0.0199	0.0179 ± 0.0015	n.d.	n.d.
		B	0.0536–0.1319	0.0877 ± 0.0328	0.0056–0.0062	0.0059 ± 0.0002
		A–B	**0.0165–0.1319**	**0.0528 ± 0.0419**	**0.0056–0.0062**	**0.0059 ± 0.0002**

Table 4.S14 Data for TOC analysis, ICP OES analysis and IC analysis from the soil solutions obtained in situ from the Calcaric Gleysol (Bg2) and the Salic Tidalic Fluvisol (zFo and zFr).

Soil type (–)	Soil horizon (–)	Sample ID (–)	Depth (cm)	DOC (mmol L^{-1})	DIC (mmol L^{-1})	$Mn_{T(ICP\ OES)}$/DOC (–)
Calcaric Gleysol	Bg2	A	90–100	0.750	6.76	0.0264
		B	90–100	1.00	7.18	0.0281
		C	90–100	1.11	7.14	0.0183
		A–C	**–**	**0.954 ± 0.151**	**7.02 ± 0.188**	**0.242 ± 0.004**
Salic tidalic fluvisol	zFo	A	0–10	2.62	3.00	0.0141
		B	0–10	0.794	3.11	0.0819
		A–B	**–**	**1.71 ± 0.915**	**3.05 ± 0.055**	**0.0480 ± 0.034**
Salic tidalic fluvisol	zFr	A	25–35	0.510	2.70	0.0416
		B	25–35	0.618	6.35	0.0067
		A–B	**–**	**0.564 ± 0.054**	**4.52 ± 1.83**	**0.0241 ± 0.017**

Table 4.S14 (continued)

Soil type (–)	Soil horizon (–)	Sample ID (–)	Fe (µmol L^{-1})	Al (µmol L^{-1})	Ca (mmol L^{-1})	K (mmol L^{-1})
Calcaric Gleysol	Bg2	A	0.172	2.41	2.38	0.256
		B	0.204	2.81	2.59	0.258
		C	0.109	2.12	2.55	0.309
		A–C	**0.162 ± 0.039**	**2.45 ± 0.282**	**2.51 ± 0.094**	**0.275 ± 0.025**
Salic tidalic fluvisol	zFo	A	8.56	0.474	11.0	10.0
		B	2.54	0.619	12.6	9.90
		A–B	**5.55 ± 3.01**	**0.547 ± 0.072**	**11.8 ± 0.836**	**10.0 ± 0.064**
Salic tidalic fluvisol	zFr	A	5.62	0.630	10.9	9.82
		B	0.206	1.91	5.96	5.96
		A–B	**2.91 ± 2.71**	**1.27 ± 0.638**	**8.42 ± 2.46**	**7.89 ± 1.93**

Table 4.S14 (continued)

Soil type (–)	Soil horizon (–)	Sample ID (–)	Mg (mmol L^{-1})	Na (mmol L^{-1})	Cl^- (mmol L^{-1})	SO_4^{2-} (mmol L^{-1})
Calcaric Gleysol	Bg2	A	0.942	0.478	0.422	0.173
		B	0.946	0.496	0.542	0.312
		C	1.24	0.570	0.490	0.179
		A–C	**1.04 ± 0.139**	**0.515 ± 0.040**	**0.485 ± 0.049**	**0.221 ± 0.064**
Salic tidalic fluvisol	zFo	A	21.4	204	395	20.4
		B	37.3	342	399	20.4
		A–B	**29.3 ± 7.98**	**273 ± 69.2**	**397 ± 1.86**	**20.4 ± 0.014**
Salic tidalic fluvisol	zFr	A	40.0	292	380	19.5
		B	22.0	183	206	9.80
		A–B	**31.0 ± 9.01**	**238 ± 54.6**	**293 ± 87.0**	**14.6 ± 4.85**

References

Johnson, K. L., McCann, C. M., Wilkinson, J.-L., Jones, M., Tebo, B. M., West, M., Elgy, C., Clarke, C. E., Gowdy, C. and Hudson-Edwards, K. A. 2018. “Dissolved Mn(III) in water treatment works: Prevalence and significance.” *Water Research*, 140: 181–190. https://doi.org/10.1016/j.watres.2018.04.038

Madison, A. S., Tebo, B. M. and Luther 3rd, G. W. 2011. “Simultaneous determination of soluble manganese(III), manganese(II) and total manganese in natural (pore)waters.” *Talanta*, 84, no. 2: 374–381. https://doi.org/10.1016/j.talanta.2011.01.025

Markelova, E., Parsons, C. T., Couture, R.M., Smeaton, C. M., Madé, B., Charlet, L. and Van Cappellen, P. 2018. “Deconstructing the redox cascade: what role do microbial exudates (flavins) play?” *Environmental Chemistry*, 14, no. 8: 515–524. https://doi.org/10.1071/EN17158

Lux, C. and Mansfeldt, T. 2023. “Evidence of dissolved trivalent manganese in acidic forest soils.” *Journal of Plant Nutrition and Soil Science*, 186, no. 3: 321–329. https://doi.org/10.1002/jpln.202200271

Lux, C., Ufer, K. and Mansfeldt, T. 2025. “Dissolved trivalent manganese in forest soils - interactions of natural organic ligands with manganese oxides.” *Environmental Science: Processes & Impacts*, 27, no. 9: 2875–2893. https://doi.org/10.1039/D5EM00388A

Posit team, RStudio. 2025. “*Integrated Development Environment for R.”* Version 2025.05.1, Posit Software, PBC, Boston, MA. http://www.posit.co/, accessed October 2025.

R Core Team, R. 2025. “*A Language and Environment for Statistical Computing.” R Foundation for Statistical Computing.* Version 4.5.1, Vienna, Austria. https://www.R-project.org/, accessed October 2025.

Thibault de Chanvalon, A., Luther 3rd, G. W. 2019. Mn speciation at nanomolar concentrations with a porphyrin competitive ligand and UV-vis measurements. Talanta, 200: 15–21. https://doi.org/10.1016/j.talanta.2019.02.069

Chapter 5: Comprehensive discussion

This thesis provides experimental evidence for the occurrence of dissolved Mn^{3+} in soil solutions, thereby requiring reconsideration of the $Mn^{2+} \leftrightarrow Mn^{IV}$ paradigm. The cumulative approach establishes the porphyrin method as a reliable analytical approach for dissolved Mn_T speciation in soil solutions, enabling its application across laboratory and field-based settings to assess the occurrence and stability of Mn^{3+}. To evaluate whether Mn^{3+} constitutes an integral component of the soil Mn cycle, this comprehensive discussion synthesizes the findings of individual studies and critically discusses their combined, hypothesis-driven contributions to the overarching research question: "*Is dissolved trivalent manganese a ubiquitous part of the total dissolved manganese in soil solutions?"*

Hypothesis I: ***The porphyrin method can be adapted to soil solutions in order to speciate dissolved*** $\boldsymbol{Mn_T}$***.***

To evaluate this hypothesis, *in situ*-sampled forest floor solutions (n = 12) and soil solutions (n = 41) from an acidic forest site were investigated (Chapter 2). Results showed that Mn^{3+}–NOL complexes accounted for substantial proportions relative to Mn_T, ranging from 10–87% in forest floor solutions and 0.5–74% in soil solutions at pH 3.4–6.3. These results provide strong initial evidence that Mn^{3+}–NOL complexes can represent a major component of Mn_T. Complementary evidence was reported in Chapter 3, where Mn^{3+}–NOL complex formation (0–87%) was observed during interactions between NOLs and Mn oxides (pH 3.0–7.0). Methodological challenges, including prevailing acidic conditions and DOM-induced coloration of solutions, were systematically addressed through appropriate and practicable modifications (Chapter 2), resulting in robust and reliable outcomes that were independently validated by ICP OES analysis and, on average, were as precise as those reported by Madison et al. (2011). Furthermore, the fundamental kinetic model equations were adapted to complement manual operation and to account for soil-inherent reaction kinetics. Based on parameter estimates for the rate constant k_1 obtained with $MnCl_2 \cdot 4H_2O$ standards, the reaction rates were approximately an order of magnitude slower than those reported by Madison et al. (2011). One possible explanation for this discrepancy is variations in constant laboratory temperatures, which likely contributed to

the lower observed k_1 and k_2 values. This bias was explicitly considered in all studies within the kinetic modeling framework and should be regarded in future investigations.

With the establishment of the porphyrin method, a reliable and methodical approach is available for performing Mn speciation analysis in forest floor solutions and soil solutions. Beyond methodological feasibility, these findings suggest that Mn speciation in acidic soils may have been systematically oversimplified in previous studies, with potentially important implications for the interpretation of Mn redox cycling in forest ecosystems.

Method criticism

The limitations of the porphyrin method can be categorized into practical constraints, challenges related to kinetic modeling, and interferences arising from the solution matrix.

A major practical limitation of the method is the substantial time required for manual sample preparation, UV/Vis measurements, and subsequent data evaluation using kinetic modeling. Consequently, the method is less suitable for high-throughput studies. Another challenge concerns the *in situ* Mn speciation analysis, as the reaction kinetics of the substitution reactions are highly sensitive to temperature fluctuations. Thus, measurements must be conducted under strictly controlled conditions, which necessitates access to a (mobile) laboratory near to the sampling site.

Data evaluation introduces additional methodological challenges related to kinetic modeling. Reaction kinetics are evaluated using multi-exponential equations in order to derive several parameters (Chapter 1), which is considered “an ill-posed problem” and presents a critical analytical challenge (Kim et al., 2022). Robust parameterization requires highly reproducible kinetic curves, typically obtained from triplicate measurements, as even minor procedural inaccuracies can substantially compromise parameter stability. The approach is inherently susceptible to the well-known multi-exponential problem (Lanczos, 1956), which can result in non-unique (e.g., $k_1 \approx k_2$) or unstable parameter estimates. These issues can be mitigated by improving manual precision, ensuring accurate early-phase measurements, and applying parameter bounds informed by prior knowledge. Nevertheless, a residual degree of uncertainty remains in the parameter estimation.

Additional limitations arise from the pronounced heterogeneity of NOLs in natural soil solutions. Although the porphyrin method enables discrimination between

Mn^{3+}–NOL_{weak} complexes and Mn^{3+}–NOL_{strong} complexes, it is unlikely that all NOL species can be individually resolved. Reaction kinetics of isolated model ligands can be determined under controlled laboratory conditions and subsequently grouped into ligand classes (Oldham et al., 2015). Yet behaviors observed in these simplified systems may not directly translate to natural soil solutions, which comprise heterogeneous NOL pools with overlapping binding properties. Accounting for all sample-specific NOL species in the model is impractical due to unknown exact NOL composition (Kim et al., 2022). This highlights a fundamental trade-off between methodological resolution and environmental realism and underscores the need for complementary approaches capturing NOL complexity.

In microcosm experiments with Haplic Gleysol (Petrogleyic) soil suspensions comprising high Fe contents, a systematic increase in the absorption signal was observed. It is hypothesized that enhanced reductive dissolution of Fe oxides leads to substantial release of ferrous iron (Fe^{2+}), resulting in pronounced sample coloration in addition to DOM contributions. This affects the Soret band at 468 nm, leading to increased absorption signals and overestimation of dissolved Mn_T. Further studies are needed to determine whether the porphyrin method is unsuitable for soils exhibiting strong Fe-induced coloration or whether an empirical “Fe correction factor” can be applied.

Competitive interactions from NOLs, such as soil-inherent porphyrin-like molecules with higher $Mn^{2+/3+}$ affinity or the T(4-CP)P itself, may promote $Mn^{2+/3+}$ decomplexation from $Mn^{2+/3+}$–T(4-CP)P (Wang et al., 2024). Such competition can alter apparent reaction kinetics, leading to systematic under- or overestimation of specific dissolved Mn species, particularly in chemically heterogeneous samples.

Micro- and nano-sized Mn oxides may pass through 0.2 µm filters and cannot be fully excluded (Wang et al., 2024). Hydroxylamine hydrochloride, the reducing agent used in the porphyrin method, reduces Mn oxides (Zhu-Barker et al., 2015), potentially causing overestimation of Mn^{3+}–NOL_{strong} complexes. The LBB assay (Jones et al., 2019; Krumbein and Altmann, 1973) can assess the presence of nanoparticulate Mn oxides prior to kinetic modeling.

In summary, while the porphyrin method is a valuable analytical approach for Mn_T speciation, the aforementioned limitations must be considered in experimental design and

data interpretation. Explicit acknowledgment of these limitations enhances reliability, transparency, and scientific rigor.

- *Despite the analytical challenges outlined above, the porphyrin method was successfully adapted, modified, and validated. The method enables, for the first time, reliable dissolved Mn_T speciation in chemically heterogeneous soil solutions. Consequently, hypothesis I is confirmed.*

Hypothesis II: ***Terrestrial SOM-derived NOLs stabilize dissolved Mn^{3+}.***

To test this hypothesis, Mn_T speciation was performed on samples collected under laboratory and field conditions from study sites with distinct, site-specific OM inputs (Chapters 2–4). Overall, Mn^{3+}–NOL complexes accounted for up to 90% of Mn_T, supporting the role of SOM-derived NOLs in complexing and stabilizing Mn^{3+}. Johnson et al. (2018) previously applied the porphyrin method during different stages of a water treatment process supplied by terrestrial peaty surface waters containing natural OM and detected Mn^{3+}–NOL complexes comprising up to 83% of Mn_T. However, their study did not include natural soil solutions. In contrast, this thesis provides novel Mn_T speciation data for soil solutions under both laboratory and field conditions. Moreover, these findings independently confirm earlier interpretations by Oldham et al. (2017a–c) that terrigenous NOLs complex and stabilize Mn^{3+}.

To explore the role of NOL availability, the Mn_T:DOC ratio was used as an indicator to assess whether higher relative NOL concentrations promote Mn^{3+}–NOL complex formation. This ratio differentiated strongly acidic (≥0.08) from moderately acidic to circumneutral conditions (≤0.08) in soil extracts (Chapter 3). Notably, the threshold value of 0.08 was derived from soil extracts in the absence of competitive cations (e.g., Al^{3+}, Fe^{3+}), representing a chemically simplified system. Accordingly, its applicability is likely limited to systems of reduced complexity. Results from Chapter 4 support this interpretation, where under circumneutral to weakly alkaline conditions the threshold was not exceeded, highlighting the context dependency and limitations of the Mn_T:DOC ratio. Collectively, these findings indicate that Mn^{3+}–NOL complex formation is governed primarily by the quality and type of NOL functional groups, as well as their density relative to the molecular C backbone, rather than by NOL quantity alone.

The broad range of estimated k_2 rate constants of all samples (0.0012–0.0453 s^{-1}) reflects substantial variability in NOL binding strengths and thus functional group chemistry, characterizing the heterogeneity of the investigated NOL pools. Data provided by Johnson et al. (2018) showed k_2 values (0.0019–0.0101 s^{-1}) of similar magnitudes, which also indicate a high degree of diversity within the NOL pool studied. As conceptualized by Thibault de Chanvalon and Luther (2019), such variability allows the heterogeneous pool of weakly binding NOLs to be subdivided into distinct ligand pools, initially distinguished by the criterion $k_1 \geq 3 \cdot k_2$, which differentiates Mn^{2+} from Mn^{3+}–NOL_{weak} complexes. Thus, the investigated soil solutions likely comprise multiple, functionally distinct NOL_{weak} ligand pools. For example, LMWOAs are ubiquitous compounds characterized by a high density of functional groups (1–3 carboxyl groups and hydroxyl groups) relative to their short-chain C backbone (1–6 C atoms), rendering them effective metal chelators in soils (Peña, 2022). Consistent with this, earlier studies demonstrated that LMWOAs (e.g., citrate and oxalate) as well as siderophores effectively bind Mn^{3+} (e.g., Duckworth and Sposito, 2005a,b; Klewicki and Morgan, 1998; Xyla et al., 1992). Oldham et al. (2015) further showed that a range of phenolic model ligands containing carboxyl, hydroxamate, hydroxyl, and sulfonate functional groups bind Mn^{3+} with complex stabilities ranging from minutes to several weeks. Although simplified, these model ligands capture key molecular properties such as aromaticity, high electron-donor density, and multidentate coordination, which are also prevalent in SOM-derived NOLs and thus might promote the formation and stabilization of Mn^{3+}–NOL complexes. However, natural soil solutions may introduce additional complexity not captured by these simplified models.

- *The results provide experimental evidence that SOM-derived NOLs constitute an effective Mn^{3+}-stabilizing ligand pool in soil solutions, supporting Hypothesis II and highlighting their central role in regulating Mn redox cycling in terrestrial environments.*

Hypothesis III: ***Abiotic and biotic redox pathways contribute to Mn^{3+}–NOL complex formation.***

To evaluate hypothesis III under controlled yet environmentally relevant conditions, the pH- and time-dependent influence of NOLs on the dissolution of the synthetic Mn oxides

birnessite and manganite was investigated using batch experiments (Chapter 3). The experimental design was intentionally simplified to isolate abiotic pathways, which are difficult to resolve in fully coupled biotic–abiotic soil systems. Dissolved Mn_T speciation enabled quantitative determination of Mn^{3+}–NOL complexes, which constituted up to 87% of dissolved Mn_T. Dissolution of Mn oxides proceeded via four principal abiotic pathways: ligand-promoted reductive dissolution, ligand-promoted non-reductive dissolution, H^+-promoted dissolution, and ligand exchange. In addition, oxidative pathways involving $Mn^{2+/3+}$ complexation, with or without subsequent oxidation, as well as surface-catalyzed oxidation, contributed to Mn redox cycling.

Under circumneutral conditions, Mn^{3+}–NOL complexes dominated, accounting for up to 87% in NOL–birnessite and up to 69% in NOL–manganite interactions. The prevailing dissolution pathways were strongly mineral-specific. Ligand-promoted reductive dissolution prevailed in birnessite batch experiments, whereas ligand-promoted non-reductive dissolution governed Mn^{3+} release from manganite (Chapter 3).

Similar mechanisms may be active in limed forest floor solutions (Chapter 2), which exhibited the highest relative abundance of Mn^{3+}–NOL complexes, accounting for up to 87% of Mn_T. Therefore, Mn^{3+}–NOL complex formation is governed by pH, the effects of Mn oxide crystal structure, the inherent Mn valence states, surface reactivity, and the composition of NOLs.

With decreasing pH, H^+-promoted dissolution increasingly dominated Mn release, consistent with dissolution thresholds for birnessite (pH < 5.5) and manganite (pH < 6) (Banerjee and Nesbitt, 1999, 2001; Ramstedt and Sjöberg, 2005). However, these thresholds are not fixed and may shift depending on redox conditions, ionic strength, oxide crystallinity, and the presence of redox-active organic or inorganic ligands (Stone and Morgan, 1984a,b). High proportions of Mn^{3+}–NOL complexes were observed during early stages of NOL–Mn oxide interactions, reaching 39–85% within the first 6 h for birnessite and 8–57% within 3 h for manganite at pH 3–4 (Chapter 3). Non-limed forest floor solutions showed similar Mn^{3+}–NOL complex proportions (10–79%) relative to Mn_T (Chapter 2). In conclusion, the findings obtained under laboratory conditions demonstrate that abiotic pathways are responsible for the formation of Mn^{3+}–NOL complexes under field conditions, in addition to biotic pathways. Moreover, it is hypothesized that L and O horizons are important hotspots for Mn^{3+}–NOL complex formation in forest soils.

The rapid decrease in Mn^{3+}–NOL complex proportions after 6 h for birnessite (≤5%) and 3 h for manganite (≤2%) indicates that reductive mechanisms increasingly dominate Mn cycling under strongly acidic conditions. Although ligand-promoted reductive dissolution became more important under acidic conditions, the persistence of Mn^{3+}–NOL complexes was limited, consistent with previous studies reporting rapid transformation of organically complexed Mn^{3+} (Duckworth and Sposito, 2005a; Klewicki and Morgan, 1998). Intramolecular electron transfer within Mn^{3+}–NOL complexes, leading to reduction of Mn^{3+} to Mn^{2+} and accompanying ligand transformation, potentially via decarboxylation, offers a mechanistically plausible explanation (Duckworth and Sposito, 2005a). Consequently, measured Mn^{3+}–NOL concentrations reflect not only formation pathways but also the efficiency of NOL transformation and decay, which are both strongly pH-dependent. However, it should be noted that rapid decomposition of Mn^{3+}–NOL complexes at low pH prior to sample preparation may lead to underestimation of their concentrations in both laboratory and field studies.

Overall, the Mn_T speciation data support the proposed abiotic pathways, consistent with mechanistic assumptions in the literature (Li et al., 2021; Oldham et al., 2017a–c). Under strongly acidic conditions, however, abiotic Mn^{3+}–NOL complex formation is limited, highlighting the potential role of biotic pathways in stabilizing Mn^{3+} in natural soil systems.

Although biotic pathways were not directly resolved by experimental design, the microcosm experiments presented in Chapter 4 indicate that abiotic and biotic pathways operate concurrently in soils, collectively influencing Mn^{3+}–NOL complex formation (Li et al., 2021; Xi et al., 2025). In particular, dissimilatory reduction, in which Mn oxides serve as electron acceptors, can promote their dissolution and lead to the formation of Mn^{3+}, which may subsequently be stabilized as Mn^{3+}–NOL complexes via one-electron transfer reactions (Li et al., 2021; Oldham et al., 2017b), thereby complementing abiotic dissolution pathways. Coinciding with the highest observed proportions of Mn^{3+}–NOL complexes (<64%) during aeration (Chapter 4), biotic oxidation of Mn^{2+} can be assumed as an important pathway besides abiotic oxidation during aeration in soils. Oxidative formation of Mn^{3+}–NOL complexes also contributed to their stabilization against rapid oxidation to Mn oxides, consistent with the assumptions of Oldham et al. (2021). Madison et al. (2013) reported that oxidation by O_2, whether biotic or abiotic, accounted for up to 100% of the observed Mn^{3+} production.

Looking at the multiple pathways, Mn^{3+}–NOL formation is not a singular process but emerges from a network of competing abiotic and biotic dissolution and oxidation reactions. The challenge to disentangle biotic from abiotic pathways represents a key limitation of the present thesis but also highlights the environmental relevance of Mn^{3+}–NOL complexes as products of tightly coupled abiotic–biotic redox cycling. The experimental design in Chapter 3 allowed for the isolated consideration of abiotic reaction pathways. However, a deliberate neglect of contributions from biotic reaction pathways inevitably results in a potential distortion in Mn_T speciation when compared to natural systems. Nonetheless, the quantitative determination of Mn^{3+}–NOL complexes under both laboratory and field conditions suggests that the conventional $Mn^{2+} \leftrightarrow Mn^{IV}$ paradigm in soils needs reconsideration.

- *Abiotic redox pathways clearly drive Mn^{3+}–NOL complex formation, while biotic pathways remain an important yet unresolved research frontier. Hypothesis III is therefore partially confirmed.*

Hypothesis IV: *Mn^{3+}–NOL complexes are part of dissolved Mn_T under varying redox and pH conditions.*

To test this hypothesis, bulk soil from two horizons (AhBg and Bg) of a Calcaric Gleysol was incubated in a microcosm. Each incubation underwent two redox cycles (I: oxidizing → weakly reducing → moderately reducing → reoxidizing; II: oxidizing → strongly reducing → reoxidizing) as expressed by E_H to simulate typical redox fluctuations driven by waterlogging–aeration cycles (Chapter 4). This setup allowed Mn_T speciation under defined redox conditions.

Except under initial oxidizing conditions, Mn^{3+}–NOL complexes were abundant across all redox ($E_{H(pH\ 7)}$: +550 mV to –110 mV) and pH conditions (7.0–8.2). The influence of changing redox regimes on the formation of Mn^{3+}–NOL complexes was mainly expressed by the change of the predominant formation pathways. Under reducing conditions, abiotic and biotic reductive pathways dominated in the absence of O_2, whereas abiotic and biotic oxidative pathways clearly facilitated Mn^{3+}–NOL complex formation during aeration. Previous concepts largely treated Mn^{3+} as a transient species due to its assumed instability in aqueous systems and limited analytical accessibility. The present results

demonstrate that complexation with NOLs fundamentally alters the Mn^{2+}↔Mn^{IV} paradigm by stabilizing Mn^{3+} across fluctuating redox regimes. Conclusively, Mn^{3+}–NOL complexes are redox-active intermediates in one-electron transfer reactions in the “redox wheel” of Mn^{2+} and Mn^{IV}. It should be noted that the observations made were limited to the Calcaric Gleysol. Future studies should expand the experimental design to include soils subjected to waterlogging–aeration cycles and acidic conditions. However, these findings are not restricted to redoximorphic soils and can be transferred to other soil inherent environments. For example, anoxic microsites featuring sharp redox gradients at the anoxic–oxic interface can serve as dynamic hotspots (Lacroix et al., 2023). Rapid changes in redox conditions may shorten the frequency between Mn^{3+}–NOL complex formation and decay.

The formation and stabilization of Mn^{3+}–NOL complexes was demonstrated across a broad, environmentally relevant pH range (3.0–8.0). In the Dystric Cambisol, laboratory analyses revealed Mn^{3+}–NOL complex proportions ranging from 0–87% (pH: 3.0–7.0) relative to Mn_T (Chapter 3), similar to those observed in forest floor solutions (10–87%; pH: 3.4–6.3) and soil solutions (0.5–74%; pH: 3.9–4.7) (Chapter 2). Temporal patterns indicate that Mn^{3+}–NOL complexes are metastable under strongly acidic conditions but are stabilized under circumneutral conditions or continuously renewed via abiotic and biotic oxidation (Chapter 3). These results extend the integration of Mn^{3+}–NOL complexes into the Mn cycle to acidic conditions, whereas previous research applied Mn speciation only under circumneutral to weakly alkaline conditions (Madison et al., 2011, 2013; Oldham et al., 2017a–c).

In the investigated redoximorphic soils, these complexes constituted a major component of dissolved Mn_T under both laboratory and field conditions (Chapter 4), again showing that circumneutral to weakly alkaline conditions can contribute to the formation of Mn^{3+}–NOL complexes. Excess Ca^{2+} may competitively bind to deprotonated functional groups of NOLs, effectively blocking binding sites (Chapter 3). Since this process was not mechanistically resolved, it represents a key uncertainty and highlights the need for mechanistic investigations into competitive cation binding effects.

The quantitative results presented here demonstrate that the formation of Mn^{3+}–NOL complexes is not restricted to narrow redox or pH conditions at the investigated study sites. Instead, they highlight the pronounced dynamics of this redox-active species, which can form across a wide range of environmental settings. Consequently, Mn^{3+} has

the potential to influence biogeochemical cycling more strongly than previously assumed, particularly the C cycle but also other elemental cycles. Accordingly, the role of Mn^{3+} in biogeochemical processes should be regarded as more important than previously suggested.

- *In summary, these results demonstrate that Mn^{3+}–NOL complexes form and persist across a broad range of redox and pH conditions, supporting a revision of the conventional $Mn^{2+} \leftrightarrow Mn^{IV}$ paradigm. Hypothesis IV is therefore confirmed.*

Hypothesis V: *Dissolved Mn^{3+}, in the form of Mn^{3+}–NOL complexes, is a ubiquitous part of dissolved Mn_T in soil solutions.*

By integrating the preceding hypotheses, Hypothesis V addresses the thesis' central research question. Building on pioneering work in marine geochemistry (Madison et al., 2011; Oldham et al., 2015), the findings here demonstrate that Mn^{3+}, in the form of Mn^{3+}–NOL complexes, constitutes a substantial component of dissolved Mn_T in soil solutions across the investigated soil types under both laboratory and field conditions (Chapters 2–4). Consequently, Mn^{3+}–NOL complexes are as prevalent in soils as in marine environments (Madison et al., 2011, 2013; Oldham et al., 2015, 2017a–c). Because organically complexed Mn^{3+} can function as both electron acceptor and electron donor in one-electron-transfer reactions (Klewicki and Morgan, 1998), its quantification has broad environmental implications.

In forest ecosystems, Mn plays a critical role in SOM decomposition, soil organic C cycling, and CO_2 emission (Berg et al., 2007, 2015; Hofrichter, 2002; Stendahl et al., 2017; Whalen et al., 2018). Increased proportions of redox-reactive Mn^{3+}–NOL complexes relative to dissolved Mn_T accelerate decomposition rates of SOM, although microbial activity, competing metals, and soil mineralogy may modulate these effects. The high proportions of Mn^{3+}–NOL complexes in the forest soil (Chapters 2 and 3) support earlier interpretations of Jones et al. (2020) and Keiluweit et al. (2015) that reactive Mn^{3+}, rather than crystalline Mn oxides, is the predominant Mn species in the L and O soil horizons. Organic horizons likely represent hotspots of Mn^{3+}–NOL complex formation. Consistent with the proposed Mn^{3+} depth gradient (Jones et al., 2020), the results indicate a decreasing proportion of reactive Mn^{3+}–NOL complexes with increasing soil depth, from organic to

mineral horizons in non-limed and limed study areas (Chapter 2). Accordingly, Mn^{3+}–NOL complexes appear to be an integral component of the Mn cycle, exhibiting a distinct spatial distribution. In the future, additional dissolved Mn_T speciation data are required to confirm these trends. Evidence indicates that organically complexed Mn^{3+} can form abiotically, particularly under moderately acidic to circumneutral pH, in addition to biotic pathways (Chapter 3). Forest sites subjected to liming may experience enhanced SOM decomposition due to Mn^{3+}–NOL complexes, potentially supporting biotic pathways and increasing overall decomposition rates. Conversely, under strongly acidic conditions, complex formation is limited, slowing abiotic SOM degradation, which may be partially compensated by biotic processes (e.g., microbial decomposition).

Laboratory and field investigations in redoximorphic soils (Chapter 4) expanded the understanding of Mn^{3+}–NOL complexes as a component of the soil Mn cycle in two respects: their stability under reducing conditions and their dynamic formation during fluctuating redox conditions. Complex formation has been demonstrated across redox boundaries, from oxidizing to strongly reducing conditions, and their stability against strong reducing agents such as Fe^{2+} confirms their persistence under conditions traditionally assumed to favor Mn^{3+} reduction (Oldham et al., 2017b). Transitions between anaerobic and aerobic conditions promote both abiotic and biotic formation of Mn^{3+}–NOL complexes, facilitating rapid Mn redox cycling. Madison et al. (2013) reported similar findings for sediment porewaters along anoxic–oxic gradients. More recently, Jones et al. (2018) outlined Mn^{3+}–NOL complexes, formed at the anoxic–oxic interface, as important contributors to the oxidation of particulate organic C to CO_2, which is a potent greenhouse gas.

Complementary findings from Chapters 2–4 indicate that Mn^{3+}–NOL complexes constitute a substantial proportion of dissolved Mn_T across a wide range of redox and pH conditions. Although numerous studies have investigated redox- and pH-controlled Mn mobilization in soils under both laboratory (e.g., Gotoh and Patrick, 1972; Patrick and Henderson, 1981; Patrick and Jugsujinda, 1992; Schwab and Lindsay, 1983) and field conditions (e.g., Gao et al., 2002; Hseu et al., 2000; Mansfeldt, 2004), methodological limitations have generally precluded the explicit consideration of Mn^{3+}–NOL complexes. In retrospect, this omission indicates that reported Mn_T data are incomplete with respect to Mn speciation. Because Mn^{3+}–NOL complexes can act as either electron donors or

acceptors, the redox and buffering capacity of dissolved Mn_T in soil solutions has been underestimated. By adapting and validating the porphyrin method throughout this dissertation, this methodological advance enables future studies to explicitly resolve Mn redox dynamics at temporal and spatial scales previously inaccessible.

Overall, Mn^{3+}–NOL complexes are likely ubiquitous redox-reactive intermediates in soil solutions, facilitating one-electron transfer reactions in biogeochemical Mn cycling. The classical $Mn^{2+}\leftrightarrow Mn^{IV}$ paradigm has to be revised to include Mn^{3+}–NOL complexes as an integral component (Figure 5.1):

$$Mn^{2+}\leftrightarrow Mn^{3+}\text{–NOL complexes}\leftrightarrow Mn^{IV}.$$

- *This dissertation expands our understanding of dissolved Mn^{3+} as a substantial component of dissolved Mn_T in soil solutions, highlights its role in the redox cycle, and urges the reconsideration of the $Mn^{2+}\leftrightarrow Mn^{IV}$ paradigm. Although the results strongly support Mn^{3+}–NOL complexes as a widespread and functionally important part of dissolved Mn_T in soil solutions, hypothesis V cannot yet be fully resolved with respect to their ubiquity across all soil types and environmental conditions.*

Future perspectives

This thesis provides the first insights into Mn_T speciation in soils and identifies Mn^{3+}–NOL complexes as a significant component of soil solutions. Beyond establishing this foundational understanding, these findings highlight several key challenges and opportunities for future research aimed at elucidating the formation, stability, and environmental relevance of Mn^{3+}–NOL complexes.

Investigating a broader range of soil types is essential to confirm the ubiquity of Mn^{3+}–NOL complexes in soil solutions. Expanded field measurements and long-term monitoring would provide insights into the seasonal and spatial variability of Mn^{3+}–NOL complex formation and identify the key environmental drivers.

Targeted laboratory experiments should complement field observations. Combining the porphyrin method with advanced spectroscopic techniques (e.g., extended X-ray absorption fine structure, X-ray absorption near edge structure) would enable a more detailed characterization of NOL–Mn oxide interactions at the mineral–water interface. Employing well-defined components (e.g., model ligands, NOL extracts from

different soil types and horizons with varying NOL quality and quantity, and synthetic Mn oxide derivatives) may further clarify biotic and abiotic redox pathways of Mn^{3+}–NOL complex formation.

Structural and functional characterization of NOLs is critical for understanding their role in Mn^{3+}–NOL complex formation. Techniques such as EEM spectroscopy with subsequent parallel factor analysis, nuclear magnetic resonance spectroscopy, ATR FT-IR spectroscopy, and size-dependent DOM fractionation (e.g., 1 kDa, 10 kDa, 100 kDa) can identify functional groups and determine the relative contributions of LMW or HMW NOLs to Mn^{3+}–NOL formation.

Assessing matrix effects associated with co-occurring metals and sample coloration is crucial. Excess $Fe^{2+/3+}$ can interfere with absorption signals through strong coloration or by hindering T(4-CP)P-mediated substitution reactions, as observed in microcosm experiments. Similarly, forest floor solutions or soil solutions exhibiting more intense DOM-induced coloration than those investigated here may complicate Mn_T speciation analysis. Systematic assessment of these matrix effects is essential to develop standardized sample pretreatment protocols and ensure reliable Mn speciation.

The development of novel quantitative techniques for detecting dissolved Mn^{3+} species, whether organically or inorganically complexed, would enhance analytical precision and complement the porphyrin method, thereby improving predictive models of Mn cycling.

Finally, generating dissolved Mn_T speciation datasets that explicitly include Mn^{3+}–NOL complexes, as presented in this thesis, will enable refinement of biogeochemical models. Integrating field- and laboratory-based findings with ecosystem-scale processes will support the development of a more comprehensive conceptual framework for the Mn cycle and its coupling to other elemental cycles.

Collectively, these research directions provide a roadmap for advancing mechanistic understanding of Mn^{3+}–NOL complexes in terrestrial biogeochemical processes.

Final thoughts: Dissolved trivalent manganese – revising the paradigm

Building on the new insights into dissolved Mn_T speciation, this thesis necessitates a paradigm shift in our understanding of the Mn cycle in soils.

Old Mn^{2+}↔Mn^{IV} paradigm: Dissolved Mn_T in soil solutions has traditionally been assumed to exist predominantly as Mn^{2+}, while Mn^{3+} was considered highly unstable due to rapid disproportionation. Consequently, the Mn "redox wheel" was conceptualized as cycling exclusively between dissolved Mn^{2+} and solid Mn^{IV} (Figure 1.5).

Revised Mn^{2+}↔Mn^{3+}–NOL complexes↔Mn^{IV} paradigm: This thesis provides evidence that dissolved Mn^{3+} can be stabilized by NOLs, forming Mn^{3+}–NOL complexes. These complexes act as redox-active intermediates, constituting an integral component of the soil Mn redox cycle (Figure 5.1).

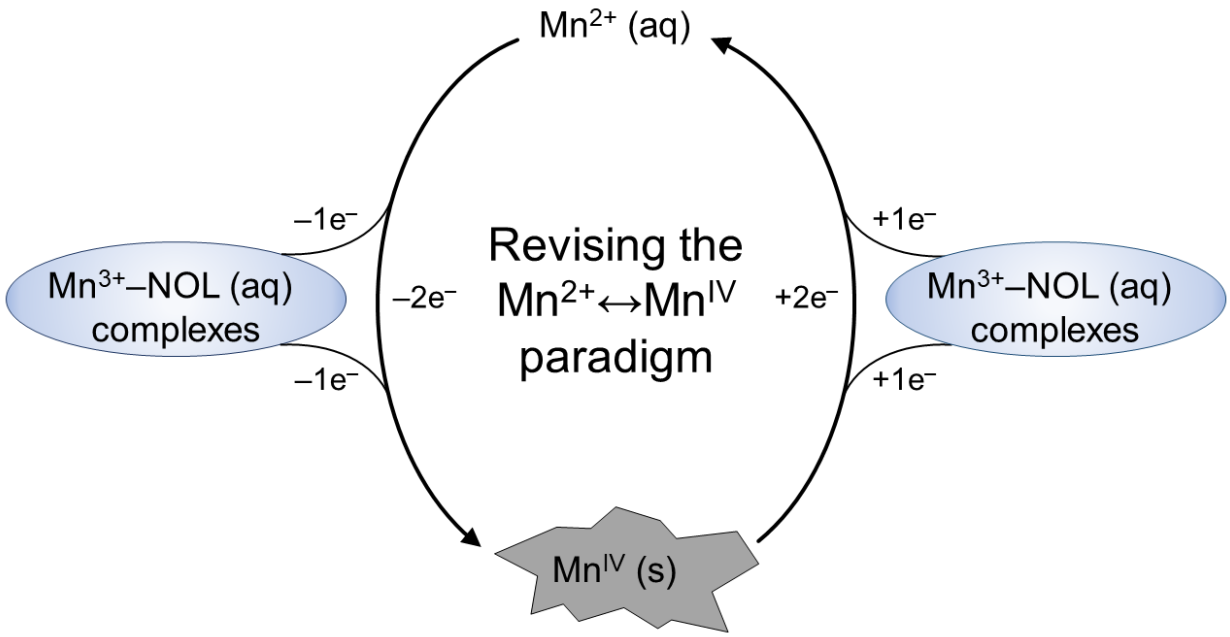

Figure 5.1 Schematic representation of the revised manganese (Mn) redox cycle incorporating Mn^{3+}–NOL complexes, thereby refining the conventional Mn^{2+}↔Mn^{IV} paradigm. NOL = natural organic ligand (own illustration).

Chapter 6: References

Chapter 1 and 5

Adriano D. C. (2001). *Trace Elements in Terrestrial Environments – Biogeochemistry, Bioavailability, and Risk of Metals* (2nd ed.). Springer, New York.

Aiken G. R., Hsu-Kim H. and Ryan J. N. (2011). Influence of dissolved organic matter on the environmental fate of metals, nanoparticles, and colloids. *Environmental Science & Technology* **45**, 3196–3201.

Altzitser S. S., Mishael Y. G. and Schwartz N. (2025). Organic pollutant oxidation on manganese oxides in soils – the role of calcite indicated by geoelectrical and chemical analyses. *SOIL* **11**, 95–104.

Amelung W., Blume H.-P., Fleige H., Horn R., Kandeler E., Kögel-Knabner I., Kretzschmar R., Stahr K. and Wilke B. M. (2018). *Scheffer/Schachtschabel – Lehrbuch der Bodenkunde* (17th ed.). Springer, Berlin.

Banerjee D. and Nesbitt H. W. (1999). XPS study of reductive dissolution of birnessite by oxalate: rates and mechanistic aspects of dissolution and redox processes. *Geochimica et Cosmochimica Acta* **63**, 3025–3038.

Banerjee D. and Nesbitt H. W. (2001). XPS study of dissolution of birnessite by humate with constraints on reaction mechanism. *Geochimica et Cosmochimica Acta* **65**, 1703–1714.

Berg B., Steffen K. T. and McClaugherty C. (2007). Litter decomposition rate is dependent on litter Mn concentrations. *Biogeochemistry* **82**, 29–39.

Berg B., Erhagen B., Johansson M.-B., Nilsson M., Stendahl J., Trum F. and Vesterdal L. (2015). Manganese in the litter fall-forest floor continuum of boreal and temperate pine and spruce forest ecosystems – a review. Forest Ecology and Management **358**, 248–260.

Biedermann G. and Palombari R. (1978). On the hydrolysis of the manganese(III) ion. *Acta Chemica Scandinavica* A **32**, 381–390.

Biesaga M., Pyrzyńska K. and Trojanowicz M. (2000). Porphyrins in analytical chemistry. A review. *Talanta* **51**, 209–224.

Bolan N. S., Park J. H., Robinson B., Naidu R. and Huh K. Y. (2011). Phytostabilization: a green approach to contaminant containment. In D. L. Sparks (Ed.), *Advances in Agronomy* (Vol. 112). Academic Press, San Diego, pp. 145–204.

Borch T., Kretzschmar R., Kappler A., Van Cappellen P., Ginder-Vogel M., Voegelin A. and Campbell K. (2010). Biogeochemical redox processes and their impact on contaminant dynamics. *Environmental Science & Technology* **44**, 15–23.

Brewer P. G. and Spencer D. W. (1971). Colorimetric determination of manganese in anoxic waters. *Limnology and Oceanography* **16**, 107–110.

Chantigny M. H., Angers D. A., Kaiser K. and Kalbitz K. (2007). Extraction and characterization of dissolved organic matter. In M. R. Carter and E. G. Gregorich (Eds.), *Soil Sampling and Methods of Analysis* (2nd ed.). CRC Press, Boca Raton, pp. 617–635.

Chin C. S., Johnson K. S. and Coale K. H. (1992). Spectrophotometric determination of dissolved manganese in natural waters with 1-(2-pyridylazo)-2-naphthol: application to analysis in situ in hydrothermal plumes. *Marine Chemistry* **37**, 65–82.

Chiswell B. and O'Halloran K. R. (1991). Comparison of three colorimetric methods for the determination of manganese in freshwaters. *Talanta* **38**, 641–647.

Cloyd R. A., Koren S. A. and Abisambra J. F. (2018). Manganese-enhanced magnetic resonance imaging: overview and central nervous system applications with a focus on neurodegeneration. *Frontiers in Aging Neuroscience* **10**, 403.

Cotrufo M. F. and Lavallee J. M. (2022). Soil organic matter formation, persistence, and functioning: A synthesis of current understanding to inform its conservation and regeneration. In D. L. Sparks (Ed.), *Advances in Agronomy* (Vol. 172). Academic Press, San Diego, pp. 1–66.

Crossgrove J. and Zheng W. (2004). Manganese toxicity upon overexposure. *NMR in Biomedicine* **17**, 544–553.

Daugherty E. E., Gilbert B., Nico P. S. and Borch T. (2017). Complexation and redox buffering of iron(II) by dissolved organic matter. *Environmental Science & Technology* **51**, 11096–11104.

Davies G. (1969). Some aspects of the chemistry of manganese(III) in aqueous solution. *Coordination Chemistry Reviews* **4**, 199–224.

Dellwig O., Schnetger B., Brumsack H.–J., Grossart H.–P. and Umlauf L. (2012). Dissolved reactive manganese at pelagic redoxclines (part II): hydrodynamic conditions for accumulation. *Journal of Marine Systems* **90**, 31–41.

Dion H. G. and Mann P. J. G. (1946). Three-valent manganese in soils. *The Journal of Agricultural Science* 36, 239–245.

Dorau K. and Mansfeldt T. (2016). Comparison of redox potential dynamics in a diked marsh soil: 1990 to 1993 versus 2011 to 2014. *Journal of Plant Nutrition and Soil Science* **179**, 641–651.

Duckworth O. W. and Sposito G. (2005a). Siderophore–manganese(III) interactions. I. Air-oxidation of manganese(II) promoted by desferrioxamine B. *Environmental Science & Technology* **39**, 6037–6044.

Duckworth O. W. and Sposito G. (2005b). Siderophore–manganese(III) interactions. II. Manganite dissolution promoted by desferrioxamine B. *Environmental Science & Technology* **39**, 6045–6051.

Ehrlich H. L. (1987). Manganese oxide reduction as a form of anaerobic respiration. *Geomicrobiology Journal* **5**, 423–431.

Faulkner K. M., Stevens R. D. and Fridovich I. (1994). Characterization of Mn(III) complexes of linear and cyclic desferrioxamines as mimics of superoxide dismutase activity. *Archives of Biochemistry and Biophysics* **310**, 341–346.

Forschungsanstalt für Waldökologie und Forstwirtschaft (FAWF) Rheinland-Pfalz (2016), Dauerbeobachtungsfläche 101: Idar-Oberstein (Umweltkontrollstation). Available at: https://fawf.wald.rlp.de/indexphp?id=12306 (Last accessed: February 2026).

Feng X. H., Zhai L. M., Tan W. F., Liu F. and He J. Z. (2007). Adsorption and redox reactions of heavy metals on synthesized Mn oxide minerals. *Environmental Pollution* **147**, 366–373.

Fernando D. R. and Lynch J. P. (2015). Manganese phytotoxicity: new light on an old problem. *Annals of Botany* **116**, 313–319.

Fischel M. H. H., Clarke C. E. and Sparks D. L. (2024). Arsenic sorption and oxidation by natural manganese-oxide-enriched soils: reaction kinetics respond to varying environmental conditions. *Geoderma* **441**, 116715.

Gao S., Tanji K. K., Scardaci S. C. and Chow A. T. (2002). Comparison of redox indicators in a paddy soil during rice-growing season. *Soil Science Society of America Journal* **66**, 805–817.

Gilkes R. J. and McKenzie R. M. (1988). Geochemistry and mineralogy of manganese in soils. In R. D. Graham, R. J. Hannam and N. C. Uren (Eds.), *Manganese in Soils and Plants*. Springer, Dordrecht, pp. 23–35.

Gmach M. R., Cherubin M. R., Kaiser K. and Cerri C. E. P. (2020). Processes that influence dissolved organic matter in the soil: a review. *Scientia Agricola* **77**, e20180164.

Gotoh S. and Patrick W. H. (1972). Transformation of manganese in a waterlogged soil as affected by redox potential and pH. *Soil Science Society of America Proceedings* **36**, 738–742.

Gottfreund J., Schmitt G. and Schweisfurth R. (1983). Chemische und mikrobiologische Untersuchungen an Komplexverbindungen des Mangans. *Mitteilungen der Deutschen Bodenkundschaftlichen Gesellschaft* 38, 325–330.

Greathouse J. A., Johnson K. L. and Greenwell C. (2014). Interaction of natural organic matter with layered minerals: recent developments in computational methods at the nanoscale. *Minerals* **4**, 519–540.

Hatten J. and Liles G. (2019). A ‘healthy’ balance – The role of physical and chemical properties in maintaining forest soil function in a changing world. In M. Busse, C. P. Giardina, D. M. Morris and D. S. Page-Dumroese (Eds.), *Developments in Soil Science* (Vol. 36). Elsevier, Amsterdam, pp. 373–396.

He Z. L., Shentu J. and Yang X. E. (2010). Manganese and selenium. In P. S. Hooda (Ed.), *Trace Elements in Soils*. Wiley, West Sussex, pp. 481–495.

Heintze S. G. and Mann P. J. G. (1949). Studies on soil manganese. *The Journal of Agricultural Science* **39**, 80–95.

Hem J. D. (1963). Chemical equilibria and rates of manganese oxidation. Chemistry of manganese in natural water. U.S. Geological Survey Water–Supply Paper 1667–A. United States Government Printing Office, Washington. Available at: https://pubs.usgs.gov/wsp/1667a/report.pdf (Last accessed: February 2026)

Herndon E. M., Martínez C. E. and Brantley S. L. (2014). Spectroscopic (XANES/XRF) characterization of contaminant manganese cycling in a temperate watershed. *Biogeochemistry* **121**, 505–517.

Herbert B. E. and Bertsch P. M. (1995). Characterization of dissolved and colloidal organic matter in soil solution: A review. In W. W. McFee and J. M. Kelly (Eds.), *Carbon Forms and Functions in Forest Soils*. Soil Science Society of America, Madison, pp. 63–88.

Hoffmann D. (1991). Sea level changes at the Schleswig-Holsteinian North Sea coast during the last 3000 years. *Quaternary International* **9**, 61–65.

Hofrichter M. (2002). Review: lignin conversion by manganese peroxidase (MnP). *Enzyme and Microbial Technology* **30**, 454–466.

Hseu Z.-Y., Chen Z.-S. and Leu I.-Y. (2000). Soil solution composition, water tables, and redox potentials of anthraquic ultisols in a toposequence. *Soil Science* **165**, 869–880.

IUSS Working Group WRB (2022). World Reference Base for Soil Resources. International soil classification system for naming soils and creating legends for soil maps (4th ed.). International Union of Soil Sciences (IUSS), Vienna, Austria. Available at: https://www.isric.org/sites/default/files/WRB_fourth_edition_2022-12-18.pdf (Last accessed: February 2026).

Ishii H., Koh H. and Satoh K. (1982). Spectrophotometric determination of manganese utilizing metal ion substitution in the cadmium-α,β,γ,δ-tetrakis(4-carboxylphenyl)porphine complex. *Analytica Chimica Acta* **136**, 347–352.

Jahn H. A. and Teller E. (1937). Stability of polyatomic molecules in degenerate electronic states. I. Orbital degeneracy. *Proceedings of the Royal Society A* **161**, 220–235.

Johnson K. L., McCann C. M., Wilkinson J.-L., Jones M., Tebo B. M., West M., Elgy C., Clarke C. E., Gowdy C. and Hudson-Edwards K. A. (2018). Dissolved Mn(III) in water treatment works: prevalence and significance. *Water Research* **140**, 181–190.

Jones M. E., Nico P. S., Ying S., Regier T., Thieme J. and Keiluweit M. (2018). Manganese-driven carbon oxidation at oxic-anoxic interfaces. *Environmental Science & Technology* **52**, 12349–12357.

Jones M. R., Luther III G. W., Mucci A. and Tebo B. M. (2019). Concentrations of reactive Mn(III)-L and MnO_2 in estuarine and marine waters determined using spectrophotometry and the leuco base, leucoberbelin blue. *Talanta* **200**, 91–99.

Jones M. E., LaCroix R. E., Zeigler J., Ying S. C., Nico P. S. and Keiluweit M. (2020). Enzymes, manganese, or iron? Drivers of oxidative organic matter decomposition in soils. *Environmental Science & Technology* **54**, 14114–14123.

Kaiser K. and Kalbitz K. (2012). Cycling downwards – dissolved organic matter in soils. *Soil Biology & Biochemistry* **52**, 29–32.

Keiluweit M., Nico P., Harmon M. E., Mao J., Pett-Ridge J. and Kleber M. (2015). Long-term litter decomposition controlled by manganese redox cycling. *Proceedings of the National Academy of Sciences of the United States of America* **112**, E5253–E5260.

Kim B., Lingappa U. F., Magyar J., Monteverde D., Valentine J. S., Cho J. and Fischer W. (2022). Challenges of measuring soluble Mn(III) species in natural samples. *Molecules* **27**, 1661–1671.

Kleber M., Bourg I. C., Coward E. K., Hansel C. M., Myneli S. C. B. and Nunan N. (2021). Dynamic interactions at the mineral–organic matter interface. *Nature Reviews Earth & Environment* **2**, 402–421.

Klewicki J. K. and Morgan J. J. (1998). Kinetic behavior of Mn(III) complexes of pyrophosphate, EDTA and citrate. *Environmental Science & Technology* **32**, 2916–2922.

Kögel-Knabner I. (2002). The macromolecular organic composition of plant and microbial residues as inputs to soil organic matter. *Soil Biology & Biochemistry* **34**, 139–162.

Kostka J. E., Luther III G. W. and Nealson K. H. (1995). Chemical and biological reduction of Mn(III)-pyrophosphate complexes: potential importance of dissolved Mn(III) as an environmental oxidant. *Geochimica et Cosmochimica Acta* **59**, 885–894.

Krumbein W. E. and Altman H. J. (1973). A new method for the detection and enumeration of manganese oxidizing and reducing microorganisms. *Helgoland Marine Research* **25**, 347–356.

Lacroix E. M., Aeppli M., Boye K., Brodie E., Fendorf S., Keiluweit M., Naughton H. R., Noel V. and Sihi D. (2023). Consider the anoxic microsite: acknowledging and appreciating spatiotemporal redox heterogeneity in soils and sediments. *ACS Earth and Space Chemistry* **7**, 1592–1609.

Lanczos C. (1956). *Applied Analysis.* Prentice-Hall, New Jersey.

Lavallee J. M., Soong J. L. and Cotrufo M. F. (2020). Conceptualizing soil organic matter into particulate and mineral-associated forms to address global change in the 21st century. *Global Change Biology* **26**, 261–273.

Lee S. A., Lee J. J., You G. R., Choi Y. W. and Kim C. (2015). Distinction between Mn(III) and Mn(II) by using a colorimetric chemosensor in aqueous solution. *RCS Advances* **5**, 95618–95630.

Lee S., Pyun J. and Chae M. S. (2025). Next-generation electrode materials for safe and sustainable manganese-based aqueous batteries. *ChemElectroChem* **12**, e202500306.

Leeper G. W. (1947). The forms and reaction of manganese in the soil. *Soil Science* **63**, 79–94.

Li Z., Huang B., Huang J., Chen G., Zhang C., Nie X., Luo N., Yao H., Ma W. and Zeng G. (2015). Influence of removal of organic matter and iron and manganese oxides on cadmium adsorption by red paddy soil aggregates. *RCS Advances* **5**, 90588–90595.

Li H., Santos F., Butler K. and Herndon E. (2021). A critical review on the multiple roles of manganese in stabilizing and destabilizing soil organic matter. *Environmental Science & Technology* **55**, 12136–12152.

Li H., Fu B., Huang H., Wu S., Ge J., Zhang J., Li F. and Qu P. (2022). Catalytic degradation of organic pollutants by manganese oxides: a comprehensive review. *Environmental Pollutants and Bioavailability* **34**, 395–406.

Li F., Yin H., Zhu T. and Zhuang W. (2024). Understanding the role of manganese oxides in retaining harmful metals: insights into oxidation and adsorption mechanisms at microstructure level. *Eco-Environment & Health* **3**, 89–106.

Liu M., Han X., Liu C.-Q., Guo L., Ding H. and Lang Y. (2021). Differences in the spectroscopic characteristics of wetland dissolved organic matter binding with Fe^{3+}, Cu^{2+}, Cd^{2+}, Cr^{3+} and Zn^{2+}. *Science of the Total Environment* **800**, 149476.

Lv Y., Han C., Zhu Y., Zhang T., Yao S., He Z., Dai L. and Wang L. (2021). Recent advances in metals and metal oxides as catalysts for vanadium redox flow battery: properties, structures, and perspectives. *Journal of Materials Science & Technology* **75**, 96–109.

Luther III G. W. (2005). Manganese(ii) oxidation and Mn(IV) reduction in the environment–two one-electon transfer steps versus a single two-electron step. *Geomicrobiology Journal* **22**, 195–203.

Luther III G. W., Madison A. S., Mucci A., Sundby B. and Oldham V. E. (2015). A kinetic approach to assess the strengths of ligands bound to soluble Mn(III). *Marine Chemistry* **173**, 93–99.

Madison A. S., Tebo B. M. and Luther III G. W. (2011). Simultaneous determination of soluble manganese(III), manganese(II) and total manganese in natural (pore)waters. *Talanta* **84**, 374–381.

Madison A. S., Tebo B. M., Mucci A., Sundby B. and Luther III G. W. (2013). Abundant porewater Mn(III) is a major component of the sedimentary redox system. *Science* **341**, 875–878.

Mansfeldt T. (2003). In situ long-term redox potential measurements in a dyked marsh soil. *Journal of Plant Nutrition and Soil Science* **166**, 210–219.

Mansfeldt T. (2004). Redox potential of bulk soil and soil solution concentration of nitrate, manganese, iron, and sulfate in two Gleysols. *Journal of Plant Nutrition and Soil Science* **167**, 7–16.

Martin S. T. (2005). Precipitation and dissolution of iron and manganese oxides. In V. H. Grassian (Ed.), *Environmental Catalysis*. CRC Press, Boca Raton, pp. 61–82.

Millaleo R., Reyes-Díaz M., Ivanov A. G., Mora M. L. and Alberdi M. (2010). Manganese as essential and toxic element for plants: transport, accumulation and resistance mechanisms. *Journal of Soil Science and Plant Nutrition* **10**, 476–494.

Matsanga N., Tangstad M., Kalenga M. W. and Nheta W. (2025). Manganese alloy production–a review of the SAF process and emerging technologies. *ACS Omega* **10**, 44840–44857.

Morgan J. J. (2005). Kinetics of reaction between O_2 and Mn(II) species in aqueous solutions. *Geochimica et Cosmochimica Acta* **69**, 35–48.

Myers C. R. and Nealson K. H. (1988a). Bacterial manganese reduction and growth with manganese oxide as the sole electron acceptor. *Science* **240**, 1319–1321.

Myers C. R. and Nealson K. H. (1988b). Microbial reduction of manganese oxides: interactions with iron and sulfur. *Geochimica et Cosmochimica Acta* **52**, 2727–2732.

Nash J. C. (2016). *nlmrt: Functions for Nonlinear Least Squares Solution.* R package version 2016.3.2. Available at: https://CRAN.R-project.org/package=nlmrt (Last accessed: February 2026)

Nebbioso A. and Piccolo A. (2013). Molecular characterization of dissolved organic matter (DOM): a critical review. *Analytical and Bioanalytical Chemistry* **405**, 109–124.

Obeng S. K., Kulhánek M., Balík J., Černý J. and Sedlář O. (2024). Manganese: from soil to human health–a comprehensive overview of its biological and environmental significance. *Nutrients* **16**, 3455.

Oldham V. E., Owings S. M., Jones M. R., Tebo B. M. and Luther III G. W. (2015). Evidence for the presence of strong Mn(III)-binding ligands in the water column of the Chesapeake Bay. *Marine Chemistry* **171**, 58–66.

Oldham V. E., Mucci A., Tebo B. M. and Luther III G. W. (2017a). Soluble Mn(III)−L complexes are abundant in oxygenated waters and stabilized by humic ligands. *Geochimica et Cosmochimica Acta* **199**, 238–246.

Oldham V. E., Miller M. T., Jensen L. T. and Luther III G. W. (2017b). Revisiting Mn and Fe removal in humic rich estuaries. *Geochimica et Cosmochimica Acta* **209**, 267–283.

Oldham V. E., Jones M. R., Tebo B. M. and Luther III G. W. (2017c). Oxidative and reductive processes contributing to manganese cycling at oxic-anoxic interfaces. *Marine Chemistry* **195**, 122–128.

Oldham V. E., Siebecker M. G., Jones M. R., Mucci A., Tebo B. M. and Luther III G. W. (2019). The speciation and mobility of Mn and Fe in estuarine sediments. *Aquatic Geochemistry* **25**, 3–26.

Oldham V. E., Chmiel R., Hansel M. H., DiTullio G. R., Rao D. and Saito M. (2021). Inhibited manganese oxide formation hinders cobalt scavenging in the Ross Sea. *Global Biogeochemical Cycles* **35**, e2020GB006706.

Oscarson D. W., Huang P. M., Defosse C. and Herbillon A. (1981). Oxidative power of Mn(IV) and Fe(III) oxides with respect to As(III) in terrestrial and aquatic environments. *Nature* **291**, 50–51.

Paul E. A. (2016). The nature and dynamics of soil organic matter: plant inputs, microbial transformation, and organic matter stabilization. *Soil Biology & Biochemistry* **98**, 109–126.

Patrick W. H. and Henderson R. E. (1981). Reduction and reoxidation cycles of manganese and iron in flooded soil and in water solution. *Soil Science Society of America Journal* **45**, 855–859.

Patrick W. H. and Jugsujinda, A. (1992). Sequential reduction and oxidation of inorganic nitrogen, manganese, and iron in flooded soil. *Soil Science Society of America Journal* **56**, 1071–1073.

Patrick W. H. and Turner F. T. (1968). Effect of redox potential on manganese transformation in waterlogged soil. *Nature* **220**, 476–478.

Peña A. (2022). A comprehensive review of recent research concerning the role of low molecular weight organic acids on the fate of organic pollutants in soil. *Journal of Hazardous Materials* **434**, 128875.

Post J. E. (1999). Manganese oxide minerals: crystal structures and economic and environmental significance. *Proceedings of the National Academy of Sciences of the United States of America* **96**, 3447–3454.

Ramstedt M., Andersson B. M., Shchukarev A. and Sjöberg S. (2004). Surface properties of hydrous manganite (γ-MnOOH). A potentiometric, electroacoustic, and X-ray photoelectron spectroscopy study. *Langmuir* **20**, 8224–8229.

Ramstedt M. and Sjöberg S. (2005). Phase transformations and proton promoted dissolution of hydrous manganite (γ-MnOOH). *Aquatic Geochemistry* **11**, 413–431.

R Core Team (2021). *R: A language and environment for statistical computing.* R Foundation for Statistical Computing, Vienna, Austria. Available at: https://www.R-project.org/ (Last accessed: February 2026).

Reddy K. R., DeLaune R. D. and Inglett P. W. (2023). *Biogeochemistry of Wetlands. Science and Applications* (2nd ed.). CRC Press, Boca Raton.

Remucal C. K. and Ginder-Vogel M. (2014). A critical review of the reactivity of manganese oxides with organic contaminants. *Environmental Science: Processes & Impacts* **16**, 1247–1266.

Rudolph W. W. and Irmer G. (2013). Hydration and speciation studies of Mn^{2+} in aqueous solution with simple monovalent anions (ClO_4^-, NO_3^-, Cl^-, Br^-). *Dalton Transactions* **42**, 14460.

Rudnick R. L. and Gao S. (2014). Composition of the continental crust. In K. Turekian and H. Holland (Eds.), *Treatise on Geochemistry* (2nd ed., Vol. 4). Elsevier, Oxford, pp. 1–51.

Schmidt M. W. I., Torn M. S., Abiven S., Dittmar T., Guggenberger G., Janssens I. A., Kleber M., Kögel-Knabner I., Lehmann J., Manning D. A. C., Nannipieri P., Rasse D. P., Weiner S. and Trumbore S. E. (2011). Persistence of soil organic matter as an ecosystem property. *Nature* **487**, 49–56.

Schnetger B. and Dellwig O. (2012). Dissolved reactive manganese at pelagic redoxclines (part I): a method for determination based on field experiments. *Journal of Marine Systems* **90**, 23–30.

Schwab A. P. and Lindsay W. L. (1983). The effect of redox on the solubility and availability of manganese in a calcareous soil. *Soil Science Society of America Journal* **47**, 217–220.

Scott M. J. and Morgan J. J. (1996). Reactions at oxide surfaces. 2. Oxidation of Se(IV) by synthetic birnessite. *Environmental Science & Technology* **30**, 1990–1996.

Sparrow L. A. and Uren N. C. (2014). Manganese oxidation and reduction in soils: effects of temperature, water potential, pH and their interactions. *Soil Research* **52**, 483–494.

Stendahl J., Berg B. and Lindahl B. D. (2017). Manganese availability is negatively associated with carbon storage in northern coniferous forest humus layers. *Scientific Reports* **7**, 15487.

Stepniewska Z., Bucior K. and Bennicelli R.P. (2004). The effects of MnO_2 on sorption and oxidation of Cr(III) by soils. *Geoderma* **122**, 291–296.

Stumm W. and Morgan J. J. (1996). *Aquatic Chemistry* (3rd ed.). Wiley Interscience, New York.

Stone A. T. and Morgan J. J. (1984a). Reduction and dissolution of manganese(III) and manganese(IV) oxides by organics. 1. Reaction with hydroquinone. *Environmental Science & Technology* **18**, 450–456.

Stone A. T. and Morgan J. J. (1984b). Reduction and dissolution of manganese(III) and manganese(IV) oxides by organics. 2. Survey of the reactivity of organics. *Environmental Science & Technology* **18**, 617–624.

Sun Y., Im J., Shobnam N., Fanourakis S. K., He L., Anovitz L. M., Erickson P. R., Sun H., Zhuang J. and Löffler F. E. (2021). Degradation of adsorbed Bisphenol A by soluble Mn(III). *Environmental Science & Technology* **55**, 13014–13023.

Tan W., Lu S., Liu F., Feng X., He J. and Koopal L. K. (2008). Determination of the point-of-zero charge of manganese oxides with different methods including an improved salt titration method. *Soil Science* **173**, 277–286.

Tebo B. M. (1991). Manganese(II) oxidation in the suboxic zone of the Black Sea. *Deep-Sea Research* **38**, 883–905.

Tebo B. M., Bargar J. R., Clement B. G., Dick G. J., Murray K. J., Parker D., Verity R. and Webb S. M. (2004). Biogenic manganese oxides: properties and mechanisms of formation. *Annual Review of Earth and Planetary Sciences* **32**, 287–328.

Thibault de Chanvalon, A. and Luther III G. W. (2019). Mn speciation at nanomolar concentrations with a porphyrin competitive ligand and UV–vis measurements. *Talanta* **200**, 15–21.

Thurman E. M. (1985). *Organic geochemistry of natural waters*. Junk Publishers, Dordrecht.

Trouwborst R. E., Clement B. G., Tebo B. M., Glazer B. T. and Luther III G. W. (2006). Soluble Mn(III) in suboxic zones. *Science* **313**, 1955–1957.

Villalobos M., Bargar J. and Sposito G. (2005). Mechanisms of Pb(II) sorption on a biogenic manganese oxide. *Environmental Science & Technology* 39, 569–576.

Wiberg N., Wiberg E. and Holleman A. F. (2017). *Holleman/Wiberg – Anorganische Chemie* (103rd ed.). de Gruyter, Berlin.

Wang X., Yao J., Wang S., Pan X., Xiao R., Huang Q., Wang Z. and Qu R. (2018). Phototransformation of estrogens mediated by Mn(III), not by reactive oxygen species, in the presence of humic acids. *Chemosphere* **201**, 224–233.

Wang X., Jones M. R., Pan Z., Lu X., Deng Y., Zhu M. and Wang Z. (2024). Trivalent manganese in dissolved forms: occurrence, speciation, reactivity and environmental geochemical impact. *Water Research* **263**, 122198.

Webb S. M., Dick G. J., Bargar J. R. and Tebo B. M. (2005). Evidence for the presence of Mn(III) intermediates in the bacterial oxidation of Mn(II). *Proceedings of the National Academy of Sciences of the United States of America* **102**, 5558–5563.

Weng L., Temminghoff E. J. M., Lofts S., Tipping E. and Van Riemsdijk W. H. (2002). Complexation with dissolved organic matter and solubility control of heavy metals in a sandy soil. *Environmental Science & Technology* **36**, 4804–4810.

Whalen E. D., Smith R. G., Stuart Grandy A. and Frey S. D. (2018). Manganese limitation is a mechanism for reduced decomposition in soils under atmospheric nitrogen deposition. *Soil Biology & Biochemistry* **127**, 252–263.

Wu R., Yao F., Li X., Shi C., Zang X., Shu X., Liu H. and Zhang W. (2022). Manganese Pollution and its remediation: a review of biological removal and promising combination strategies. *Microorganisms* **10**, 2411.

Xi H., Hong J., Zhu Z., Xu Y., Sun Y., Zhang C., Wang H., Wang W. and Long X. (2025). Geochemical behavior and environmental implications of Mn(III): synthesis, redox dynamics, and pollutant removal. *Journal of Water Process Engineering* **79**, 109005.

Xyla A. G., Sulzberger B., Luther III G. W., Hering J. G., Van Cappellen P. and Stumm W. (1992). Reductive dissolution of manganese(III,IV) (hydr)oxides by oxalate: the effect of pH and light. *Langmuir* **8**, 95–103.

Yakushev E., Pakhomova S., Sørenson K. and Skei J. (2009). Importance of the different manganese species in the formation of water column redox zones: observations and modeling. *Marine Chemistry* **117**, 59–70.

Zhang S., Li B., Chen Y., Zhu M., Pedersen J. A., Gu B., Wang Z., Li H., Liu J., Zhou X.-Q., Hao Y.-Y., Jiang H., Liu F., Liu Y.-R. and Yin H. (2023). Methylmercury degradation by trivalent manganese. *Environmental Science & Technology* **57**, 5988–5998.

Zhu-Barker X., Cavazos A. R., Ostrom N. E., Horwath W. R. and Glass J. B. (2015). The importance of abiotic reactions for nitrous oxide production. *Biogeochemistry* **126**, 251–267.

Zsolnay Á. (1996). Dissolved humus in soil waters. In A. Piccolo (Ed.), *Humic Substances in Terrestrial Ecosystems*. Elsevier, Amsterdam, pp. 171–223.

Zsolnay Á. (2003). Dissolved organic matter: artefacts, definitions, and functions. *Geoderma* **113**, 187–209.

Appendix

Dissolved Mn_T speciation, including Mn^{2+}, Mn^{3+}–NOL_{weak} complexes, and Mn^{3+}–NOL_{strong} complexes, was performed using a custom-developed R code for the three-parameter equation (A–1) and the five-parameter equation (A–2). The utilization of red font is indicative of sections of the code that require modification when executing the code for each individual sample.

A–1: R-Code for kinetic modeling (three-parameter equation)

```
{r}
# Definition of the workingspace:
setwd("C:/Users/... ")                                  # define working directory
library("pacman")
packages <- c("qpcR", "readxl", "tidyverse", "nlmrt")    # R packages needed
pacman::p_load(packages, character.only = T)
rm(list=ls())
options(scipen = 999)

# Definition of the data and the needed parameters:
data <- "sample.xlsx"                                   # loading of the .xlsx sheet
save <- "porphyrin method/sample A1.png"                # Location of the resulting image of the fit
title <- "sample A1 2360"                               # image title (e.g., sample name + sample volume)
time_shift <- 0                                         # shifts curve to origin of the coordinate system
volume <- 2360                                          # sample pipetting volume in µL
background <- 0                                         # sample background-colorization correction

# Definition of the start parameters as well as the lower and upper estimation constraints:
st <- c(a = 0.1, k = 0.01, t0 = 1)                      # define start of parameter estimation
low <- c(a = 0, k = 0.0001, t0 = 0)                     # define lower boundaries
up <- c(a = 1, k = 0.1, t0 = 10)                        # define upper boundaries

# Loading and modification of the data:
df <- read_excel(data)
names(df) <- c("time", "absorption")
df <- df %>%
 mutate(time = time + time_shift) %>%
 mutate(absorption = absorption - background) %>%
 mutate(concentration = 0) %>%
 #mutate(concentration = (absorption*10*3000/volume*54.94)/(0.9534*1000)) # mg L-1

# calculating in µmol L-1; 10 = cuvette pathlength; 0.9534 = absorption coefficient
mutate(concentration = (((absorption*10*3000/volume*54.94)/(0.9534*1000))/(54938))*(1000*1000)) # µmol L-1

# Definition of the model function:
eq <- concentration ~ a*(1-exp(-k*(time-t0)))           # three-parameter modeling equation

# Fitting of the function:
fit <- wrapnls(formula = eq, data = df, start = st, lower = low, upper = up, trace = TRUE)

# Plotting of the data:
par(mar = c(5, 7.5, 4, 3) + 0.1)
plot(concentration~time, df, type = "p", pch = 4, cex = 3, lwd = 3, main = title, cex.main = 4, font.main =
20, bty = "n",
     ylim = c(0, 30),
     xlim = c(0, 300),
     yaxs = "i", xaxs = "i", cex.axis = 2, ylab = "", xlab = "", las = 1)
title(ylab = expression("Mn"[T]*" (µmol L"^-1*")"), line = 4.3, cex.lab = 3)
title(xlab = "Time (s)", line = 3.3, cex.lab = 3)
#abline(v=90, col="blue")
```

```
# Plotting of the model fit:
x = df$time
y = fitted(fit)
lines(y~x, col ="red", lwd = 3)
coefs <- coef(fit)
RMSE <- RMSE(fit, which = NULL)                          # root mean square

# Creating a legend:
legendA <- bquote(Mn[T] == .(format(coefs [1], digits = 5))*~µM~L^-1 * "," ~~ k == .(format(coefs [2], digits
= 4))*~s^-1)
legendB <- bquote(RMSE == .(format(RMSE, digits = 4)) * "," ~~ Comment == "/")
legendC <- bquote(time_shift == "11 s" * "," ~~ t0 == .(format(coefs [3], digits = 3)))
text(150, 2.5, legendA, cex = 3)
text(150, 2.25, legendB, cex = 3)
text(150, 2, legendC, cex = 3)

# Saving Plot:
dev.print(png, save, height = 1000, width = 1400)
```

A–2: R-Code for kinetic modeling (five-parameter equation)

```
{r}
#| echo: false
# Definition of the workingspace:
setwd("C:/Users/... ")                                   # define working directory
library("pacman")
packages <- c("qpcR", "readxl", "tidyverse", "nlmrt")    # R packages needed
pacman::p_load(packages, character.only = T)
rm(list=ls())
options(scipen = 999)

# Definition of the data and the needed parameters:
data <- "sample.xlsx"                                    # loading of the .xlsx sheet
save <- "porphyrin method/sample A2.png"                 # Location of the resulting image of the fit
title <- "sample A1 2360"                                # image title (e.g., sample name + sample volume)
time_shift <- 0                                          # shifts curve to origin of the coordinate system
volume <- 2360                                           # sample pipetting volume in µL
background <- 0                                          # sample background-colorization correction

# Definition of the start parameters as well as the lower and upper estimation constraints:
st <-  c(a1 = 0.1, k1 = 0.01,  a2 = 0.1,  k2 = 0.001,  t0 = 1)    # define start of parameter estimation
low <- c(a1 = 0,   k1 = 0.001, a2 = 0,    k2 = 0.0001, t0 = 0)    # define lower boundaries
up <-  c(a1 = 10,  k1 = 0.1,   a2 = 10,   k2 = 0.05,   t0 = 10)  # define upper boundaries

# Loading and modifying the data:
df <- read_excel(data)
names(df) <- c("time", "absorption")
df <- df %>%
 mutate(time = time + time_shift) %>%
 mutate(absorption = absorption - background) %>%
 mutate(concentration = 0) %>%
 #mutate(concentration = (absorption*10*3000/volume*54.94)/(0.9534*1000))        # mg L^-1

# calculating in µmol L^-1; 10 = cuvette pathlength; 0.9534 = absorption coefficient
 mutate(concentration = (((absorption*10*3000/volume*54.94)/(0.9534*1000))/(54938))*(1000*1000)) # µmol L^-1


# Definition of the model function:
eq <- concentration ~ (a1*(1-exp(-k1*(time-t0)))+a2*(1-exp(-k2*(time-t0))))      # five-parameter equation

# Fitting of the function:
fit <- wrapnls(formula = eq, data = df, start = st, lower = low, upper = up, trace = TRUE, control=
list(maxiter=1000, warnOnly=TRUE))

# Plotting of the data:
par(mar = c(5, 7.5, 4, 3) + 0.1)
```

```
plot(concentration~time, df, type = "p", pch = 4, cex = 3, lwd = 3, cex.main = 4, font.main = 20, bty="n",
yaxs = "i", xaxs = "i", cex.axis = 2, ylab = "", xlab = "", las = 1, main = title,
     ylim = c(0, 30),
     xlim = c(0, 300))
title(ylab = expression("Mn"[T]*" (µmol L"^-1*")"), line = 4.3, cex.lab = 3)
title(xlab = "Time (s)", line = 3.3, cex.lab = 3)
abline(v=90, col="blue")

# Plotting of the model fit:
x = df$time
y = fitted(fit)
lines(y~x, col ="red", lwd = 3)
coefs <- coef(fit)
RMSE <- RMSE(fit, which = NULL)

# Creating a legend:
legendA <- bquote(Mn(II) == .(format(coefs [1], digits = 3))*~µmol~L^-1
 * "," ~~ k[1] == .(format(coefs [2], digits = 4))*~s^-1)
legendB <- bquote(Mn(III) == .(format(coefs [3], digits = 3))*~µmol~L^-1
* "," ~~ k[2] == .(format(coefs [4], digits = 4))*~s^-1)
legendC <- bquote(RMSE == .(format(RMSE, digits = 4))
 * "," ~~ comment == "/")
legendD <- bquote(time_shift == "20 s" * "," ~~ t0 == .(format(coefs [5], digits = 3)))
text(400, 15, legendA, cex =3)
text(400, 12.5, legendB, cex =3)
text(400, 10, legendC, cex =3)
text(400, 7.5, legendD, cex =3)

# Saving the plot:
dev.print(png, save, height = 1000, width = 1400)
```